Two Photon Exchange Radiative Correction to Electron-Proton Elastic Scattering

by

Jaseer Ahmed

A Thesis submitted to the Faculty of Graduate Studies of
The University of Manitoba
in partial fulfilment of the requirements of the degree of

Doctor of Philosophy

Department of Physics and Astronomy
University of Manitoba

Abstract

The extraction of hadron structure information from precision electron-proton elastic scattering experiments to date requires precise knowledge of the electromagnetic interaction via multi-photon exchange. The proton structure-dependent radiative correction two-photon exchange (TPE) is a promising source to resolve the existing discrepancy in the measurement of the proton electric to magnetic form factor ratio $\mu_p G_E/G_M$, but contains significant uncertainty in its calculation. We use a recently developed dispersive approach to compute TPE corrections to elastic electron-proton scattering, including contributions from hadronic $J^P = 1/2^\pm$ and $3/2^\pm$ resonant intermediate states below 1.8 GeV. For the transition amplitudes from the proton ground state to the resonant excited states we employ new exclusive meson electroproduction data from CLAS at $Q^2 \lesssim 5$ GeV^2, and assess for the first time the effects of finite widths for the Breit-Wigner resonances. Among the resonant states, the $N(1520)3/2^-$ becomes dominant for $Q^2 \gtrsim 2$ GeV^2, with an opposite sign compared to the $\Delta(1232)3/2^+$ correction, leading to an overall increase of the TPE correction to the cross section at higher Q^2 values. The results are in good agreement with recent e^+p to e^-p cross section ratio and polarization transfer measurements, and provide a partial resolution of the electric to magnetic form factor ratio discrepancy. This same model is also applied to the inelastic processes involving the imaginary part of TPE amplitudes, as seen in single-spin asymmetries, with either beam or target being polarized normal to the scattering plane.

Acknowledgements

At first, I would like to thank my advisor Dr. Peter Blunden for his constant support and intellectual input during this long journey to reach the final moment. Thank you Dr. Blunden, it was pleasure to work with you. I remember the mental support I have got from your words every time I have visited your office whenever I felt down regarding any academic issues and even beyond including homesickness. I would also like to thank Dr. Wally Melnitchouk for his suggestions, ideas and everything to help me in bringing the outcomes of the projects.

Thanks to the excellent, friendly and helpful staff of the department of Physics and Astronomy, University of Manitoba. Special thanks to Susan Beshta. I never saw her gloomy face! Thanks to Maiko Langelaar for the help every time I had an issue with my desktop.

I acknowledge the funding from University of Manitoba Graduate Fellowship and Sir Gordon Wu Scholarship during the first four years of my PhD program.

In the end, I come to my family. It is my parents for whom I have come to this point today. I remember my recently deceased father who gave me the freedom of taking decisions of my life since early childhood. Thanks are never enough for my mother who never had the opportunity to get any academic learning but shaped me the way I am today by her smart guidance with the will of almighty Allah. I acknowledge here the inspiration and support I have got from my siblings during the journey. I never had any unfulfilled desire due to my siblings.

Thanks to my lovely wife for being with me. Thanks for your support during the tough times in last couple of years. Sorry to my daughter for not giving enough care due to busyness with my thesis.

Finally, thanks to almighty Allah for everything.

Contents

Abstract i

Acknowledgements ii

List of Figures vi

List of Tables xv

1 Introduction 1
- 1.1 Scattering kinematics . . . 2
- 1.2 Hadronic current operator parametrization . . . 3
- 1.3 The proton structure information from cross section measurement . . . 4
  - 1.3.1 Form factors from Rosenbluth separation formula . . . 6
  - 1.3.2 Alternative measurement of the form factors . . . 8
- 1.4 Overview of the work . . . 12
- 1.5 Outline . . . 13

2 Revisit to the $\mu_p G_E/G_M$ discrepancy 15
- 2.1 Early reanalyses of Rosenbluth separation data . . . 15
- 2.2 Experimental effort to reconcile $\mu_p G_E/G_M$ ratio discrepancy . . . 16
- 2.3 Radiative corrections to e-p elastic scattering . . . 18
- 2.4 Recent reanalysis of the Rosenbluth separation data . . . 25
- 2.5 Potential solution to the $\mu_p G_E/G_M$ discrepancy . . . 28
- 2.6 Summary and discussion . . . 29

3 Two-photon exchange 30
- 3.1 Two-photon exchange amplitude . . . 31
  - 3.1.1 TPE in terms of generalized form factors . . . 34
  - 3.1.2 Infrared divergence . . . 38
- 3.2 TPE calculation review . . . 42
  - 3.2.1 High Q^2 partonic and pQCD approach . . . 43

3.2.2 Direct loop integral . . . 45
3.2.2.1 Elastic intermediate state . . . 45
3.2.2.2 Excited resonance intermediate state . . . 47
3.2.3 Dispersive method . . . 51
3.3 Phenomenological extraction of TPE effect . . . 56
3.4 Direct measurement of TPE correction . . . 57
3.5 Polarization observables . . . 65
3.6 Summary and discussion . . . 67

4 Dispersive Method of TPE Calculation 68
4.1 Dispersive method . . . 68
4.1.1 General framework . . . 69
4.1.2 Analytical continuation to unphysical region . . . 71
4.2 TPE in e-μ scattering . . . 74
4.2.1 Passarino-Veltman (PV) functions . . . 75
4.2.2 Dispersive method . . . 77
4.2.3 Results and conclusion . . . 78

5 Numerical Evaluation of TPE in e-p Elastic Scattering 81
5.1 TPE with elastic nucleon intermediate state . . . 82
5.2 Resonance transition current operators . . . 85
5.3 Form factors from electrocouplings . . . 89
5.3.1 Resonance electrocouplings . . . 89
5.3.2 Relations between form factors and electrocouplings . . . 90
5.3.3 Input electrocouplings . . . 92
5.4 Resonance finite widths . . . 100

6 Results and Discussions 103
6.1 Generalized form factors . . . 103
6.1.1 Imaginary part . . . 104
6.1.2 Real part . . . 105
6.2 TPE correction to the e^--p elastic scattering cross section . . . 109
6.2.1 Resonance intermediate state contribution to TPE . . . 109
6.2.2 Nonzero resonance widths . . . 115
6.2.3 Spin, isospin and parity dependence . . . 119
6.3 TPE-sensitive observables . . . 121
6.3.1 e^+p to e^-p elastic scattering ratio . . . 122
6.3.2 Polarization observables . . . 125
6.3.3 Electric to magnetic form factor ratio $\mu_p G_E/G_M$ . . . 126

7 Imaginary Part of TPE Amplitude 130
7.1 Single Spin Asymmetry (SSA) . . . 130
7.2 Review of SSA . . . 131

7.3 Calculation of SSA 134

8 SSA Results and Discussions **140**
8.1 Beam normal single spin asymmetry 140
8.1.0.1 Experimental values 143
8.2 Target normal single spin asymmetry (A_n) 147
8.2.0.1 Comparison with other sources 149

9 Conclusions **151**

A Scattering Kinematics in CM frame **154**

B Generalized form factors **157**
B.1 Imaginary part of form factors for $\Delta(1232)3/2^+$ 157
B.2 Imaginary part of form factors for all resonances 158
B.3 Real part of the form factors 159

C Maximon-Tjon vs. Mo-Tsai prescriptions **160**

D Width effect in A_n **162**

Bibliography **164**

List of Figures

1.1 Elastic scattering of an electron (with four-momentum k) from a proton (p) to a final state electron (k') and recoil proton (p'), with $q = k - k' = p' - p$ the four-momentum transfer, in the Born approximation. 3

1.2 Extraction of the electric (G_E) and magnetic (G_M) form factors from the reduced Born cross section σ_R^{Born} using the Rosenbluth (LT) separation method. The data points are taken from Ref. [22] and the line is a linear fit to the data. 7

1.3 Proton electric to magnetic form factor ratio $\mu_p G_E/G_M$ extracted using Rosenbluth LT separation method. The blue squared data are by Walker *et al.* [2], black triangles from Walker's global analysis [2], and the red circles correspond to the extraction of Andivahis *et al.* [3]. The black solid line corresponds to the scaling $\mu_p G_E/G_M = 1$. Note that some overlapping LT data points are slightly offset for clarity. 9

1.4 The electric to magnetic form factor ratio $\mu_p G_E/G_M$ extracted by (a) the PT measurement, and (b) the LT separation method (along with the PT method result), are shown for several values of Q^2 ranging up to ~ 8.5 GeV^2. The green band is a nonlinear fit to the PT data with 99% confidence level. The LT data in (b) are taken from three updated sources of Refs. [2, 3]. For LT data, some overlapping points are slightly offset for clarity. Note that the scale on the right is different. 11

2.1 Proton electric to magnetic form factor ratio from the Super Rosenbluth measurement of Qattan *et al.* [4] (open black diamonds), along with the data from Refs. [2, 3]. The green band corresponds to a non-linear fit to polarization transfer data [7–9]. 18

2.2 Feynman diagrams for next to leading order radiative corrections. The top row is for electron (left two) and proton (right two) self energy corrections. First diagram of the bottom row corresponds to the vacuum polarization, and the next two correspond to $e^- - \gamma - e^-$ and proton$-\gamma-$proton vertex corrections. 19

2.3 Feynman diagrams for single real photon emission from either electron or proton external legs in e-p scattering. 23

2.4 The radiative tail predicted using soft photon approximation (blue dashed) and from the sum of soft and hard internal bremsstrahlung (red solid line).The points are simulated data from Ref. [81] 27

2.5 TPE contaminated LT data (open diamonds) for proton electric to magnetic form factor ratio, $\mu_p G_E/G_M$, from Ref. [35], and the corresponding TPE corrected data (green circles and red squares) by Blunden *et al.* [37] are compared with the polarization transfer data(black open circles)[7–9] on the left. On the right a similar comparison is shown, but here the PT data are TPE corrected (red circles). The TPE corrected LT points (green circles) on the left panel are obtained assuming a linear relation of the TPE cross section with ε in the range 0.5 to 0.8, while the points with red squares used the ε range of 0.2 to 0.9. Plots are taken from Ref. [37]. 29

3.1 Two-photon exchange amplitude Feynman diagram for s-channel box (left panel) and u channel x-box (right panel). The two exchanged photons carry momenta q_1 and q_2. 31

3.2 Difference between the IR divergent parts of the TPE cross section from Refs. [76] and [75] as a function of virtual photon polarization ε at fixed values of $Q^2 = 0.2$, 1.0, 3.0, and 5.0 GeV^2. 42

3.3 e-p elastic scattering in the (a) single photon exchange, and (b,c) TPE approximations, at the quark level interaction. The kinematics is same as those in Fig. 3.1. Three constituent quarks of proton are represented by three internal lines with arrows to demonstrate the interaction with individual photons. Both photons interact with same quark in (b) and different quarks in (c). Other combinations of gluon exchange are available in Ref. [45]. 43

3.4 Reduced cross section $\sigma_{\rm R}$ scaled by μ_p^2 times the dipole form factor G_D^2 as a function of ε at $Q^2 = 4$ and 5 GeV^2, calculated by Afanasev *et al.* [43]. The solid red and dashed blue curves correspond to the TPE corrected $\sigma_{\rm R}$ using two different models for the GPD. The dotted blue line is the result obtained by using $G_{E,M}$ from polarization transfer data [5, 6]. Plots are adjusted from Ref. [43]. 44

3.5 The generalized TPE amplitude $\delta\mathcal{G}_M/G_M$ as a function of Q^2 at (a) $\varepsilon = 0.5$, and (b) $\varepsilon = 0.1$, calculated by Borisyuk and Kobushkin in pQCD framework (solid line). The corresponding results in hadronic approach with two different form factors is also compared. Plots are taken from Ref. [45]. 45

3.6 TPE cross section correction δ, relative to Mo-Tsai soft photon approximation, from the nucleon intermediate state in e-p elastic scattering for $Q^2 = 0.001$ to 1.0 GeV^2 (left) and $Q^2 = 1.0$ to 6.0 GeV^2 (right) [37]. Plots are adjusted from Ref. [29]. 46

3.7 $\Delta(1232)$ intermediate state contribution to the TPE total cross section δ as a function of virtual photon polarization ε at $Q^2 = 3$ GeV^2. The red dotted line corresponds to the evaluation with electric and magnetic form factors of dipole form, having $\Gamma_\Delta = 0.84$, by Kondratyuk *et al.* [40]. The black solid and blue dashed lines are the results from Ref. [38]. Figure source is Ref. [29, 38]. 49

3.8 TPE cross section correction from nucleon (a,b) and $\Delta(1232)3/2^+$ (c,d) resonance intermediate states calculated by Graczyk [100] and Lorenz *et al.* [101]. The effect of nucleon form factor variations are compared in (a,c). Q^2 values are given in units of GeV^2. Diagrams are adjusted from Refs. [100, 101] 50
3.9 Extraction of the imaginary part of the TPE amplitude by putting the intermediate lepton and hadron in the TPE box diagram on-shell. The corresponding crossed-box has no imaginary part. 53
3.10 TPE cross section correction from $\Delta(1232)3/2^+$ resonance intermediate state calculated by Blunden *et al.* [46] using direct loop integral (blue dashed and green dotted lines) and dispersive method (red solid line) as a function of (a) ε, and (b) beam energy E, at $Q^2 = 3.0$ GeV^2. For simplicity only the magnetic form factor is considered here. Diagram taken from Ref. [46]. 54
3.11 TPE cross section correction δ, in percent, from πN intermediate states evaluated using dispersion formalism by Borisyuk *et al.* [50] at fixed Q^2: (a) 1.0 GeV^2, and (b) 5.0 GeV^2. Figure courtesy of Ref. [50]. 55
3.12 TPE amplitudes Y_E (red dotted), Y_M (blue dashed), and Y_3 (dark red dot-dashed) from phenomenological extraction of Ref. [105] as a function of ε at Q^2: (a) 0.5 GeV^2, (b) 1 GeV^2, and (c) 3 GeV^2. 57
3.13 Measured $R_{2\gamma}$ plotted as a function of Q^2 (left panel) in a logarithmic scale and as a function of virtual photon polarization ε (right panel) from the measurements of Refs. [108–113]. Source of data points are labelled in the plot legends using authors name and year of publication. The line in the right panel is the fit reproduced from the reanalysis of Ref. [36]. Plots are taken from Ref. [29]. 60
3.14 Measured $R_{2\gamma}$ by VEPP-3 experiment [115] (black solid circles) at Novosibirsk plotted as a function of ε for mono-energetic beams of energy $E = 1.594$ GeV for run-I (left panel), and $E = 0.998$ GeV for run-II (right panel). The statistical uncertainties are represented by the error bars, while the shaded bands correspond to the total systematic uncertainty and the bin size for each data point. The estimated lines correspond to Refs. [48] (cyan dot-dashed), [37] (red thin solid), [21] (blue thick), [118] (grey long-dashed), [36] (magenta dashed), and [106] (black dotted). Plots are taken from the original work of Ref. [115]. 61
3.15 Measured $R_{2\gamma}$ by CLAS experiment [116] at Jefferson Lab plotted as a function of ε (left panel) at fixed values of averaged $\langle Q^2 \rangle = 0.85$ (top) and 1.45 GeV^2 (bottom), and as a function of Q^2 (right panel) at fixed averaged $\langle \varepsilon \rangle = 0.45$ (top) and 0.88 (bottom). Plots are taken from the original work of Ref. [116]. 62

3.16 Measured $R_{2\gamma}$ by OLYMPUS experiment [117] at DESY plotted as a function of ε (corresponding Q^2 scale is also shown) at the beam energy $E = 2.01$ GeV. Compared are the theoretical predictions of Blunden *et al.* [46] (blue dashed and solid lines), Tomalak *et al.* [51] (Green solid), and the phenomenological fit of Bernauer *et al.* [21]. Plot is taken from the original work of Ref. [117]. 64

3.17 TPE effect on (a) the longitudinal polarization transfer P_L relative to the Born approximation $P_L^{(0)}$, and (b) the ratio R_{TL}, as a function of ε at fixed $Q^2 \approx 2.5$ GeV^2. The data points (black solid circles) with the associated systematic and statistical uncertainty are taken from Ref. [119], while the blue dashed and the solid red lines are the calculated results by Blunden and Melnitchouk [46] with nucleon and sum of nucleon with $\Delta(1232)3/2^+$ intermediate states, respectively. 66

4.1 Specification of physical and unphysical regions of the dimensionless variable ν covered by the dispersive integral of Eq. (4.4c) at fixed values of four-momentum transfer squared Q^2. The shaded region bordered by solid red line corresponds to the physical region, and the green dashed (nucleon), blue dashed ($\Delta(1232)$), dark-red dotted ($N(1520)$), and orange dot-dashed ($N(1720)$) lines specify the $\nu_{\rm min}$ of the fixed Q^2 dispersive integral. The black horizontal line represents a fixed value of Q^2. 72

4.2 Imaginary part of the generalized form factors F_1' (top row), F_2' (middle row), and G_a' (bottom row) for TPE in e-μ scattering at a representative four-momentum transfer squared $Q^2 = 3$ GeV^2. The red long-dashed curve represents the result using the numerical contour integration, while the blue dotted curve corresponds to that using the imaginary parts of the Passarino-Veltman functions obtained by direct loop integrals. The left column shows the results in the incident electron energy (E) range from 0.001 to 1 GeV, and the right column is for the range from $E = 1$ to 100 GeV. 79

4.3 TPE cross section correction in unpolarized e-μ scattering at $Q^2 = 3$ GeV^2 as a function of virtual photon polarization ε. The red long-dashed curve (a) used the dispersive method to get the real part of the generalized form factors from the imaginary parts obtained by numerical contour integration. The blue dotted curve (b) used the same method to get the real part from the imaginary part of F_1', F_2', and G_a' using the imaginary parts of the Passarino-Veltman functions obtained by direct loop integrals. The green dashed curve (c) used the direct loop integrals using LoopTools. 80

5.1 Nucleon electric (G_E) (a) and magnetic (G_M) (b) form factors parametrization by J.J. Kelly [126] (red long-dashed), Arrington *et al.* (AMT) [72] (blue dotted), and Venkat *et al.* [127] (black dashed). G_E is scaled by the standard dipole form factor G_D, and G_M is scaled by proton magnetic moment μ_p times G_D. 84

5.2 Two-photon exchange relative cross section correction δ_N (in percent) due to elastic nucleon intermediate state alone, (a) as a function of virtual photon polarization ε at $Q^2 = 3$ GeV^2, and (b) as a function of Q^2 at fixed $\varepsilon = 0.2$. The results represented by the red long-dashed curve uses the parametrization of Kelly [126], blue dotted curve uses AMT parametrization [72], and black dashed curve uses Venkat et.al. [127]. . 84

5.3 Parametrizations of transverse ($A_{1/2}$, $A_{3/2}$), and longitudinal ($S_{1/2}$) electrocouplings of photon-nucleon to $\Delta(1232)3/2^+$ resonance transition by CLAS [54, 125] (red dashed line) and by Aznauryan *et al.* [46, 53] (blue dot-dashed line) as function of Q^2. The squared dark-red points are the CLAS $N\pi$ electroproduction data [54], and the blue triangles are the PDG18 value [129] at $Q^2 = 0$ GeV^2. 93

5.4 Comparison of magnetic (G_M^*), electric (G_E^*), and Coulomb (G_C^*) form factor parametrizations for the transition into $\Delta(1232)3/2^+$ intermediate state from Refs. [53, 54] as a function of Q^2. 94

5.5 Phenomenological fit [125] of the transverse $A_{3/2}$ (red long-dashed) and $A_{1/2}$ (blue dotted), and the longitudinal $S_{1/2}$ (green dashed) electrocouplings for the spin-3/2 states $N(1520)3/2^-$, $\Delta(1700)3/2^-$, and $N(1720)3/2^+$. The red squared ($A_{3/2}$), blue circled ($A_{1/2}$), and green triangle ($S_{1/2}$) data are from Ref. [54]. The dark-red points for $A_{3/2}$ and $A_{1/2}$ are the PDG [125] values at $Q^2 = 0$ GeV^2. 95

5.6 CLAS fit [125] of the electrocouplings $A_{1/2}$ (blue dotted) and $S_{1/2}$ (green dashed) for the spin-1/2 states $N(1440)1/2^+$, $N(1535)1/2^-$, $\Delta(1620)1/2^-$, $N(1650)1/2^-$, and $N(1710)1/2^+$. The blue circled ($A_{1/2}$) and green squared ($S_{1/2}$) data are from Ref. [54]. The dark-red circled data for $A_{1/2}$ are the PDG [125] values at $Q^2 = 0$ GeV^2. 98

6.1 Imaginary parts of the generalized TPE form factors F_1' (a,b), F_2' (c,d), and G_a' (e,f) versus ε at fixed $Q^2 = 3$ GeV^2 for the nine resonance intermediate states $\Delta(1232)3/2^+$, $N(1440)1/2^+$, $N(1520)3/2^-$, $N(1535)1/2^-$, $\Delta(1620)1/2^-$, $N(1650)1/2^-$, $\Delta(1700)3/2^-$, $N(1710)1/2^+$, and $N(1720)3/2^+$ contributions. The plot legends are as identified in (e) and (f). 104

6.2 Generalized TPE form factors F_1' (a,b), F_2' (c,d), and G_a' (e,f), scaled by the dipole form factor G_D, versus ε at fixed $Q^2 = 1$ GeV^2 (left column) and 5 GeV^2 (right column) for the nucleon elastic (red dashed lines), $\Delta(1232)3/2^+$ (blue long-dashed lines), $N(1520)3/2^-$ (green dot-dashed lines), $N(1720)3/2^+$ (black dotted lines), and total TPE (red solid lines) contributions. 107

6.3 Generalized TPE form factors $\mathcal{G}_E$ (a,b) and $\mathcal{G}_M$ (c,d), scaled by the dipole form factor G_D, at fixed $\varepsilon = 0.2$ for low Q^2 ($Q^2 \leq 2$ GeV^2, left column) and high Q^2 ($1 \leq Q^2 \leq 5$ GeV^2, right column), for the nucleon elastic (red dashed lines), $\Delta(1232)3/2^+$ (blue long-dashed lines), $N(1520)3/2^-$ (green dot-dashed lines), $N(1720)3/2^+$ (black dotted lines), and total TPE (red solid lines) contributions. 108

6.4 TPE cross section correction δ from $\Delta(1232)3/2^+$ resonance intermediate state as a function of ε at fixed values of Q^2: (a) 1 GeV^2, (b) 3 GeV^2, and (c) 5 GeV^2. The blue dot-dashed curve represents the result using Aznauryan [53] parametrization of G_M^*, G_E^*, and G_C^*, while the red dashed curve shows that using CLAS parametrization [54, 125]. 110

6.5 Relative contributions δ (in percent) to the TPE cross section for the nine spin-1/2 and spin-3/2 nucleon and Δ intermediate state resonances, as indicated in the legend, versus the virtual photon polarization ε for fixed Q^2 values: (a) 0.5 GeV^2, (b) 1 GeV^2, (c) 2 GeV^2, (d) 3 GeV^2, and (d) 5 GeV^2. Note the vertical scale is different in each panel. 111

6.6 Contributions to the TPE correction δ (in %) versus the virtual photon polarization ε for (a) nucleon only, and (b) all spin-parity $1/2^\pm$ and $3/2^\pm$ states including the nucleon, at $Q^2 = 0.2$ GeV^2 (green dashed line), 0.5 GeV^2 (dark red long-dashed), 1 GeV^2 (red solid), 3 GeV^2 (orange dot-dashed),4 GeV^2 (black dotted), and 5 GeV^2 (blue dashed). The shaded bands in (b) correspond to the uncertainty propagated from the input electrocouplings. 112

6.7 Contributions to the TPE correction δ (in %) versus Q^2 at backward scattering angles, $\varepsilon = 0.2$, for (a) nucleon only (blue dashed line), $N + \Delta(1232)$ (green dotted) and the sum of all resonances (red solid line, with uncertainty band), and (b) the major individual contributors at the same kinematics, including the $\Delta(1232)$ (red solid), $N(1440)$ (black dashed), $N(1520)$ (blue solid), $N(1535)$ (green solid), $\Delta(1700)$ (orange dot-dashed), and $N(1720)$ (blue dashed). 113

6.8 Effect of a finite resonance width on the TPE correction δ (in %) from three significant resonance intermediate states, $\Delta(1232)3/2^+$ (a–c), $N(1520)3/2^-$ (d–f), and $N(1720)3/2^+$ (g–i), as a function of ε at fixed Q^2 values. The kinematical kinks in the zero-width results (blue dashed lines) are smoothed out by the effect of the nonzero, constant width (red solid lines). 116

6.9 Comparison of the TPE correction δ (in %) computed for resonances with zero width (blue dashed lines), constant width (red solid lines) and a dynamical width (green dotted lines) for $Q^2 = 1$ GeV^2 (left panels) and 3 GeV^2 (right panels). Contributions from the $\Delta(1232)3/2^+$ (a–b) and $N(1520)3/2^-$ (c–d) states are shown separately, along with the sum of all resonance contributions (e–f). 118

6.10 Comparison between the contributions to the TPE correction δ (in %) from intermediate state resonances with spin $J = 1/2$ and $J = 3/2$ (a–b), isospin $I = 1/2$ and $I = 3/2$ (c–d), and even parity $P = +1$ and odd parity $P = -1$ (e–f), for $\varepsilon = 0.2$ (left columns) and $\varepsilon = 0.9$ (right columns). The nucleon-only contribution (black dotted lines), which is not included in the other curves, and the total (red solid lines) are shown for comparison in each panel. 120

6.11 Ratio $R_{2\gamma}$ of e^+p to e^-p elastic cross sections from CLAS [116] (a) versus Q^2 for fixed averaged $\langle\varepsilon\rangle = 0.45$, and (b) $\langle\varepsilon\rangle = 0.88$, (c) versus ε for fixed averaged $\langle Q^2\rangle = 0.85$ GeV^2, and (d) $\langle Q^2\rangle = 1.45$ GeV^2, compared with the nucleon only (blue dashed lines), sum of nucleon and $\Delta(1232)$ (green dot-dashed lines), and sum of all intermediate state contributions (red solid lines). The experimental statistical and systematic uncertainties are indicated by the (black) inner and (grey) outer error bars, respectively. 123

6.12 Ratio $R_{2\gamma}$ of e^+p to e^-p elastic cross sections versus ε from the VEPP-3 experiment [115] for beam energy (a) $E = 0.998$ GeV, and (b) $E = 1.594$ GeV, compared with the nucleon only (blue dashed lines), sum of nucleon and $\Delta(1232)$ (green dot-dashed lines), and sum of all intermediate state contributions (red solid lines). The experimental statistical and systematic uncertainties are indicated by the (black) inner and (grey) outer error bars, respectively. 124

6.13 Ratio $R_{2\gamma}$ of e^+p to e^-p elastic cross sections versus ε from the OLYMPUS experiment [117] with beam energy $E = 2.01$ GeV, compared with the nucleon only (blue dashed lines), sum of nucleon and $\Delta(1232)$ (green dot-dashed lines), and sum of all intermediate state contributions (red solid lines). The experimental statistical and systematic uncertainties are indicated by the (black) inner and (grey) outer error bars, respectively. 124

6.14 Effect of TPE corrections on polarization observables from the GEp2γ experiment at Jefferson Lab [119] for (a) longitudinal polarization P_L relative to the Born level result $P_L^{(0)}$, and (b) polarization transfer ratio R_{TL} at $Q^2 = 2.49$ GeV^2, compared with calculations including nucleon only (blue dashed lines), sum of nucleon and $\Delta(1232)$ (green dot-dashed lines), and sum of all intermediate state contributions (red solid lines). The experimental statistical and systematic uncertainties are indicated by the (black) inner and (grey) outer error bars, respectively. 126

6.15 Reduced cross section $\sigma_R^{\rm Born}$ at $Q^2 = 4$ GeV^2, scaled by τ times the dipole form factor squared G_D^2. Open circles are the original data points from Ref. [3]. Filled circles (slightly offset for clarity) include improved standard RCs from Ref. [39], together with the TPE corrections from the present work. The weighted least squares fits (solid lines) determine G_E^2 and G_M^2. Data points from the 8 GeV spectrometer are shown in red, while the data point from the 1.6 GeV spectrometer (which is separately normalized [3]) is shown in blue. 128

6.16 (a) Ratio of the proton electric to magnetic form factors, $\mu_p G_E/G_M$, versus Q^2, extracted using LT separation data [2–4]. A nonlinear fit to the combined PT results [5–9] at the 99% confidence limit is shown by the green band. (b) The ratio $\mu_p G_E/G_M$ extracted from a reanalysis of the LT data using improved standard RCs from Ref. [39], together with the TPE effects from the present work. 128

8.1 Elastic nucleon and resonance intermediate states contributions to the beam normal single spin asymmetry B_n, along with the total, as a function of the centre-of-mass scattering angle θ_{cm} at three representative beam energies E: (a) 0.5 GeV, (b) 1.0 GeV, and (c) 3.026 GeV, in the target rest (Lab) frame. 141
8.2 Non-zero finite resonance width effect on the calculated total beam normal single spin asymmetry B_n at three representative beam energies E_{Lab}: (a) 0.5 GeV, (b) 1.0 GeV, and (c) 3.026 GeV. The dashed red line corresponds to zero width approximation and the solid blue line represents the results considering constant total decay width of each resonance. . . 142
8.3 Beam normal single spin asymmetry B_n as a function of the centre-of-mass scattering angle θ_{cm} at the kinematics of the Q_{weak} [138] experiment. The red line represents the B_n from nucleon intermediate state alone, while the blue line accounts all the 4 and 3-star, spin-1/2, and -3/2 resonances along with the elastic nucleon. The data point is the measured B_n by Q_{weak} collaboration. A magnified version is presented in the right panel. 144
8.4 Beam normal single spin asymmetry B_n as a function of the centre-of-mass scattering angle θ_{cm} at the kinematics of (a) HAPPEX Collaboration [60], (b-d) G0 Collaboration [58, 59]. The red line represents the nucleon intermediate state contribution, while the blue line accounts all the 4 and 3-star, spin-1/2, and -3/2 resonances along with elastic nucleon. 145
8.5 B_n vs. θ_{cm} plots at the kinematics of the PVA4 Collaboration [62–64]. The filled circles are the most updated data in the forward angles from Ref. [64], filled squares in the backward angles are from Ref. [63], and the filled triangles are from Ref. [62]. 146
8.6 Elastic nucleon and individual resonance intermediate state contributions to the target normal single spin asymmetry A_n, along with the total, as a function of θ_{cm} at five representative beam energies E: (a) 0.5 GeV, (b) 1.0 GeV, (c) 1.245 GeV, (d) 2.425 GeV, and (e) 3.605 GeV, in the Lab frame. 148

B.1 Imaginary part of the form factors F_1', F_2', and G_a' as a function of energy E for $\Delta(1232)3/2^+$ intermediate state at $Q^2 = 3$ GeV^2. Note that the energy is in logarithmic scale. 157
B.2 Imaginary part of the form factors F_1' (top row), F_2' (middle row), and G_a' (bottom row) for all the resonance intermediate states as a function of energy E at fixed $Q^2 = 1$ GeV^2 (left panel) and $Q^2 = 5$ GeV^2 (right panel). 158
B.3 Real part of the form factors F_1' (top row), F_2' (middle row), and G_a' (bottom row) for $N(1440)1/2^+$, $N(1535)1/2^-$, $\Delta(1620)1/2^-$, $N(1650)1/2^-$, and $N(1720)1/2^+$ resonance intermediate states as a function of energy E at fixed $Q^2 = 1$ GeV^2 (left panel) and $Q^2 = 5$ GeV^2 (right panel). . . . 159

C.1 Comparison of the IR finite TPE correction δ (in %) using the treatments of (a) Maximon and Tjon [76], and (b) Mo and Tsai [75], to separate the IR divergent part from the hard TPE. The chosen kinematics are the same as Fig. 6.6, *i.e.* at $Q^2 = 0.2$ GeV^2 (green dashed line), 0.5 GeV^2 (dark red long-dashed), 1 GeV^2 (red solid), 3 GeV^2 (orange dot-dashed), 4 GeV^2 (black dotted), and 5 GeV^2 (blue dashed). 160

D.1 Effect of constant total decay width and zero-width approximation of resonance intermediate states of TPE box diagram in $A_{\rm n}$. The red dashed lines represent the results assuming zero-width approximation and the blue dot-dashed lines correspond to that assuming a constant total decay width in Breit-Wigner distribution. 162

List of Tables

5.1 Parameters used in the fittings as a ratio of polynomials (Eq. (5.3)) for the Sachs electric (G_E) and magnetic (G_M) form factors by three different groups of authors, Arrington *et al.* (AMT) [72], J. J. Kelly [126], and Venkat *et al.* [127]. 83

5.2 Kinematics at which threshold cusp effects appear for the $\Delta(1232)$, $N(1520)$, and $N(1720)$ resonances, at several typical Q^2 values relevant phenomenologically. 101

7.1 Beam normal single spin asymmetry $B_{\rm n}$ from various experiments, along with the corresponding kinematics. 132

8.1 A comparison of the target normal single spin asymmetry $A_{\rm n}$ (for proton target) from elastic nucleon (N), and sum of nucleon (N) and all the resonance intermediate states at the kinematics of Ref. [135]. The last two columns show the values used as input in Ref. [135] from the source [136] and third columns are the corresponding results calculated in this work. . 150

Chapter 1

Introduction

Scattering experiments have been a long-standing tool in search of the fundamental constituents of matter since its early use by Ernest Rutherford to reveal the existence of dense and positively charged nucleus at the centre of atom in 1911 [1]. With the rapid development of both theory and experiment, it was soon realized that the constituents of the nucleus (*i.e.* nucleons) themselves have internal structure. The magnetic moment of a point-like (structureless) proton is supposed to be $\mu_{\mathrm{p}} = \mu_{\mathrm{N}}$, μ_{N} being the nuclear magneton, and for chargeless neutron (point-like) μ_{n} should be zero. But the measured magnetic moments of proton and neutron are found to be $\mu_{\mathrm{p}} \simeq 2.79\mu_{\mathrm{N}}$ and $\mu_{\mathrm{n}} \simeq -1.91\mu_{\mathrm{N}}$, respectively, which indicates the substructure of nucleons. However, the concrete details of nucleon structure are yet to be unveiled.

With the electron being a fundamental particle, elastic electron–nucleon scattering has become one of the most indispensible tools to probe the internal structure of nucleons through the determination of their electromagnetic form factors. For many decades the proton electric, $G_E(Q^2)$, and magnetic, $G_M(Q^2)$, elastic form factors have been measured in unpolarized scattering experiments using the Rosenbluth separation technique [2–4]. These experiments found that the ratio $\mu_p\, G_E/G_M$ hovered consistently around 1 over a large range of the four-momentum transfer squared, Q^2, up to 8.83 GeV^2. More recently, measurements of the electric to magnetic form factor ratio with significantly reduced

uncertainties were performed at Jefferson Lab using the polarization transfer technique, and found in contrast a linear fall-off of the ratio from 1 with increasing Q^2 in the range up to $Q^2 \approx 8.5$ GeV^2 [5–9]. Proper account of the two-photon exchange (TPE) radiative correction in cross section data is expected to resolve the discrepancy of $\mu_p G_E/G_M$ ratio measurements [10, 11]. Before diving into the details of the TPE radiative correction, I present here a brief overview of the methods of proton structure information extraction from electron–proton elastic scattering.

To begin the discussion about electron-proton elastic scattering, it is a good approximation to assume the interaction is mediated by the exchange of a single virtual photon. In principle, the electromagnetic interaction of *e-p* involves an infinite series of virtual photons exchange, but each additional photon introduces two new vertices which in turn brings in roughly the factor of fine structure constant $\alpha = e^2/4\pi \simeq 1/137$ in the corresponding amplitude. Therefore, apparently the series can safely be attenuated at the one photon exchange approximation, or Born approximation, with a fairly precise prediction of the measured observables. However, the precision level achieved in measurement with the aid of the modern experimental facilities compels the theorists to look for the higher order effects, which will also be discussed in subsequent chapters, in the observable quantities. In the next section I explain *e-p* scattering kinematics within the Born approximation before going for the details of the methods of revealing the proton's internal structure.

1.1 Scattering kinematics

The kinematics of the elastic electron–proton scattering process are shown in Fig. 1.1 for the one-photon exchange approximation. Here an electron with four-momentum $k = (E, \boldsymbol{k})$ is scattered from a proton initially at rest, $p = (M, 0)$ in the target rest frame, to an electron in the final state with four-momentum $k' = (E', \boldsymbol{k'})$. The transferred four-momentum from the electron to the proton is $q = k - k'$, and the proton recoils with four-momentum $p' = p + q$.

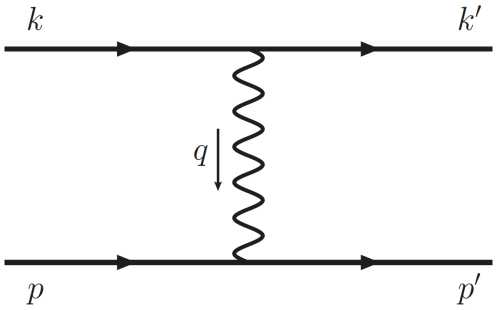

FIGURE 1.1: Elastic scattering of an electron (with four-momentum k) from a proton (p) to a final state electron (k') and recoil proton (p'), with $q = k - k' = p' - p$ the four-momentum transfer, in the Born approximation.

For the one-photon exchange (Born approximation), the amplitude $\mathcal{M}_\gamma$ for scattering an electron from a proton can be written as [12]

$$\mathcal{M}_\gamma = -e^2\, j_\mu \frac{1}{q^2} J^\mu, \tag{1.1}$$

where e is the charge of the proton, and the characteristic Lorentz invariant, q^2, of the process can be written in terms of the electron energy E and scattering angle θ as $q^2 = -4EE' \sin^2(\theta/2)$. For space like virtual photon, it is convenient to introduce the positive quantity $Q^2 \equiv -q^2$. The electron transition current is given by $j_\mu = \bar{u}(k')\,\gamma_\mu\, u(k)$, where the Dirac spinor for an electron of mass m and four-momentum k is $u(k) = \left(\sqrt{E+m}, \boldsymbol{\sigma}\cdot\boldsymbol{k}/\sqrt{E+m}\right)\chi_s$, with $\boldsymbol{\sigma}$ and χ_s being the standard Pauli spin matrices and the two component spinors, respectively. The proton transition current is $J^\mu = \bar{u}(p')\,\Gamma^\mu(q)\,u(p)$, where $\Gamma^\mu(q)$ is the current operator at the hadronic vertex.

1.2 Hadronic current operator parametrization

The hadronic current operator Γ^μ could be replaced by γ^μ if it were a point-like particle. But, for the extended structure of the proton, it has to be parametrized using appropriate form factors that take into account the proton's internal structure. Since Γ^μ has to be a Lorentz four vector, hence this should be constructed in a general form using the relevant Lorentz four vectors p^μ, p'^μ, q^μ, and the Dirac matrices, γ^μ at the

proton-photon-proton vertex as [13–15],

$$\Gamma^{\mu} = f_1\gamma^{\mu} + f_2 q^{\mu} + f_3 p^{\mu} + f_4 p'^{\mu}. \tag{1.2}$$

Parity conservation does not allow the terms involving γ^5 in Γ^{μ}. The Lorentz scalar coefficients f_i have inter dependency. Conservation of momentum, $q^{\mu} = p'^{\mu} - p^{\mu}$, at the hadronic vertex allows to set $f_2 = 0$. For the on-shell external legs of hadron, the Ward identity, $q^{\mu}J^{\mu} = 0$, leaves $f_3 = f_4$. Therefore, it is left with only two independent Lorentz vectors and one can write the hadronic current operator as,

$$\Gamma^{\mu} = F_1\gamma^{\mu} + F_2(p + p')^{\mu}. \tag{1.3}$$

Here one can choose the Dirac F_1 and Pauli F_2 form factors as the Lorentz scalar coefficients. For a free on-shell particle, F_1 and F_2 depend only on Q^2. Using the Gordon identity,

$$\bar{u}(p')\,\gamma^{\mu}(q)\,u(p) = \bar{u}(p')\left[\frac{p^{\mu} + p'^{\mu}}{2M} + \frac{i\sigma^{\mu\nu}(p'_{\nu} - p_{\nu})}{2M}\right]u(p), \tag{1.4}$$

hadronic current can also be written as,

$$\Gamma^{\mu}(Q^2) = F_1(Q^2)\gamma^{\mu} + F_2(Q^2)\frac{i\sigma^{\mu\nu}q_{\nu}}{2M}, \tag{1.5}$$

where M is the proton mass.

1.3 The proton structure information from cross section measurement

The differential cross section for single photon exchange is proportional to the square of the scattering amplitude $\mathcal{M}_{\gamma}$. Plugging the expression of Γ^{μ} in $\mathcal{M}_{\gamma}$, the differential

cross section in the Born approximation can thus be written as

$$\begin{aligned}\left(\frac{d\sigma}{d\Omega}\right)_0 &= \left(\frac{\alpha E'}{4MQ^2E}\right)^2 |\mathcal{M}_\gamma|^2 \\ &= \sigma_{\text{Mott}}\left[\left(F_1^2+\tau F_2^2\right)+\frac{Q^2}{2M^2}\left(F_1+F_2\right)^2\tan^2(\theta/2)\right],\end{aligned} \tag{1.6}$$

where $\tau = Q^2/4M^2$ and σ_{Mott} corresponds to the cross section if the target proton were a structureless point particle instead. Ignoring the recoil of the proton, *i.e.* in the limit of $M \to \infty$ (or, $E \ll M$), σ_{Mott} can be given by

$$\sigma_{\text{Mott}} = \frac{4\alpha^2 E'^3\cos^2(\theta/2)}{EQ^4}. \tag{1.7}$$

Therefore, it is evident that the structure information of proton contains entirely within the form factors $F_i(Q^2)$ $(i = 1, 2)$. In other words, for a point like Dirac target particle the form factors would take the form $F_1(Q^2) = 1$ and $F_2(Q^2) = 0$, so that the cross section reduces to σ_{Mott} in the limit of $M \to \infty$. Note that the form factors $F_1(Q^2)$ and $F_2(Q^2)$ are normalized such that

$$F_1(0) = 1, \qquad F_2(0) = 1.79, \tag{1.8}$$

i.e. probing with the long wavelength photons ($Q^2 \to 0$) one does not see any internal structure of proton but only a point particle of charge e and magnetic moment $\mu_p = 2.79$. The physical meaning of the form factor can be better understood with the convention of the Sachs electric and magnetic form factors G_E and G_M, which are defined as linear combinations of the Dirac and Pauli form factors [16, 17],

$$G_E(Q^2) = F_1(Q^2) - \tau F_2(Q^2), \qquad G_M(Q^2) = F_1(Q^2) + F_2(Q^2). \tag{1.9}$$

In Breit frame[1] and in the non-relativistic limit of $Q^2 \ll M^2$, the form factors G_E and G_M can be interpreted as the Fourier transform of the spatial charge and magnetization

[1]The Breit frame or the brick wall frame is the special Lorentz frame where $\boldsymbol{p'} = -\boldsymbol{p}$. In this frame the scattered electron does not transfer any energy to the target proton.

distribution, respectively. On the basis of such interpretation, G_E and G_M are normalized to the charge and magnetic moment of proton, respectively, in the limit of $Q^2 = 0$, *i.e.*

$$G_E(0) = 1, \qquad G_M(0) = \mu_p. \tag{1.10}$$

One specific advantage of using the Sachs electric and magnetic form factors is that the cross section does not have any cross terms of the form factors. The differential cross section, diagonal in G_E and G_M, is given by

$$\left(\frac{d\sigma}{d\Omega}\right)_0 = \frac{\sigma_{\text{Mott}}\left[\varepsilon G_E^2(Q^2) + \tau G_M^2(Q^2)\right]}{\varepsilon\,(1+\tau)}, \tag{1.11}$$

where the dimensionless quantity

$$\varepsilon = \left[1 + 2\,(1+\tau)\tan^2\left(\theta/2\right)\right]^{-1}, \tag{1.12}$$

is the virtual photon polarization. It is useful to introduce the reduced (Born) cross section $\sigma_{\text{R}}^{\text{Born}}$, defined by

$$\sigma_{\text{R}}^{\text{Born}} = \varepsilon\,(1+\tau)\left(\frac{d\sigma}{d\Omega}\right)_0 \Big/ \sigma_{\text{Mott}} = \varepsilon G_E^2(Q^2) + \tau G_M^2(Q^2), \tag{1.13}$$

for future use in the coming sections. Equation (1.11) is known as the Rosenbluth or the Longitudinal-Transverse (LT) separation formula [18].

1.3.1 Form factors from Rosenbluth separation formula

The Rosenbluth separation formula of Eq. (1.13) is very useful in extraction of the internal structure of proton. Using this form of the reduced cross section, the electric (G_E) and magnetic (G_M) form factors, hence the internal structure of proton, can be extracted by measuring $\sigma_{\text{R}}^{\text{Born}}$ in unpolarized e-p elastic scattering at a specific value of Q^2 by varying the scattering angle θ and the beam energy E. A plot of the measured reduced cross section as a function of ε at fixed Q^2 is expected to be a straight line following Eq. (1.13), interception of which provides τ times the square of the magnetic

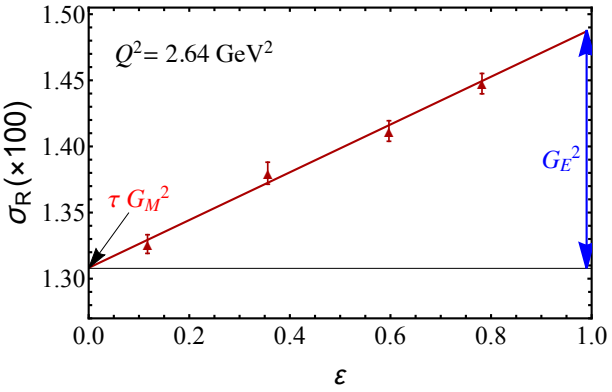

FIGURE 1.2: Extraction of the electric (G_E) and magnetic (G_M) form factors from the reduced Born cross section σ_R^{Born} using the Rosenbluth (LT) separation method. The data points are taken from Ref. [22] and the line is a linear fit to the data.

form factor G_M, and the square of the electric form factor G_E can be obtained from the slope. This method of Rosenbluth (LT) separation has been traditionally used for several decades to measure the form factors G_E and G_M of proton [3, 4, 19–21]. For clarity, one such measurement from JLab [4] is illustrated in Fig. 1.2. Here the reduced cross section is measured at several ε points corresponding to different scattering angle and beam energies but at fixed $Q^2 = 2.64$ GeV^2. The magnetic form factor can be obtained from the interception point with the vertical axis as addressed in the plot. The slope of the fitted line gives G_E^2 for that particular Q^2 value.

It is important to address that the experimentally measured cross sections are not the Born cross section, rather it contains the contributions from the exchange of more than one photon, known as radiative corrections. For the earlier scattering experiments with low Q^2, it might be acceptable to ignore the higher order (in α) correction terms, but the high precision experiments to date [3, 4, 19–21] reaching $Q^2 \simeq 9.0$ GeV^2 require to take into account of the cross section corrections coming from at least the next to leading order Feynman diagrams. Before exploiting Eq. (1.13) during the extraction of the form factors it is required to eliminate the higher order corrections from the measured cross section $\left(\frac{d\sigma}{d\Omega}\right)_{\text{meas}}$ and isolate the measured Born cross section so that the real form factors can be obtained. In reaching that objective, $\left(\frac{d\sigma}{d\Omega}\right)_{\text{meas}}$ (or, σ_R^{meas}) can be expressed using a correction term relative to the Born (leading order) cross section

$\left(\frac{d\sigma}{d\Omega}\right)_0$ (or, $\sigma_{\rm R}^{\rm Born}$) as

$$\left(\frac{d\sigma}{d\Omega}\right)_{\rm meas} = \left(\frac{d\sigma}{d\Omega}\right)_0 (1+\delta), \tag{1.14}$$

where δ is the relative cross section correction coming from every possible Feynman diagrams, in principle. Comparing the measured cross section with the left side of Eq. (1.14) and plugging in the calculated higher order cross section corrections δ on the right one can separate the measured Born cross section from the total. However, several independent measurements [2, 3, 19, 23–28] of G_E and G_M using Rosenbluth separation method found consistently the same asymptotic behaviour for the ratio $\mu_p G_E/G_M \simeq 1$ at large Q^2 in coherence with the normalizing condition of Eq. (1.10) at $Q^2 = 0$ GeV^2. Figure 1.3 illustrates the scenario with the data extracted by Walker *et al.*[2] (open blue squares), Andivahis *et al.* [3] (open red circles). The black triangles are from the global analysis of Walker *et al.* [2] with the original data source from Refs. [23, 24, 24–28]. All the data points are close to the scale of $\mu_p G_E/G_M = 1$, within the uncertainty range, up to $Q^2 = 8.83$ GeV^2 even though there are some scatter among the values.

1.3.2 Alternative measurement of the form factors

It is a common and basic practice in science to reproduce the results of the observable quantities in variety of methods having its own dependencies, both in theory and experiment. One such alternative method to measure the ratio of the form factors $\mu_p G_E/G_M$ is to scatter the longitudinally polarized electron ($\vec{e}$) beam from an unpolarized proton target (p) and detecting the polarization transfer to the recoiled proton $\vec{p}$. In the Born approximation of $\vec{e}$-$p \rightarrow e$-$\vec{p}$ elastic scattering, the scattering cross section with the recoiled proton being polarized longitudinally with respect to its recoiling momentum is given by [12, 29]

$$\frac{d\sigma^{(L)}}{d\Omega} = h\,\sigma_{\rm Mott}\,\frac{E+E'}{M}\sqrt{\frac{\tau}{1+\tau}}\,\tan^2\left(\frac{\theta}{2}\right) G_M^2, \tag{1.15}$$

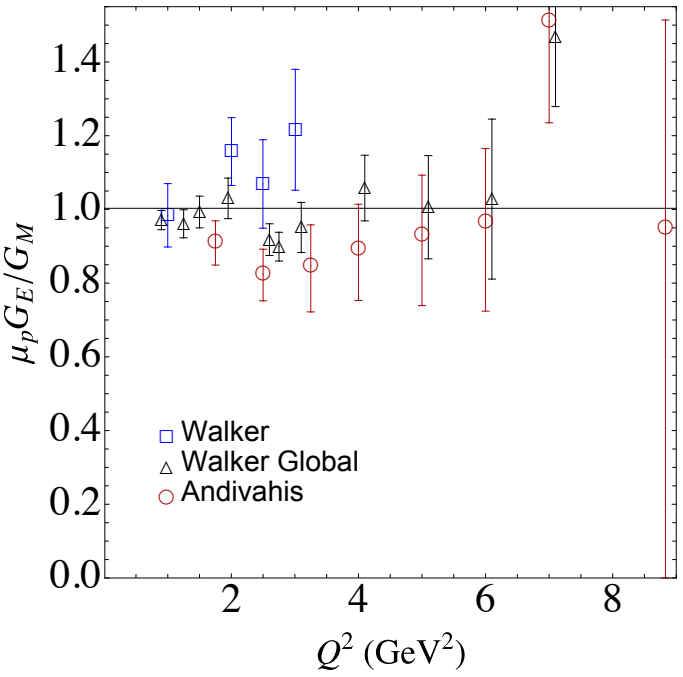

FIGURE 1.3: Proton electric to magnetic form factor ratio $\mu_p G_E/G_M$ extracted using Rosenbluth LT separation method. The blue squared data are by Walker *et al.* [2], black triangles from Walker's global analysis [2], and the red circles correspond to the extraction of Andivahis *et al.* [3]. The black solid line corresponds to the scaling $\mu_p G_E/G_M = 1$. Note that some overlapping LT data points are slightly offset for clarity.

where h is the electron helicity and θ is still the electron scattering angle. The cross section for the recoiled proton having transverse (in the scattering plane) polarization is

$$\frac{d\sigma^{(T)}}{d\Omega} = 2\,h\,\sigma_{\text{Mott}}\sqrt{\frac{\tau}{1+\tau}}\,\tan\left(\frac{\theta}{2}\right)G_E\,G_M. \tag{1.16}$$

Having defined the longitudinal and transverse polarization transfers to the recoiled proton, P_L and P_T respectively, in the Born approximation by

$$P_L = \frac{\tau\sqrt{1-\varepsilon^2}}{\sigma_{\text{R}}^{\text{Born}}}\,G_M^2, \tag{1.17a}$$

$$P_T = -\frac{\sqrt{2\,\varepsilon\,(1-\varepsilon)\,\tau}}{\sigma_{\text{R}}^{\text{Born}}}\,G_E\,G_M, \tag{1.17b}$$

one can obtain the electric to magnetic form factor ratio $\mu_p G_E/G_M$ from the ratio of the transverse to longitudinally polarized recoiled proton cross sections as [12, 29]

$$R_{TL} = -\mu_p \sqrt{\frac{\tau(1+\varepsilon)}{2\varepsilon}} \frac{P_T}{P_L} = -\mu_p \frac{E+E'}{2M} \tan\left(\frac{\theta}{2}\right) \frac{P_T}{P_L} = \mu_p \frac{G_E}{G_M}. \tag{1.18}$$

Note that the normal component of the polarization transfer is zero in Born approximation. In case of the LT separation measurement, G_M dominates the total cross section of Eq. (1.13) in the large Q^2 region suppressing the G_E contribution, while for $Q^2 \to 0$ it is basically the electric form factor G_E that contributes to the cross section. Such suppression of G_E by G_M in the large Q^2 region makes the determination imprecise. On the other hand, the exact values of the form factors G_E and G_M cannot be extracted in the method of polarization transfer (PT), but it provides a direct measurement of the ratio $\mu_p G_E/G_M$ precisely over a wide range of Q^2. It will be clear from the discussions in the coming chapters that the ratio of the polarization transfer measurement is relatively insensitive to the hadron structure-dependent radiative corrections, especially the two-photon exchange, which reduces the level of uncertainty in the measurement. Considering the precision aspect of the PT measurement technique a series of experiments [5–9, 30–34] at Jefferson Lab have been performed in last two decades using longitudinally polarized electron beams to determine the ratio $\mu_p G_E/G_M$ up to $Q^2 = 8.5$ GeV^2. The results for $\mu_p G_E/G_M$ obtained in those experiments using PT measurement method is shown in Fig. 1.4(a) including a nonlinear fit to data with a green band at 99% confidence level. Surprisingly the results of the ratio, having an approximately linear falloff above $Q^2 = 1$ GeV^2, are in clear disagreement with that obtained from the LT separation measurement as compared in Fig. 1.4(b). The consistent discrepancy between the LT separation and PT measurement methods of the ratio $\mu_p G_E/G_M$ brought significant theoretical efforts, along with the experimental activity, mostly focusing on the reanalysis of the radiative corrections. Since the relative contribution of the electric form factor G_E in reduced cross section decreases with increasing Q^2 any error in radiative corrections comparable to G_E^2 makes the extraction of G_E meaningless. Thus the improved treatment of the radiative corrections has

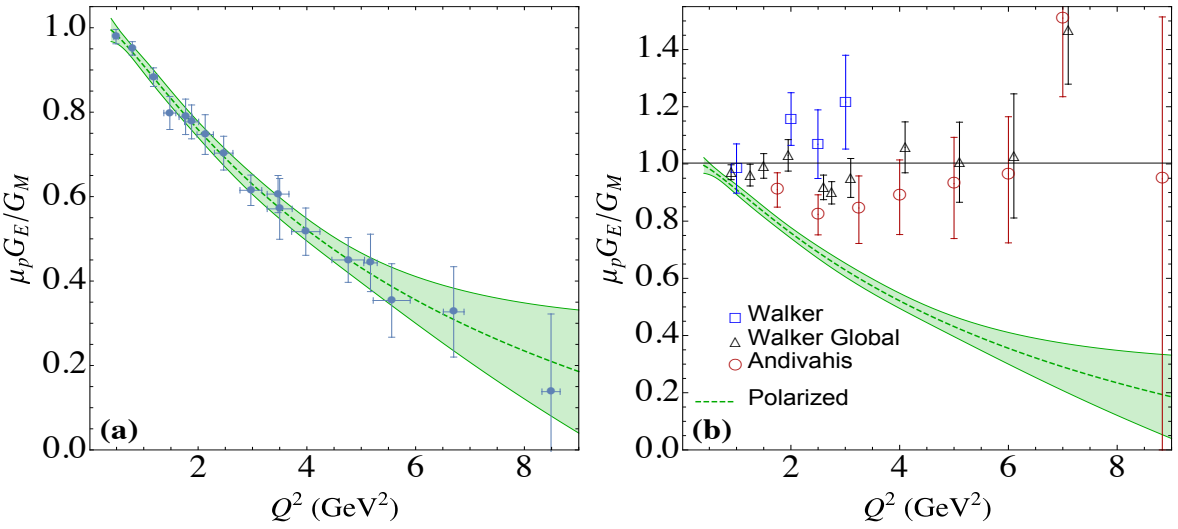

FIGURE 1.4: The electric to magnetic form factor ratio $\mu_p G_E/G_M$ extracted by (a) the PT measurement, and (b) the LT separation method (along with the PT method result), are shown for several values of Q^2 ranging up to ~ 8.5 GeV^2. The green band is a nonlinear fit to the PT data with 99% confidence level. The LT data in (b) are taken from three updated sources of Refs. [2, 3]. For LT data, some overlapping points are slightly offset for clarity. Note that the scale on the right is different.

been emphasized in most of the reanalyses [10, 35–39]. Particularly, $\mu_p G_E/G_M$ ratio discrepancy motivated studies of the hadron structure-dependent two-photon exchange radiative correction which is found to give ε-dependent cross section itself, and the problem was generally believed to be resolved with the inclusion of these effects [10, 11].

Subsequent years have seen a growing sophistication in the theoretical efforts that have been made to better understand the TPE phenomena using various approaches. These have included using hadronic models to compute the real part of the TPE amplitude through loop integrals with (on-shell) transition form factors [37, 38, 40, 41], and using generalized parton distributions (GPD) [42, 43] and perturbative QCD framework [44, 45] to model the high-energy behaviour of the intermediate state hadrons at the quark level. But the use of GPD and pQCD based calculation is preferable in the high Q^2 limit.

The use of hadronic degrees of freedom can be thought as a reasonable approximation for low to moderate values of $Q^2 \lesssim 5$ GeV^2, where hadrons can be expected to retain their identity. However, for excited intermediate states of higher spin, such as the Δ

isobar, in the forward angle limit [46] the on-shell approximation gives rise to unphysical divergences in the TPE amplitude. This problem of unphysical behaviour can be resolved using the dispersive method described in Refs. [46–52], where the on-shell form factors are used explicitly to calculate the imaginary part of the TPE amplitude from unitarity, with the real part then obtained from dispersion theory.

1.4 Overview of the work

Early model estimations of TPE effects [10, 11], which have significant uncertainties in their calculations, found that TPE partially resolves the $\mu_p G_E/G_M$ ratio discrepancy. In this work I decided to further investigate the TPE correction to shed light on the issue of the form factor ratio measurement. In evaluation of the real part of the TPE effect, we follow the dispersive approach developed in Ref. [46], but generalize the calculation to transition form factors that are arbitrary functions of the momentum transfer, rather than restricted to be sums of monopoles as in Ref. [46]. Unlike previous calculations which made use of the narrow resonance approximation, here we allow a Breit-Wigner shape with a nonzero width for each individual resonance contribution, with either a fixed width or a dynamical width that depends on the final state hadron mass. Furthermore, in addition to the $\Delta(1232)3/2^+$ resonance intermediate state, we also compute the TPE contribution from all the established $J^P = 1/2^\pm$ and $3/2^\pm$ states below 1.8 GeV, including the $N(1440)1/2^+$ Roper resonance, $N(1520)3/2^-$, $N(1535)1/2^-$, $\Delta(1620)1/2^-$, $N(1650)1/2^-$, $\Delta(1700)3/2^-$, $N(1710)1/2^+$, and $N(1720)3/2^+$ resonances. With the exception of the $\Delta(1232)3/2^+$, for which we use the fit by Aznauryan and Burkert [53], for the resonance electrocouplings at the hadronic vertices we use the most recent helicity amplitudes extracted from the analysis of CLAS meson electroproduction data [54–56].

The imaginary part of the TPE amplitude generates an observable quantity single spin asymmetry (SSA) at its leading order in e-p scattering with either beam or target being polarized normal to the scattering plane. While the target normal SSA is of order $10^{-3}-10^{-2}$, the beam normal SSA is of order $10^{-6}-10^{-5}$. Having such a small numerical

value, the beam normal SSA still plays a vital role in parity violating electron scattering experiments to improve the precision level, as the SSA appears as a false asymmetry there. For example, the highly precise Q_{Weak} experiment [57] at Jefferson Lab attempts to determine the weak charge of the proton in search of physics beyond standard model requires to know this particular source of systematic error from the background beam normal single spin asymmetry. Recently, Q_{Weak} collaboration published their own measured value of this observable quantity at some forward scattering angle ($\theta_{\text{Lab}} = 7.9^{\circ}$) and $Q^2 = 1.149$ GeV^2. Several other parity violating experiments [58–61] including A4 collaboration [62–64] have also measured the quantity but the results are little scattered. The significant disagreement between the measured value [60] of beam normal SSA and the corresponding estimation [65] for heavier target nucleus ^{208}Pb raised question about the estimations in general. More importantly the theory predictions from different groups [66–71] are not also consistent.

To better understand both the beam and target normal single spin asymmetries originating from the mentioned spin-parity $1/2^{\pm}$ and $3/2^{\pm}$ resonance intermediate states associated with πN and $\pi\pi N$ channels, we apply the same elctrocouplings data from CLAS [54–56] in evaluation of the imaginary part of the TPE amplitude in polarized *e-p* elastic scattering. Along with the resonance states the effect of elastic nucleon intermediate state is also accounted using $G_{E,M}(Q^2)$ from the parametrization of Arrington *et al.* [72]. Alike the real part, here again the Breit-Wigner shaped width is assigned for each resonance state.

1.5 Outline

This dissertation continues with a brief review of the efforts to reconcile the form factor ratio, $\mu_p G_E/G_M$ discrepancy in chapter 2. For completeness, the relevant radiative corrections in analysis of *e-p* elastic scattering cross section data for $Q^2 \lesssim 9$ GeV^2 is also discussed in the same chapter (Sec. 2.3). Finally, the TPE emerges as a potential candidate to reconcile the existing discrepancy between the two different measurements

of electric to magnetic form factor ratio in the end of the chapter. Chapter 3 describes the general formalism of the TPE radiative correction followed by a detailed review of the previous calculations and experimental extractions of the hadron structure-dependent correction. My input in this thesis partially starts from chapter 4. In chapter 4, I explain the foundation (*i.e.* dispersive method) of the model we have prepared, published in Ref. [73], to numerically evaluate the TPE amplitude and test it with a simple warm up problem of electron-muon scattering. After having a convincing outcome of the method in the simple test problem, in chapter 5, I apply it in evaluation of the TPE correction in e-p scattering with elastic nucleon intermediate state for completeness, results of which are already well estimated though. A complete discussion of the model to estimate the resonance states' effect in total TPE correction is explained in the same chapter. The obtained results for the TPE effects in unpolarized e-p scattering are then discussed in chapter 6. Following a brief review of the polarization observable, SSA, sensitive to the imaginary part of the TPE amplitude in beam/target polarized e-p scattering, a detailed description of the numerical calculation of SSA is presented in chapter 7. Results of the beam and target normal single spin asymmetry are discussed in chapter 8. Finally, the conclusion of this work is drawn in chapter 9.

Chapter 2

Revisit to the $\mu_p G_E/G_M$ discrepancy

Observing the somewhat scatter of the LT separation data of $\mu_p G_E/G_M$ around ≈ 1 (Fig. 1.3), at the initial time when the discrepancy between the LT separation and PT measurement was popped up, three issues were mainly addressed by several groups of authors. One anticipation was that the discrepancy is perhaps due to an error in the early cross section measurements and the two other issues were regarding the data analysis, *i.e.* either inappropriate treatment of the relative normalization uncertainty in analyzing multiple cross section data sets or an effect from unaccounted radiative corrections are responsible for the disagreement in two different methods of measurement for the same physical quantity. This chapter reviews the major efforts, both theoretical and experimental, to reconcile the discrepancy.

2.1 Early reanalyses of Rosenbluth separation data

Considering the two points about normalization uncertainty and radiative corrections Arrington preformed two series of reanalyses [35, 36] of the world data, only excluding some erroneous small angle ($< 20^\circ$) data from Walker's work, in Ref. [2]. In Ref. [35], Arrington first figured out that the independent analysis of the individual LT separation measurements give consistent results for $\mu_p G_E/G_M$ scaling around ≈ 1, meaning an

insignificant impact on the results from the normalization uncertainty between different measurements. Then in the global analysis he investigated several potential effects in hope of a solution to the problem. Exclusion of data sets for $\theta < 20^\circ$ due to a missing correction in those data required to use in that small angle limit, random exclusion of data sets at high Q^2 to see if any particular data with error strongly influences the result, addition of some newly published data in the analysis, updating some double count of the normalization uncertainty in some previous global analysis, determination of an overall normalization uncertainty for each data set other than the point-to-point systematic uncertainty and use of independent normalization uncertainties for the data from each detectors when multiple detectors were used in a single experiment were some key features particularly focused in the global analysis. For the radiative corrections, some improved treatment of the vacuum polarization with muon and quark loops have also been applied in some previous measurements along with the Schwinger term even though it had very little ε dependence resulting in negligible effect on the form factor ratio. Note that the previous global analysis by Walker [2] had also accounted for such massive loops in vacuum polarization in addition to the radiative corrections from Mo and Tsai prescriptions [74]. Unfortunately, the re-examination of the world data in Refs. [35, 36] did not find any concrete reason of the discrepancy. The Rosenbluth separation data were still self-consistent around the scale $\mu_p G_E/G_M = 1$. However, the author suggested any missing ε-dependent correction in the measured cross section with $\approx 6\%$ ε dependence is required to resolve the discrepancy.

2.2 Experimental effort to reconcile $\mu_p G_E/G_M$ ratio discrepancy

Alongside the initial reanalyses of the Rosenbluth separation data, from the experimental side, there was continued effort in extraction of form factors using Rosenbluth LT separation method more precisely. One major problem in the Rosenbluth separation method is the extraction of electric form factor G_E at larger Q^2 where the magnetic form

factor G_M part dominates the total reduced cross section as discussed in Sec. 1.3.2. Since at larger Q^2, G_E contributes a very small fraction in total cross section, any amount of ε-dependent correction would significantly alter the extracted G_E. In fact, this issue was one of the motivations of initiating polarization transfer measurement. From the experimental perspective, the cross section of detecting the scattered electron, and its momentum have strong ε dependence at fixed Q^2 measurements. Thus, any rate- or momentum-dependent correction will also impact the extraction of G_E significantly. In contrast, the cross section of proton detection is less sensitive on ε and the proton momentum remains constant at fixed value of Q^2. Moreover, the ε-dependent inelastic bremsstrahlung correction, and any offsets in beam energy and scattering angle has less impact if the proton is detected instead of electron. Considering these points regarding the proper extraction of G_E a modified Rosenbluth experiment [4, 22] was initiated to measure the form factors where the recoiled proton was detected instead of the scattered electron. The precision level of this experiment was comparable to those in the polarization transfer method because of the improvements achieved by switching from scattered electron detection to the recoiled proton detection basically. Among the radiative corrections, they accounted the bremsstrahlung, vertex and vacuum polarization corrections following the Mo and Tsai prescription [74, 75] along with the improvements done by Walker [2]. For two-photon exchange correction they only considered the correction from the soft photons exchange. The measured $\mu_p G_E/G_M$ from this experiment (black diamonds) is represented in Fig. 2.1 along with some selected data sets from Andivahis *et al.* [3] (red circles) and Walker *et al.* [2] (blue squares). The obtained results from such a precise experiment were still incompatible with that from the polarization transfer measurements. This finding at least ruled out the possibility that the discrepancy is due to any error in previous LT measurements.

However, there were several recent reanalyses [10, 37–39] of the Rosenbluth separation data focusing particularly on the inclusion of the updated radiative corrections. Before proceeding to the effects of the improved estimations of radiative corrections in unpolarized cross section data, in the next section, the radiative corrections relevant for the form factor measurement experiments are discussed in detail followed by the review of

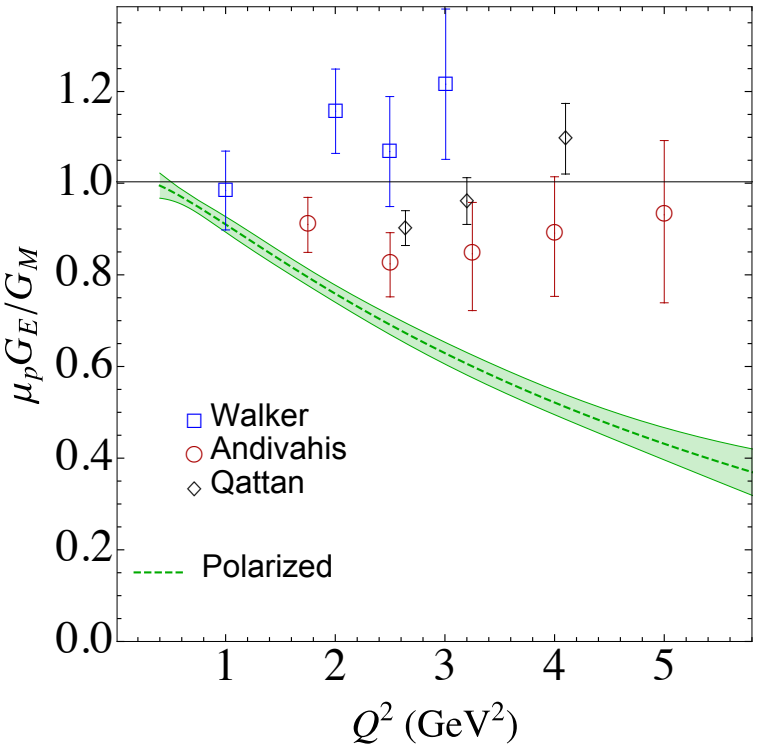

FIGURE 2.1: Proton electric to magnetic form factor ratio from the Super Rosenbluth measurement of Qattan *et al.* [4] (open black diamonds), along with the data from Refs. [2, 3]. The green band corresponds to a non-linear fit to polarization transfer data [7–9].

a latest reanalysis by Gramolin and Nikolenko [39]. After that the structure-dependent two-photon exchange radiative correction and its impact on $\mu_p G_E/G_M$ measurement is discussed in a separate section.

2.3 Radiative corrections to e-p elastic scattering

In perturbative QED the elastic scattering of e-p involves the exchange and emission of series (in principle infinite) of photons. Part of the photons are virtual and they do contain Feynman loop diagrams. Apart from the loop, there is emission of real photons from the external legs of the Feynman diagrams, known as bremsstrahlung, as well. It is interesting to note that the emission and exchange of the real and virtual photons are both important and need to take them into account simultaneously to keep the prediction of the observable quantities finite in QED. It would be clear from the

detailed discussion ahead. However, the discussion will be restricted within the next to leading order (up to order α^2) radiative corrections relevant to the experiments for the low energy precision tests of standard model. Within this limit, the relevant Feynman diagrams with the exchange of an additional virtual photon are shown in Fig. 2.2, while Fig. 2.3 corresponds to the diagrams with an additional real photon emission either from electron or proton leg.

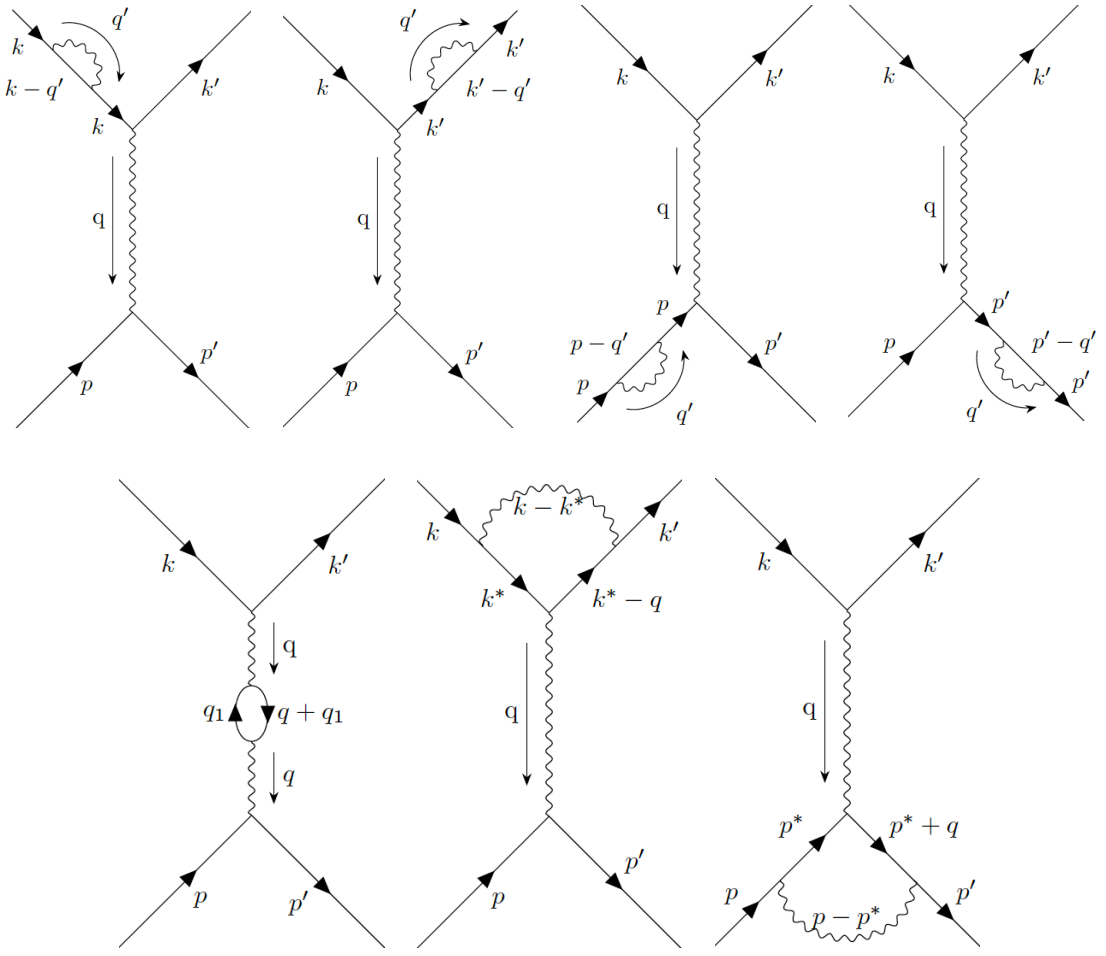

FIGURE 2.2: Feynman diagrams for next to leading order radiative corrections. The top row is for electron (left two) and proton (right two) self energy corrections. First diagram of the bottom row corresponds to the vacuum polarization, and the next two correspond to $e^- - \gamma - e^-$ and proton $-\gamma-$ proton vertex corrections.

Ignoring the corrections beyond order α^2 one can approximate the measured reduced cross section by

$$\sigma_{\rm R}^{\rm exp} \simeq C_{\rm RC}\ (\sigma_{\rm R}^{\rm Born}), \tag{2.1}$$

where $C_{\rm RC}$ is the sum of cross section corrections, relative to Born cross section, coming from the vacuum polarization ($\delta_{\rm vp}$), electron and proton vertex ($\delta^e_{\rm vertex}$ and $\delta^p_{\rm vertex}$), hadron structure-dependent two-photon exchange $\delta_{\gamma\gamma}$, and the real bremsstrahlung $\delta_{\rm brems}$, *i.e.*

$$C_{\rm RC} = 1 + \delta_{\rm vp} + \delta^e_{\rm vertex} + \delta^p_{\rm vertex} + \delta_{\gamma\gamma} + \delta_{\rm brems}. \tag{2.2}$$

Traditionally most of the experimental analyses use the approximate estimation of these corrections from the analysis of Mo and Tsai [74, 75]. The evaluation of these radiative corrections are tedious and almost impossible without simplifying assumptions. Mo and Tsai [74, 75] also had to make some assumptions, particularly in the evaluation of $\delta^p_{\rm vertex}$, $\delta_{\gamma\gamma}$, and $\delta_{\rm brems}$ they assumed standard soft photon approximation for the additional exchanged or emitted photon. The term soft means the photon momentum is vanishingly small. More recently, an improved estimation of these Feynman diagrams by Maximon and Tjon [76] has been used in some contemporary experiments like Ref. [21]. Due to the differences in the assumptions used in evaluation of these corrections, the results are also different in some cases. The vacuum polarization and electron vertex correction results agree fairly well, while the proton vertex and the soft part of the two-photon exchange are significantly different due to the variation in assumptions. The difference in the soft part of the TPE correction between the two treatments will be discussed in Sec. 3.1.2. However, having the same assumptions in both calculations for the soft bremsstrahlung the results are still different and that was due to an incorrect substitution, which was updated by Tsai in a later preprint [77] but still with an error in sign, as pointed out in Ref. [78]. Due to such variations in the outcomes of the model estimations of radiative corrections one needs to be cautious about the used treatment while comparing data from different experiments, particularly in case of any global analysis of the Rosenbluth separation data. For example, Walker *et al.* [2] used the Mo and Tsai prescription [75] of the radiative corrections but with the corrected sign in the proton vertex correction along with the inclusion of the heavier lepton and hadron loops in vacuum polarization. For completeness, I discuss here the results from the Mo-Tsai [75] and Maximon-Tjon [76] prescriptions.

The corrections $\delta^e_{\rm vertex}$ and $\delta_{\rm vp}$ from electron vertex and vacuum polarization are well estimated in literature. Considering only the virtual lepton loops (e^+e^-, $\mu^+\mu^-$, and $\tau^+\tau^-$ pairs) in vacuum polarization diagram of Fig. 2.2, $\delta_{\rm vp}$ can be given a general form as [39, 76, 78]

$$\delta^l_{\rm vp} = \frac{2\alpha}{3\pi}\Bigg\{ -\frac{5}{3} + \frac{4\,m_l^2}{Q^2} + \left(1 - \frac{2\,m_l^2}{Q^2}\right)\sqrt{1+\frac{4\,m_l^2}{Q^2}} \times \ln\left[\frac{Q^2}{4\,m_l^2}\left(1+\sqrt{1+\frac{4\,m_l^2}{Q^2}}\right)^2\right]\Bigg\}, \tag{2.3}$$

where m_l is the lepton mass. Only for the e^+e^- loop (as was considered in Ref. [75] by Mo and Tsai) in the limit of $Q^2 \gg m^2$, applicable for most high Q^2 experiments, Eq. (2.3) reduces to a simplified form

$$\delta_{\rm vp} \simeq \frac{\alpha}{\pi}\frac{2}{3}\left\{-\frac{5}{3} + \ln\left(\frac{Q^2}{m^2}\right)\right\}. \tag{2.4}$$

Walker *et al.* [2] included the contributions from all three lepton pairs in his global reanalysis of the Rosenbluth data in an attempt to reconcile the discrepancy in form factor measurements. Note that Ref. [2] has a misprint for the corresponding expression of $\delta_{\rm vp}$ which is corrected in Eq. (2.3) following Ref. [39]. However, in addition to the lepton loops, Walker *et al.* also included quark loop contributions parametrized from the measured data of e^+e^- annihilation into hadron with a simple fit of the form of Eq. (2.3) (correcting for the charge and colour factors) as

$$\delta^q_{\rm vp} = 0.002\ \left[1.513 + 2.822\ln(1+1.218Q^2)\right]. \tag{2.5}$$

Ideally, one should also consider the effect of structure-less spin zero Bosons (can be obtained from Refs. [79, 80]), pion structure and spin-one mesons like ρ mesons.

The electron vertex correction term from Mo-Tsai work is also identical with the Maximon-Tjon result given by

$$\delta^e_{\text{vertex}} = \frac{\alpha}{\pi}\left\{-K(k,k') + K(k,k) + \frac{3}{2}\ln\left(\frac{Q^2}{m^2}\right) - 2\right\}, \tag{2.6}$$

where $K(k,k')$ can be given by [78]

$$K(k_i,k_j) = k_i \cdot k_j \int \frac{dy'}{k^2_{y'}} \ln\left(\frac{k^2_{y'}}{\lambda^2}\right), \tag{2.7}$$

with $k_{y'} = k_i y' + k_j(1-y')$ following the convention of Ref. [74]. Evaluation of the integrals gives [75, 78]

$$\delta^e_{\text{vertex}} = \frac{\alpha}{\pi}\left\{\ln\frac{m^2}{\lambda^2}\left(1 - \ln\frac{Q^2}{m^2}\right) + \frac{3}{2}\ln\left(\frac{Q^2}{m^2}\right) - 2 - \frac{1}{2}\ln^2\left(\frac{Q^2}{m^2}\right) + \frac{\pi^2}{6}\right\}. \tag{2.8}$$

The correction δ^e_{vertex} is infrared (IR) divergent. But the λ-dependent divergent term will exactly be cancelled by a counter term from the real soft photon emission cross section represented in Eq. (2.10) with no Z-term.

For the proton vertex correction, Maximon-Tjon [76] improved the work of Mo-Tsai [75] by applying a more realistic assumption that takes proton structure-dependent correction into account, while Mo-Tsai used the simple soft photon approximation for the additional exchanged photon at the proton vertex, *i.e.* the proton is treated as a point particle in the later treatment. To account the proton structure effect in δ^p_{vertex}, Ref. [76] used monopole or dipole form of the Dirac and Pauli form factors F_1 and F_2. For computational simplicity they further assumed the two form factors be equal in form. To compare with the Mo-Tsai results, Maximon-Tjon separated the structure-dependent part $\delta^{p(1)}_{\text{vertex}}$ ($\delta^{(1)}_{el}$ in Maximon-Tjon notation) from the structure independent contribution $\delta^{p(0)}_{\text{vertex}}$, *i.e.* $\delta^p_{\text{vertex}} = \delta^{p(0)}_{\text{vertex}} + \delta^{p(1)}_{\text{vertex}}$. The structure independent $\delta^{p(0)}_{\text{vertex}}$, common to both Mo-Tsai and Maximon-Tjon, consists the IR divergence and can be written as [76]

$$\delta^{p(0)}_{\text{vertex}} = \frac{\alpha Z^2}{\pi}\left\{-K(p,p') + K(p,p)\right\}. \tag{2.9}$$

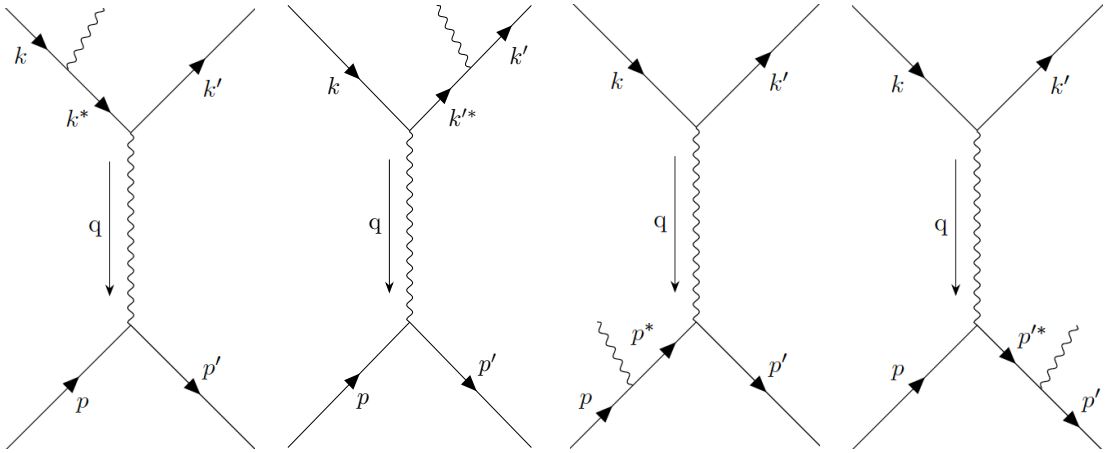

FIGURE 2.3: Feynman diagrams for single real photon emission from either electron or proton external legs in e-p scattering.

The structure-dependent $\delta^{p(1)}_{\text{vertex}}$ was found small relative to other contributions in the total cross section. Numerical value of $\delta^{p(1)}_{\text{vertex}}$ was smaller than 0.0068 for $Q^2 < 6$ GeV^2 but it keeps increasing with Q^2 and beam energy. Similar to the case of $\delta^{e}_{\text{vertex}}$, proton vertex correction is also IR divergent and this divergent term is also cancelled by the inelastic cross section of real photon emission from the proton legs. It is important to note that the corrections from the electron and proton self energy diagrams in Fig. 2.2 are also included in evaluation of the corresponding vertex corrections [76]. However, the corrections discussed up to this point does not show any ε dependence. Therefore, they do not have any significant influence in LT separation data apart from the effect of a normalization factor.

On the other hand, the corrections from the real soft photon emission and the soft part of the two-photon exchange radiative correction have significant ε dependence as pointed out by both group of authors of Refs. [75, 76]. More importantly the outcomes for these corrections estimated by the two prescriptions are different. The discussion on the IR divergent soft photon contribution in TPE is left as a separate section in chapter 3 (Sec. 3.1.2). As pointed out before, the real soft photon emission correction calculated by Mo-Tsai is different from that by Maximon-Tjon due to an incorrect substitution made in Ref. [75] which needs to be taken care if one uses the earlier prescription, as was done by Walker *et al.* [2] in his reanalysis. However, I prefer to show here the cross

section correction, $\delta_{\rm brems}$ from the real single photon bremsstrahlung within the soft photon approximation obtained by Maximon-Tjon as

$$\begin{aligned}\delta_{\rm brems} &= \frac{\alpha}{\pi}\Bigg\{\left[\ln\left(\frac{Q^2}{m^2}\right)-1\right]\ln\left(\frac{(\eta\, m\,\Delta E)^2}{EE'\lambda^2}\right)+\frac{1}{2}\ln^2\left(\frac{Q^2}{m^2}\right)-\frac{1}{2}\ln^2\eta+{\rm Li}_2\left(\cos^2\frac{\theta}{2}\right)\\ &\quad -\frac{\pi^2}{3}+2Z\left[\ln\eta\,\ln\left(\frac{(2\,\eta\Delta E)^2}{y\lambda^2}\right)+{\rm Li}_2\left(1-\frac{\eta}{y}\right)-{\rm Li}_2\left(1-\frac{1}{\eta y}\right)\right]\\ &\quad +Z^2\left[\left(\frac{E_{p'}}{|\boldsymbol{p}'|}\ln y-1\right)\ln\left(\frac{(2\,\eta\Delta E)^2}{\lambda^2}\right)\right.\\ &\quad \left.-\frac{E_{p'}}{|\boldsymbol{p}'|}\left[\ln^2 y-\ln y+{\rm Li}_2\left(1-\frac{1}{y^2}\right)\right]-1\right]\Bigg\},\end{aligned} \tag{2.10}$$

where $\eta = E/E^{'}$, ${\rm Li}_2$ is the dilogarithm function, $y = 1+2\tau+2\sqrt{\tau(1+\tau)}$, $E_{p'}$ is the energy of the final proton and ΔE is the cut off energy below which soft photon can not be detected due to detector acceptance [12]. In Eq. (2.10), the terms with Z^0, Z^1, and Z^2 correspond to the cross section corrections from electron bremsstrahlung, the interference between electron and proton bremsstrahlung, and the proton bremsstrahlung, respectively. Note since Z is the charge number it becomes 1 for e-p scattering. Further note that each of the terms coming from three different bremsstrahlung corrections has λ-dependent parts, *i.e.* IR divergent parts. The λ-dependent parts in the terms proportional to Z^0 and Z^2 will be cancelled out by similar counter terms from electron and proton vertex corrections, respectively, as pointed out before. The IR divergence in the interference term (proportional to Z^1) will also be cancelled out once the TPE correction is taken into account.

A comparison of the Mo-Tsai findings for the soft bremsstrahlung correction with that from Maximon-Tjon in terms of their difference ($\Delta_{\rm brems}$) would be convenient for any future global analysis of LT separation data. The difference in bremsstrahlung correction

between the two prescriptions, $\Delta_{\rm brems}$ can be written as [78]

$$\begin{aligned}\Delta_{\rm brems} &= \frac{\alpha}{\pi}\Bigg\{\left[{\rm Li}_2\left(\cos^2\frac{\theta}{2}\right)-\frac{\pi^2}{6}\right]-2Z\left[\ln\ \eta\ \ln x-{\rm Li}_2\left(1-\frac{\eta}{x}\right)+{\rm Li}_2\left(1-\frac{1}{\eta x}\right)\right.\\ &\left.+\frac{1}{2}{\rm Li}_2\left(1-\eta\frac{2E_{p'}}{M}\right)-\frac{1}{2}{\rm Li}_2\left(1-\frac{2E_{p'}}{\eta M}\right)\right]+Z^2\left[\frac{E_{p'}}{|\boldsymbol{p}'|}\left(\ln x-{\rm Li}_2\left(1-\frac{1}{x^2}\right)\right.\right.\\ &\left.\left.+{\rm Li}_2\left(-\frac{1}{x^2}\right)+\frac{\pi^2}{12}\right)-\ln\left(\frac{4E_{p'}}{M}\right)+1\right]\Bigg\},\end{aligned}\tag{2.11}$$

where $x=(E_{p'}+|\boldsymbol{p}'|)/M$. Note that the difference is independent of λ, *i.e.* the IR divergent part is same irrespective of the prescription used.

Adding up all the elastic and inelastic radiative corrections of Figs. 2.2 and 2.3 gives the total cross section correction (finite) in Maximon-Tjon evaluation as

$$\begin{aligned}\delta_{\rm MTj} &= \frac{\alpha}{\pi}\Bigg\{\frac{13}{6}\ln\left(\frac{Q^2}{m^2}\right)-\frac{28}{9}-\left[\ln\left(\frac{Q^2}{m^2}\right)-1\right]\ln\left(\frac{4EE'}{(2\eta\Delta E)^2}\right)-\frac{1}{2}\ln^2\eta\\ &+{\rm Li}_2\left(\cos^2\frac{\theta}{2}\right)-\frac{\pi^2}{6}\Bigg]+\frac{2\alpha Z}{\pi}\Bigg[-\ln\eta\ln\left(\frac{Q^2y}{(2\eta\Delta E)^2}\right)+{\rm Li}_2\left(1-\frac{\eta}{y}\right)\\ &-{\rm Li}_2\left(1-\frac{1}{\eta y}\right)\Bigg]+\frac{\alpha Z^2}{\pi}\Bigg[\frac{E_{p'}}{|\boldsymbol{p}'|}\left(-\frac{1}{2}\ln^2 y-\ln y\ln\left(\frac{\rho^2}{M^2}\right)+\ln y\right)\\ &-\left(\frac{E_{p'}}{|\boldsymbol{p}'|}\ln y-1\right)\ln\left(\frac{M^2}{(2\eta\Delta E)^2}\right)+1\\ &+\frac{E_{p'}}{|\boldsymbol{p}'|}\left(-{\rm Li}_2\left(1-\frac{1}{y^2}\right)+2{\rm Li}_2\left(-\frac{1}{y}\right)+\frac{\pi^2}{6}\right)\Bigg\}+\delta^{p(1)}_{\rm vertex}.\end{aligned}\tag{2.12}$$

2.4 Recent reanalysis of the Rosenbluth separation data

In a recent reanalysis of the LT separation data [39], Gramolin and Nikolenko used a selective data set from Refs. [2, 3], for which the detailed information about the radiative correction is available. In the reanalysis they substituted the Mo-Tsai corrections from the original literature by the Maximon-Tjon corrections given in Eq. (2.12) but

neglected the proton structure-dependent term $\delta^{p(1)}_{\text{vertex}}$. Apart from this substitution, they also added the vacuum polarization correction from the two more leptonic, $\mu^+\mu^-$ and $\tau^+\tau^-$, loops using Eq. (2.3) and the hadron loop using Eq. (2.5). Note that the the vacuum polarization correction form e^+e^- loop is already included in Eq. (2.12). In addition to the updates mentioned above they also included an estimated hard internal bremsstrahlung correction given by

$$\delta_{\text{int.brems}} = \frac{2\alpha}{\pi}\left(\ln\frac{Q^2}{m^2} - 1\right)\ln\frac{\delta E}{\Delta E} + \left[\left(\frac{d\sigma}{d\Omega}\right)_0(E)\right]^{-1}\int_{E'-\Delta E}^{E'-\delta E}\frac{d^2\sigma_{\text{int.brems}}}{d\Omega\, dE''}dE'', \quad (2.13)$$

where the cutoff energy δE should be chosen such that $\delta E \ll \Delta E$ (authors considered $\delta E = 10^{-4}$ GeV) and the integrand is given by

$$\frac{d^2\sigma_{\text{int.brems}}}{d\Omega\, dE''} = \frac{M + (E-\omega_1)(1-\cos\theta)}{M - E''(1-\cos\theta)}\frac{t_1}{\omega_1}\left(\frac{d\sigma}{d\Omega}\right)_0(E-\omega_1) + \frac{t_3}{\omega_3}\left(\frac{d\sigma}{d\Omega}\right)_0(E), \quad (2.14)$$

with

$$\begin{aligned} t_{1,3} &= \frac{\alpha}{\pi}\left[\frac{1+x_{1,3}^2}{2}\ln\frac{2EE''(1-\cos\theta)}{m^2} - x_{1,3}\right], \quad R = \frac{M + E(1-\cos\theta)}{M - E''(1-\cos\theta)}, \\ x_1 &= \frac{E-\omega_1}{E}, \quad x_3 = \frac{E''}{E''+\omega_3}, \quad \omega_1 = R\omega_3, \quad \omega_3 = E' - E''. \end{aligned} \quad (2.15)$$

Here E'' is the measured energy of the scattered electron and E' can be interpreted as the peak energy of the scattered electron in case of the hard bremsstrahlung. The improved prediction of the radiative tail given in Eq. (2.14) is compared with that estimated using the approximation of soft photon emission is compared in Fig. 2.4. The kinematic consideration in plotting the analytical results of the radiative tail were $E = 1.0$ GeV, $\theta = 70^\circ$ and the elastic peak energy $E' = 0.588$ GeV. Clearly, the inclusion of the hard bremsstrahlung makes a big difference with the soft photon approximation for smaller E''. However, with this addition of the hard internal bremsstrahlung correction the total radiative correction factor C_{RC} can be written as

$$C_{\text{RC}} = \left(1 + \delta_{\text{MTj}} + \delta^{\mu,\tau,q}_{\text{vp}} + \delta_{\text{int.brems}} + \delta_{\text{ext.brems}}\right)C_L, \quad (2.16)$$

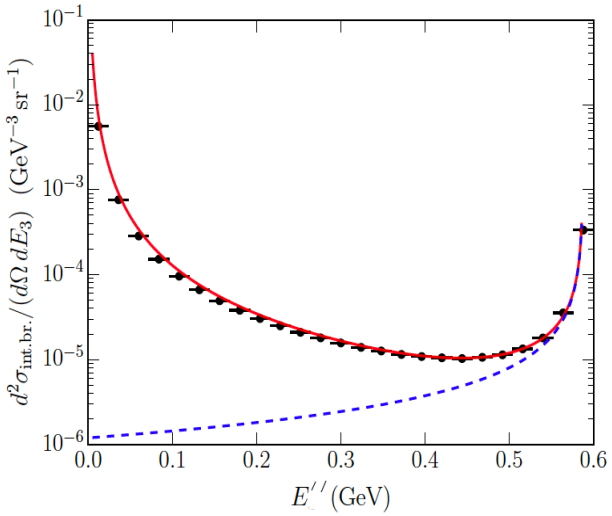

FIGURE 2.4: The radiative tail predicted using soft photon approximation (blue dashed) and from the sum of soft and hard internal bremsstrahlung (red solid line).The points are simulated data from Ref. [81]

where $\delta_{\text{ext.brems}}$ and C_L account for the external bremsstrahlung and the ionization losses in the target materials. Ref. [39] took the exponentiation of the cross section corrections from the additional single photon emissions discussed above to take into account the effect of an arbitrary number of soft photons and thus C_{RC} takes the form

$$C_{\text{RC}} = C_L \ \exp(\delta_{\text{RC}}), \tag{2.17}$$

with

$$\delta_{\text{RC}} = \delta_{\text{MTj}} + \delta_{\text{vp}}^{\mu,\tau,q} + \delta_{\text{int.brems}} + \delta_{\text{ext.brems}}. \tag{2.18}$$

The extracted electric and magnetic form factors using these updated treatment of the radiative corrections in just two sets of Rosenbluth data Gramolin and Nikolenko found better agreement with the polarization transfer data of the ratio $\mu_p G_E/G_M$. It is important to note here that this reanalysis did not take account of the ε-dependent hard TPE effect which makes the analysis partly incomplete.

2.5 Potential solution to the $\mu_p G_E/G_M$ discrepancy

The proton structure-dependent radiative correction two-photon exchange (hard) is a potential candidate to resolve the discrepancy in proton electric to magnetic form factor ratio $\mu_p G_E/G_M$ as it is found an ε-dependent correction. Approximately half of the discrepancy was resolved once the TPE correction was applied indirectly in some previously extracted ratio $\mu_p G_E/G_M$ using LT separation method, where this correction term was ignored during the initial extraction, by Blunden *et al.* [10, 37]. In their hadronic calculation, the TPE cross section correction $\delta_{\gamma\gamma}$ was found nearly linear in polarization ε, at least in the interval of $0.2 \leq \varepsilon \leq 0.9$. Therefore, the correction factor $1 + \delta_{\gamma\gamma}$ to the reduced Born cross section $\sigma_{\mathrm{R}}^{\mathrm{Born}}$ is fitted to a function of the form $a + b\varepsilon$ for corresponding Q^2 values of the experiments satisfying the condition that the $(1 + \delta_{\gamma\gamma}) \to 1$ in the limit of $\varepsilon \to 1$. Then knowing the fitted parameters a and b the TPE corrected form factor ratio $R = \mu_p G_E/G_M$ was extracted from the TPE contaminated ratio $\tilde{R}$ using,

$$R^2 = \frac{\tilde{R}^2 - b\tau\mu_p^2/a}{1 + \bar{\varepsilon}b/a}, \tag{2.19}$$

where $\tilde{R}$ is the TPE contaminated ratio and $\bar{\varepsilon}$ is an approximated average value of the total ε range of data.

The TPE corrected results for $\mu_p G_E/G_M$ along with the TPE contaminated ones from the reanalysis of the unpolarized Rosenbluth data by Arrington [35] are compared with the polarization transfer data from [5, 6, 9] in Fig. 2.5(a). Note also that the TPE effect on $\mu_p G_E/G_M$ data from polarization transfer measurements were also investigated and found very negligible change due to inclusion of TPE correction as shown in Fig. 2.5(b). This is because the PT data were mostly in the region $\varepsilon \approx 0.7 - 0.8$ where the TPE correction was found very small.

At the then contemporary time of Blunden's work [10], Guichon and Vanderhaeghen [11] also emphasized on hard TPE correction as the source of the discrepancy. Their conclusion was coherent with that of Refs. [10, 37] that the Rosenbluth data are sensitive to the hard TPE correction while the PT data are relatively blind about TPE.

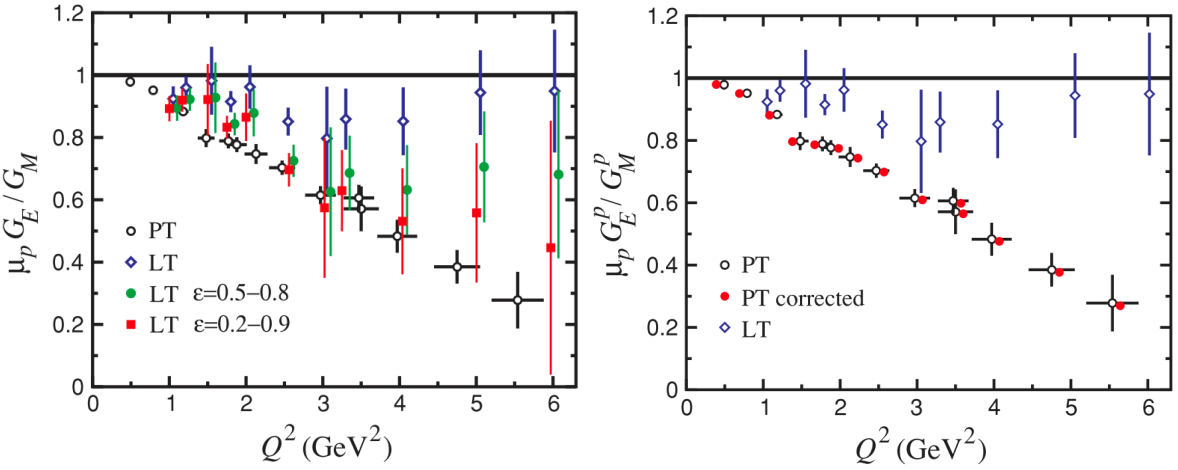

FIGURE 2.5: TPE contaminated LT data (open diamonds) for proton electric to magnetic form factor ratio, $\mu_p G_E/G_M$, from Ref. [35], and the corresponding TPE corrected data (green circles and red squares) by Blunden *et al.* [37] are compared with the polarization transfer data(black open circles)[7–9] on the left. On the right a similar comparison is shown, but here the PT data are TPE corrected (red circles). The TPE corrected LT points (green circles) on the left panel are obtained assuming a linear relation of the TPE cross section with ε in the range 0.5 to 0.8, while the points with red squares used the ε range of 0.2 to 0.9. Plots are taken from Ref. [37].

2.6 Summary and discussion

Having discussed the details of the existing discrepancy between the two different methods of measurement (LT and PT) of the electric to magnetic form factor ratio $\mu_p G_E/G_M$, it turns out to be a puzzle. This so-called puzzle seems to have its solution in a neglected correction which actually is not negligible, at least due to its significant ε dependence. Thus, I see hope in hard two-photon exchange. But the correction itself has large uncertainty in its calculation which needs to be taken under control either by any improvement in the model estimation or by direct experimental extraction (or both). Plenty of efforts has already been applied to better understand the correction since the first observation of the effect as a potential candidate to resolve the $\mu_p G_E/G_M$ puzzle. Before carrying out a rigorous and improved numerical estimation of the TPE correction in chapter 4 it is important to discuss the general formalism of TPE amplitude and review its quantitative estimations and/or measurements to date. In the next chapter, the details of the hadron structure-dependent TPE radiative correction will be discussed along with a review of the previous works in the specific topic.

Chapter 3

Two-photon exchange

This chapter describes the basic formalism (Sec. 3.1) and a brief review of the model calculations (Sec. 3.2) along with the direct experimental (Sec. 3.4) and phenomenological (Sec. 3.3) measurements of the two-photon exchange radiative correction, the evaluation of which is the main subject matter of this thesis. The formalism illustrated in Sec. 3.1 is basically focused on the inelastic resonance intermediate states for which the subscript R is used in the notations of intermediate hadron momenta and the corresponding transition currents even though the specific description of the spin half intermediate states is also applicable for the elastic nucleon. Representation of the TPE amplitude and corresponding cross section in terms of the generalized form factors is discussed in Sec. 3.1.1 followed by the description of the infrared divergence in TPE (Sec. 3.1.2). Finally the necessity of the used method and the extended breadth in calculation of the real part of TPE amplitude will be summed up in the last section (Sec. 3.6).

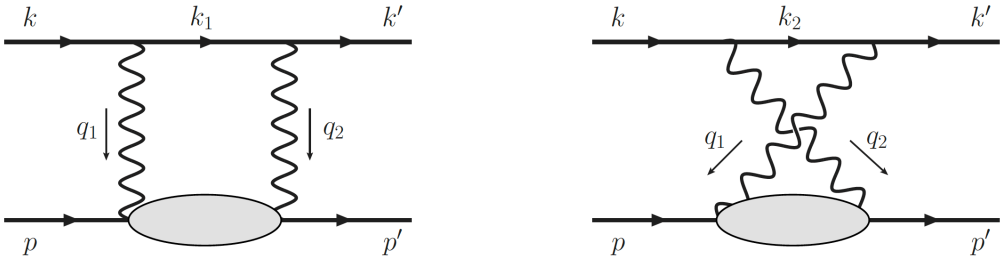

FIGURE 3.1: Two-photon exchange amplitude Feynman diagram for s-channel box (left panel) and u channel x-box (right panel). The two exchanged photons carry momenta q_1 and q_2.

3.1 Two-photon exchange amplitude

The two-photon exchange amplitude, $\mathcal{M}_{\gamma\gamma}$, is the sum of contributions from the s-channel box (left panel) and u- channel crossed-box diagrams (right panel) of Fig. 3.1,

$$\mathcal{M}_{\gamma\gamma} = \mathcal{M}^{\text{box}}_{\gamma\gamma} + \mathcal{M}^{\text{xbox}}_{\gamma\gamma}. \tag{3.1}$$

In general, the box and crossed-box diagram amplitudes $\mathcal{M}^{\text{box}}_{\gamma\gamma}$ and $\mathcal{M}^{\text{xbox}}_{\gamma\gamma}$ can be written as an integral over loop momenta q_1 or q_2 of the exchanged photons [12],

$$\mathcal{M}^{\text{box}}_{\gamma\gamma} = -ie^4 \int \frac{d^4q_1}{(2\pi)^4} \frac{L^{\text{box}}_{\mu\nu} H^{\mu\nu}_R}{(q_1^2-\lambda^2)(q_2^2-\lambda^2)}, \tag{3.2a}$$

$$\mathcal{M}^{\text{xbox}}_{\gamma\gamma} = -ie^4 \int \frac{d^4q_1}{(2\pi)^4} \frac{L^{\text{xbox}}_{\mu\nu} H^{\mu\nu}_R}{(q_1^2-\lambda^2)(q_2^2-\lambda^2)}, \tag{3.2b}$$

where an infinitesimal photon mass λ is introduced to regulate infrared divergences. Note a sum over all the intermediate states (R) is implicit in Eq. (3.2b) to get the total TPE correction. The leptonic tensor $L_{\mu\nu}$ in Eq. (3.2b) is given by

$$L^{\text{box}}_{\mu\nu} = \bar{u}_e(k')\gamma_\mu S_F(k_1, m_e)\gamma_\nu u_e(k), \tag{3.3}$$

where $k_1 = k - q_1$ is the intermediate lepton four-momentum, m_e is the electron mass (which can in practice be taken to zero at the kinematics considered here), and S_F is

the electron propagator defined by

$$S_F(k_1, m_e) = \frac{(\not{k}_1 + m_e)}{k_1^2 - m_e^2 + i0^+}. \tag{3.4}$$

The hadronic tensor $H_R^{\mu\nu}$ (same for box and crossed-box TPE) for each intermediate state R can be expressed as

$$H_R^{\mu\nu} = \bar{u}_N(p')\,\Gamma^{\mu\alpha}_{R\to\gamma N}(p_R, -q_2)\,S_{\alpha\beta}(p_R, W)\,\Gamma^{\beta\nu}_{\gamma N\to R}(p_R, q_1)\,u_N(p), \tag{3.5}$$

in terms of the transition operators $\Gamma^{\beta\nu}_{\gamma N\to R}$ ($\Gamma^{\mu\alpha}_{R\to\gamma N}$) between the initial (final) nucleon and intermediate resonance R (or, elastic nucleon) states, where $p_R = p + q_1$ is the four-momentum of the intermediate state and W its (in principle running) mass.

For spin 1/2 baryon intermediate states the propagator $S_{\alpha\beta}(p_R, W)$ reduces to the usual spin-1/2 propagator

$$S_{\alpha\beta}(p_R, W) = \delta_{\alpha\beta}\frac{(\not{p}_R + W)}{p_R^2 - W^2 + i0^+} = \delta_{\alpha\beta}\,S_F(p_R, W), \tag{3.6}$$

for a particle with mass W. The hadronic tensor for spin-1/2 baryons can then be written

$$H_R^{\mu\nu} = \bar{u}_N(p')\,\Gamma^{\mu}_{R\to\gamma N}(p_R, -q_2)\,S_F(p_R, W)\,\Gamma^{\nu}_{\gamma N\to R}(p_R, q_1)\,u_N(p), \tag{3.7}$$

where the operator $\Gamma_{\gamma N\to R}$ describes the transition to a baryon resonance with spin 1/2. Note that this hadronic tensor will remain identical for the case of elastic nucleon intermediate state except the mass W will be replaced by the nucleon mass M and the transition operators will be substituted by the operator shown in Eq. (1.5).

For the hadronic propagator of spin-3/2 states the form

$$S_{\alpha\beta}(p_R, W) = -\mathcal{P}^{3/2}_{\alpha\beta}(p_R)\,\frac{(\not{p}_R + W)}{p_R^2 - W^2 + i0^+}, \tag{3.8}$$

is used, where the spin-3/2 projection operator $\mathcal{P}^{3/2}_{\alpha\beta}$ is defined by

$$\mathcal{P}^{3/2}_{\alpha\beta}(p_R) = g_{\alpha\beta} - \frac{1}{3}\gamma_\alpha\gamma_\beta - \frac{1}{3p_R^2}\left(\not{p}_R\gamma_\alpha(p_R)_\beta + (p_R)_\alpha\gamma_\beta\not{p}_R\right). \tag{3.9}$$

The resonance transition currents $\Gamma^{\beta\nu}_{\gamma N\to R}(p_R, q_1)$ and $\Gamma^{\mu\alpha}_{R\to\gamma N}(p_R, -q_2)$ at the two hadron vertices can be parametrized using the form factors G_1, G_2, and G_3 [53, 82, 83]. These parametrizations are not unique. They can also be parametrized in terms of the electric (G_E^*), magnetic (G_M^*), and Coulomb (G_C^*) form factors [82]. Details of the transition current are discussed in Sec. 5.2.

The TPE crossed-box amplitude $\mathcal{M}^{\text{xbox}}_{\gamma\gamma}$ can be calculated by using the lepton tensor $L^{\text{xbox}}_{\mu\nu}$ in Eq. (3.2) as

$$L^{\text{xbox}}_{\mu\nu} = \bar{u}_e(k')\,\gamma_\nu\,S_F(k_2, m_e)\,\gamma_\mu u_e(k), \tag{3.10}$$

where the intermediate lepton momentum is $k_2 = k - q_2$. The crossed-box amplitude can also be obtained from the crossing symmetry relation [46]

$$\mathcal{M}^{\text{xbox}}_{\gamma\gamma}(u,t) = -M^{\text{box}}_{\gamma\gamma}(s,t)\Big|_{s\to u}, \tag{3.11}$$

where the Mandelstam variables s, t, and u are defined by

$$s = (k+p)^2 = (k'+p')^2, \tag{3.12a}$$
$$t = (k-k')^2 = q^2, \tag{3.12b}$$
$$u = (p-k')^2 = (p'-k)^2. \tag{3.12c}$$

Note however, that unlike the box amplitude, which is complex, the crossed-box amplitude is purely real. In the dispersive approach it is therefore not necessary to consider the crossed-box term explicitly. It will be shown explicitly in Sec. 4.2 that the imaginary part of the TPE amplitude entirely comes from the box diagram of Fig. 3.1 and that the real part of the TPE amplitude from the direct analytic calculation and numerical calculation are identical considering the simple case of point-like target particle, *i.e.* in e-μ scattering. Including the one- and two-photon exchange contributions, the total

squared amplitude can be written

$$\begin{aligned} |\mathcal{M}_\gamma + \mathcal{M}_{\gamma\gamma}|^2 &\approx |\mathcal{M}_\gamma|^2 + 2\,\mathrm{Re}(\mathcal{M}_\gamma^\dagger \mathcal{M}_{\gamma\gamma}) \\ &\equiv |\mathcal{M}_\gamma|^2 (1 + \delta_{\gamma\gamma}), \end{aligned} \tag{3.13}$$

where terms of order α^4 and beyond have been neglected, and we have defined the relative two-photon exchange correction to the cross section as

$$\delta_{\gamma\gamma} = \frac{2\,\mathrm{Re}(\mathcal{M}_\gamma^\dagger \mathcal{M}_{\gamma\gamma})}{|\mathcal{M}_\gamma|^2}. \tag{3.14}$$

For the nucleon intermediate state the TPE cross section correction is infrared divergent in the soft photon limit, but this divergence is exactly cancelled by a corresponding divergence in the real photon emission from the electron and proton, discussed in Sec. 2.3. It is useful, however, to define a finite TPE correction which has the IR divergent contribution subtracted. This correction will not be unique, as it depends on the prescription used for the regularization [12, 46, 75, 76]. For most of the theoretical results presented in this analysis the prescription of Maximon and Tjon [76],

$$\delta = \delta_{\gamma\gamma} - \delta_{\gamma\gamma}^{\mathrm{IR}}(\mathrm{MTj}), \tag{3.15}$$

is used. Note that the notation δ is dedicated for the IR subtracted TPE cross section correction from now on. For comparisons with experimental data, however, we use the Mo and Tsai prescription [75], which has traditionally been employed in analyses of electron-proton scattering.

3.1.1 TPE in terms of generalized form factors

The general amplitude of the elastic scattering between two spin-1/2 particles involves 16 helicity amplitudes. The discrete symmetries, parity and charge conjugation invariances, leaves only 6 independent helicity amplitudes or invariant amplitudes [84]. Three of them flip the lepton helicity, while the other three do not [11, 68]. The amplitudes that

flips the helicity are of the order of lepton mass (m_e), *i.e.* the amplitude is factored by the lepton mass. In other words, in the massless limit lepton helicity is conserved in every order of perturbation theory in a gauge theory [11]. As a consequence, only three helicity amplitudes, $T_{hh'\lambda\lambda'}$ survive in this limit. Here h and h' are the helicity of the incident and scattered lepton, while λ and λ' are that of the target and recoiled particle. The surviving set of amplitudes may be: T_{++++}, T_{++--}, and $T_{++-+} = T_{+++-}$; or T_{--++}, T_{----}, and $T_{---+} = T_{--+-}$, for example. Therefore, in the massless electron limit, which is a reasonably good approximation in the kinematics of the experiments mentioned in this thesis, the general form of the scattering amplitude can be decomposed into three Lorentz structures with coefficients being the generalized form factors F_1', F_2', and G_a', as [43, 46]

$$\begin{aligned}\mathcal{M} &= -\frac{e^2}{q^2}\bar{u}_e(k')\gamma_\mu u(k)\,\bar{u}_N(p')\left[F_1'(Q^2,\nu)\gamma^\mu + F_2'(Q^2,\nu)\frac{i\sigma^{\mu\nu}q_\nu}{2M}\right]u_N(p) \\ &\quad -\frac{e^2}{q^2}\bar{u}_e(k')\gamma_\mu\gamma_5 u(k)\,\bar{u}_N(p')G_a'(Q^2,\nu)\gamma^\mu\gamma_5 u_N(p), \end{aligned} \tag{3.16}$$

where these are functions of Q^2 and the dimensionless variable

$$\nu \equiv \frac{s-u}{4M^2} = \sqrt{\frac{\tau(1+\tau)(1+\varepsilon)}{1-\varepsilon}}. \tag{3.17}$$

Including only the TPE correction, the generalized amplitude and the form factors can further be decomposed as

$$\mathcal{M} = \mathcal{M}_\gamma + \mathcal{M}_{\gamma\gamma}, \tag{3.18a}$$

$$F_1'(Q^2,\nu) = F_1(Q^2) + F_{1_{\gamma\gamma}}'(Q^2,\nu), \tag{3.18b}$$

$$F_2'(Q^2,\nu) = F_2(Q^2) + F_{2_{\gamma\gamma}}'(Q^2,\nu), \tag{3.18c}$$

$$G_a'(Q^2,\nu) = G_{a_{\gamma\gamma}}'(Q^2,\nu), \tag{3.18d}$$

i.e. in the One Photon Exchange (OPE) limit, the generalized form factors, $F_1'(Q^2,\nu)$, and $F_2'(Q^2,\nu)$ will be reduced to the the Dirac and Pauli form factors $F_1(Q^2)$ and $F_2(Q^2)$, respectively, and $G_a'(Q^2,\nu) \to 0$. Thus, the OPE amplitude in that limit takes the usual

form

$$\mathcal{M}_\gamma = -\frac{e^2}{q^2}\bar{u}_e(k')\gamma_\mu u(k)\,\bar{u}_N(p')\left[F_1(Q^2)\gamma^\mu + F_2(Q^2)\frac{i\sigma^{\mu\nu}q_\nu}{2M}\right]u_N(p). \quad (3.19)$$

The TPE amplitude, $\mathcal{M}_{\gamma\gamma}$ can be written as

$$\begin{aligned}\mathcal{M}_{\gamma\gamma} = & -\frac{e^2}{q^2}\bar{u}_e(k')\gamma_\mu u(k)\,\bar{u}_N(p')\left[F'_{1_{\gamma\gamma}}(Q^2,\nu)\gamma^\mu + F'_{2_{\gamma\gamma}}(Q^2,\nu)\frac{i\sigma^{\mu\nu}q_\nu}{2M}\right]u_N(p) \\ & -\frac{e^2}{q^2}\bar{u}_e(k')\gamma_\mu\gamma_5 u(k)\,\bar{u}_N(p')G'_{a_{\gamma\gamma}}(Q^2,\nu)\gamma^\mu\gamma_5 u_N(p). \quad (3.20)\end{aligned}$$

For simplicity of notation, the subscript "$\gamma\gamma$" in the generalized form factor corrections from TPE will be omitted in the remainder of the thesis. Therefore, $F'_1(Q^2,\nu)$, $F'_2(Q^2,\nu)$, and $G'_a(Q^2,\nu)$ will imply the TPE correction to the generalized form factors in rest of the thesis. To eliminate any confusion in future use the TPE amplitude $\mathcal{M}_{\gamma\gamma}$ is written again in terms of these TPE generalized form factors correction as

$$\begin{aligned}\mathcal{M}_{\gamma\gamma} = & -\frac{e^2}{q^2}\bar{u}_e(k')\gamma_\mu u_e(k)\,\bar{u}_N(p')\left[F'_1(Q^2,\nu)\gamma^\mu + F'_2(Q^2,\nu)\frac{i\sigma^{\mu\nu}q_\nu}{2M}\right]u_N(p) \\ & -\frac{e^2}{q^2}\bar{u}_e(k')\gamma_\mu\gamma_5 u_e(k)\,\bar{u}_N(p')G'_a(Q^2,\nu)\gamma^\mu\gamma_5 u_N(p). \quad (3.21)\end{aligned}$$

The TPE cross section can then be expressed in terms of the generalized TPE form factors as [46]

$$\delta_{\gamma\gamma} = 2\mathrm{Re}\frac{\varepsilon G_E(F'_1 - \tau F'_2) + \tau G_M(F'_1 + F'_2) + \nu(1-\varepsilon)G_M G'_a}{\varepsilon G_E^2 + \tau G_M^2}. \quad (3.22)$$

An alternative representation for the TPE cross section combines the F'_1, F'_2, and G'_a generalized TPE form factors into combinations that resemble the electric and magnetic Sachs form factors at the Born level. Namely, defining [48]

$$\mathcal{G}_E \equiv F'_1 - \tau F'_2, \quad (3.23a)$$

$$\mathcal{G}_M \equiv F'_1 + F'_2 + \frac{\nu}{\tau}(1-\epsilon)G'_a, \quad (3.23b)$$

the TPE cross section can be written in a simplified form analogous to the diagonal structure of the Born cross section of Eq. (1.13),

$$\delta_{\gamma\gamma} = 2\mathrm{Re}\frac{\varepsilon G_E \mathcal{G}_E + \tau G_M \mathcal{G}_M}{\varepsilon G_E^2 + \tau G_M^2}. \tag{3.24}$$

However, the representation of the scattering amplitude and hence the TPE amplitude in terms of the generalized form factors is not unique. Some authors [11] prefer the convention of the form factors $\tilde{F}_1, \tilde{F}_2$, and $\tilde{F}_3$, in terms of which $\mathcal{M}_{\gamma\gamma}$ is given by

$$\begin{aligned}\mathcal{M}_{\gamma\gamma} &= -\frac{e^2}{q^2}\bar{u}_e(k')\gamma_\mu u_e(k) \times \bar{u}_N(p')\Big[\tilde{F}_1(Q^2,\nu)\gamma^\mu + \tilde{F}_2(Q^2,\nu)\frac{i\sigma^{\mu\nu}q_\nu}{2M} \\ &\quad + \tilde{F}_3(Q^2,\nu)\frac{\not{k}p^\mu}{M^2}\Big]u_N(p).\end{aligned} \tag{3.25}$$

The relationship between the two sets of form factors can easily be established as

$$F_1' = \tilde{F}_1 + \nu\tilde{F}_3, \tag{3.26a}$$

$$F_2' = \tilde{F}_2, \tag{3.26b}$$

$$G_a' = -\tau\tilde{F}_3. \tag{3.26c}$$

For completeness, the lepton helicity-flipping Lorentz structures involve three more complex-valued coefficients $\tilde{F}_4$, $\tilde{F}_5$, and $\tilde{F}_6$, known as the generalized form factors that construct the helicity-flipped part of the most general form of the scattering amplitude $\mathcal{M}$. In the later convention of Ref. [11], the helicity-flipping amplitude is given by [85]

$$\begin{aligned}\mathcal{M}^{\mathrm{flip}} &= -\frac{m_e}{M}\frac{e^2}{q^2}\Big[\bar{u}_e(k')u_e(k)\,.\,\bar{u}_N(p')\Big(\tilde{F}_4(Q^2,\nu) + \tilde{F}_5(Q^2,\nu)\frac{\not{k}+\not{k}'}{2M}\Big)u_N(p) \\ &\quad + \tilde{F}_6(Q^2,\nu)\bar{u}_e(k')\gamma_5 u_e(k)\bar{u}_N(p')\gamma_5 u_N(p)\Big].\end{aligned} \tag{3.27}$$

Here all three form factors vanish in the Born approximation, *i.e.* $\tilde{F}_{4,5,6}^{\mathrm{Born}} = 0$.

3.1.2 Infrared divergence

The TPE amplitude $\mathcal{M}_{\gamma\gamma}$ of Eq. (3.2b) has IR poles at the soft photon limit of either of the two exchanged virtual photons, *i.e.* at either $q_1 \to 0$ or $q_2 \to 0$. To regulate the IR divergences originating from these poles, the infinitesimally small parameter λ is introduced in the two virtual photon propagators' denominator. In general the calculated TPE cross section correction, for nucleon intermediate state, is thus λ-dependent. Fortunately, a similar term originating from the cross section due to the interference between the emission of real photon (bremsstrahlung) from electron and from proton, as shown in Fig. 2.3, cancels the λ-dependent divergent term from the total e-p elastic scattering cross section [76]. Therefore, separating out the λ-dependent divergent part from the finite part of the TPE calculation is useful since only the finite part will eventually be accounted in observable quantities. However, isolating the divergent part from the finite part is not unique. The IR divergent part obtained by the old traditional prescription of Mo and Tsai [75] is mostly used in experimental analyses for historical reasons, perhaps. On the other hand, in theoretical calculations the updated prescriptions by Maximon and Tjon [76] is preferred. One needs to be cautious during the comparison of experimentally measured observable with the theoretical predictions. Also, it is preferable to use the same prescription for isolating the IR divergent parts both from TPE and real bremsstrahlung corrections as the later in Mo-Tsai treatment has a wrong substitution that leads to the different results even after having the same assumptions.

In evaluation of the box and crossed-box diagram of Fig. 3.1 at such poles, Maximon and Tjon considered the single soft photon approximation, *i.e.* $q_1 = 0$ (or $q_1 = q$), and $q_2 = q$ (or $q_2 = 0$), only in the numerator of Eq. (3.2b) for nucleon intermediate state, while Mo and Tsai [75] treated both numerator and denominator with single soft photon approximation. Taking the soft photon approximation at a hadronic vertex is actually equivalent to treating the nucleon as a point-like particle, *i.e.* one of the hadronic vertices, where soft photon is assumed, will have the substitution $\Gamma^\mu(0) \to \gamma^\mu$ for the transition current operator, whereas the other hadronic vertex will have the current

operator as $\Gamma^{\nu}(q)$. With this approximation, the pole contribution (divergent) becomes proportional to the Born amplitude and hence the TPE cross section correction coming from the pole contribution remains independent of the structure of proton. Thus the total TPE amplitude with the soft photon approximation becomes [12, 76]

$$\begin{aligned}\mathcal{M}_{\gamma\gamma}^{\rm IR} &= e^4 N_{\rm box}(0)\int\frac{d^4q_1}{(2\pi)^4}\frac{1}{[q_1^2-\lambda^2][q_2^2-\lambda^2][k_1^2-m_e^2][(p+q_1)^2-M^2]} \\ &\quad + e^4 N_{\rm xbox}(0)\int\frac{d^4q_1}{(2\pi)^4}\frac{1}{[q_1^2-\lambda^2][q_2^2-\lambda^2][k_2^2-m_e^2][(p+q_1)^2-M^2]},\end{aligned} \tag{3.28}$$

where $N_{\rm box}(0)$ and $N_{\rm xbox}(0)$ are obtained after using the soft photon approximation, for corresponding box and crossed-box diagrams, respectively, at either of the exchanged photons as [37, 76]

$$N_{\rm box}(0) = N_{\rm box}(q) = 4i\,k\cdot p\,\frac{q^2\,\mathcal{M}_\gamma}{e^2}, \tag{3.29a}$$

$$N_{\rm xbox}(0) = N_{\rm xbox}(q) = 4i\,k'\cdot p\,\frac{q^2\,\mathcal{M}_\gamma}{e^2}. \tag{3.29b}$$

It is interesting to note that the soft photon approximation for either of the two exchanged virtual photons gives the same result since the TPE amplitude is symmetric under the interchange of $q_1 \Leftrightarrow q_2$. The integral of Eq. (3.28) can be expressed as four-point Passarino–Veltman functions $D_0(s)$ and $D_0(u)$ for box and crossed-box contributions, respectively, by [12]

$$\mathcal{M}_{\gamma\gamma}^{\rm IR} = -\frac{\alpha}{2\pi}q^2\mathcal{M}_\gamma\Big[(s-M^2)D_0(s)-(u-M^2)D_0(u)\Big], \tag{3.30}$$

where s and u are the Mandelstam variables defined in Eq. (3.12c). The asymptotic expansion of the IR divergent four point Passarino-Veltman functions $D_0(s)$ is available from Ref. [86]. In the limit of $s-M^2 \gg (m_e^2, m_e M)$ or $\lambda^2 \ll Q^2$, $D_0(s)$ can be written as

$$D_0(s) = \frac{2}{(s-M^2)q^2}\ln\left(\frac{M^2-s}{Mm_e}\right)\ln\left(\frac{-q^2}{\lambda^2}\right). \tag{3.31}$$

Exploiting the crossing symmetry of $\mathcal{M}^{\rm xbox}_{\gamma\gamma}(u,t) = -\mathcal{M}^{\rm box}_{\gamma\gamma}(s,t)\,|_{s\to u}$, one can write the IR divergent part of total TPE amplitude $\mathcal{M}^{\rm IR}_{\gamma\gamma}$ as

$$\begin{aligned}\mathcal{M}^{\rm IR}_{\gamma\gamma} &= -\frac{\alpha}{\pi}\mathcal{M}_\gamma\left[\ln\left(\frac{M^2-s}{Mm_e}\right)\ln\left(\frac{-q^2}{\lambda^2}\right) - \ln\left(\frac{M^2-u}{Mm_e}\right)\ln\left(\frac{-q^2}{\lambda^2}\right)\right] \\ &= -\frac{\alpha}{\pi}\mathcal{M}_\gamma\left[\ln\left(\frac{M^2-s}{M^2-u}\right)\ln\left(\frac{Q^2}{\lambda^2}\right)\right]. \end{aligned} \tag{3.32}$$

Therefore, the IR singularity in the TPE cross section using Maximon and Tjon treatment is given by,

$$\delta_{\gamma\gamma}(\text{IR-divergent}) = -2\frac{\alpha}{\pi}\left[\ln\left(\frac{M^2-s}{M^2-u}\right)\ln\left(\frac{Q^2}{\lambda^2}\right)\right]. \tag{3.33}$$

Equation 3.33 contains both real and imaginary parts in it. For completeness, extracting the explicit forms of the real and imaginary parts of $\delta_{\gamma\gamma}$ (IR-divergent) as

$$\delta^{\rm IR}_{\gamma\gamma}(\text{MTj}) \equiv \text{Re}\,\delta_{\gamma\gamma}(\text{IR-divergent}) = -2\frac{\alpha}{\pi}\left[\ln\left(\frac{s-M^2}{M^2-u}\right)\ln\left(\frac{Q^2}{\lambda^2}\right)\right], \tag{3.34a}$$

$$\text{Im}\,\delta_{\gamma\gamma}(\text{IR-divergent}) = 2\alpha\ln\left(\frac{Q^2}{\lambda^2}\right), \tag{3.34b}$$

even though the real part is of particular interest in this work. Here the convention of $\ln(-x) = \ln(x) - i\pi$ for $x > 0$ is used. The λ-dependent logarithmic IR singularity on $\text{Re}\,\delta^{\rm IR}_{\gamma\gamma}(\text{MTj})$ is exactly cancelled by by a term proportional to Z^1 in the bremsstrahlung cross section of Eq. (2.10). To see the cancellation one needs to use the expressions of the Mandelstam variables s and u in terms of initial and final electron energies E and E' in lab frame as

$$s = M^2 + 2ME, \qquad u = M^2 - 2ME'. \tag{3.35}$$

Providing the results obtained by Mo and Tsai [75] for the IR divergent part of TPE cross section would be helpful to compare the calculated values of the observable quantities, e.g. $\mu_p G_E/G_M$ ratio, with the measured ones to avoid any unwanted ambiguity arising due to the preference of one treatment over other. By the application of the

soft photon approximation at the denominator of Eq. (3.2b) along with the numerator reduces the loop integral to three point Passarino-Veltman functions $C_0(s)$ and $C_0(u)$ for box and crossed-box part, respectively. Since no simple analytic form is available for the asymptotic expansion of the three point Passarino-Veltman function in the limit of $s - M^2 \gg m_e^2, m_e M$ or $\lambda^2 \ll Q^2$, Mo and Tsai further used a mathematical approximation of replacing $p \to -p$ in the three point function for the TPE box diagram alone which gives the final expression of the IR singularity in the TPE cross section as [12]

$$\begin{aligned}\delta_{\gamma\gamma}^{\rm IR}({\rm MoT}) &= \frac{2\alpha}{\pi}\left[{\rm Li}_2\left(1-\frac{M}{2E}\right)-{\rm Li}_2\left(1-\frac{M}{2E'}\right)\right.\\ &\left.-\frac{1}{2}\ln\left(\frac{s-M^2}{M^2-u}\right)\ln\left(\frac{4M^2EE'}{\lambda^4}\right)\right].\end{aligned} \tag{3.36}$$

Note that the λ-dependent terms in both treatments, *i.e.* in Eqs. (3.34b) and (3.36), are same even though the cross section results of the soft photon approximation are not identical. Therefore, the elimination of the IR pole singularity from the total cross section, by a same counter term coming from the Bremsstrahlung cross section, is guaranteed in either prescriptions. However, it is important to analyze the virtual photon polarization, ε dependence of the difference $\Delta^{\rm IR} = \delta_{\gamma\gamma}^{\rm IR}({\rm MTj}) - \delta_{\gamma\gamma}^{\rm IR}({\rm MoT})$, especially for the extraction of the ratio $\mu_p G_E/G_M$ using Rosenbluth (LT) separation technique [18]. Fig. 3.2 illustrates the difference $\Delta^{\rm IR}$ as a function of ε at the representative squared four-momentum transfers $Q^2 = 0.2$, 1.0, 3.0, and 5.0 GeV^2. It is evident that the treatments are almost identical at small Q^2 values and forward angles (large ε) but as Q^2 increases the difference exceeds even 1% at the backward angles corresponding to smaller ε for $Q^2 = 5$ GeV^2. A visible non-linearity of $\Delta^{\rm IR}$ in ε is also observed with increasing Q^2. These differences in the soft photon treatments are significant in LT separation data and hence in the discrepancy of $\mu_p G_E/G_M$ ratio [10]. $\Delta^{\rm IR}$ alone reduces the $\mu_p G_E/G_M$ discrepancy by 3% and 7% for $Q^2 = 3$ and 6 GeV^2, respectively [10]. It is important to note that the divergence in TPE amplitude at the soft photon limit exists only for elastic nucleon intermediate states. In case of excited resonance intermediate states every terms in the numerator of Eq. (3.2b) contains the four-momentum factor

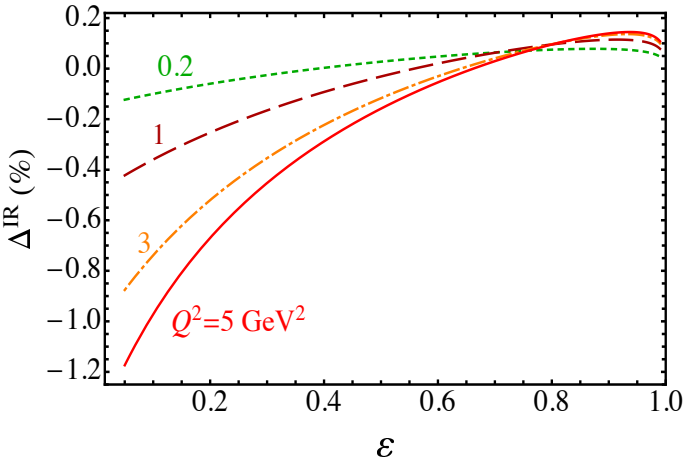

FIGURE 3.2: Difference between the IR divergent parts of the TPE cross section from Refs. [76] and [75] as a function of virtual photon polarization ε at fixed values of $Q^2 = 0.2$, 1.0, 3.0, and 5.0 GeV^2.

q coming from the parametrizations of the hadronic transition currents at the two vertices described in Sec. 5.2. As a consequence the numerator also vanishes in the limit of $Q^2 \to 0$ and the amplitude remains finite in that limit.

3.2 TPE calculation review

The hadron structure-dependent part of the TPE box and crossed-box diagrams have been evaluated by several groups of authors from nearly two decades starting from the work of Blunden *et al.* [10]. All the model estimations can be categorized into three methods of evaluation. One such method assumes the interaction of the virtual photons at the quark level of the hadron [43], while the two other methods consider that the hadron retains its properties during interaction [10, 37, 40, 41, 45, 46, 48–52, 87–89]. Within the hadronic degrees of freedom the early estimations directly evaluated the real part of the TPE amplitude [10, 37, 40, 41], while the updated scheme of dispersive approach evaluated the imaginary part from which the real part was generated using dispersion relations [45, 46, 48–52, 88, 89]. The TPE calculation in these three approaches are reviewed in the following subsections.

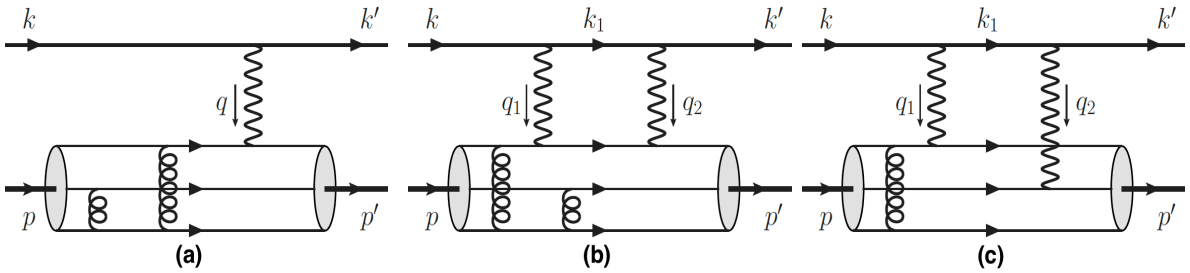

FIGURE 3.3: e-p elastic scattering in the (a) single photon exchange, and (b,c) TPE approximations, at the quark level interaction. The kinematics is same as those in Fig. 3.1. Three constituent quarks of proton are represented by three internal lines with arrows to demonstrate the interaction with individual photons. Both photons interact with same quark in (b) and different quarks in (c). Other combinations of gluon exchange are available in Ref. [45].

3.2.1 High Q^2 partonic and pQCD approach

The TPE calculation assuming the interaction with the constituents of the proton was first performed in a partonic approach relating the Generalized Parton Distributions (GPD) with TPE amplitude in Ref. [42, 43] following the formulation in Ref. [90] for wide angle Compton scattering. The underlying assumption was that both the photons interact with a single quark. These calculations found non-linearity in the reduced cross section as a function of ε, especially in the forward directions, at the Q^2 values of the $\mu_p G_E/G_M$ ratio data extracted by Andivahis *et al.* [3] providing compelling evidence to resolve the discrepancy between the LT and PT measurements. The authors compared their TPE corrected reduced cross sections with the measured cross sections of Ref. [3] scaled by μ_p^2 times the square of the dipole form factor $G_D = (1 + Q^2/0.71)^{-2}$ as shown in Fig. 3.4. The TPE corrected curves move closer to the data points, indicating a resolution of the form factor measurement discrepancy once the TPE effect is taken into account. Based on their analysis, the authors suggested a global re-analysis of the large Q^2 data to determine the correct values of $G_{E,M}$ although the applicability of the partonic approach is questionable at the kinematics of the existing discrepancy in $\mu_p G_E/G_M$ measurement. However, Borisyuk and Kobushkin [45], and Kivel and Vanderhaeghen [44] estimated the TPE correction in the perturbative QCD (pQCD) framework claiming that the interaction of the two photons are with two different quarks, especially at the backward angles. As shown in Fig. 3.3, the TPE diagram with two photons interacting

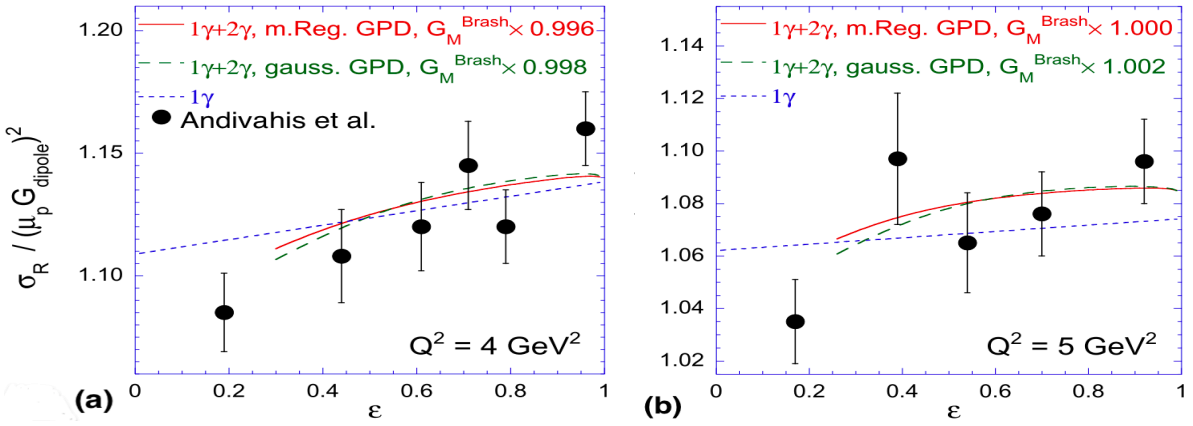

FIGURE 3.4: Reduced cross section $\sigma_{\rm R}$ scaled by μ_p^2 times the dipole form factor G_D^2 as a function of ε at $Q^2 = 4$ and 5 GeV^2, calculated by Afanasev *et al.* [43]. The solid red and dashed blue curves correspond to the TPE corrected $\sigma_{\rm R}$ using two different models for the GPD. The dotted blue line is the result obtained by using $G_{E,M}$ from polarization transfer data [5, 6]. Plots are adjusted from Ref. [43].

with two different quarks involves only one gluon (hard) that enhances the TPE cross section δ by a factor of $1/\alpha_s$, α_s being the strong coupling, compared to the diagrams involving two gluons where the photons interact with only one quark. Borisyuk and Kobushkin obtained negative value for the TPE cross section with an approximately linear ε dependence and logarithmic growth with Q^2 reaching 7% near 30 GeV^2. They also tried to establish the bridge between the pQCD based results and the results obtained using the hadronic approximation in the low Q^2 limit as illustrated in Fig. 3.5 for the generalized TPE amplitudes $\delta\mathcal{G}_M/G_M$ (note $\delta\mathcal{G}_M$ of Ref. [45] is equivalent to the $\mathcal{G}_M$ defined in Eq. (3.23b)). For $Q^2 \leq 3.0$ GeV^2, the results for $\delta\mathcal{G}_M/G_M$ from the two methods of pQCD and hadronic degrees of freedom are shown to almost coincide where only nucleon intermediate state is considered in the later method. But the application of the pQCD approach in the low Q^2 ($\simeq 3.0$ GeV^2) limit still remains doubtful. On the other side, inclusion of the effect of the higher excited resonance intermediate state is also required in the hadronic limit to better compare the results around $Q^2 \sim 3.0$ GeV^2.

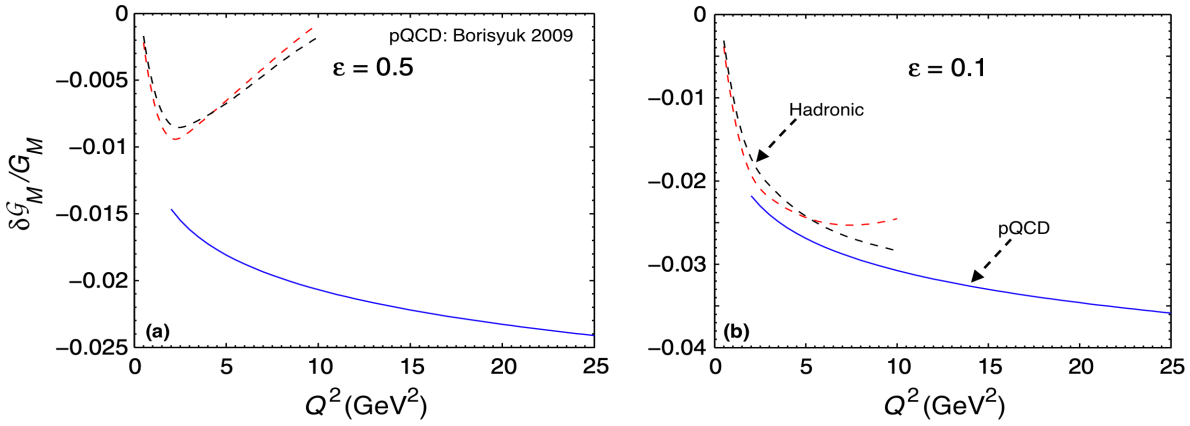

FIGURE 3.5: The generalized TPE amplitude $\delta\mathcal{G}_M/G_M$ as a function of Q^2 at (a) $\varepsilon = 0.5$, and (b) $\varepsilon = 0.1$, calculated by Borisyuk and Kobushkin in pQCD framework (solid line). The corresponding results in hadronic approach with two different form factors is also compared. Plots are taken from Ref. [45].

3.2.2 Direct loop integral

The early estimations of the TPE correction assumed only elastic nucleon intermediate state. Later on some excited intermediate states had also been taken into account. Based on the intermediate state considerations in the gradual development of the direct loop integration calculation the discussion can be sub-categorized into elastic and inelastic intermediate states considerations.

3.2.2.1 Elastic intermediate state

In the low to intermediate region of Q^2 (≤ 5 GeV^2), where most of the TPE sensitive observable quantities are experimentally investigated, the hadron is expected to retain its identity fairly well. Therefore in these kinematic region most of the early theoretical efforts in estimation of the TPE effects have evaluated the one-loop integral of Eq. (3.2b) for both box and crossed-box diagram within the hadronic framework. Starting from the calculation of the hadron structure-dependent TPE effects by Blunden *et al.* [10] a series of evaluations of the TPE loop integrals directly within hadronic degrees of freedom has been initiated [37, 38, 40, 41]. Reference [10] considered only the elastic nucleon intermediate state with the simple monopole form of the form factors as $G_{E,M} \sim$

$\Lambda^2/(\Lambda^2 + Q^2)$ having $\Lambda = 0.84$ GeV. The model dependence of the TPE cross section δ (with nucleon intermediate state only) has been investigated in Ref. [37] by varying the form factors input at the two hadronic vertices. While the default consideration of the form factors was a sum of monopole form, results with the dipole form and separate empirical fits from the LT separation [36, 91] and PT data [36, 92] were compared which indicates a negligible dependence on the choice of form factors as they appear in both the numerator and denominator of $\delta_{\gamma\gamma}$ in Eq. (3.22). The authors evaluated the one-loop integrals of Eq. (3.2b) analytically in terms of the scalar four point Passarino-Veltman (PV) functions [93] and the numerical evaluation of the PV functions were obtained using the program FF [94].

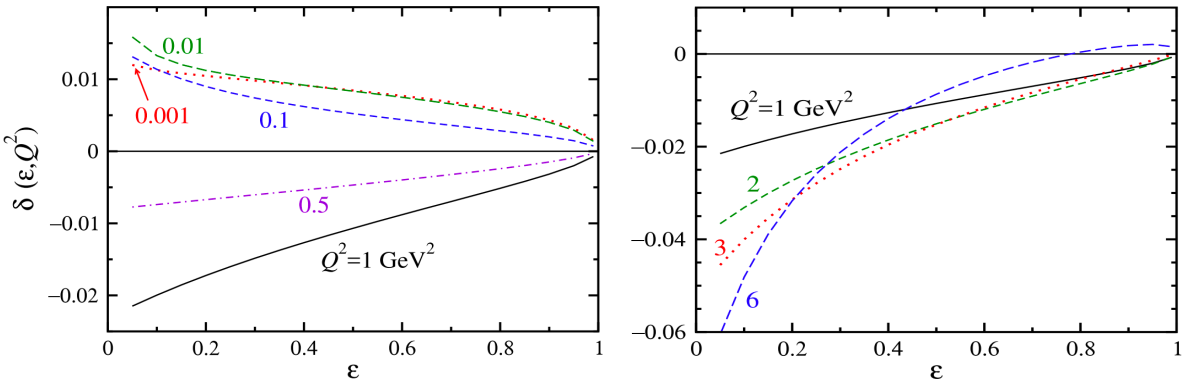

FIGURE 3.6: TPE cross section correction δ, relative to Mo-Tsai soft photon approximation, from the nucleon intermediate state in e-p elastic scattering for $Q^2 = 0.001$ to 1.0 GeV^2 (left) and $Q^2 = 1.0$ to 6.0 GeV^2 (right) [37]. Plots are adjusted from Ref. [29].

The results obtained for the hard TPE cross section correction δ relative to the Mo-Tsai soft photon approximation is shown in Fig. 3.6 as a function of the virtual photon polarization ε at Q^2 values ranging from 0.001 to 1.0 GeV^2 (left) and 1.0 to 6.0 GeV^2 (right). In general, the absolute value of the TPE cross section is maximal at the backward angles (smaller ε) with non-negligible values ranging from approximately $\sim +1.5\%$ to -6% in the kinematics considered in Fig. 3.6 and it essentially vanishes in the forward direction ($\varepsilon \to 1$) in coherence with the unitarity condition. For lower values of Q^2 (< 0.3 GeV^2), δ becomes positive and at some point near $Q^2 \sim 0.001$ GeV^2 it

reaches the so-called Feshbach correction

$$\delta_F = \alpha\,\pi\,\frac{\sin(\theta/2) - \sin^2(\theta/2)}{\cos^2(\theta/2)}, \tag{3.37}$$

independent of energy E, evaluated as the second Born approximation to the Coulomb scattering from structureless, massive target by McKinley and Feshbach [74, 95]. Therefore, for the $Q^2 \to 0$ limit, which is equivalent to the static limit of $M \to \infty$, the TPE cross section due to nucleon intermediate state alone can be approximated by Feshbach correction term that can also be written in terms of ε as [29]

$$\delta_N \to \frac{\alpha\,\pi}{x+1}, \qquad x = \sqrt{\frac{1+\varepsilon}{1-\varepsilon}}. \tag{3.38}$$

In the left diagram of Fig. 3.6, *i.e.* for $Q^2 \leq 1.0$ GeV^2, roughly a linear behaviour of δ with respect to ε is observed, while some non-linearity is visible with increasing Q^2 (> 1 GeV^2), as shown in the right plot. More importantly the negative value and the positive slope at $Q^2 > 1$ GeV^2 is in favour of resolving the existing discrepancy between the two methods (LT separation and PT) of measurements of the electric to magnetic form factor ratio, $\mu_p G_E/G_M$.

3.2.2.2 Excited resonance intermediate state

The hadronic intermediate state, represented by the blob, in the TPE diagrams of Fig. 3.1 can also be anything (both resonance and non-resonant background) beyond elastic nucleon itself satisfying the energy momentum conservation at the two vertices. Among the possibilities, $\Delta(1232)3/2^+$ being the first and most prominent excited resonance state of proton is anticipated to be an essential part in theoretical analyses of the TPE effects. An analytical evaluation of the loop integral of the TPE amplitude in Eq. (3.2b) with resonance intermediate state $\Delta(1232)3/2^+$ was performed in terms of the PV functions in Ref. [40] considering the zero resonance width approximation for $\Delta(1232)3/2^+$. The parametrization of the transition current $\Gamma_{\gamma N\to\Delta}$ from nucleon to the off-shell $\Delta(1232)3/2^+$ resonance by the absorption of a virtual photon was adopted

from the same parametrization given in Refs. [82, 96] for on-shell particles as

$$\begin{aligned}\Gamma^{\alpha\mu}_{\gamma N\to\Delta}(p_\Delta,q) &= \frac{1}{2M_\Delta^2}\sqrt{\frac{2}{3}}\Big\{g_1(Q^2)\Big[g^{\alpha\mu}\not{q}\not{p}_\Delta - \not{q}\gamma^\alpha p^\mu_\Delta - \gamma^\alpha\gamma^\mu q.p_\Delta + \not{p}_\Delta\gamma^\mu q^\alpha\Big] \\ &+ g_2(Q^2)\Big[q^\alpha p^\mu_\Delta - g^{\alpha\mu}q.p_\Delta\Big] + \frac{g_3(Q^2)}{M_\Delta}\Big[q^2(\gamma^\alpha p^\mu_\Delta - g^{\alpha\mu}\not{p}_\Delta) \\ &+ q^\mu(q^\alpha\not{p}_\Delta - \gamma^\alpha q.p_\Delta)\Big]\Big\}\gamma_5, \end{aligned} \tag{3.39}$$

where M_Δ is the mass of the resonance state $\Delta(1232)3/2^+$, p_Δ, and q are the momenta of the outgoing Δ and incoming photon, respectively. Note that $\Gamma_{\gamma N\to\Delta}$ of Eq. (3.39) satisfies the gauge invariance condition $q_\mu\Gamma^{\alpha\mu}_{\gamma N\to\Delta} = 0$, and the relation $p_\alpha\Gamma^{\alpha\mu}_{\gamma N\to\Delta} = 0$, which ensures the safe removal of the unphysical spin 1/2 component of the Rarita-Schwinger propagator of Eq. (3.8). The form factors g_1, $g_2 - g_1$, and g_3 are related with the magnetic G^*_M, electric G^*_E, and Coulomb G^*_C form factors, respectively. The details of G^*_M, G^*_E, and G^*_C will be discussed in Sec. 6.3.3. However, Ref. [40] assumed the dipole shape for the form factors $g_i(Q^2)$, $i = 1$, 2, and 3, as $g_i(Q^2) = g_i(0)(1+Q^2/\Lambda^2_\Delta)^{-2}$, with the dipole mass parameter $\Lambda_\Delta = 0.84$. As $g_3(Q^2)$ is very small compared to $g_1(Q^2)$ and $g_2(Q^2)$, the authors considered only the later two (neglecting $g_3(Q^2)$) with the coupling constants $g_1 \equiv g_1(0) = 7$, $g_2 \equiv g_2(0) = 9$ taken from the dressed K-matrix model [96]. Later on, Zhou and Yang [38] used a more realistic form of the form factors by fitting the then existing electroproduction data to sum of monopoles. They also compared the effect of the Coulomb equivalent form factor g_3 in the evaluation and found a negligible impact on the cross section. Figure 3.7 compares the TPE cross section correction from the Δ intermediate state obtained in Ref. [40] and [38] as a function of ε at $Q^2 = 3.0$ GeV^2. Use of a realistic form factor for transition to the excited $\Delta(1232)3/2^+$ resonance suppresses the corresponding TPE cross section effect as seen from the comparison of δ_Δ between the use of dipole form factor (dashed red line) [40] and the fit to sum of monopoles (solid black line) [38]. Overall, the $\Delta(1232)3/2^+$ state partially cancels the nucleon effect alone by $\sim 1.8\%$ having positive cross section at $Q^2 = 3.0$ GeV^2. The behaviour in the forward direction ($\varepsilon > 1$, $Q^2 \to 0$) creates some sort of tension since it tends to diverge in that limit indicating the violation of unitarity. A similar divergence in the

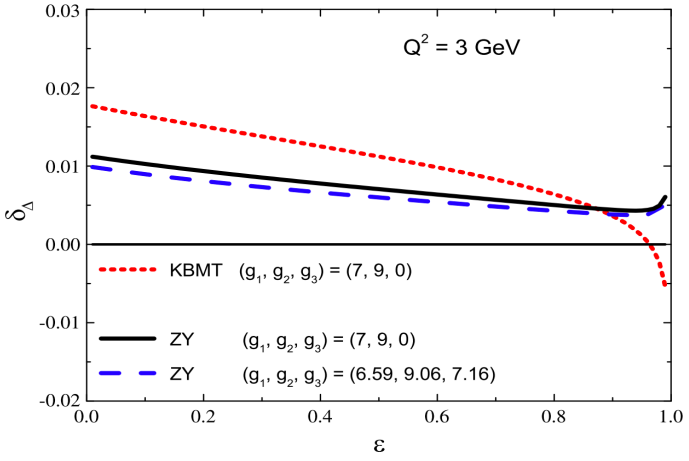

FIGURE 3.7: $\Delta(1232)$ intermediate state contribution to the TPE total cross section δ as a function of virtual photon polarization ε at $Q^2 = 3$ GeV^2. The red dotted line corresponds to the evaluation with electric and magnetic form factors of dipole form, having $\Gamma_\Delta = 0.84$, by Kondratyuk *et al.* [40]. The black solid and blue dashed lines are the results from Ref. [38]. Figure source is Ref. [29, 38].

forward angle limit, $\varepsilon \to 1$, is also visible in Refs. [97–99] for $\Delta(1232)3/2^+$ intermediate state in parity violating electron-proton elastic scattering.

Figure 3.8 represents the TPE cross section results δ obtained for the nucleon and $\Delta(1232)3/2^+$ intermediate states from further work by Lorenz *et al.* (left column) [101] and Graczyk (right column) [100] within the same hadronic approximation. Lorenz *et al.* analyzed the model dependence by changing the nucleon electric and magnetic form factor inputs in both cases of nucleon and $\Delta(1232)3/2^+$ intermediate states at $Q^2 = 3.0$ GeV^2. For nucleon, they reproduced the results of Blunden *et al.* [37] using sum of monopole fits and overall, the form factor dependence was found negligible by comparing it with the dipole form. In contrast to the nucleon case the dependence on the parametrization of $G^*_{E,M}$ was found significant. Note that the $\gamma N\Delta$ transition form factors are parametrized using the helicity amplitude formulation (details of these are discussed in Sec. 5.3) in this particular work. At $Q^2 = 3.0$ GeV^2, the $\Delta(1232)3/2^+$ contribution to the TPE cross section δ, using the dipole times a monopole shaped form factor, evaluated by Graczyk [100] (Fig. 3.8(d)) shows almost the same behaviour as obtained by Lorenz *et al.* (Fig. 3.8(c)), especially in the backward direction reaching $\delta \sim +(1 \text{ to } 1.2)\%$ at $\varepsilon \sim 0.1$. In summary, the common features of all those above

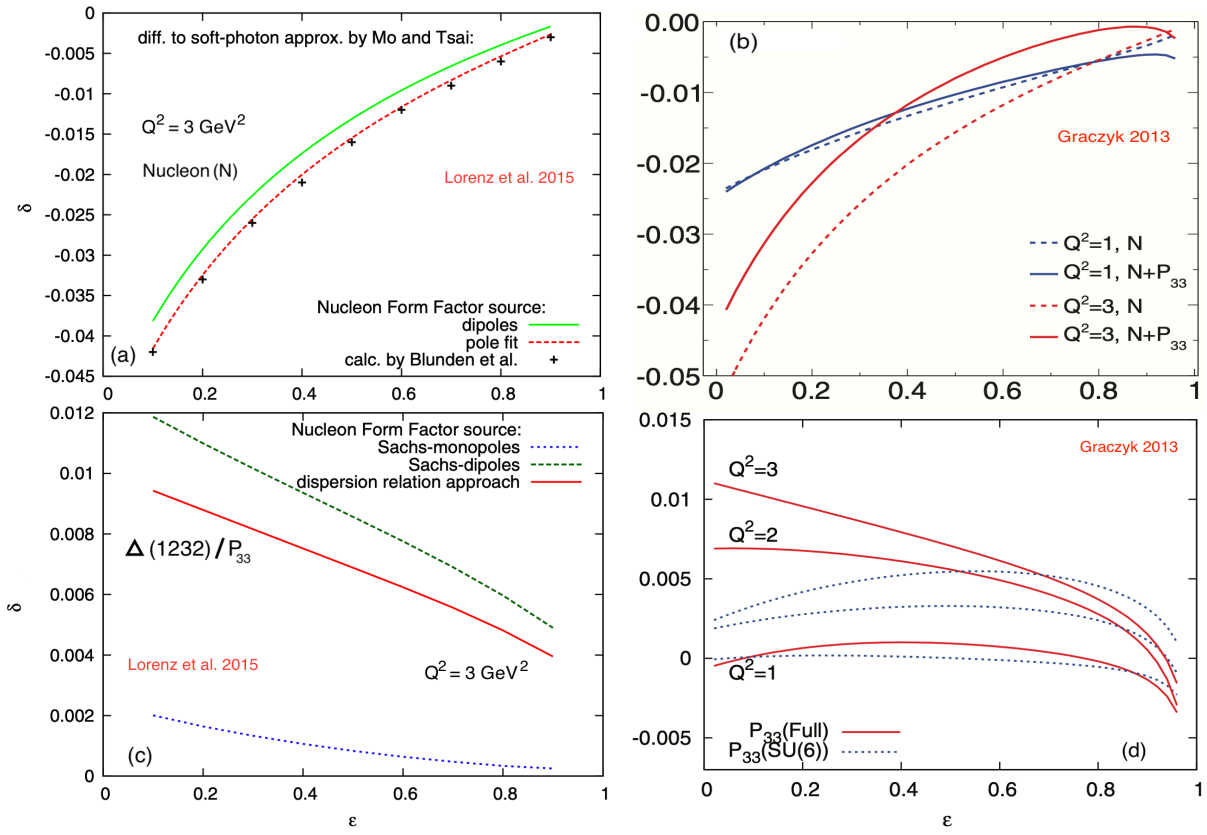

FIGURE 3.8: TPE cross section correction from nucleon (a,b) and $\Delta(1232)3/2^+$ (c,d) resonance intermediate states calculated by Graczyk [100] and Lorenz *et al.* [101]. The effect of nucleon form factor variations are compared in (a,c). Q^2 values are given in units of GeV^2. Diagrams are adjusted from Refs. [100, 101]

discussed calculations are the suppression of the magnitude of net TPE correction δ by the $\Delta(1232)3/2^+$ intermediate state contribution and the divergence of δ in the forward direction corresponding to $\varepsilon \to 1$ for all three Q^2 values, as observed in Figs. 3.7 and 3.8(d) (Lorenz *et al.* didn't extend the evaluation in that much forward direction).

However, within the same approach of Ref. [37] the effect of the heavier resonance states including, $N(1440)1/2^+$, $N(1520)3/2^-$, $N(1535)1/2^-$, $\Delta(1620)1/2^-$, and $\Delta(1700)3/2^-$ were also investigated by Kondratyuk and Blunden in Ref. [41]. Here again the dipole shape of the transition form factors were assumed with the coupling constants determined from the dressed K-matrix model [96]. The authors ignored the Coulomb couplings in this evaluation as well, assuming the dominance of the magnetic coupling applicable in all the resonance intermediate states. Among the resonances, the state $N(1520)3/2^-$ is claimed to have the significant TPE effect after $\Delta(1232)3/2^+$ with a

maximal effect of +0.7% in the smallest possible ε, coherent with the TPE cross section correction from elastic nucleon state. The net effect of all the resonances is to nullify the nucleon contribution in δ.

Aside from the issue of divergence of the cross section for inelastic resonance intermediate state $\Delta(1232)3/2^+$ in the forward angles, the direct evaluation of the TPE amplitude has a significant source of uncertainty due to the use of the on-shell parametrization of the transition currents at the two hadronic vertices γNN^* and γN^*N with off-shell intermediate states N^*. It is also anticipated as the source of the divergence of TPE cross sections at the limit of $\varepsilon \to 1$ as shown in Figs.3.7 and 3.8.

3.2.3 Dispersive method

The ambiguity of the off-shell parametrizations of the hadronic transition currents at the vertices in Fig. 3.1 can be eliminated by applying the dispersion relation formula in evaluation of $\mathcal{M}_{\gamma\gamma}$ [48, 70]. The primary motivation of this formulation comes from the unitarity of the scattering matrix S, originating from the requirement of the conservation of probability, that allows the use of the on-shell parametrization of the hadronic transition currents. Having defined the scattering matrix S as

$$S = 1 + i\mathcal{T}, \tag{3.40}$$

where the matrix element of the non-trivial transfer matrix $\mathcal{T}$, which in principle describes the interaction, is defined by

$$\langle f|\mathcal{T}|i\rangle = (2\pi)^4\,\delta^4(p_i - p_f)\mathcal{M}_{i\to f}. \tag{3.41}$$

The unitarity condition $S^\dagger S = 1$ then leads to the generalized optical theorem [13, 102]

$$\mathcal{M}_{i\to f} - \mathcal{M}^*_{f\to i} \;=\; i\sum_n \int d\Pi_n\,(2\pi)^4\delta^4(p_i - p_n)\,\mathcal{M}_{i\to n}\,\mathcal{M}^*_{f\to n}. \tag{3.42}$$

Here the sum is over the complete set of intermediate states, n, of any Feynman loop diagram. Note that the right side of Eq. (3.42) is a product of amplitudes whereas the left side is just an amplitude. Thus the left side must correspond to a loop diagram implying a relation with the tree level Feynman diagram on the right so that the two sides are of same order of perturbation theory. The physical implication of the generalized optical theorem can be better understood with the simplified but important special case of forward scattering when the initial and final states being equal, $|i\rangle = |f\rangle$. In this limit, one can relate the imaginary part of a loop diagram with the total tree level cross section of getting the intermediate state of the loop diagram as the final state by

$$\mathrm{Im}\,\mathcal{M}_{i\to i} = 2E_{\mathrm{cm}}\,|\boldsymbol{p}_i| \sum_n \sigma_{i\to n}. \tag{3.43}$$

This result is very important as the motivation of using the dispersion method in calculating the TPE amplitude. Since the imaginary part of the TPE amplitude is directly linked with the experimentally accessible cross section the phenomenological input form factor parametrizations for the on-shell particles can now be used in evaluation of the imaginary part of the specific one loop amplitude without any ambiguity.

In practice of theory, the imaginary part of any loop amplitude can be directly accessed by putting the intermediate particles on-shell by using the following Cutkosky cutting rules [103]:

- cut through the loop diagram in every possible ways so that the cut propagators are on-shell simultaneously, and also obey the momentum conservation.
- substitute the propagator factors by

$$\frac{1}{p^2 - m^2 + i\epsilon} \to -2\pi i\,\delta(p^2 - m^2)\,\theta(p^0), \tag{3.44}$$

  for each cut propagator.
- sum of all cuts provides the discontinuity, and hence the imaginary part of the loop diagram, as $\mathrm{Disc}(i\mathcal{M}) = -2\,\mathrm{Im}\,\mathcal{M}$.

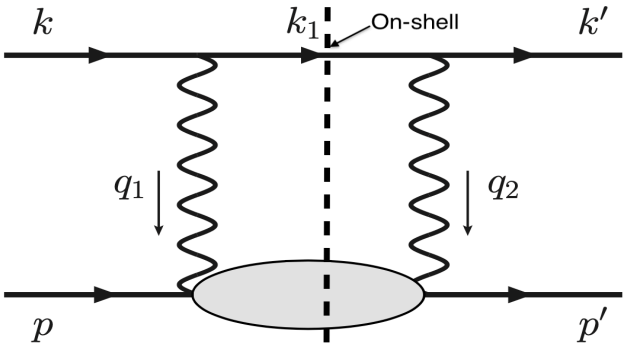

FIGURE 3.9: Extraction of the imaginary part of the TPE amplitude by putting the intermediate lepton and hadron in the TPE box diagram on-shell. The corresponding crossed-box has no imaginary part.

For the specific case of TPE amplitude the scenario is illustrated in Fig. 3.9 by putting the intermediate lepton and hadron propagators on-shell with the substitutions followed by Eq. (3.44). Only the box diagram is shown here as the crossed-box part is purely real. With the evaluated imaginary part of the TPE amplitude one can obtain the real part by exploiting the Cauchy integral theorem that leads to the dispersion relation [12]

$$\mathrm{Re}\,\mathcal{M}_{\gamma\gamma}(s) = \frac{1}{\pi}\mathcal{P}\int_{-\infty}^{\infty}\frac{\mathrm{Im}\,\mathcal{M}_{\gamma\gamma}(s')}{s'-s}\,ds', \tag{3.45}$$

relating the real and imaginary parts of the TPE amplitude $\mathcal{M}_{\gamma\gamma}(s)$, provided $\mathcal{M}_{\gamma\gamma}(s)$ is an analytic function everywhere within the contour in the complex plane of the variable s. Here $\mathcal{P}$ denotes the principal value of the integral. Details of the dispersive formulation will be discussed in Sec. 4.1.

The use of the dispersion formalism resolves the issue of divergence in δ coming from the inelastic intermediate states in the forward angle or high energy limit corresponding to $\varepsilon \to 1$ as explained in Fig. 3.10 taken from Ref. [46]. Clearly, the red solid line representing the dispersive evaluation at $Q^2 = 3.0$ GeV^2 with magnetic form factor only (for simplicity of calculation) converges as (a) $\varepsilon \to 1$, and (b) energy keeps increasing. By contrast, the direct loop integration results represented by the blue dashed line diverges in that limit.

Before the calculation of Ref. [46], Borisyuk and Kobushkin used the dispersive approach in calculation of the TPE correction in a series of papers starting from the simplified

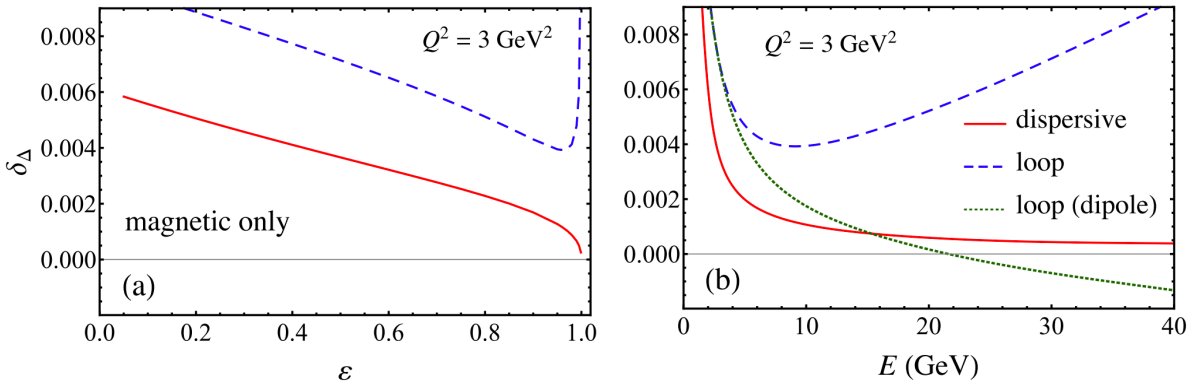

FIGURE 3.10: TPE cross section correction from $\Delta(1232)3/2^+$ resonance intermediate state calculated by Blunden *et al.* [46] using direct loop integral (blue dashed and green dotted lines) and dispersive method (red solid line) as a function of (a) ε, and (b) beam energy E, at $Q^2 = 3.0$ GeV^2. For simplicity only the magnetic form factor is considered here. Diagram taken from Ref. [46].

case of nucleon intermediate state [48] and later on extending the formulation to include the intermediate $\Delta(1232)3/2^+$ resonance with zero width approximation and sum of monopoles type input form factors fit [88]. More recently they used helicity amplitudes input from MAID model [104] at the hadronic transition current to account the πN intermediate state contribution in total TPE amplitude [49, 50].

In these updated evaluations non-zero width and background effects were also considered. The result for the P_{33} channel evaluated at $Q^2 = 1.0$ and 5.0 GeV^2 is still the dominant one, among all the channels considered, having the positive cross section correction in coherence with the results from the direct loop integral method applied by Kondratyuk *et al.* [41], as shown in Fig.3.11. But the next significant contributions are coming from the spin half channels S_{11} and P_{11} in contrast to Ref. [41], where the spin 3/2 channel D_{13} was the major contributor, with negative cross section, after P_{33}. However, the important feature is that the cross section in this dispersive method is also converging in the limit of $\varepsilon \to 1$.

The method is also applied by Tomalak *et al.* in some recent TPE evaluations at low Q^2 values [51, 52, 89]. They transformed the phase space integral into an elliptic coordinate system to perform the integration as a contour integration in a complex plane during the evaluation of the imaginary part of the TPE amplitude with nucleon intermediate

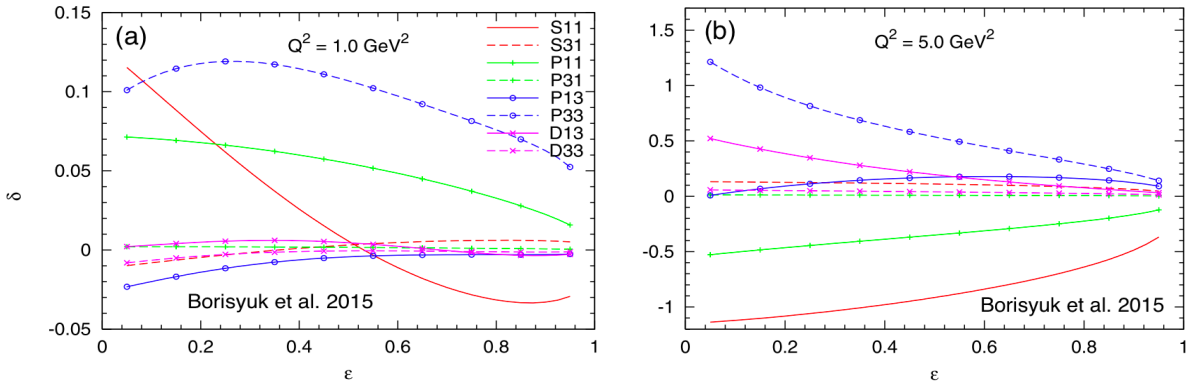

FIGURE 3.11: TPE cross section correction δ, in percent, from πN intermediate states evaluated using dispersion formalism by Borisyuk *et al.* [50] at fixed Q^2: (a) 1.0 GeV^2, and (b) 5.0 GeV^2. Figure courtesy of Ref. [50].

state [51]. The introduced contour allows the integral to be analytically continued into some unphysical region by a deformation of the contour, for dipole shaped nucleon form factors, which is required to utilize the dispersion relation above some definite kinematics (details are discussed in Sec. 4.1). Later on they further calculated the TPE effects coming from the inelastic πN intermediate states at small Q^2 values of 0.05 and 0.005 GeV^2 where the analytical continuation is not required. The input pion electroproduction amplitudes were also taken from the MAID 2007 parametrizations [104]. The result shows a good agreement with the empirical extraction of the TPE cross section of Ref. [21] in the forward angles, while in the backward direction a significant disagreement suggests a re-analysis of the data in the backward angles and small Q^2 values to better extract the proton magnetic form factors.

An improved version of the deformed contour was introduced in Ref. [46] in evaluation of the inelastic $\Delta(1232)3/2^+$ intermediate state contribution in the total TPE cross section. With this deformed contour of integration a more generalized class of form factors can be used, other than the dipole shape only, as input. This particular contour prescription will also be used in this thesis to evaluate the resonance contributions in the total δ.

3.3 Phenomenological extraction of TPE effect

Guichon and Vanderhaeghen [11] extracted the TPE amplitude by comparing the form factor ratio, $\mu_p G_E/G_M$, data from Rosenbluth LT separation method and the polarization transfer method. In the analysis they used the LT separation data from Ref. [3] and the polarization data from Refs. [5, 6]. The main assumption in the phenomenological extraction was that the TPE effect is entirely responsible for the discrepancy between the two measurements of the ratio $\mu_p G_E/G_M$. The extraction was basically carried out in terms of the generalized form factors $\tilde{G}_M$, $\tilde{G}_E$, and $Y_{2\gamma}$ defined by the decomposition of the TPE amplitude similar to Eq. (3.25) with a small change of convention as

$$\begin{aligned}\mathcal{M}_{\gamma\gamma} &= -\frac{e^2}{q^2}\bar{u}_e(k')\gamma_\mu u_e(k) \times \bar{u}_N(p')\Big[\tilde{G}_M(Q^2,\nu)\gamma^\mu - \tilde{F}_2(Q^2,\nu)\frac{P^\mu}{M} \\ &\quad +\tilde{F}_3(Q^2,\nu)\frac{\not{K}P^\mu}{M^2}\Big]u_N(p),\end{aligned} \tag{3.46}$$

where $K = (k+k')/2$ and $P = (p+p')/2$. The form factors $\tilde{G}_E$ and $Y_{2\gamma}$ are explicitly related to $\tilde{F}_2$ and $\tilde{F}_3$ by

$$\begin{aligned}\tilde{G}_E(Q^2,\nu) &= \tilde{G}_M(Q^2,\nu) - (1+\tau)\tilde{F}_2(Q^2,\nu), \\ Y_{2\gamma}(Q^2,\nu) &= \mathrm{Re}\left(\frac{\nu\,\tilde{F}_3}{\tilde{G}_M}\right).\end{aligned} \tag{3.47}$$

Note that the definition of $Y_{2\gamma}$ is adjusted with the definition of ν used in this thesis. $\tilde{G}_M$ and $\tilde{G}_E$ can also be decomposed into the Born and TPE correction part as

$$\tilde{G}_{E,M}(\nu,Q^2) = G_{E,M}(Q^2) + \delta\tilde{G}_{E,M}(\nu,Q^2). \tag{3.48}$$

However, Guichon and Vanderhaeghen [11] ignored the TPE correction in the ratio $\tilde{G}_E/\tilde{G}_M$ by further assuming that the TPE correction in $\tilde{G}_{E,M}$ is small and of similar magnitude. As a result the form factor $\tilde{F}_3$ was considered to be coming entirely from the TPE effect. The obtained $Y_{2\gamma}$ was almost independent of ν (or, ε) and a few percent in magnitude. But such a small correction of $Y_{2\gamma}$ (or, $\tilde{F}_3$) was still able to bring the

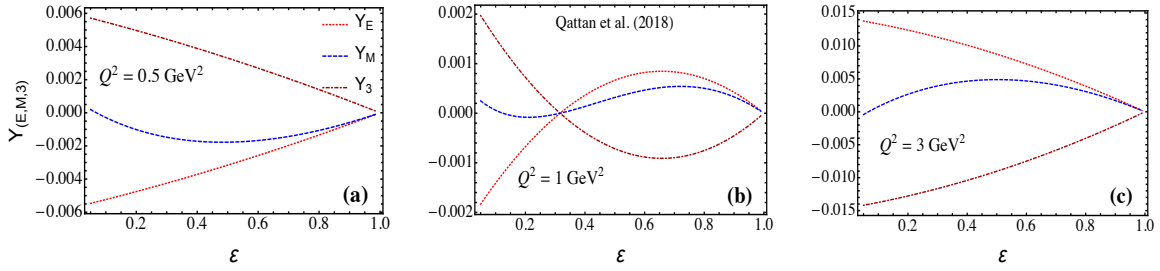

FIGURE 3.12: TPE amplitudes Y_E (red dotted), Y_M (blue dashed), and Y_3 (dark red dot-dashed) from phenomenological extraction of Ref. [105] as a function of ε at Q^2: (a) 0.5 GeV^2, (b) 1 GeV^2, and (c) 3 GeV^2.

Rosenbluth data close to the polarization transfer data. It was also explained that polarization transfer data has little effect from the TPE correction.

Qattan *et al.* [22, 105–107] carried out a series of phenomenological extraction of the TPE amplitude from the cross section ($\sigma_{\rm R}$) data following a similar treatment but including a wider range of unpolarized data from Refs. [2, 3, 21]. The results obtained from the latest analysis is shown in Fig. 3.12 for $Q^2 = 3.0$ GeV^2 in terms of a slightly modified convention of amplitudes Y_E, Y_M, and Y_3 defined by

$$Y_E = \mathrm{Re}\left(\frac{\delta\tilde{G}_E}{G_M}\right), \qquad Y_M = \mathrm{Re}\left(\frac{\delta\tilde{G}_M}{G_M}\right), \qquad Y_3(Q^2,\nu) = \mathrm{Re}\left(\frac{\nu\,\tilde{F}_3}{G_M}\right). \tag{3.49}$$

The figure illustrates that in contrast to the findings of Ref. [11], the TPE effect in $\tilde{G}_E$ and $\tilde{F}_3$ are almost cancelling each other, and the magnetic equivalent $\tilde{G}_M$ carries the most part of the TPE correction to $\sigma_{\rm R}$ rather than $\tilde{F}_3$ (*i.e.* $Y_{2\gamma}$ or Y_3).

3.4 Direct measurement of TPE correction

The defining equation of the TPE cross section correction δ (or, IR divergent $\delta_{\gamma\gamma}$) in Eq. (3.14) contains three lepton vertices which indicates δ must be a charge-dependent quantity. As a consequence δ in e^+p and e^-p elastic scattering have opposite signs. One direct extraction of the TPE cross section correction δ is thus to analyze the ratio of the total cross sections $\sigma_{\rm R}(e^\pm p)$ in unpolarized e^+p and e^-p elastic scattering. The total amplitude of the elastic scattering of either e^+p or e^-p can be written in a common

form as

$$\begin{aligned}\mathcal{M} &= \mathcal{M}_{\gamma} + \mathcal{M}^{e}_{\text{vertex}} + \mathcal{M}^{p}_{\text{vertex}} + \mathcal{M}_{\text{vp}} + \mathcal{M}_{\gamma\gamma} \\ &= q_e q_p \left[M_{\gamma} + q_e^2 M^{e}_{\text{vertex}} + q_p^2 M^{p}_{\text{vertex}} + q^2_{e/p} M_{\text{vp}} + q_e q_p M_{\gamma\gamma} \right]. \end{aligned} \tag{3.50}$$

In the second line, the charge factors q_e and q_p coming from the electron and proton vertices, respectively, are taken out to see the charge dependence of the individual radiative corrections explicitly. The radiative corrections at electron and proton vertex, and vacuum polarization (corresponding to $\mathcal{M}^{e,p}_{\text{vertex}}$, and $\mathcal{M}_{\text{vp}}$) in Eq. (3.50) are discussed in Sec. 2.3. Neglecting the terms beyond order α^3, the square of the amplitudes can be given by

$$|\mathcal{M}|^2 = e^4 \left[M_{\gamma}^2 + 2e^2 M_{\gamma}^{*} \,\text{Re}\left(M^{e}_{\text{vertex}} + M^{p}_{\text{vertex}} + M_{\text{vp}} \right) + 2 q_e q_p M_{\gamma}^{*} \,\text{Re}\, M_{\gamma\gamma} \right]. \tag{3.51}$$

Here the the charges q_e and q_p are replaced by e where it enters as squared. Since the vertex corrections (both electron and proton) and vacuum polarization contain even power of electric charge they must be identical in e^+p and e^-p scattering. Only the correction from the TPE amplitude is sensitive to the lepton charge having odd power of q_e. Therefore, the TPE cross section correction δ can be extracted from the comparison of the measured cross sections $\sigma_{\text{R}}(e^{\pm}p)$ with known input from other radiative corrections.

However, in practice, the measured elastic cross section can not be isolated with infinite precision from the inelastic bremsstrahlung effect, described also in Sec. 2.3, which also needs to be taken into account in $\sigma_{\text{R}}(e^{\pm}p)$ analysis. More importantly the interference between the bremsstrahlung amplitudes from electron and proton also contains odd power of lepton charge. Including the inelastic real bremsstrahlung effect one can write the amplitude squared as

$$\begin{aligned}|\mathcal{M}|^2 &= e^4 \Big\{ M_{\gamma}^2 + 2e^2 M_{\gamma}^{*} \,\text{Re}\left(M^{e}_{\text{vertex}} + M^{p}_{\text{vertex}} + M_{\text{vp}} \right) \\ &\quad + 2 q_e q_p \left[M_{\gamma}^{*} \,\text{Re}\, M_{\gamma\gamma} + M^{e^*}_{\text{brems}} M^{p}_{\text{brems}} \right] \Big\}. \end{aligned} \tag{3.52}$$

Note that the real bremsstrahlung correction is coming from the interference between the amplitudes of the real photon emission from electron and proton legs. The total reduced cross section can now be written in terms of the relative cross section corrections with respect to the Born contribution as

$$\sigma_{\rm R}(e^{\pm}p) = \sigma_{\rm R}^{\rm Born}\left[1 + \delta_{\rm even} \mp (\delta_{\gamma\gamma} + \delta_{\rm brems})\right], \tag{3.53}$$

where $\sigma_{\rm R}^{\rm Born}$ is the Born reduced cross section, $\delta_{\rm even}$ is the sum of all charge even relative cross sections and the charge odd contributions from TPE and bremsstrahlung are $\delta_{\gamma\gamma}$ and $\delta_{\rm brems}$, respectively. Interestingly, the charge odd pieces in the parentheses cancel out the IR divergences of each other as well. The ratio of the cross sections of e^+p and e^-p can now be given by

$$\begin{aligned} R = \frac{\sigma(e^+p)}{\sigma(e^-p)} &\approx \frac{1 + \delta_{\rm even} - \delta_{\gamma\gamma} - \delta_{\rm brems}}{1 + \delta_{\rm even} + \delta_{\gamma\gamma} + \delta_{\rm brems}} \\ &\approx 1 - \frac{2(\delta_{\gamma\gamma} + \delta_{\rm brems})}{1 + \delta_{\rm even}}. \end{aligned} \tag{3.54}$$

with the convention of the sign of $\delta_{\gamma\gamma}$ and $\delta_{\rm brems}$ such that they appear as additive correction in e^-p scattering. In the second approximated equation, the logarithmic enhanced behaviour $\sim \log(Q^2/m_e^2)$ of the vacuum polarization and vertex corrections are exploited which is absent in case of charge asymmetric corrections $\delta_{\gamma\gamma}$ and $\delta_{\rm brems}$. After plugging in the calculated $\delta_{\rm even}$ and $\delta_{\rm brems}$ corrections in the above equations one is left with entirely the TPE effect in the cross section ratio as

$$R_{2\gamma} \approx 1 - 2\delta_{\gamma\gamma}. \tag{3.55}$$

Since the ratio R remains IR finite, I switch to the usual notation of IR finite TPE cross section δ used in this thesis and the TPE sensitive part of the ratio is given the form

$$R_{2\gamma} \approx 1 - 2\delta. \tag{3.56}$$

Any deviation of $R_{2\gamma}$ from unity thus clearly indicates the presence of TPE effect.

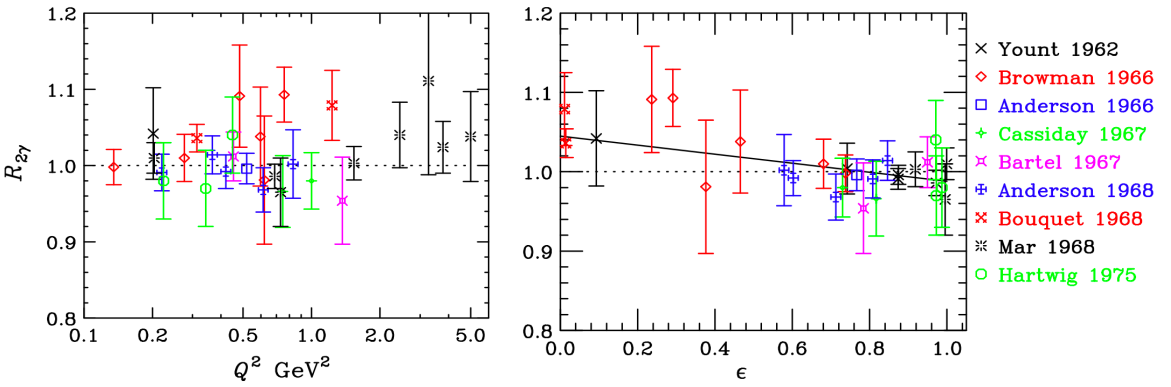

FIGURE 3.13: Measured $R_{2\gamma}$ plotted as a function of Q^2 (left panel) in a logarithmic scale and as a function of virtual photon polarization ε (right panel) from the measurements of Refs. [108–113]. Source of data points are labelled in the plot legends using authors name and year of publication. The line in the right panel is the fit reproduced from the reanalysis of Ref. [36]. Plots are taken from Ref. [29].

Starting from the work of Yount *et al.* [114] in 1962, there has been several efforts [108–113] in determination of the TPE effect directly exploiting this particular method of analyzing the unpolarized $e^{\pm}p$ elastic scattering cross section ratio during the 1960s and 1970s. The results of those measurements, showed in the left panel of Fig. 3.13 as a function of Q^2 (with data sets for varying ε though), hints a very small TPE effect ($< 1\%$). The large uncertainty of the data points for $R_{2\gamma}$ also compels one to conclude that $R_{2\gamma} = 1$, meaning no TPE correction. Note that the experiments mentioned above are performed mostly in the low Q^2 and/or large ε corresponding to the forward angle scattering where TPE effect is also expected to be tiny from the model estimations discussed in Sec. 3.2. Realizing the importance of the ε dependence of the TPE correction in the form factor extraction using Rosenbluth LT separation method, a global reanalysis of the $R_{2\gamma}$ data was performed in Ref. [36]. The results are shown in the right panel of Fig. 3.13. The fit to data shows a linear ε dependence of $R_{2\gamma}$ with nearly 5.7% increase from the forward to backward angles (small ε). This much ε dependence can resolve almost half of the $\mu_p G_E/G_M$ discrepancy but the large angle (small ε) $R_{2\gamma}$ data in this reanalysis covered only the range of $Q^2 \leq 0.5$ GeV^2 where the discrepancy is not evident. Even though the data indicates a non-zero TPE effect, it is not convincing enough since most of the data are in the large ε region and also due to the inconsistent use of the model-dependent input of bremsstrahlung correction (which

is also charge asymmetric) to isolate the TPE contribution from the total cross section ratio.

More recently, three updated and precise experiments dedicated to extract the TPE effect from $R_{2\gamma}$ were performed at Novosibirsk [115], Jefferson Lab [116] and DESY [117] covering an wider kinematic region. The VEPP-3 experiment at Novosibirsk [115] and OLYMPUS experiment at DESY [117] both used monoenergetic beams of energies 0.998 and 1.594 GeV, and 2.01 GeV, respectively, from a storage ring directed to an internal gas target, while the CLAS experiment at Jefferson Lab's Hall B [116] used mixed simultaneous beam of electron and positron with energies ranging from ≈ 0.85 to 3.50 GeV directed to a liquid hydrogen target.

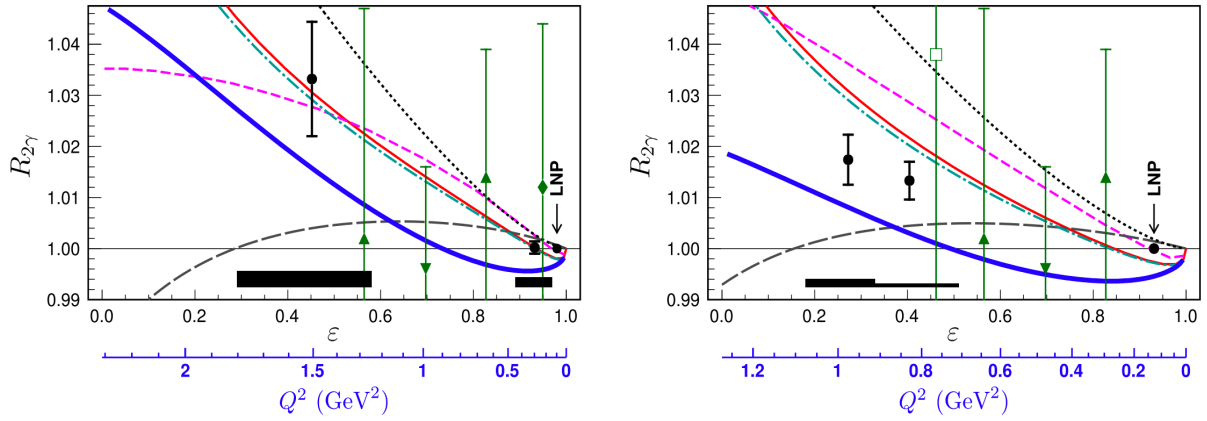

FIGURE 3.14: Measured $R_{2\gamma}$ by VEPP-3 experiment [115] (black solid circles) at Novosibirsk plotted as a function of ε for mono-energetic beams of energy $E = 1.594$ GeV for run-I (left panel), and $E = 0.998$ GeV for run-II (right panel). The statistical uncertainties are represented by the error bars, while the shaded bands correspond to the total systematic uncertainty and the bin size for each data point. The estimated lines correspond to Refs. [48] (cyan dot-dashed), [37] (red thin solid), [21] (blue thick), [118] (grey long-dashed), [36] (magenta dashed), and [106] (black dotted). Plots are taken from the original work of Ref. [115].

The VEPP-3 experiment being the first of the new and precise extractions of the TPE effect directly, compared their results with some selected old data that had similar kinematics and found good agreement with a clear indication of non-zero TPE effect at the intermediate to lower values of ε. They also compared the results with some early theoretical predictions [37, 48], considering mostly the nucleon intermediate state, and with the phenomenological values of Refs. [21, 106] along with the predictions of

Refs. [36, 118] even though the data were required to use the model predicted values of $R_{2\gamma}$ at the normalization points to get some more reliable conclusion. However, the theoretical predictions of Refs. [37, 48] had very good agreement with data from the first run, while the second run was off by $\approx$ 1-1.5% from the predicted ones. On the other hand, the phenomenological values obtained by Bernauer *et al.* [21] underestimated $R_{2\gamma}$ according to the measurement of VEPP-3 experiment. The rest of the comparison had worse agreement. But, overall, the outcome of this experiment shows the presence of significant TPE effect.

The experiment at Jefferson Lab using CLAS spectrometer covered almost the entire range of ε from $\approx$ 0.2 to 0.9. Along with the ε dependence of $R_{2\gamma}$ at fixed average $\langle Q^2 \rangle = 0.85$ and 1.45 GeV^2, they also presented the result at fixed average $\langle \varepsilon \rangle = 0.45$ and 0.88 with varying Q^2. Figure 3.15 demonstrates the original representation of the results in their work. A reasonably good agreement is observed with the calculated $R_{2\gamma}$ by Zhou

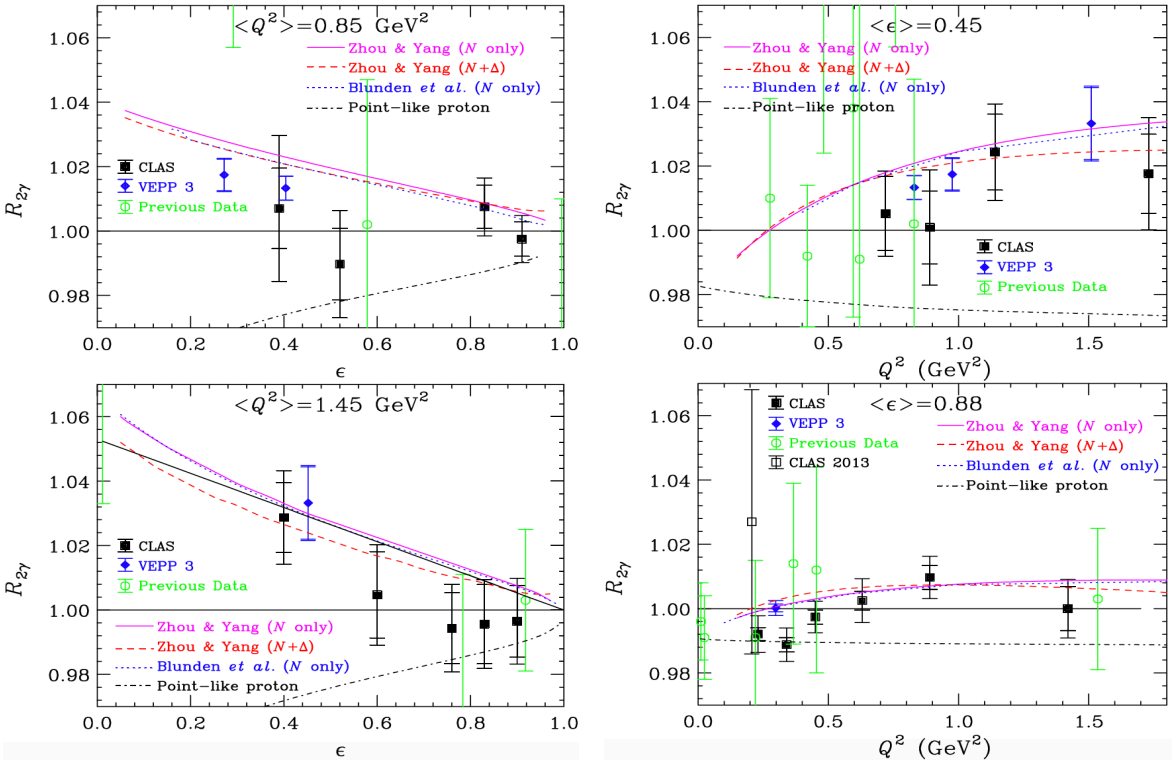

FIGURE 3.15: Measured $R_{2\gamma}$ by CLAS experiment [116] at Jefferson Lab plotted as a function of ε (left panel) at fixed values of averaged $\langle Q^2 \rangle = 0.85$ (top) and 1.45 GeV^2 (bottom), and as a function of Q^2 (right panel) at fixed averaged $\langle \varepsilon \rangle = 0.45$ (top) and 0.88 (bottom). Plots are taken from the original work of Ref. [116].

and Yang once the $\Delta(1232)3/2^+$ resonance is included [3.15(a)]. The results from other hadronic approach calculations [37, 38] with nucleon intermediate state only are still in close match with the measured values within the large systematic and statistical uncertainty at the kinematics of this experiments, *i.e.* at averaged $\langle Q^2 \rangle = 0.85$ and 1.45 GeV^2. The ε dependence of the TPE cross section correction obtained from the linear fit to data brings the Rosenbluth LT separation data for $\mu_p G_E/G_M$ by Andivahis *et al.* [3] at $Q^2 = 1.75$ GeV^2 within 1σ agreement to the polarization transfer data of Punjabi *et al.* [9] at $Q^2 = 1.77$ GeV^2. To be specific, the ratio $\mu_p G_E/G_M$ of LT method shifts from ~ 0.91 to 0.829 once the ε dependence of the TPE cross section from CLAS measurement is accounted. The plots as a function of Q^2 shown in Fig. 3.15 (right column) also hints the presence of TPE effect at the backward angle (low ε) with increasing Q^2 in coherence with the calculation, even though the line for $R_{2\gamma} = 1$ (*i.e.* no TPE) is still within the uncertainty range of the measured values. A global analysis with 12 CLAS and 4 non-normalization data points of VEPP-3, with 0.3% systematic scale-type uncertainty accounting the high ε normalization variation with VEPP-3 measurement, were performed in the same paper and obtained an improved agreement with the hadronic calculations eliminating the no-TPE hypothesis at 5.3σ level.

The OLYMPUS results for $R_{2\gamma}$ were also published soon after the CLAS ones. They detected the elastically scattered leptons within the scattering angles interval of $\approx 20^\circ < \theta < 80^\circ$ corresponding to the virtual photon polarization range $0.456 < \varepsilon < 0.978$ using the formerly used MIT-Bates BLAST detector. Applying the Mo and Tsai prescription for all order radiative corrections in extraction of $R_{2\gamma}$, they compared the results with the updated theoretical predictions using the dispersive approach by Blunden *et al.* [46] and Tomalak *et al.* [51] along with the phenomenological fit of Ref. [21] as shown in Fig. 3.16. Note that the results using Maximon and Tjon prescription [76] of radiative correction are also available in that paper. Unlike the two other measurements of VEPP-3 and CLAS, $R_{2\gamma}$ in the large ε region are basically negative, implying a positive TPE effect at that kinematics, even though the results are in the close vicinity of $R_{2\gamma} = 1$ there. However, the phenomenological fit of Bernauer *et al.* [21] and the subtracted dispersive

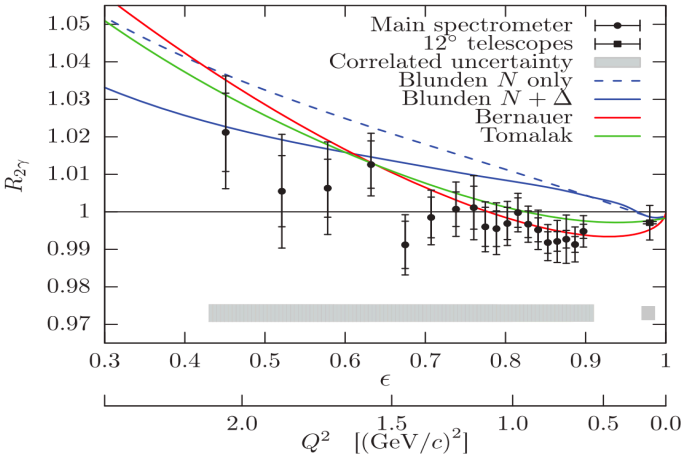

FIGURE 3.16: Measured $R_{2\gamma}$ by OLYMPUS experiment [117] at DESY plotted as a function of ε (corresponding Q^2 scale is also shown) at the beam energy $E = 2.01$ GeV. Compared are the theoretical predictions of Blunden *et al.* [46] (blue dashed and solid lines), Tomalak *et al.* [51] (Green solid), and the phenomenological fit of Bernauer *et al.* [21]. Plot is taken from the original work of Ref. [117].

calculation of Tomalak [51], which used the proton form factor input from Bernauer's work, agrees reasonably well with the data. In contrast, Blunden's estimation with nucleon intermediate state alone seems to overestimate the TPE effect compared to the data. But the inclusion of the $\Delta(1232)3/2^+$ resonance intermediate state in Blunden's work negates the nucleon effect and brings the curve little closer to the data, at least at lower ε. This observation stimulates one to further investigate the effect of the higher mass resonance intermediate states within the dispersive method to see if that brings in any dramatic change in TPE effect.

In a recent review paper [29], Afanasev *et al.* carried out an analysis on the combined data sets of $R_{2\gamma}$ from all three contemporary experiments of VEPP-3, CLAS and OLYMPUS to test the existence of no-TPE hypothesis and compare the agreement between model predictions and measured values by investigating the difference, $R_{2\gamma} - R_{2\gamma}^{\text{calc}}$ between the measured and the calculated values of $R_{2\gamma}$. Considering only the independent data sets from CLAS and complete sets from rest of the experiments, the authors used two different statistical approaches to account the scale-type normalization uncertainty that is available for CLAS and OLYMPUS experiment only. In the first approach adding the normalization uncertainty with the statistical and uncorrelated systematic

uncertainties of CLAS and OLYMPUS experiment in quadrature they ruled out the hypothesis of absence of TPE effect with 98% confidence level. An alternative treatment of the normalization uncertainty, allowing the floating of the CLAS and OLYMPUS data independently to bring in a new normalization factor $\mathcal{N}$ by minimizing the reduced χ^2 for each data set, also rules out the possibility of no-TPE hypothesis with an even improved confidence level of 99.5%. However, one can not reach any definite conclusion about the strength of the claim that the TPE effect alone can resolve the proton form factor ratio discrepancy yet with the available data that mostly fall in the kinematic region where the TPE effect is relatively smaller in magnitude (according to the model predictions) and also because the form factor discrepancy becomes apparent above that region.

3.5 Polarization observables

Another way to see the TPE effect experimentally is to observe the ε dependence of the polarization transfer ratio R_{TL} introduced in Sec. 1.3.2. The defining equations of P_L and P_T in Eq. (1.17b) relates the electric and magnetic form factors G_E and G_M at the Born level, so does the ratio R_{TL} with $\mu_p G_E/G_M$ ratio at the same approximation. However, including the TPE effects P_T and P_L can be given by [11, 43, 46, 73]

$$\begin{aligned} P_T &= -\frac{\sqrt{2\tau\varepsilon(1-\varepsilon)}}{\sigma_{\mathrm{R}}}\Bigg[G_E(Q^2)G_M(Q^2) + G_M(Q^2)\,\mathrm{Re}\,\mathcal{G}_E(\varepsilon,Q^2) \\ &\quad + G_E(Q^2)\,\mathrm{Re}\left(\mathcal{G}_M(\varepsilon,Q^2) + \frac{\nu\varepsilon}{\tau}G'_a(\varepsilon,Q^2)\right)\Bigg], \qquad (3.57a) \\ P_L &= \frac{\tau\sqrt{1-\varepsilon^2}}{\sigma_{\mathrm{R}}}\Bigg[G_M^2(Q^2) + 2G_M(Q^2) \\ &\quad \times \mathrm{Re}\left(\mathcal{G}_M(\varepsilon,Q^2) + \frac{\nu\varepsilon^2}{\tau(1+\varepsilon)}G'_a(\varepsilon,Q^2)\right)\Bigg], \qquad (3.57b) \end{aligned}$$

where the electric and magnetic equivalent generalized form factors $\mathcal{G}_E$ and $\mathcal{G}_M$ are introduced in Eqs. (3.23a) and (3.23b). In the Born approximation, the ratio R_{TL} thus

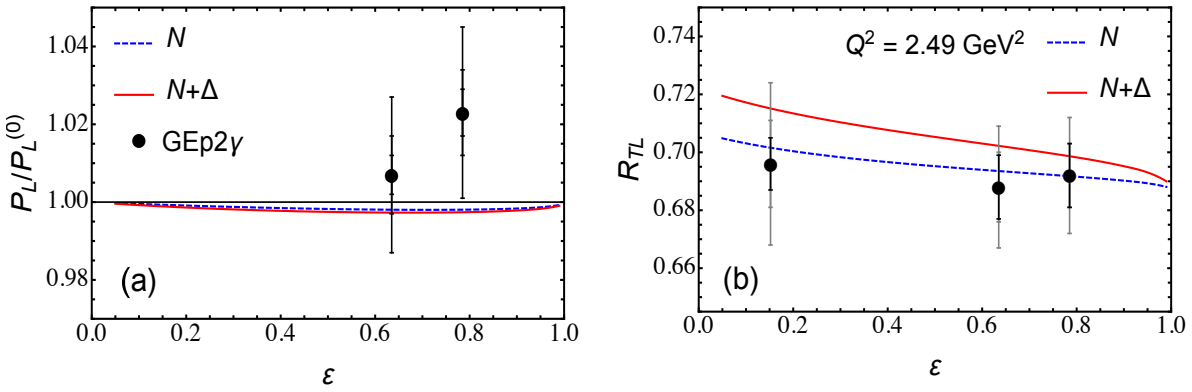

FIGURE 3.17: TPE effect on (a) the longitudinal polarization transfer P_L relative to the Born approximation $P_L^{(0)}$, and (b) the ratio R_{TL}, as a function of ε at fixed $Q^2 \approx 2.5$ GeV^2. The data points (black solid circles) with the associated systematic and statistical uncertainty are taken from Ref. [119], while the blue dashed and the solid red lines are the calculated results by Blunden and Melnitchouk [46] with nucleon and sum of nucleon with $\Delta(1232)3/2^+$ intermediate states, respectively.

reduces to $\mu_p G_E/G_M$ which is independent of ε. Therefore, any ε dependence in R_{TL} is a good check of the effects beyond single photon exchange approximation. On the other hand, the ratio $\mu_p G_E/G_M$ extracted from the polarization transfer measurement was found relatively insensitive to the TPE correction [11, 37]. But, that is perhaps due to the fact that the data range were mostly in the high ε region, $\varepsilon \approx 0.7 - 0.8$, where the TPE effect is small. However, in search of the effect to better constrain the theoretical estimations, the GEp2γ collaboration at Jefferson Lab [119] has measured R_{TL}, and P_L relative to its calculated Born approximation $P_L(0)$ at $Q^2 = 2.5$ GeV^2 covering a wide range of ε. The ratio R_{TL} was found almost independent of ε at the 1.5% level whereas the longitudinal polarization P_L shows an enhancement of $\approx 2\%$ over the range of $0.635 \leq \varepsilon \leq 0.785$ relative to $P_L(0)$. In contrast to the findings of GEp2γ collaboration, the theoretical predictions based on hadronic TPE calculation [37] with nucleon intermediate state shows some ε dependence of R_{TL} taking the numerical values away from the measured ones at the backward angles, and no ε dependence for P_L. The GPD [43] and pQCD [120] based calculations also show non-zero slope of the R_{TL} vs. ε curve, but with an opposite sign. Later on, an improved calculation [46] in the dispersive approach with nucleon intermediate state shows very good agreement with the data of Ref. [119], but inclusion of the excited resonance $\Delta(1232)3/2^+$ took the curve away from the measured values in the backward direction, as shown in Fig. 3.17(b). Note that the

legends for the curves of R_{TL} in Fig. 16(b) of Ref. [46] were swapped, which has been corrected in Fig. 3.17. The shift of the R_{TL} line due to inclusion of $\Delta(1232)3/2^+$ state compels one to further investigate the effect of the higher mass resonance intermediate states, particularly at large momentum transfer squared. However, P_L is still found insensitive to the TPE correction in the entire range of ε (Fig. 3.17(a)).

3.6 Summary and discussion

The brief review of the model estimations of the TPE correction illustrates the pros and cons of three different approaches. The GPD and pQCD based calculations are more suitable for the high Q^2 interactions whereas most of the experiments discussed above are within the range of $Q^2 \leq 8.83$ GeV^2. In the range of $5.00 \leq Q^2 \leq 8.83$ GeV^2, only a limited number of data are available from the LT separation and PT method of measuring the ratio $\mu_p G_E/G_M$. But the discrepancy is clearly visible even for $Q^2 \leq 5$ GeV^2. On the other hand, the hadronic approach is a reasonable approximation for Q^2 up to ~ 5 GeV^2. But the direct loop integration of the TPE box and crossed-box diagram within the hadronic assumption contains a large source of uncertainty in its calculation due to off-shell ambiguity of the hadronic intermediate state. More importantly, the TPE cross section correction diverges in the forward angle limit violating unitarity once the resonance intermediate states are accounted. Considering these issues along with the kinematics of most of the existing experimental data, we find the dispersive method very convincing in evaluation of the TPE effects. However, it is also important to account the effects of the higher mass resonances with a realistic width consideration and up to date input parameters. In the next chapter, I adopt the dispersive formalism following Ref. [46] and start with an warm up TPE calculation in electron scattering off a simplified point-like target, muon. Once convinced with the outcome, I then apply the method to evaluate the TPE correction in e-p elastic scattering with all the 4- and 3-star, spin $1/2^{\pm}$ and $3/2^{\pm}$ intermediate states below 1.8 GeV in Chapter 5.

Chapter 4

Dispersive Method of TPE Calculation

This chapter describes the technical details of the dispersive method to calculate the TPE quantum correction in electron-proton elastic scattering within hadronic degrees of freedom. At first, the general framework is explained (Sec. 4.1) focusing on nucleon and resonance intermediate state, and then the method is applied to a simple test case of the TPE correction in unpolarized electron-muon scattering (Sec. 4.2).

4.1 Dispersive method

The dispersive approach, based on the principle of unitarity of the scattering matrix, is the most compelling method to calculate the TPE amplitudes as it can utilize the on-shell input parametrizations of the hadronic transition currents and the corresponding form factors at the two vertices. As a consequence, the issue of unphysical divergence in the forward angle limit for the resonance intermediate state can be resolved. The idea behind the dispersive method is to put the intermediate hadron and lepton on-shell which generates the imaginary part of the amplitude. Based on this basic concept the

detailed framework to calculate the TPE amplitude is discussed in the following two sub-sections.

4.1.1 General framework

The TPE amplitude of the box diagram of Fig. 3.1 has both the real and imaginary parts, while the corresponding cross box part of TPE has purely real values.Using the Cutkosky cutting rules [103], one can put the intermediate lepton and hadron states on-shell by substituting the propagator factors as

$$\frac{1}{p_R^2 - W^2 + i0^+} \quad \rightarrow \quad -2\pi i\, \theta(p_R^0)\, \delta(p_R^2 - W^2), \tag{4.1a}$$

$$\frac{1}{k_1^2 - m_e^2 + i0^+} \quad \rightarrow \quad -2\pi i\, \theta(k_1^0)\, \delta(k_1^2 - m_e^2), \tag{4.1b}$$

to obtain the imaginary part of the TPE amplitude $\mathcal{M}_{\gamma\gamma}$ of Eqs. (1.1) and (3.21), and hence the imaginary part of the generalized TPE form factors F_1', F_2', and G_a'. Note that the intermediate lepton and hadron are now on-shell. Therefore, one can use the on-shell parametrization of the hadronic transition current operator at the two hadronic vertices of Fig. 3.1. Thus, the model uncertainty due to the use of on-shell parametrizations for off-shell intermediate hadrons is eliminated. The substitutions of the propagator factors shown in Eq. (4.1b) into Eq. (1.1) reduces the four dimensional integration in $\mathcal{M}_{\gamma\gamma}$ to a comparatively simpler two dimensional integral over the four-momentum transfer squared Q_1^2 and Q_2^2 of the two virtual photons. After mapping the TPE amplitude $M_{\gamma\gamma}$ of Eq. (3.2b) onto the generalized form given in Eq. (3.21), the integration for the imaginary part of the generalized TPE form factors can be given a generic form in terms of an integration over the solid angle Ω_{k_1}, which can also be expressed in terms of Q_1^2 and Q_2^2, of the intermediate state lepton,

$$I_\delta = \frac{s - W^2}{4s} \int d\Omega_{k_1} \frac{G_i(Q_1^2)\, G_j(Q_2^2)\, f_{ij}(Q_1^2, Q_2^2)}{(Q_1^2 + \lambda^2)(Q_2^2 + \lambda^2)}, \tag{4.2}$$

where $G_i(Q_1^2)$ and $G_j(Q_2^2)$ are the form factors at the two respective γNR (or, γNN for nucleon) vertices with $i, j = 1, 2, 3$ $(i, j = 1, 2)$, and the function $f_{ij}(Q_1^2, Q_2^2)$ is a polynomial of combined degree 4 (2 for nucleon) in $Q_{1,2}^2$. The imaginary part of the generalized TPE form factors can be computed from Eq. (4.2) for each resonance state at a specific value of W, such as at the peak of the resonance, $W^2 = W_R^2$. The numerical evaluation of the integral I_δ in Eq. (4.2) at $W^2 = W_R^2$ gives the imaginary part of the generalized TPE form factors, and hence the amplitude, as a function of electron energy E, at fixed values of the four-momentum transfer squared Q^2. The same can be done for the elastic nucleon intermediate state with the substitution of $W = M(\text{nucleon mass})$ and the appropriate form factors. The detailed discussion for the input form factors will be discussed in Sec. 5.1 for nucleon intermediate state and in Sec. 5.3.3 for resonance intermediate states. Note that the numerator of the integrand here vanishes in the limit of $Q_{1,2}^2 \to 0$ for resonance intermediate states which will be clear from the expressions of the transition currents into spin-1/2 and -3/2 resonance states discussed in Sec. 5.2. As a consequence, the integral becomes IR finite, while a subtraction of the IR divergent part is required for the nucleon case following the discussion of Sec. 3.1.2.

The Cauchy principal value integral formula provides the basis of the dispersion relation to generate the real part of the generalized TPE form factors, and hence the TPE amplitude $M_{\gamma\gamma}$, from the corresponding imaginary parts. Using the symmetry properties

$$F'_{1,2}(Q^2, -\nu) = -F'_{1,2}(Q^2, \nu), \tag{4.3a}$$

$$G'_a(Q^2, -\nu) = G'_a(Q^2, \nu), \tag{4.3b}$$

the real parts of the TPE amplitudes can then be computed from the dispersion relations [46, 48, 51, 70],

$$\mathrm{Re}\, F_1'(Q^2,\nu) = \frac{2}{\pi}\mathcal{P}\int_{\nu_{\rm min}}^{\infty} d\nu' \,\frac{\nu}{\nu'^2-\nu^2}\,\mathrm{Im}\, F_1'(Q^2,\nu'), \tag{4.4a}$$

$$\mathrm{Re}\, F_2'(Q^2,\nu) = \frac{2}{\pi}\mathcal{P}\int_{\nu_{\rm min}}^{\infty} d\nu' \,\frac{\nu}{\nu'^2-\nu^2}\,\mathrm{Im}\, F_2'(Q^2,\nu'), \tag{4.4b}$$

$$\mathrm{Re}\, G_a'(Q^2,\nu) = \frac{2}{\pi}\mathcal{P}\int_{\nu_{\rm min}}^{\infty} d\nu' \,\frac{\nu'}{\nu'^2-\nu^2}\,\mathrm{Im}\, G_a'(Q^2,\nu'), \tag{4.4c}$$

where $\mathcal{P}$ refers to the Cauchy principal value integral, with $\nu_{\rm min} = E_{\rm min}/M - \tau$ and $E_{\rm min} = (W^2 - M^2)/2M$ is the minimum energy required to excite a state of invariant mass W. For elastic nucleon intermediate states, the minimum energy is $E_{\rm min} = 0$, so that one has $\nu_{\rm min} = -\tau$.

4.1.2 Analytical continuation to unphysical region

The physical threshold for electron scattering at $\varepsilon = 0$, or backward angles, $\cos\theta = -1$, is $\nu_{\rm th} \equiv \sqrt{\tau(1+\tau)}$. In other words, the threshold energy for physical scattering to take place is $E_{\rm th} = M(\tau + \nu_{\rm th})$. Figure 4.1 marks the physical region of the integration of Eq. (4.4c) from the unphysical ones by the solid red curve where the shaded area corresponds to the physical range of ν. The inclined green dashed, blue long-dashed, dotted dark-red and dot-dashed orange lines identify the minimum limit of the dimensionless variable $\nu_{\rm min}$ in the integral of Eq. (4.4c) for some representative intermediate states nucleon, $\Delta(1232)3/2^+$, $N(1520)3/2^-$, and $N(1720)3/2^+$, respectively, at fixed values of Q^2. It is evident from the diagram that the integrals in Eqs. (4.4c) extend into the unphysical region at certain limits of the values of W and Q^2. For example, for the $\Delta(1232)3/2^+$ resonance, at $Q^2 = 0.5$ GeV^2 and $W = 1.232$ GeV the physical threshold $\nu_{\rm th} \cong 0.4$, whereas the integration runs from $\nu_{\rm min} \cong 0.22$. On the other hand, for nucleon intermediate state, the integration needs information from the unphysical region for any value of Q^2. Thus, an analytical continuation of the imaginary parts of the form factors into the unphysical region is required to obtain the real parts from the dispersion

relations. The analytic continuation of the integral I_δ in Eq. (4.2) into the unphysical

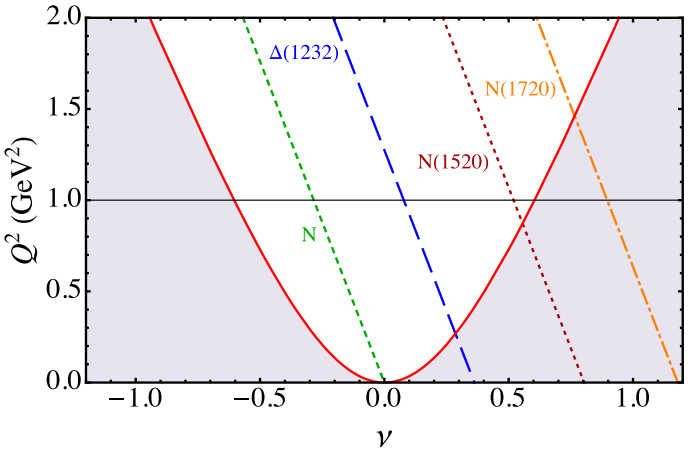

FIGURE 4.1: Specification of physical and unphysical regions of the dimensionless variable ν covered by the dispersive integral of Eq. (4.4c) at fixed values of four-momentum transfer squared Q^2. The shaded region bordered by solid red line corresponds to the physical region, and the green dashed (nucleon), blue dashed ($\Delta(1232)$), dark-red dotted ($N(1520)$), and orange dot-dashed ($N(1720)$) lines specify the $\nu_{\rm min}$ of the fixed Q^2 dispersive integral. The black horizontal line represents a fixed value of Q^2.

region is discussed in Ref.[51] to apply it at a specific case of monopole type nucleon form factors. Blunden *et al.* [46] modified the contour in the complex plane to calculate the integral I_δ in the unphysical region for a more general class of the form factors for which the poles not only in the timelike region of Q^2 but also in the spacelike region is acceptable within some restrictions as addressed in there work. The phase space integration $\int d\Omega_{k_1} = \int d\cos\theta_{k_1} d\phi_{k_1}$ can be expressed in terms of the integration over Q_1^2 and Q_2^2. The definition of θ_{k_1} and ϕ_{k_1} can be understood from the centre-of-mass (CM) frame kinematics explained in Appendix A. The region covered by the integral I_δ forms an elliptic shape in the Q_1^2 vs. Q_2^2 plane having the centre at $\{Q_0^2, Q_0^2\}$ with,

$$Q_0^2 = \frac{(s-M^2)(s-W^2)}{2\,s}. \tag{4.5}$$

Having defined the electron momenta in CM frame as Eq. (A.1d), one can express the virtual photon momenta Q_1^2 and Q_2^2 in the form,

$$Q_1^2 = Q_0^2\,(1-\cos\theta_{k_1}), \tag{4.6a}$$

$$Q_2^2 = Q_0^2\,(1-\cos\theta\cos\theta_{k_1}-\sin\theta\sin\theta_{k_1}\sin\phi_{k_1}). \tag{4.6b}$$

In elliptic coordinates $\{\alpha,\theta_{k_1}\}$, following Ref. [46, 51],the phase space integral can be transferred as,

$$\int d\Omega_{k_1} = \int d\cos\theta_{k_1}\int d\phi_{k_1} \to 2\int_0^1 d\alpha\int_0^{2\pi} d\theta_{k_1}, \tag{4.7}$$

and thus the two four momenta take the form,

$$Q_1^2 = Q_0^2\,(1-r\,\cos\theta_{k_1}), \tag{4.8a}$$

$$Q_2^2 = Q_0^2\,(1-r\,\cos\theta\cos\theta_{k_1}-r\,\sin\theta\sin\theta_{k_1}), \tag{4.8b}$$

where $r=\sqrt{1-\alpha^2}$ is the radial parameter of the concentric ellipses for the contours of constant α, with $\alpha=\sin\theta_{k_1}\sin\phi_{k_1}$. To analytically continue the integral I_δ into the unphysical region the integral over θ_{k_1} is transformed as a contour integral over the contour [46]

$$z = e^{i\theta_{k_1}}, \tag{4.9}$$

for the physical region, while the deformed contour [46]

$$z = \frac{1}{2}(1+\beta)+\frac{1}{2}(1-\beta)e^{i\theta_{k_1}}, \tag{4.10}$$

with β being defined in Eq. (4.12), is used for the calculation of I_δ in the unphysical region ($\cos\theta<-1$), so that any arbitrary poles in the timelike region along with some restricted poles in the spacelike region of the form factors are accounted. With this change of variable, the two four-momentum transfer squared $Q_1^2(r,z)$ and $Q_2^2(r,z)$ are

now functions of radial parameter r and the new complex variable z as,

$$Q_1^2 = Q_0^2 \left[1 - \frac{r}{2}\left(z + \frac{1}{z}\right)\right], \tag{4.11a}$$

$$Q_2^2 = Q_0^2 \left[1 - \frac{r}{2}\left(\frac{z}{\beta} + \frac{\beta}{z}\right)\right], \tag{4.11b}$$

where

$$\beta \equiv \begin{cases} e^{i\theta}, & \text{for } -1 \leq \cos\theta \leq +1, \\ \cos\theta - \sqrt{\cos^2\theta - 1}, & \text{for } \cos\theta \leq -1. \end{cases} \tag{4.12}$$

The contour integration using the contours of Eqs. (4.9) and (4.10) for the physical and unphysical regions, respectively, is tested for e-μ scattering case in the next section. Then the procedure is implemented in case of elastic e-p elastic scattering to obtain the imaginary parts of the generalized TPE form factors at specific values of Q^2 and a grid of electron energy E for elastic nucleon intermediate state in Sec. 5.1 followed by the discussions to include the resonance intermediate states from Sec. 5.2.

4.2 TPE in e-μ scattering

In this section, the contour integration and the overall dispersive method discussed above is tested by applying it into the simple case of scattering of electron off a pointlike target particle muon, μ. Since μ is a fundamental particle and has no internal structure hence no structure-dependent input is required at the two target particle vertices of the TPE Feynman diagram. Therefore, the numerical dispersive method result for this simple case is expected to be identical with that from the direct loop integral results obtained using Passarino-Veltman (PV) functions [93, 121]. The TPE amplitude for unpolarized e-μ scattering simplifies to the form:

$$\mathcal{M}_{\gamma\gamma}^{e-\mu(\text{box})} = -ie^4 \int \frac{d^4q_1}{(2\pi)^4} \frac{\bar{u}_e(k')\gamma_\alpha(\not{k}_1 + m_e)\gamma_\beta u_e(k)\bar{u}_\mu(p')\,\gamma^\alpha\,(\not{p}^* + m_\mu)\,\gamma^\beta\,u_\mu(p)}{(q_1^2 - \lambda^2)(q_2^2 - \lambda^2)(k_1^2 - m_e^2 + i0^+)(p^{*2} - m_\mu^2 + i0^+)}, \tag{4.13}$$

where $p^* = p + q_1$ is the four-momentum of the intermediate muon and m_μ is the muon mass. Rest of the quantities are as defined before for the case of e-p elastic scattering. The explicit form of the corresponding crossed-box amplitude is,

$$\mathcal{M}_{\gamma\gamma}^{e-\mu(\text{xbox})} = -ie^4 \int \frac{d^4q_1}{(2\pi)^4} \frac{\bar{u}_e(k')\gamma_\alpha(\not{k}_2 + m_e)\gamma_\beta u_e(k)\bar{u}_\mu(p')\,\gamma^\alpha\,(\not{p}^* + m_\mu)\,\gamma^\beta\,u_\mu(p)}{(q_1^2-\lambda^2)(q_2^2-\lambda^2)(k_2^2-m_e^2+i0^+)(p^{*2}-m_\mu^2+i0^+)} \quad (4.14)$$

As discussed before, the crossed-box TPE amplitude can also be obtained using the crossing symmetry relation of Eq. (3.11). The total TPE amplitude, $M_{\gamma\gamma}^{e-\mu} = M_{\gamma\gamma}^{e-\mu(\text{box})} + M_{\gamma\gamma}^{e-\mu(\text{xbox})}$, can be evaluated either by direct loop integral evaluation or by the dispersive method. One can also express the amplitude in terms of the generalized TPE form factors $F_1^{'}$, $F_2^{'}$, and $G_a^{'}$ of Eq. (3.21) and mapping of $M_{\gamma\gamma}^{e-\mu}$ onto the generalized $M_{\gamma\gamma}$ of Eq. (3.21) provides the expressions of $F_1^{'}$, $F_2^{'}$, and $G_a^{'}$ for the simplified case of e-μ scattering. The evaluated generalized TPE form factors can be used in Eq. (3.22) to get the cross section correction. The Born cross section of Eq. (1.13) will be substituted by

$$\sigma_{\text{R}}^{\text{Born}}(e-\mu) = \varepsilon + \tau, \quad (4.15)$$

for this case. It is important to mention that only $F_1^{'}$ is infrared divergent for point like target and that is subtracted using Maximon and Tjon prescription [76]. In rest of the part of this section, the two methods of evaluation are discussed and the obtained results are compared.

4.2.1 Passarino-Veltman (PV) functions

To evaluate the one-loop integrals of Eqs. (4.13) and (4.14), I use the Mathematica package FeynCalc [122, 123] that generates the results in terms of a set of the two point, three point and four point scalar PV functions B_0, C_0, and D_0, respectively. For

the s-channel box diagram the general expression of these scalar functions are,

$$B_0(s) \equiv \frac{1}{i\pi^2}\int \frac{d^4q_1}{[(k-q_1)^2-m_e^2+i0^+]\,[(p+q_1)^2-m_\mu^2+i0^+]}, \quad (4.16a)$$

$$C_0(s;\lambda^2) \equiv \frac{1}{i\pi^2}\int \frac{d^4q_1}{[q_1^2-\lambda^2]\,[(k-q_1)^2-m_e^2+i0^+]} \times \frac{1}{[(p+q_1)^2-m_\mu^2+i0^+]}, \quad (4.16b)$$

$$D_0(s;\lambda_1^2,\lambda_2^2) \equiv \frac{1}{i\pi^2}\int \frac{d^4q_1}{[q_1^2-\lambda_1^2]\,[q_2^2-\lambda_2^2]} \times \frac{1}{[(k-q_1)^2-m_e^2+i0^+]\,[(p+q_1)^2-m_\mu^2+i0^+]}. \quad (4.16c)$$

Note that the PV functions B_0, C_0, and D_0 have dependence on the variables m_e, m_μ, and Q^2 as well, which has been suppressed for simplicity of notation. However, in practice the PV functions have other variables in the TPE amplitudes coming from the numerator factors. Including the numerator variable dependence, the form of the PV functions (in Mathematica package LoopTools [124] notation) that come into the calculation of total TPE amplitudes, $M_{\gamma\gamma}^{e-\mu}$ are:

- $B_0(m_\mu^2,\lambda^2,m_\mu^2)$, $B_0(t,\lambda^2,\lambda^2)$, $B_0(s,m_e^2,m_\mu^2)$, $B_0(u,m_e^2,m_\mu^2)$
- $C_0(m_e^2,m_e^2,t,\lambda^2,m_e^2,\lambda^2)$, $C_0(m_\mu^2,m_\mu^2,t,\lambda^2,m_\mu^2,\lambda^2)$, $C_0(m_\mu^2,m_e^2,s,m_\mu^2,\lambda^2,m_e^2)$, $C_0(m_\mu^2,m_e^2,u,m_\mu^2,\lambda$
- $D_0(m_\mu^2,m_\mu^2,m_e^2,m_e^2,t,s,\lambda^2,m_\mu^2,\lambda^2,m_e^2)$, $D_0(m_\mu^2,m_\mu^2,m_e^2,m_e^2,t,u,\lambda^2,m_\mu^2,\lambda^2,m_e^2)$

Since λ_1 and λ_2 are some IR regulators, I have substituted them by the common parameter λ. The scalar functions mentioned above can be evaluated using the Mathematica package LoopTools [124]. Among these PV functions, only the functions $B_0(s,m_e^2,m_\mu^2)$, $C_0(m_\mu^2,m_e^2,s,m_\mu^2,\lambda^2,m_e^2)$, and $D_0(m_\mu^2,m_\mu^2,m_e^2,m_e^2,t,s,\lambda^2,m_\mu^2,\lambda^2,m_e^2)$ have imaginary parts and the rest are purely real. The imaginary parts of the three scalar functions can

be written as [86]

$$\text{Im}\, B_0(s, m_e^2, m_\mu^2) = \frac{\pi(s - m_\mu^2)}{s}, \tag{4.17a}$$

$$\text{Im}\, C_0(m_\mu^2, m_e^2, s, m_\mu^2, \lambda^2, m_e^2) = \frac{\pi \log[s\,\lambda^2/(s - m_\mu^2)^2]}{s - m_\mu^2}, \tag{4.17b}$$

$$\text{Im}\, D_0(m_\mu^2, m_\mu^2, m_e^2, m_e^2, t, s, \lambda^2, m_\mu^2, \lambda^2, m_e^2) = -\frac{2\pi \log[-t/\lambda^2]}{t\,(s - m_\mu^2)}. \tag{4.17c}$$

Keeping only the imaginary parts of these three functions in the expressions of generalized form factors and leaving the rest generates the imaginary parts of the corresponding form factors. The imaginary parts of $F_1^{'}$, $F_2^{'}$, and $G_a^{'}$, obtained using dispersive method, can be tested against that obtained using the above treatment.

4.2.2 Dispersive method

As discussed in Sec. 4.1, putting the intermediate leptons (for the case of e-μ scattering) on-shell using Eq. (4.1b) gives the imaginary part of the amplitude and hence the generalized form factors. The integration of Eq. (4.2) for the imaginary parts of $F_1^{'}$, $F_2^{'}$, and $G_a^{'}$ takes the simplified form

$$I_\delta^{e\mu} = \frac{s - m_\mu^2}{4s} \int d\Omega_{k_1} \frac{f(Q_1^2, Q_2^2)}{(Q_1^2 + \lambda^2)(Q_2^2 + \lambda^2)}, \tag{4.18}$$

where the function $f(Q_1^2, Q_2^2)$ is a polynomial of combined degree 2 in $Q_{1,2}^2$. As addressed before in this section that this integration can be IR divergent for $F_1^{'}$ only. To avoid this difficulty, the divergent part is subtracted off from the numerator of the respective integrand at the limit of $Q_{1,2}^2 = 0$ GeV^2 beforehand. As a consequence, the integration of Eq. (4.18) becomes independent of the value of the small mass parameter λ, and can be set to zero without any ambiguity. The real part of the form factors can then be calculated using the dispersion relations of Eq. (4.4c). For any value of nonzero Q^2 the integrand needs to be analytically continued into the unphysical region. Therefore, the analytical continuation into the unphysical region is obtained by using the deformed contour of Eq. (4.10), whereas for the physical region Eq. (4.9) is used. The obtained

results for the imaginary parts of the generalized form factors and the cross section using dispersive method is compared with that calculated using the scalar PV functions are discussed in the next section.

4.2.3 Results and conclusion

Fig. 4.2 illustrates the imaginary parts of the generalized TPE form factors $F_1^{'}$ (a,b), $F_2^{'}$ (c,d) and $G_a^{'}$ (e,f) for e-μ scattering at four-momentum transfer squared $Q^2 = 3.0$ GeV^2 as function of incident electron energy E. The left panel represents the magnified results for the smaller energy range from $E = 0.001$ to 1 GeV, while the right panel represents the same quantities for the extended range from 1 to 100 GeV. The results obtained using the numerical contour integration (red long-dashed line) and the scalar one-loop integrals (blue dotted line) are all identical which justifies the use of the contours defined in Eqs. (4.9) and (4.10). Moreover, in the higher energy region around $E = 100$ GeV, the imaginary part of $F_2^{'}$ reaches a very small constant value which justifies the use of the dispersion relation of Eq. (4.4c) to get the corresponding real part. On the other hand, the two other form factors $F_1^{'}$ and $G_a^{'}$ have non-zero and non-negligible slope even at around 100 GeV of energy. But they also reach the constant value near 1000 GeV and $10,000$ GeV, respectively. Thus the upper limit of the dispersive integrals of Eq. (4.4c) are adjusted accordingly where the plateau of the imaginary parts is reached. Since the integration is not carried up to the ideal maximum limit hence the tail effect is accounted following the procedures discussed in Sec. 5.1.

The TPE cross section correction, in percent relative to the Born cross section, for e-μ scattering is shown in Fig. 4.3. The results in Fig. 4.3(a, b) are calculated using dispersion relations but the imaginary parts are calculated in two different methods. Figure 4.3(a) uses the imaginary part obtained using the contour integration, whereas Fig. 4.3(b) make use of the imaginary part of the form factors generated by the explicit expressions of the imaginary parts of the PV functions B_0, C_0, and D_0 given in Eq. (4.17c). The third diagram of Fig. 4.3 shows the TPE cross section correction calculated by the direct one-loop integration in terms of the PV functions using Mathematica

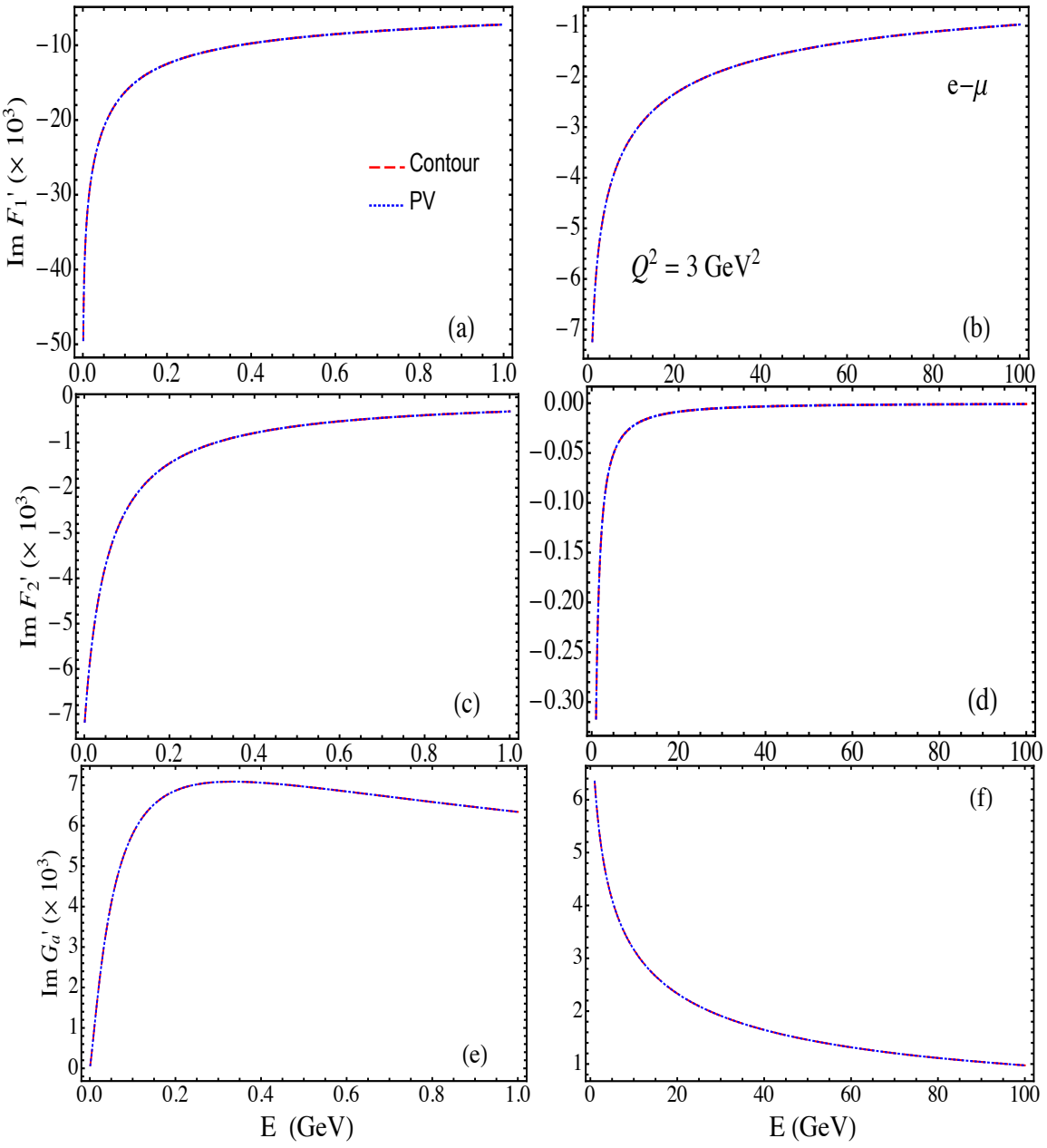

FIGURE 4.2: Imaginary part of the generalized form factors F_1' (top row), F_2' (middle row), and G_a' (bottom row) for TPE in e-μ scattering at a representative four-momentum transfer squared $Q^2 = 3$ GeV^2. The red long-dashed curve represents the result using the numerical contour integration, while the blue dotted curve corresponds to that using the imaginary parts of the Passarino-Veltman functions obtained by direct loop integrals. The left column shows the results in the incident electron energy (E) range from 0.001 to 1 GeV, and the right column is for the range from $E = 1$ to 100 GeV.

package FeynCalc [123] and LoopTools [124]. Clearly, Fig. 4.3(b) and (c) demonstrate that the dispersive method reproduces the real part of the form factors and hence the

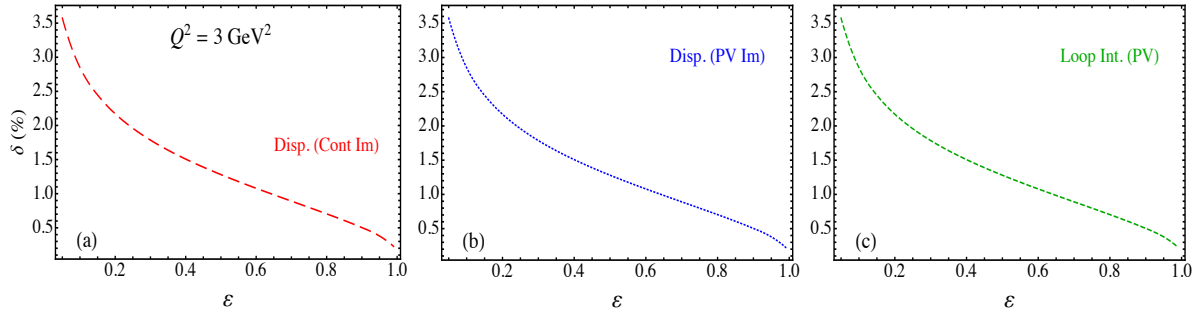

FIGURE 4.3: TPE cross section correction in unpolarized e-μ scattering at $Q^2 = 3$ GeV^2 as a function of virtual photon polarization ε. The red long-dashed curve (a) used the dispersive method to get the real part of the generalized form factors from the imaginary parts obtained by numerical contour integration. The blue dotted curve (b) used the same method to get the real part from the imaginary part of F_1', F_2', and G_a' using the imaginary parts of the Passarino-Veltman functions obtained by direct loop integrals. The green dashed curve (c) used the direct loop integrals using LoopTools.

cross section. As the imaginary parts from the contour integration and the PV functions are also identical, hence the identical cross sections in Fig. 4.3(a) and (b) motivate further to apply the dispersive method to unpolarized e-p elastic scattering. In the next chapter, the method is thus applied in case of e-p elastic scattering.

Chapter 5

Numerical Evaluation of TPE in e-p Elastic Scattering

The chapter begins with the evaluation of the TPE effect in e-p elastic scattering with nucleon intermediate state using dispersive method (Sec. 5.1). After that the discussion on the model estimation of the resonance intermediate states effect starts with the general decomposition of the hadronic transition current operators defining the transition form factors G_i $(i = 1, 2, 3)$ following Refs. [53, 83]. For the numerical calculation of the imaginary part of the TPE amplitude, input electromagnetic helicity amplitudes $A_{1/2}$, $A_{3/2}$, and $S_{1/2}$ from the CLAS exclusive electroproduction data at Jefferson Lab [125] are used in this work. Therefore, an explicit relation between the form factors and the helicity amplitudes for the proton to excited resonance intermediate states transition with spin-parity $1/2^{\pm}$ and $3/2^{\pm}$ are discussed in Sec. 5.3 including the CLAS data and fit for the electrocouplings. Inclusion of a non-zero finite resonance width in this particular model is also explained at the end of the chapter (Sec. 5.4).

5.1 TPE with elastic nucleon intermediate state

In this section, the dispersive method discussed in Sec. 4.1 is applied to calculate the TPE correction, with elastic nucleon intermediate state only, in unpolarized e-p elastic scattering. For the specific case of the nucleon intermediate state, the integration of Eq. (4.2) for the imaginary part of the generalized form factors takes the form

$$I_{\delta}^{e\mu} = \frac{s - M^2}{4s} \int d\Omega_{k_1} \frac{F_i(Q_1^2) F_j(Q_2^2) f_{i,j}(Q_1^2, Q_2^2)}{(Q_1^2 + \lambda^2)(Q_2^2 + \lambda^2)}, \tag{5.1}$$

where $F_i(Q_1^2)$ and $F_j(Q_2^2)$ are the Dirac $(i, j = 1)$ and Pauli $(i, j = 2)$ form factors at the two hadronic vertices γNN, and $f_{i,j}(Q_1^2, Q_2^2)$ is a polynomial of combined degree 2 in $Q_{1,2}^2$. Note that the transition current operator $\Gamma_{\gamma N \to N}$ of Eq. (1.5) for on-shell states are used at each hadronic vertex. The use of such on-shell parametrization of $\Gamma_{\gamma N \to N}$ is justified since the Cutkosky cutting rules put the intermediate states on-shell. However, as addressed in Sec. 4.1, the dispersive integral of Eq. (4.4c) requires the information of the imaginary part of the TPE generalized form factors in some unphysical region for any value Q^2 since the minimum energy corresponding to $\nu_{\min}$ is zero whereas the physical threshold is some non-zero positive quantity. For example, at $Q^2 = 1$ GeV^2, the physical threshold is $\nu_{\text{th}} \approx 0.604$, while the integration runs from the negative value of $\nu_{\min} = -0.284$ to infinity. Thus the integration of Eq. (5.1) is evaluated in the complex plane of four-momentum transfer squared Q^2, and the analytical continuation onto the unphysical region is done using the deformed contour of Eq. (4.10). For the physical region, the contour of Eq. (4.9) is used instead. In this specific case of nucleon intermediate state the integration for the imaginary part of the form factors F_1' and F_2' are infrared divergent. This divergent part is subtracted off from the numerator using Maximon and Tjon prescription [76], described in Sec. 3.1.2, at the limit of $Q_{1,2}^2 = 0$ GeV^2, *i.e.* $F_{1,2}' = F_{1,2}'(\text{unsubtracted}) - F_{1,2}'^{\text{IR}}$.

The input Dirac and Pauli form factors F_1 and F_2 are expressed in terms of the Sachs electric (G_E) and magnetic (G_M) form factors by inverting the relation of Eq. (1.9) as

$$F_1(Q^2) = \frac{G_E(Q^2) + \tau\, G_M(Q^2)}{1+\tau}, \tag{5.2a}$$

$$F_2(Q^2) = \frac{G_M(Q^2) - G_E(Q^2)}{1+\tau}. \tag{5.2b}$$

For G_E and G_M, a number of parametrizations are available including Refs. [72, 126, 127]. The parametrizations of Refs. [72, 126, 127] are expressed as the ratio of polynomials as

$$G_{E,M}(Q^2_{1,2}) = \frac{1 + \sum_{i=1}^{n} a_i\, Q^{2\,i}_{1,2}}{1 + \sum_{j=1}^{n} b_j\, Q^{2\,j}_{1,2}}, \tag{5.3}$$

with the coefficients given in Table 5.1 for three different parametrizations.

TABLE 5.1: Parameters used in the fittings as a ratio of polynomials (Eq. (5.3)) for the Sachs electric (G_E) and magnetic (G_M) form factors by three different groups of authors, Arrington *et al.* (AMT) [72], J. J. Kelly [126], and Venkat *et al.* [127].

Parameters	AMT [72]		Kelly [126]		Venkat [127]	
	G_E	G_M	G_E	G_M	G_E	G_M
a_1	3.439	-1.465	-0.24	0.012	2.9096	-1.43572
a_2	-1.602	1.26	0.0	0.0	-1.11542229	1.19052066
a_3	0.068	0.262	0.0	0.0	0.03866171	0.25455841
b_1	15.055	9.627	10.98	10.97	14.5187212	9.70703681
b_2	48.061	0.0	12.82	18.86	40.88333	0.00037357
b_3	99.304	0.0	21.97	6.55	99.999998	0.000006
b_4	0.012	11.179	0.0	0.0	0.00004579	9.9527277
b_5	8.65	13.245	0.0	0.0	10.3580447	12.7977739

The three parametrizations of proton electric and magnetic form factors from J.J. Kelly (red long-dashed line), Arrington *et al.* (AMT) (blue dotted line), and Venkat *et al.* (black dotted line) are compared in Fig. 5.1. All three curves behave similarly, except for a subtle difference in the Kelly parametrization for G_M at larger Q^2. However, one still needs to be cautious in choosing the parametrization of G_E and G_M due to the possibility of poles in the spacelike region of Q^2. At a first glance the three parametrizations seem to have no poles in the spacelike region since there is no negative terms in the

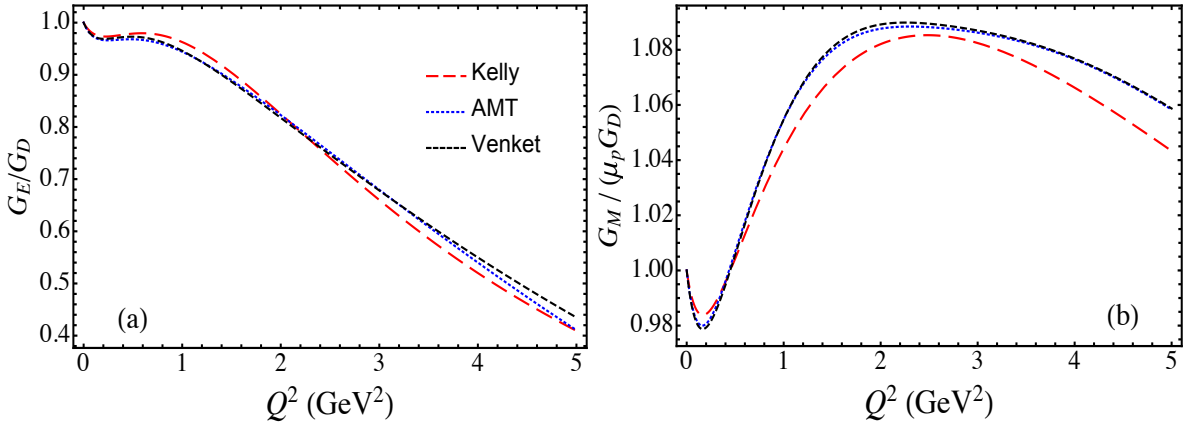

FIGURE 5.1: Nucleon electric (G_E) (a) and magnetic (G_M) (b) form factors parametrization by J.J. Kelly [126] (red long-dashed), Arrington *et al.* (AMT) [72] (blue dotted), and Venkat *et al.* [127] (black dashed). G_E is scaled by the standard dipole form factor G_D, and G_M is scaled by proton magnetic moment μ_p times G_D.

denominator. But, in the complex plane of Q^2 there is existence of poles in the AMT [72] and Venkat [127] parametrizations within the range of $Q^2 \sim 4.5$ GeV^2. Therefore, it is safe to pick the Kelly parametrization as default form of G_E and G_M in this work, unless mentioned explicitly, since the calculation is carried up to $Q^2 = 5.0$ GeV^2, and the TPE correction with nucleon intermediate state is anticipated to be a major contributor to the total correction.

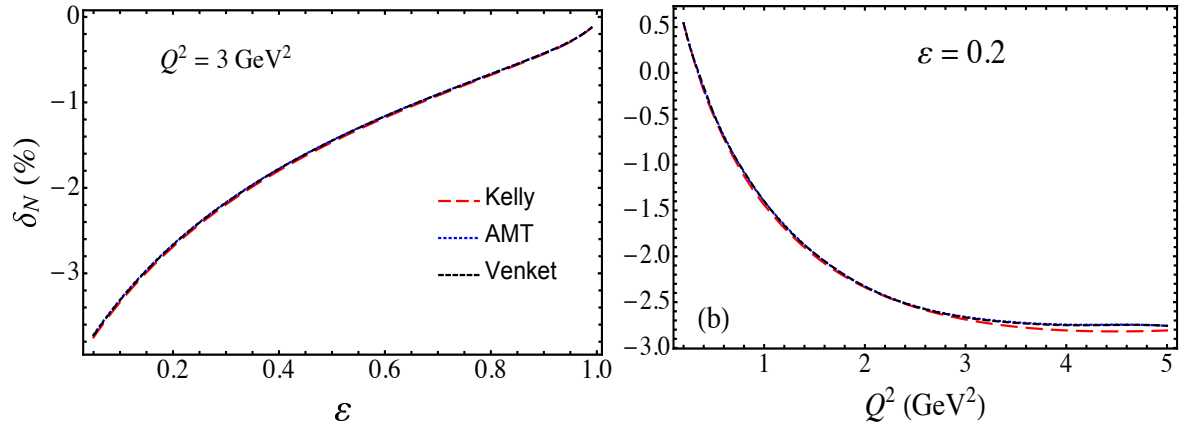

FIGURE 5.2: Two-photon exchange relative cross section correction δ_N (in percent) due to elastic nucleon intermediate state alone, (a) as a function of virtual photon polarization ε at $Q^2 = 3$ GeV^2, and (b) as a function of Q^2 at fixed $\varepsilon = 0.2$. The results represented by the red long-dashed curve uses the parametrization of Kelly [126], blue dotted curve uses AMT parametrization [72], and black dashed curve uses Venkat et.al. [127].

Nonetheless, it is also a worth checking the TPE cross section correction (δ_N) using all the mentioned parametrizations up to $Q^2 = 5.0$ GeV^2 and see if anything dramatic happens due to the pole effect above ~ 4.5 GeV^2. Figure 5.2 represents such an analysis of the TPE cross section correction. The virtual photon polarization, ε dependence at fixed value of $Q^2 = 3.0$ GeV^2 is shown in Fig. 5.2(a), while Fig. 5.2(b) illustrates the Q^2 dependence at $\varepsilon = 0.2$, corresponding to the backward angles. The results are consistent between all three parametrizations. At the backward angles, the cross section correction reaches $\sim 3.8\%$ of the Born level cross section, with negative sign, at $Q^2 = 3.0$ GeV^2. The curves show some non-linearity in ε up to $\varepsilon \sim 0.6$. Interestingly, δ_N almost reaches a saturation point with increasing Q^2 (≥ 4.0 GeV^2), as evident from Fig. 5.2(b). The TPE cross section correction, δ_N will be further discussed in Chapter 6 along with the intermediate resonance states' effect.

To estimate the TPE effects beyond elastic nucleon intermediate state, I adopt several parametrizations of the resonance transition current operators following Refs. [53, 82, 83] in the next section followed by a similar decomposition in terms of the helicity amplitudes in Sec. 5.3.

5.2 Resonance transition current operators

I begin this section by introducing the matrix element of the transition current J^ν from nucleon (N) to resonance excited state (R) and then parametrize the transition current operator $\Gamma_{\gamma N\to R}$ describing the absorption of a virtual photon, with momentum q on a nucleon N with momentum p, producing a resonant state R with momentum $p_R = p+q$. The matrix element of the transition current J^ν at the first vertex of the TPE diagram of Fig. 3.1 is defined by [53, 82],

$$\langle R(p_R)|J^\nu|N(p)\rangle \equiv e\bar{u}_R(p_R)\Gamma^\nu_{\gamma N\to R}(p_R,q)T_3^\dagger u_N(p), \tag{5.4a}$$

$$\langle R(p_R)|J^\nu|N(p)\rangle \equiv e\bar{u}_{R_\beta}(p_R)\Gamma^{\beta\nu}_{\gamma N\to R}(p_R,q)T_3^\dagger u_N(p). \tag{5.4b}$$

Equation (5.4a) corresponds to the transition of nucleon into spin-1/2 excited resonance states and (5.4b) is for the transition into spin-3/2 resonance states. For the spin-1/2 states, the usual Dirac spinors are used and for the spin-3/2 states, the Rarita-Schwinger spinor $\bar{u}_{R_\beta}$ is used in Eq. (5.4). Rarita-Schwinger spinor satisfies the relations

$$\not{p}_R u_{R_\beta} = W_R u_{R_\beta}, \qquad p_R^\beta u_{R_\beta} = 0, \qquad \gamma^\beta u_{R_\beta} = 0, \tag{5.5}$$

for the on-shell spin-3/2 states. $T_3^\dagger$ is the isospin transition operator, with normalizations $T_3^\dagger T_3 = 1$ for the transition to isospin-1/2 states and $T_3^\dagger T_3 = \frac{2}{3}$ for the transition to isospin-3/2 states. Note that q is a dummy variable here, representing the virtual photon four-momentum at each vertex, not the total four-momentum of the photons.

Analogous to the decomposition of the current operator $\Gamma_{\gamma N\to N}$ in terms of the covariants with co-efficients named Dirac (F_1) and Pauli (F_2) form factors, one can decompose $\Gamma_{\gamma N\to R}$, R being any spin 3/2 state, into several covariants in a variety of way with appropriate coefficients. The constraint from the gauge-invariance, $q_\beta \Gamma^{\beta\nu} = 0$, leaves three covariant terms to construct the $\Gamma_{\gamma N\to R}$ vertex. One choice of gauge-invariant covariants with the coefficients defining the three independent kinematic singularity-free form factors G_1, G_2, and G_3 is [53, 83]

$$\Theta_1^{\beta\nu} = \begin{pmatrix} \gamma_5 \\ \mathrm{I} \end{pmatrix} (\not{q} g^{\beta\nu} - q^\beta \gamma^\nu), \tag{5.6a}$$

$$\Theta_2^{\beta\nu} = \begin{pmatrix} \gamma_5 \\ \mathrm{I} \end{pmatrix} (q^\beta p_R^\nu - q\cdot p_R\, g^{\beta\nu}), \tag{5.6b}$$

$$\Theta_3^{\beta\nu} = \begin{pmatrix} \gamma_5 \\ \mathrm{I} \end{pmatrix} (q^\beta q^\nu - q^2 g^{\beta\nu}), \tag{5.6c}$$

where the upper and lower rows refer to positive and negative parity states, respectively. With these $\Theta_i^{\beta\nu}$ operators, $\Gamma_{\gamma N\to R}$ has the form

$$\Gamma^{\beta\nu}_{\gamma N\to R}(p_R, q) = G_1(Q^2)\,\Theta_1^{\beta\nu}(p_R, q) + G_2(Q^2)\,\Theta_2^{\beta\nu}(p_R, q) + G_3(Q^2)\,\Theta_3^{\beta\nu}(p_R, q). \tag{5.7}$$

However,this set of form factors are useful for theoretical purpose but they do not appear diagonally in the cross section formulae as they do not describe physical transitions. To analyze the resonance excitation cross section, Jones and Scadron [82] introduced the physical form factors G_M^*, G_E^*, and G_C^* corresponding to covariant couplings $\Theta_M^{\beta\nu}, \Theta_E^{\beta\nu}$, and $\Theta_M^{\beta\nu}$ inducing magnetic dipole, electric quadrupole and Coulomb quadrupole transitions, respectively. Using these multipole covariants the transition to any spin-3/2 even parity state at the first vertex of Fig. 3.1 can be decomposed as

$$\Gamma^{\beta\nu}_{\gamma N\to R}(p_R,q) = G_M^*(Q^2)\Theta_M^{\beta\nu}(p_R,q) + G_E^*(Q^2)\Theta_E^{\beta\nu}(p_R,q) + G_C^*(Q^2)\Theta_C^{\beta\nu}(p_R,q), \quad (5.8)$$

with the covariants being

$$\Theta_M^{\beta\nu}(p_R,q) = -\frac{C}{Q_+} i\epsilon^{\beta\nu}(p_R q), \quad (5.9a)$$

$$\Theta_E^{\beta\nu}(p_R,q) = -\Theta_M^{\beta\nu} - \frac{4C}{Q_+Q_-}\epsilon^{\beta\sigma}(p_R q)\epsilon_\sigma^\nu(p_R q)\gamma_5, \quad (5.9b)$$

$$\Theta_C^{\beta\nu}(p_R,q) = -\frac{2C}{Q_+Q_-} q^\beta (q^2 p_R^\nu - q.p_R q^\nu)\gamma_5, \quad (5.9c)$$

where

$$C \equiv \frac{3(W+M)}{2M}, \qquad Q_\pm \equiv (W\pm M)^2 + Q^2. \quad (5.10)$$

Here the shorthand notation $\epsilon^{\beta\nu}(p_R q) \equiv \epsilon^{\beta\nu\rho\sigma} p_{R_\rho} q_\sigma$ is used. Note in this work the convention of $\gamma_5 \equiv i\gamma^0\gamma^1\gamma^2\gamma^3$ is used and the Levi-Civita tensor $\epsilon^{\mu\nu\alpha\beta}$ is such that $\epsilon^{0123} \equiv +1$, therefore $\epsilon_{0123} \equiv -1$. Devenish *et al.* [83] provide a more general parametrization of the transition current $\Gamma_{\gamma N\to R}$ for normal and abnormal parity transition to any excited state R with spin $J \geq 3/2$ of which Eq. (5.8) is a special case. I restrict the discussion only for the transition to spin 3/2, even parity states in terms of G_M^*, G_E^*, and G_C^* since this set of form factors is used to evaluate the TPE amplitude for $\Delta(1232)3/2^+$ intermediate state only.

To relate the two sets of form factors for the transition to spin-3/2 and even parity states, *i.e.* (G_1, G_2, and G_3) with (G_M, G_E, and G_C), one can express the multipole covariants of Eq. (5.9c) in terms of the covariants of Eq. (5.6c) for on-shell transition

matrix elements and finds the relation [83]

$$
\begin{aligned}
G_1(Q^2) &= \frac{C\,W\,[G_M^*(Q^2) - G_E^*(Q^2)]}{2\,Q_+^2}, \\
G_2(Q^2) &= \frac{C}{2\,Q_+^2\,[M^2 + 2\,M^2(Q^2 - W^2) + (Q^2 + W^2)^2]} \Bigg[2\,G_C^*(Q^2)\,Q^2 Q_+^2 + \\
&\qquad G_E^*(Q^2) \Big\{ M^4 - 2M^2(Q_+^2 - Q^2 + W^2) - 2\,Q_+^2(Q^2 - W^2) + \\
&\qquad (Q^2 + W^2)^2 \Big\} - G_M^*(Q^2) \Big\{ M^4 + 2\,M^2(Q^2 - W^2) + (Q^2 + W^2)^2 \Big\} \Bigg], \\
G_3(Q^2) &= C\,\frac{4\,W^2\,G_E^*(Q^2) + G_C^*(Q^2)(M^2 + Q^2 - W^2)}{2[M^4 + 2\,M^2(Q^2 - W^2) + (Q^2 + W^2)^2]}.
\end{aligned}
\tag{5.11}
$$

For the inverse transition $R \to \gamma N$ at the second vertex in Fig. 3.1, the current operator $\Gamma^{\mu\alpha}_{R\to\gamma N}(p_R, q)$ can be obtained using the Hermitian property of the transition matrix element,

$$
\Gamma^{\mu\alpha}_{R\to\gamma N}(p_R, q) = \gamma_0 \left[\Gamma^{\alpha\mu}_{\gamma N\to R}(p_R, q)\right]^\dagger \gamma_0. \tag{5.12}
$$

For spin-1/2 resonances, on the other hand, we define the transition current operator $\Gamma^{\nu}_{\gamma N\to R}$ as

$$
\Gamma^{\nu}_{\gamma N\to R}(p_R, q) = G_1(Q^2) \begin{pmatrix} \mathrm{I} \\ \gamma_5 \end{pmatrix} \left(\not{q} q^\nu - q^2 \gamma^\nu\right) + G_2(Q^2) \begin{pmatrix} \mathrm{I} \\ \gamma_5 \end{pmatrix} \left(\not{q} P^\nu - P \cdot q\, \gamma^\nu\right), \tag{5.13}
$$

where $P = (p + p_R)/2 = p_R - q/2$, and again the upper and lower rows refer to positive and negative parity states, respectively. In analogy with (5.12), the inverse transition current operator $\Gamma^{\mu}_{R\to\gamma N}(p_R, q)$ is obtained from the Hermitian property of the transition matrix element,

$$
\Gamma^{\mu}_{R\to\gamma N}(p_R, q) = \gamma_0 \left[\Gamma^{\mu}_{\gamma N\to R}(p_R, q)\right]^\dagger \gamma_0. \tag{5.14}
$$

5.3 Form factors from electrocouplings

Since the electroproduction of resonance states is often parametrized in terms of resonance electrocouplings A_h [125], we define here the transition form factors G_i in terms of the amplitudes for specific helicity configurations.

5.3.1 Resonance electrocouplings

The resonance electrocouplings at the hadronic vertices are defined in terms of the matrix elements of the hadron electromagnetic current as [53]

$$A_{1/2} = \sqrt{\frac{2\pi\alpha}{K}}\frac{1}{e}\left\langle R, S_z^R = \tfrac{1}{2}\left|\, \epsilon_\mu^+ J^\mu_{\rm em} \,\right| N, S_z = -\tfrac{1}{2}\right\rangle, \tag{5.15a}$$

$$A_{3/2} = \sqrt{\frac{2\pi\alpha}{K}}\frac{1}{e}\left\langle R, S_z^R = \tfrac{3}{2}\left|\, \epsilon_\mu^+ J^\mu_{\rm em} \,\right| N, S_z = \tfrac{1}{2}\right\rangle, \tag{5.15b}$$

$$S_{1/2} = \sqrt{\frac{2\pi\alpha}{K}}\frac{1}{e}\left\langle R, S_z^R = \tfrac{1}{2}\left|\, \frac{|\boldsymbol{q}|}{Q}\epsilon_\mu^0 J^\mu_{\rm em} \,\right| N, S_z = \tfrac{1}{2}\right\rangle, \tag{5.15c}$$

where $\alpha = e^2/4\pi$ is the fine structure constant, e is the electron charge, and K is the equivalent photon energy at the real photon point, $K = (W^2 - M^2)/2W$. The spin projections of the nucleon and resonances R on the z-axis are labelled by S_z and S_z^R, and $\epsilon_\mu^{+,0}$ is the photon polarization vector for transversely or longitudinally polarized photons,

$$\epsilon_\mu^+ = (0; -\boldsymbol{\epsilon}^+), \qquad \boldsymbol{\epsilon}^+ = -\frac{1}{\sqrt{2}}(1, i, 0), \tag{5.16a}$$

$$\epsilon_\mu^0 = \frac{1}{Q}(|\boldsymbol{q}|; 0, 0, -q_0). \tag{5.16b}$$

The virtual photon three-momentum $\boldsymbol{q}$ is taken to be along the z-axis in the rest frame of the resonance R, and its magnitude is given in terms of the final state hadron mass W and the photon virtuality Q^2,

$$|\boldsymbol{q}| = \sqrt{Q^2 + \left(\frac{W^2 - M^2 - Q^2}{2W}\right)^2}. \tag{5.17}$$

In this work, for the input resonance electrocouplings we use the parametrizations obtained from the analysis of CLAS meson electroproduction data at Jefferson Lab [125]. To generate the electrocouplings as a function of the running invariant mass W of the intermediate state, I use Eq. (5.18), which is consistent with the prescription in the JM model of Ref. [128]. The W-dependent electrocoupling $A_h(W, Q^2)$ is given by

$$A_h(W, Q^2) = \frac{W}{W_R} \frac{|\boldsymbol{q}_R|}{|\boldsymbol{q}|} A_h^R(Q^2), \tag{5.18}$$

where A_h^R represents the electrocouplings $A_{1/2}$, $A_{3/2}$ or $S_{1/2}$ at the resonance point, W_R is the invariant mass W at the resonance point, and $\boldsymbol{q}_R$ is defined as

$$|\boldsymbol{q}_R| \;=\; \sqrt{Q^2 + \left(\frac{W_R^2 - M^2 - Q^2}{2W_R}\right)^2}. \tag{5.19}$$

5.3.2 Relations between form factors and electrocouplings

Following Devenish *et al.* [83], the hadronic transition current operator $\Gamma^{\beta\nu}_{\gamma N \to R}$ for spin-3/2 resonances can also be parametrized in terms of helicity form factors h_1, h_2, and h_3, which are given in terms of the helicity amplitudes $A_{1/2}$, $A_{3/2}$, and $S_{1/2}$ by [53]

$$h_1 = \frac{\sqrt{3}\,W}{b\,|\boldsymbol{q}|} S_{1/2}(W, Q^2), \quad h_2 = \pm\frac{1}{\sqrt{2}\,b} A_{3/2}(W, Q^2), \quad h_3 = \frac{\sqrt{3}}{\sqrt{2}\,b} A_{1/2}(W, Q^2), \tag{5.20}$$

where

$$b \equiv \sqrt{\pi\alpha \frac{(W \mp M)^2 + Q^2}{24 M W K}}, \tag{5.21}$$

and the upper (lower) sign corresponds to even (odd) parity states. (Note that the expressions for the helicity form factors h_i in terms of the electrocouplings A_h of Ref. [53] are off by a factor of $\sqrt{2/3}$, which has been corrected in Eq. (5.20).) For spin-parity

$3/2^+$ excitations, the current operator then can be written as

$$\begin{aligned}\Gamma^{\beta\nu}_{\gamma N\to R}(p,q) &= \frac{h_1}{Q_+Q_-}\,q^\beta\left[p\cdot q\,q^\nu - q^2\,p^\nu\right]\gamma_5 \\ &+ \frac{h_2}{Q_+Q_-}\left[2\epsilon^{\beta\sigma}(qp)\,\epsilon^{\nu\sigma}(qp)\gamma_5 + i\,W q^\beta\epsilon^\nu(qp\gamma)\right] i\,\frac{h_3}{Q_+Q_-}\,W q^\beta\epsilon^\nu(qp\gamma),\end{aligned} \tag{5.22}$$

while for spin-parity $3/2^-$ states it is given by

$$\begin{aligned}\Gamma^{\beta\nu}_{\gamma N\to R}(p,q) &= \frac{h_1}{Q_+Q_-}\,\gamma_5 q^\beta\left[p\cdot q\,q^\nu - q^2\,p^\nu\right]\gamma_5 \\ &+ \frac{h_2}{Q_+Q_-}\,\gamma_5\left[2\epsilon^{\beta\sigma}(qp)\,\epsilon^{\nu\sigma}(qp)\gamma_5 - i\,W q^\beta\epsilon^\nu(qp\gamma)\right] \\ &- i\,\frac{h_3}{Q_+Q_-}\,W\gamma_5\,q^\beta\epsilon^\nu(qp\gamma).\end{aligned} \tag{5.23}$$

Note again that in Eqs. (5.22) and (5.23) I use the shorthand notation $\epsilon^{\beta\sigma}(qp) \equiv \epsilon^{\beta\sigma\rho\lambda}q_\rho p_\lambda$ and $\epsilon^\nu(qp\gamma) \equiv \epsilon^{\nu\rho\lambda\alpha}q_\rho p_\lambda\gamma_\alpha$, where "$\gamma$" in the Levi-Civita tensor denotes the Dirac γ-matrix. Equating the expression of the current operator in Eq. (5.7) with that of Eqs. (5.22) or (5.23), the form factors G_i can be expressed in terms of the helicity form factors, and hence in terms of the electrocouplings A_h, as

$$G_1(W,Q^2) = \mp\frac{W(h_2+h_3)}{2\,Q_\pm}, \tag{5.24a}$$

$$G_2(W,Q^2) = \frac{Q^2h_1 + (M^2 \mp MW + Q^2)h_2 + W(W\mp M)h_3}{Q_+\,Q_-}, \tag{5.24b}$$

$$G_3(W,Q^2) = \frac{2W^2(h_2-h_3) - (M^2 - W^2 + Q^2)h_1}{2\,Q_+\,Q_-}. \tag{5.24c}$$

In a similar way, one can relate the form factors G^*_E, G^*_M, and G^*_C with the electrocouplings A_h by comparing the expressions of the current operator of Eq. (5.8) with that of Eq. (5.22) for transition into a spin-3/2 and even parity excited state as [53]

$$G^*_M = -F\left[\sqrt{3}A_{3/2} + A_{1/2}\right], \tag{5.25a}$$

$$G^*_E = -F\left[\frac{A_{3/2}}{\sqrt{3}} - A_{1/2}\right], \tag{5.25b}$$

$$G^*_C = 2\sqrt{2}\,F\frac{W}{\boldsymbol{q}}S_{1/2}, \tag{5.25c}$$

where

$$F \equiv \frac{M}{\boldsymbol{q}} \sqrt{\frac{M\,K}{4\pi\alpha W}\left[1 + \frac{Q^2}{(W\,+\,M)^2}\right]}. \tag{5.26}$$

For spin-parity $1/2^{\pm}$ resonant intermediate states, the spin-1/2 transition form factors G_1 and G_2 can be related to the electrocouplings A_h according to [53]

$$G_1(W, Q^2) = \frac{|\boldsymbol{q}|A_{1/2} + \sqrt{2}(M \pm W)S_{1/2}}{2\,b'\,|\boldsymbol{q}|\,[(M \pm W)^2 + Q^2]}, \tag{5.27a}$$

$$G_2(W, Q^2) = \frac{|\boldsymbol{q}|(M \pm W)A_{1/2} - \sqrt{2}\,Q^2 S_{1/2}}{b'\,|\boldsymbol{q}|(M \mp W)\,[(M \pm W)^2 + Q^2]}, \tag{5.27b}$$

where

$$b' \equiv \sqrt{\pi\alpha \frac{(W \mp M)^2 + Q^2}{4MWK}}, \tag{5.28}$$

in analogy with Eq. (5.21).

5.3.3 Input electrocouplings

The CLAS phenomenological fit [54, 116, 125] of the transverse $A^R_{1/2}(Q^2)$, $A^R_{3/2}(Q^2)$, and scalar (or, longitudinal) $S_{1/2}$ electrocouplings for the transition from nucleon to all the spin-parity $3/2^{\pm}$ and $1/2^{\pm}$ resonance excited states R is used as input in the hadronic transition current at each vertex of Fig. 3.1. Note that the used electrocouplings from CLAS [125] considers the excitation of nucleon to on-shell resonances. Thus to reduce the uncertainty of the model estimation of the resonance effect in TPE correction I choose the dispersive approach. However, for completeness, an analysis of the input electrocouplings for all the resonance intermediate states are described below

Figure. 5.3 represents the electro- and photo-excitation data of the first, 4-starred resonance [129], $\Delta(1232)3/2^+$ in terms of the transverse $A_{1/2}$, $A_{3/2}$, and longitudinal $S_{1/2}$ electrocouplings. The red-squared data points are basically from the CLAS analysis of the $N\pi$ electroproduction off proton along with that from JLab (Hall A and B), MAMI

and MIT/BATES [54] . Whereas the blue triangles for $A_{1/2}$ and $A_{3/2}$ correspond to the PDG18 [129] value. The phenomenological fit by CLAS, represented by red-dashed lines and numerical expressions given in Eq. (5.29c), goes close to the data at higher values of Q^2 but in the low Q^2 limit it doesn't resemble the data trend. An alternative fit by Aznauryan [46], given in terms of the magnetic (G_M^*), electric (G_E^*) and Coulomb (G_C^*) form factors in Eq. (5.30c), follows the data in the low Q^2 range and goes through the well established PDG18 values [129] at $Q^2 = 0$ GeV^2. For $S_{1/2}$ (Fig. 5.3(c)), the CLAS fit seems to show better agreement with the higher Q^2 data but the Aznauryan fit is also in agreement within the uncertainty range.

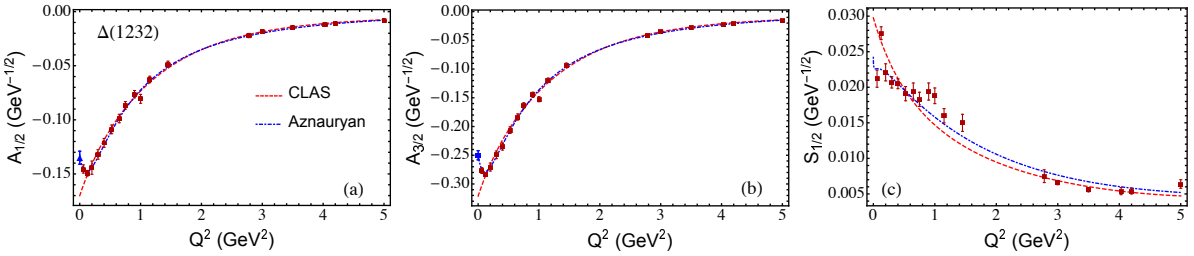

FIGURE 5.3: Parametrizations of transverse ($A_{1/2}$, $A_{3/2}$), and longitudinal ($S_{1/2}$) electrocouplings of photon-nucleon to $\Delta(1232)3/2^+$ resonance transition by CLAS [54, 125] (red dashed line) and by Aznauryan *et al.* [46, 53] (blue dot-dashed line) as function of Q^2. The squared dark-red points are the CLAS $N\pi$ electroproduction data [54], and the blue triangles are the PDG18 value [129] at $Q^2 = 0$ GeV^2.

Most of the experimental analyses of the photo- and electro-excitation data of $\Delta(1232)3/2^+$ are carried in terms of the multipole form factors (G_M^*, G_E^*, and G_C^*) and their ratios R_{EM}, the electric quadrupole to magnetic dipole ratio, and R_{SM}, the Coulomb quadrupole to magnetic dipole ratio. Therefore, a pictorial view of G_M^*, G_E^*, and G_C^* is also compared between the two fits of Aznauryan [46, 53] and CLAS [125] in Fig. 5.4. Clearly in Fig. 5.4(a), the Aznauryan fit satisfies the well established PDG18 value [129] of the magnetic dipole form factor $G_M^*(0) \approx 3.00$. Considering the trend of the fits in the low Q^2 region, the phenomenological fit of the $\Delta(1232)3/2^+$ transition form factors in Eq. (5.30c) is considered as default parametrization in this work. However, the form factor dependence of TPE correction is discussed in Sec. 6.2.1 by comparing the obtained δ (Fig. 6.4) using CLAS [125] and Aznauryan [46, 53] fits.

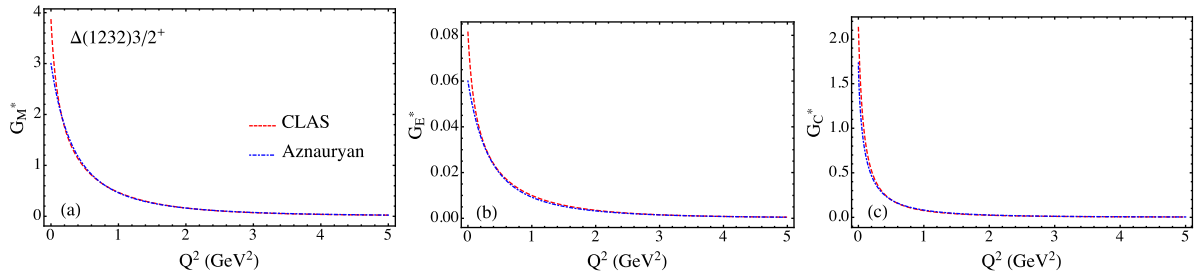

FIGURE 5.4: Comparison of magnetic (G_M^*), electric (G_E^*), and Coulomb (G_C^*) form factor parametrizations for the transition into $\Delta(1232)3/2^+$ intermediate state from Refs. [53, 54] as a function of Q^2.

Note the explicit form of the CLAS parametrizations of the electrocouplings $A_h^{\Delta(1232)}$ [125] are given as

$$A_{1/2}^{\Delta(1232)}(Q^2) = -\frac{170.06}{1000(1+Q^2)(1+0.1609\,Q^4-0.002\,Q^8)}, \tag{5.29a}$$

$$A_{3/2}^{\Delta(1232)}(Q^2) = -\frac{321.06}{1000(1+Q^2)(1+0.16\,Q^4-0.002\,Q^8)}, \tag{5.29b}$$

$$S_{1/2}^{\Delta(1232)}(Q^2) = \frac{29.76}{1000(1+Q^2)(1+0.0135\,Q^2-0.00046\,Q^8)}. \tag{5.29c}$$

The corresponding multipole amplitudes are obtained using Eq. (5.25c). On the other hand, the direct phenomenological parametrization of G_M^*, G_E^*, and G_C^* from Aznauryan [46, 53] is

$$G_M^*(Q^2) = \frac{3}{(1+Q^2/0.71)^2}\frac{\sqrt{Q_+}}{W_R+M}\exp(-0.21\,Q^2), \tag{5.30a}$$

$$G_E^*(Q^2) = -R_{EM}\,G_M^*(Q^2), \tag{5.30b}$$

$$G_C^*(Q^2) = -R_{SM}\,G_M^*(Q^2)\frac{4\,W_R^2}{\sqrt{Q_+Q_-}}, \tag{5.30c}$$

where R_{EM}, the electric quadrupole to magnetic dipole ratio, is taken to have a constant value of -0.02, for the full range of Q^2 and R_{SM}, the Coulomb quadrupole to magnetic dipole ratio, is fitted as

$$R_{SM} = 0.01(1+0.0065\,Q^4) \times (-6.066+5.807\,Q-8.5639\,Q^2+2.37058\,Q^4-0.75445\,Q^5). \tag{5.31}$$

The Aznauryan fit of the electrocouplings $A_h^{\Delta(1232)}$ are obtained by rearranging Eq. (5.25c).

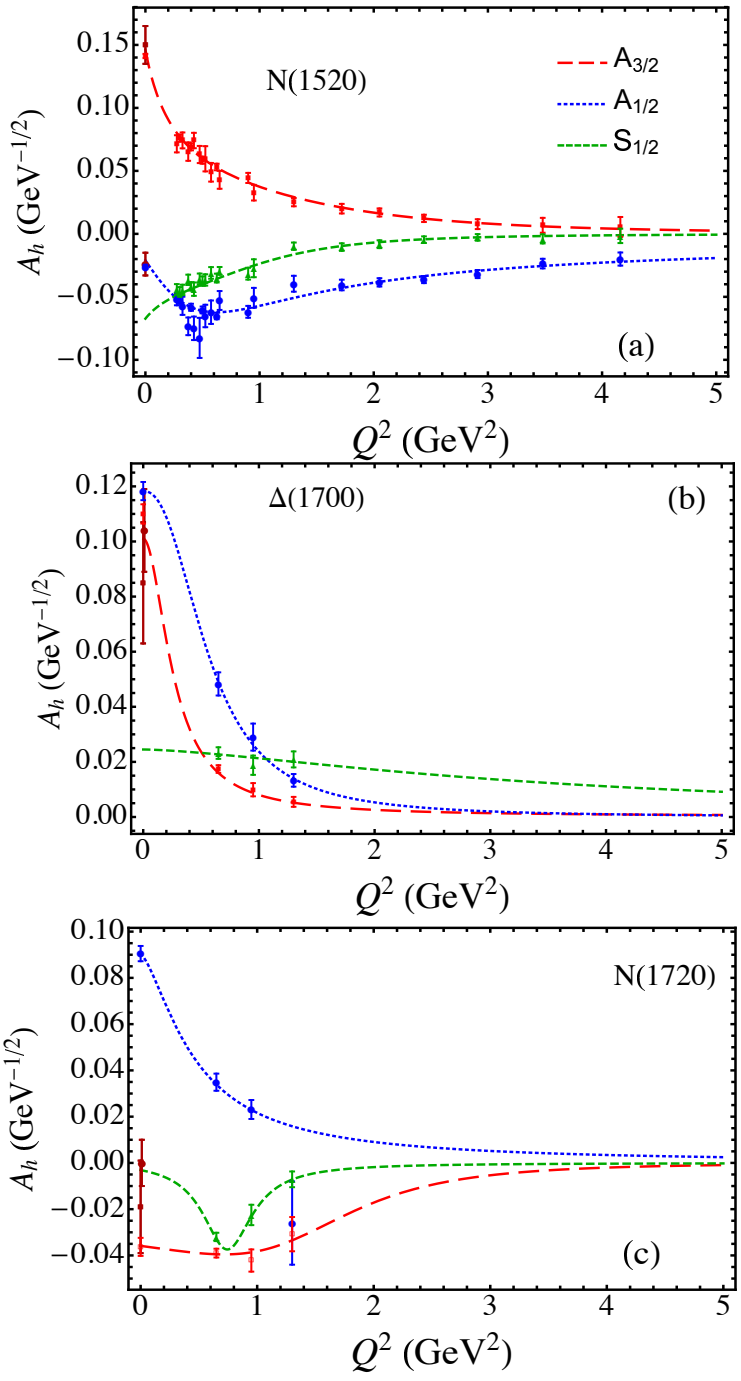

FIGURE 5.5: Phenomenological fit [125] of the transverse $A_{3/2}$ (red long-dashed) and $A_{1/2}$ (blue dotted), and the longitudinal $S_{1/2}$ (green dashed) electrocouplings for the spin-3/2 states $N(1520)3/2^-$, $\Delta(1700)3/2^-$, and $N(1720)3/2^+$. The red squared ($A_{3/2}$), blue circled ($A_{1/2}$), and green triangle ($S_{1/2}$) data are from Ref. [54]. The dark-red points for $A_{3/2}$ and $A_{1/2}$ are the PDG [125] values at $Q^2 = 0$ GeV^2.

The three amplitudes $A^R_{1/2}(Q^2)$, $A^R_{3/2}(Q^2)$, and $S^R_{1/2}(Q^2)$ for rest of the resonance states are taken from the CLAS fit [54, 125] directly. Figure 5.5 illustrates the elctrocouplings for the three 4-star and spin-3/2 resonance states of PDG18 [129] as function of Q^2. In all three diagrams of Fig. 5.5,'(a) $N(1520)3/2^-$, (b) $\Delta(1700)3/2^-$, and (c) $N(1720)3/2^+$, the solid squares (red) and circles (blue), respectively, represent the transverse $A^R_{3/2}$ and $A^R_{1/2}$ amplitudes from the CLAS analysis of $N\pi$ and $N\pi\pi$ electroproduction off proton [54], while the green solid triangles are the data for longitudinal $S_{1/2}$ amplitude from the same analysis. The dark-red solid square and circle at $Q^2 = 0$ GeV^2 are the PDG values [125] of the two transverse amplitudes for each of these spin-3/2 states. For $N(1520)3/2^-$, the explicit form of the CLAS fit of the electrocouplings is given in Eq. (5.32c) which are represented by the red long-dashed ($A^{N(1520)}_{3/2}$), blue dotted ($A^{N(1520)}_{1/2}$), and green dashed ($S^{N(1520)}_{1/2}$) lines in Fig. 5.5(a).

$$A^{N(1520)}_{1/2}(Q^2) = \frac{0.0009(-23.357 - 151.199533\,Q^2)}{1 + 2.01489898\,Q^4 - 0.2654327\,Q^4\,\sqrt{Q^2}}, \tag{5.32a}$$

$$A^{N(1520)}_{3/2}(Q^2) = \frac{0.0009\ \times 162.458285}{1 + 3.322979\,Q^2 - 2.0339966\,Q^4 + 1.622563\,Q^4\,\sqrt{Q^2}}, \tag{5.32b}$$

$$S^{N(1520)}_{1/2}(Q^2) = -\frac{0.0672}{1 + 1.73\,Q^2 - 2.8\,Q^4 + 2.91\,Q^4\,\sqrt{Q^2}}. \tag{5.32c}$$

The fit follows the PDG [125] value of the transverse amplitudes, within the uncertainty range, at $Q^2 = 0$ GeV^2, where the CLAS data and the PDG18 value themselves are also in agreement within experimental uncertainty. On the other hand, the PDG values [54] of $A^{\Delta(1700)}_{3/2}$, $A^{\Delta(1700)}_{1/2}$ (Fig. 5.5(b)), and $A^{N(1720)}_{3/2}$, $A^{N(1720)}_{1/2}$ (Fig. 5.5(c)) at $Q^2 = 0$ GeV^2 are significantly away from the CLAS analysis of $N\pi$ photo-production data [130]. The CLAS phenomenological fit of the electrocouplings of these two higher mass, spin-3/2 resonances, $\Delta(1700)3/2^-$ and $N(1720)3/2^+$, from the third resonance region of meson

electroproduction are given in Eqs. (5.33c) and (5.34c).

$$A_{1/2}^{\Delta(1700)}(Q^2) = \frac{118.28}{1000(1+0.72\,Q^4+3.26\,Q^4\,\sqrt{Q^2})}, \tag{5.33a}$$

$$A_{3/2}^{\Delta(1700)}(Q^2) = \frac{101}{1000(1+16.6\,Q^2-5.0\,Q^4\,\sqrt{Q^2})}, \tag{5.33b}$$

$$S_{1/2}^{\Delta(1700)}(Q^2) = \frac{24.5}{1000(1+0.15\,Q^2\,\sqrt{Q^2})}. \tag{5.33c}$$

$$A_{1/2}^{N(1720)}(Q^2) = \frac{90}{1000(1+3.16\,Q^2\,\sqrt{Q^2})}, \tag{5.34a}$$

$$A_{3/2}^{N(1720)}(Q^2) = \frac{-35.87-6.85\,Q^2}{(1+0.118\,Q^4)}, \tag{5.34b}$$

$$S_{1/2}^{N(1720)}(Q^2) = -\frac{3.09}{1000(1-3.7\,Q^2+2.86\,Q^2\,\sqrt{Q^2})}. \tag{5.34c}$$

It is evident from Fig. 5.5(b,c) that the CLAS phenomenological fit of Eqs. (5.33c) and (5.34c) prefers its own data at $Q^2 = 0$ GeV^2. The fitting curves well match with the $N\pi\pi$ electroproduction [125] even though the number of data are not enough and no available data in the higher range of $Q^2 \geq 1.5$ GeV^2 yet. But in that range of Q^2, the fits of Eqs. (5.33c) and (5.34c) are approximately close to the form of $\sim 1/Q^3$ or, $1/Q^5$, following quark counting rules, except $S_{1/2}^{\Delta(1700)}$.

The remaining five spin-1/2 resonances, $N(1440)1/2^+$, $N(1535)1/2^-$, $\Delta(1620)1/2^-$, $N(1650)1/2^-$, and $N(1710)1/2^+$, have only two electrocouplings $A_{1/2}$ and $S_{1/2}$. Extracted electrocouplings from the CLAS analyses of $N\pi$ and $N\pi\pi$ photo- and electroproduction are shown in Fig. 5.6. The detailed specification of the plots is same as that of Fig. 5.5. Below, I list up the CLAS fitting [125] of $A_{1/2}^R$ and $S_{1/2}^R$ for these spin-1/2 resonances. For the Roper resonance $N(1440)1/2^+$, the parametrization is

$$A_{1/2}^{N(1440)}(Q^2) = \frac{-68.7866+21.3966\,Q^2+79.8415\,\sqrt{Q^2}}{1000(1-0.7178\,Q^2+0.5663\,Q^2\,\sqrt{Q^2})}, \tag{5.35a}$$

$$S_{1/2}^{N(1440)}(Q^2) = \frac{31.19227+3.5338\,Q^2}{1000(1-0.278265\,Q^2+0.3677575\,Q^2\,\sqrt{Q^2})}. \tag{5.35b}$$

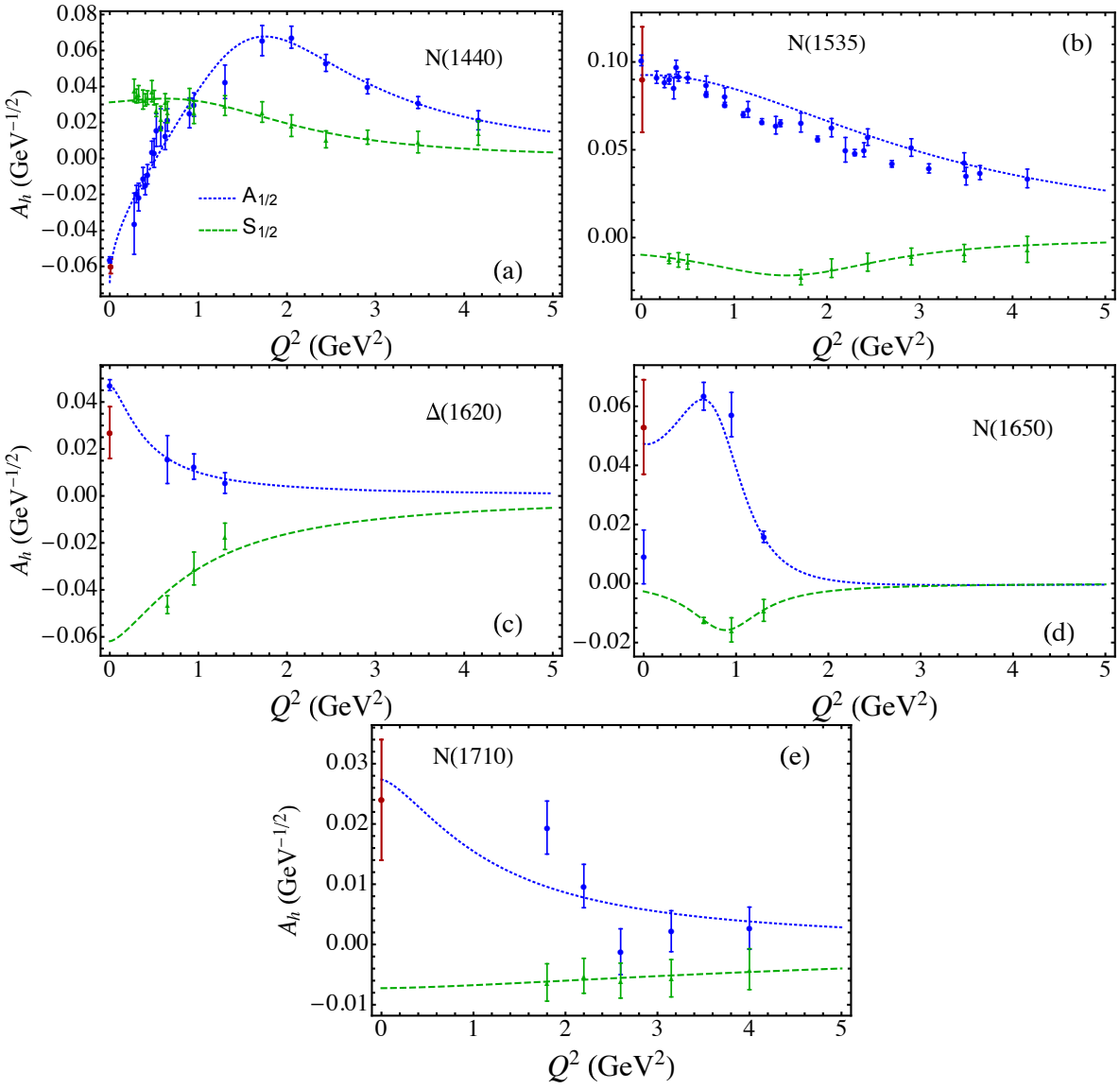

FIGURE 5.6: CLAS fit [125] of the electrocouplings $A_{1/2}$ (blue dotted) and $S_{1/2}$ (green dashed) for the spin-1/2 states $N(1440)1/2^+$, $N(1535)1/2^-$, $\Delta(1620)1/2^-$, $N(1650)1/2^-$, and $N(1710)1/2^+$. The blue circled ($A_{1/2}$) and green squared ($S_{1/2}$) data are from Ref. [54]. The dark-red circled data for $A_{1/2}$ are the PDG [125] values at $Q^2 = 0$ GeV^2.

The CLAS phenomenological fit of the electrocouplings for $N(1535)1/2^-$ is

$$A_{1/2}^{N(1535)}(Q^2) = \frac{92.5029 + 1.45023\,Q^2}{1000(1 + 0.1095\,Q^2 - 0.000322\,Q^2\sqrt{Q^2})}, \tag{5.36a}$$

$$S_{1/2}^{N(1535)}(Q^2) = \frac{-9.758811 - 4.231412\,Q^2}{1000(1 - 0.7341952\,Q^2 + 0.5087887\,Q^2\sqrt{Q^2})}. \tag{5.36b}$$

For the only isospin-3/2 and spin-1/2 state $\Delta(1620)$, the fit is given by

$$A_{1/2}^{\Delta(1620)}(Q^2) = \frac{47.2}{1000(1+3.71\,Q^2\sqrt{Q^2})}, \tag{5.37a}$$

$$S_{1/2}^{\Delta(1620)}(Q^2) = -\frac{61.864}{1000(1+Q^2\,\sqrt{Q^2})}. \tag{5.37b}$$

Note the $S_{1/2}^{\Delta(1620)}$ of Eq. (5.37b) is an arbitrary fit following the CLAS data trend and the CLAS fitting behaviour at the off-shell, spacelike photon region. The CLAS fitting for this specific electrocoupling is avoided due to existence of an unexpected singularity at $Q^2 = 0$ GeV^2. For the last two spin-1/2 resonances, $N(1650)1/2^-$ and $N(1710)1/2^+$, the electrocouplings fitting from CLAS [125] are given in Eqs. (5.38b) and (5.39b).

$$A_{1/2}^{N(1650)}(Q^2) = \frac{47.4-19.6\,Q^2}{1000(1-1.46\,Q^2\sqrt{Q^2}+1.17\,Q^6)}, \tag{5.38a}$$

$$S_{1/2}^{N(1650)}(Q^2) = -\frac{2.67}{1000(1-2.82\,Q^2+2\,Q^2\,\sqrt{Q^2})}. \tag{5.38b}$$

$$A_{1/2}^{N(1710)}(Q^2) = \frac{27.36}{1000(1+0.77\,Q^2\,\sqrt{Q^2})}, \tag{5.39a}$$

$$S_{1/2}^{N(1710)}(Q^2) = -\frac{7.25}{1000(1+0.0733\,Q^2\sqrt{Q^2})}. \tag{5.39b}$$

The values of $A_{1/2}^R$ at $Q^2 = 0$ GeV^2 from the CLAS analysis of $N\pi$ photo-production [130] and that from PDG [125] are in good agreement within the uncertainty range for $N(1440)1/2^+$ and $N(1535)$ $1/2^-$ resonances. The fit also follows the data at smaller range of Q^2, as shown in Fig. 5.6(a,b). For $\Delta(1620)1/2^-$, the PDG point of $A_{1/2}^{1620}$ is off from the value of CLAS $N\pi$ photo-production (Fig. 5.6(c)). The deviation in $A_{1/2}^R$ from the two sources is even larger for $N(1650)1/2^-$ state. Interestingly, the fit function of Eq. (5.38b) follows the PDG value at the real photon point. Whereas the $A_{1/2}^R$ fit function of Eq. (5.37b) for $\Delta(1620)1/2^-$ follows the CLAS data, as illustrated in Figs. 5.6(c, d). For these two resonances, a limited number of data are available only within the range of $Q^2 \leq 2$ GeV^2. In the higher Q^2 limit where experimental data is not available

yet the fitting curve approximately follows the $\sim 1/Q^3$ behaviour assuming the quark counting rules. A converse picture is seen in case of the resonance $N(1710)1/2^+$ for which no CLAS data available in the lower range of $Q^2 \leq 1.8$ GeV^2. At the real photon point, only the PDG value is present which is followed by the CLAS fitted curve of $A_{1/2}^{1710}$ as shown in Fig. 5.6(e). The $A_{1/2}^{1710}$ fitting also goes approximately as $\sim 1/Q^3$ in the high Q^2 limit whereas the $S_{1/2}^{1710}$ fitting is purely based on the data trend.

Overall, based on the latest experimental information, the CLAS fit for these resonance electrocouplings can be considered as a reliable input for the hadronic transition current at each of the TPE vertices for spacelike Q^2. The fittings are also extended into the timelike Q^2 region without any experimental or theoretical constrain, to carry out the analytical continuation of the integrand of Eq. (4.2) into the unphysical region.

5.4 Resonance finite widths

As the imaginary part of the TPE box diagram corresponds to real excitation, there is a discontinuity in the imaginary part of the TPE amplitudes for resonance intermediate states with zero width, at sharp $W = W_R$, such that they vanish for $E < E_{\min}(W_R)$. When put into a dispersion integral, this will translate into a cusp in the real part of the amplitude at the same energy. If the threshold energy is above the minimum energy, $E_{\rm th} \geq E_{\min}$, then this cusp is of no concern. However, if $E_{\rm th} < E_{\min}$, then there exists some physical energy E for which one may have $E = E_{\min}$. Equivalently, there is a cusp if the four-momentum transfer squared goes below a threshold value, $Q^2 < Q^2_{\rm th}$, where

$$Q^2_{\rm th} = \frac{(W^2 - M^2)^2}{W^2}. \tag{5.40}$$

In terms of the photon polarization variable ε, the cusp will occur for

$$\varepsilon_{\rm cusp}(Q^2) = \frac{2W^2\,(Q^2_{\rm th} - Q^2)}{2W^2\,(Q^2_{\rm th} - Q^2) + Q^2\,(4M^2 + Q^2)}. \tag{5.41}$$

In Table 5.2 we show the values of $Q^2_{\rm th}$ and $\varepsilon_{\rm cusp}(Q^2)$ for several physically relevant examples that illustrate the effect, specifically, for the $\Delta(1232)3/2^+$, $N(1520)3/2^-$, and $N(1720)3/2^+$ states.

TABLE 5.2: Kinematics at which threshold cusp effects appear for the $\Delta(1232)$, $N(1520)$, and $N(1720)$ resonances, at several typical Q^2 values relevant phenomenologically.

W_R (GeV)	$Q^2_{\rm th}$ (GeV^2)	$\varepsilon_{\rm cusp}(Q^2)$		
		$Q^2 = 0.2$ GeV^2	$Q^2 = 0.5$ GeV^2	$Q^2 = 1.0$ GeV^2
1.232	0.27	0.22	–	–
1.520	0.89	0.81	0.47	–
1.720	1.46	0.91	0.74	0.38

For the case of a resonance of finite width $\Gamma(W)$ that is centred at $W = W_R$ and governed by a Breit-Wigner distribution,

$$f(W^2) = \frac{1}{\pi}\frac{\Gamma(W)W_R}{(W^2 - W_R^2)^2 + \Gamma^2(W)W_R^2}, \tag{5.42}$$

the cusp behaviour is smoothed out. To consider a finite width, we assume the continuum of the invariant mass squared W^2 as an infinite set of Dirac δ functions, $\delta(W^2 - W_i^2)$, and evaluate the integral of Eq. (4.2) at a set of discrete values of W ranging from $(M + m_\pi)$ to 2 GeV for each resonance intermediate state. The corresponding real parts are calculated from Eqs. (4.4c). The set of generated real parts of the generalized TPE from factors are then interpolated using a spline fit to obtain a smooth function $F(W^2)$ for the generalized TPE form factors at fixed values of Q^2 and electron energy E. Note that the numerical errors from the fitting of the form factors F_1', F_2', and G_a' at a set of discrete W values are insignificant as the functional forms seem fairly smooth. More importantly, as will be clear from Sec. 6.2.2, the overall width effect itself doesn't bring anything dramatic in the net cross section results other than the removal of cusps in the sharp (zero width) resonance case. However, in practice, we perform the integration over W of $f(W^2)\,F(W^2)$ using

$$I_W = N\int_{(M+m_\pi)^2}^{W^2_{\rm max}} dW^2\, f(W^2)\, F(W^2), \tag{5.43}$$

where the normalization constant N ensures that the integration from $(M + m_\pi)^2$ to $W^2_{\rm max}$ is unity.

In our numerical calculations, we take $W_{\rm max} = 2$ GeV for all the resonance states except the $\Delta(1232)3/2^+$ and $N(1440)1/2^+$, for which we restrict the integration to $W_{\rm max} = 1.7$ GeV (since the contribution from the third resonance region to the total cross section for these is negligible). While the total decay widths $\Gamma(W)$ of the resonances are in general energy-dependent, for the default calculations in this work we restrict at $\Gamma(W) = \Gamma(W_R) = \Gamma_R$, the constant total decay width. The numerical values of the constant total decay width, Γ_R, and the Breit-Wigner resonance masses W_R for each of the resonance states are taken from Ref. [54]. In Sec. 6.2.2 below we will discuss the effect of the nonzero width, both constant and dynamic, on the total TPE cross section in detail.

Chapter 6

Results and Discussions

In this chapter I present the numerical results for the imaginary (Sec. 6.1.1) and real (Sec. 6.1.2) parts of the TPE generalized form factors F_1', F_2', and G_a' for excited intermediate states. Using the numerical values of the real parts of the form factors in Eq. (3.24), the obtained TPE corrections δ to the elastic scattering cross section are also discussed (Sec. 6.2.1) including a study of the effect of nonzero widths for the resonances (Sec. 6.2.2). In Sec. 6.2.3, the dependence of the TPE corrections on the spin, isospin and parity of the intermediate states is identified.

6.1 Generalized form factors

Following the discussion of Secs. 3.1.1 and 4.1.1, the TPE amplitude $M_{\gamma\gamma}$ is mapped into the generalized amplitude in terms of the generalized TPE form factors F_1', F_2', and G_a'. Thus evaluating F_1', F_2', and G_a' will provide the TPE cross section correction and other observables. In this section, I will analyze the results of these form factors starting with the imaginary parts first.

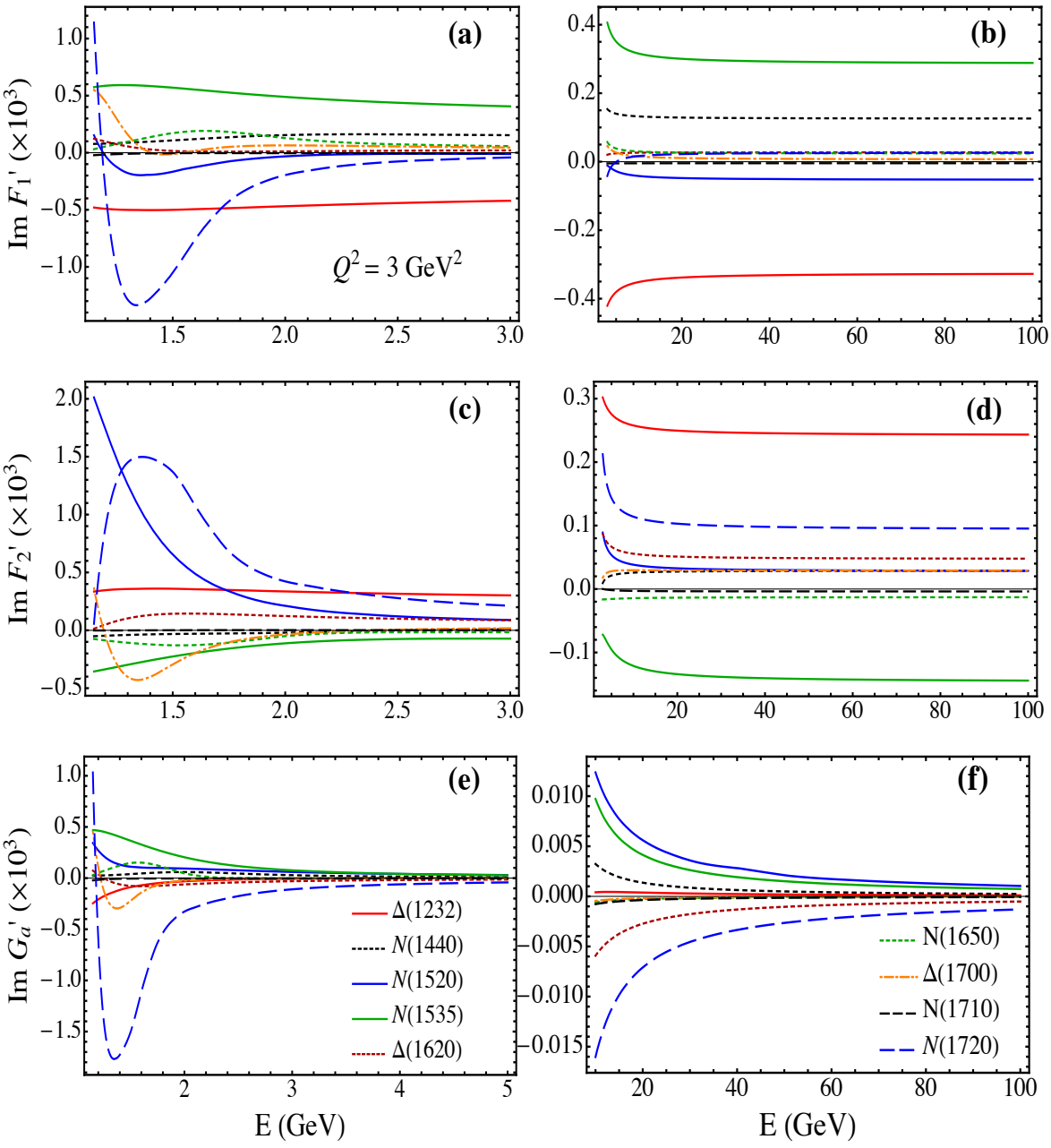

FIGURE 6.1: Imaginary parts of the generalized TPE form factors F_1' (a,b), F_2' (c,d), and G_a' (e,f) versus ε at fixed $Q^2 = 3$ GeV^2 for the nine resonance intermediate states $\Delta(1232)3/2^+$, $N(1440)1/2^+$, $N(1520)3/2^-$, $N(1535)1/2^-$, $\Delta(1620)1/2^-$, $N(1650)1/2^-$, $\Delta(1700)3/2^-$, $N(1710)1/2^+$, and $N(1720)3/2^+$ contributions. The plot legends are as identified in (e) and (f).

6.1.1 Imaginary part

For a qualitative analysis, the imaginary parts of the TPE generalized form factors for individual excited resonances $\Delta(1232)3/2^+$, $N(1440)1/2^+$, $N(1520)3/2^-$, $N(1535)1/2^-$,

$\Delta(1620)1/2^-$, $N(1650)1/2^-$, $\Delta(1700)3/2^-$, $N(1710)1/2^+$, and $N(1720)3/2^+$ at the sharp resonance point $W = W_R$, are shown in Fig. 6.1 as a function of incident electron energy E at a representative four-momentum transfer squared $Q^2 = 3$ GeV^2. The top row illustrates the correction to the imaginary part of F_1' from the mentioned individual resonances, while the middle and the bottom row represent the same for F_2' and G_a'. The left panel shows the correction down to energy $E \sim 1.15$ GeV corresponding to the minimum energy required to excite the highest mass resonance $N(1720)3/2^+$. There are some noticeable non-linearity in the low energy behaviour of all three form factors, especially for the resonances $N(1520)3/2^-$, $\Delta(1700)3/2^-$, and $N(1720)3/2^+$, as shown in the left panel of Fig. 6.1. A similar non-linearity is also observed for the lower mass resonances $\Delta(1232)3/2^+$ and $N(1440)1/2^+$ if one goes further down to the energy $E \sim 0.3$ GeV. Fig. B.1 shows such non-linearity in the imaginary part of the form factors explicitly for the most prominent resonance $\Delta(1232)3/2^+$.

Overall, the magnitude of the correction from the resonances, $N(1440)1/2^+$, $\Delta(1620)1/2^-$, $N(1650)1/2^-$, $\Delta(1700)3/2^-$, and $N(1710)1/2^+$ are tiny compared to rest of the four resonances at this specific Q^2 value, indicating a smaller correction in the real parts as well. Nevertheless, the qualitative higher energy behaviour of the imaginary parts for all the intermediate states are important to utilize the dispersion relations. It is interesting to note that the imaginary part of F_1' and F_2' both become constant at above $E \gtrsim 20$ GeV for all the resonances, whereas that for G_a' falls off as $\sim 1/E$ at higher energy for each of the excited states. Such behaviour of the form factors at high energy ensures the convergence of the dispersive integrals of Eq. (4.4c). The overall qualitative behaviour remains the same at other W values of each resonances and also at other Q^2 values. For completeness, Appendix B.2 illustrates similar behaviour at two other values of $Q^2 = 1$ and 5 GeV^2.

6.1.2 Real part

Before proceeding to the quantitative comparison of the calculated full cross sections with experimental observables sensitive to TPE effects, in this section I present the TPE

results in terms of the generalized TPE form factors introduced in Sec. 3.1.1. In Fig. 6.2 I present the ε dependence of the TPE form factors F_1', F_2', and G_a' at fixed values of $Q^2 = 1$ and 5 GeV^2, scaled by a dipole form factor G_D,

$$G_D(Q^2) = \left(\frac{\Lambda^2}{Q^2+\Lambda^2}\right)^2, \tag{6.1}$$

with mass $\Lambda = 0.84$ GeV. Illustrated are the individual contributions from the nucleon elastic intermediate state and the 3 most prominent resonance states, namely, the $\Delta(1232)3/2^+$, $N(1520)3/2^-$, and the $N(1720)3/2^+$, as well as the total of elastic nucleon and all resonances considered in this work. Rest of the states are left for Appendix B.3 since the magnitudes are tiny relative to the ones shown in Fig. 6.2.

However, clearly evident for the F_1' TPE form factor is that at $Q^2 = 1$ GeV^2 this contribution is negative at all ε values and is dominated by the nucleon elastic state. The higher-mass resonance contributions grow rapidly with increasing Q^2, but there is a strong cancellation between the (positive) $J^P = 3/2^+$ and (negative) $J^P = 3/2^-$ states, rendering the total effect to be very small and close to zero at $Q^2 = 5$ GeV^2.

For the Pauli F_2' TPE form factor, a similar pattern repeats as for the Dirac form factor, namely, at $Q^2 = 1$ GeV^2 the cancellations between the various resonance contributions leave the total TPE form factor to be negative and dominated by the nucleon elastic intermediate state. In contrast to the F_1' case, however, at larger Q^2 the main resonance contributions grow in magnitude but remain negative, so that the net effect is a coherent enhancement of the TPE form factor up to $\sim 10\%$ of the dipole at $Q^2 = 5$ GeV^2 for backward angles.

For the axial G_a' TPE form factor, the magnitude of the various resonance contributions is generally smaller than for the other two TPE form factors, with the nucleon elastic state giving negative contributions at both low and high Q^2. Once again a high degree of cancellation occurs between the (positive) $\Delta(1232)$ and $N(1520)$ states and the (negative) nucleon elastic and $N(1720)$ states, leaving an overall small positive total correction to G_a'.

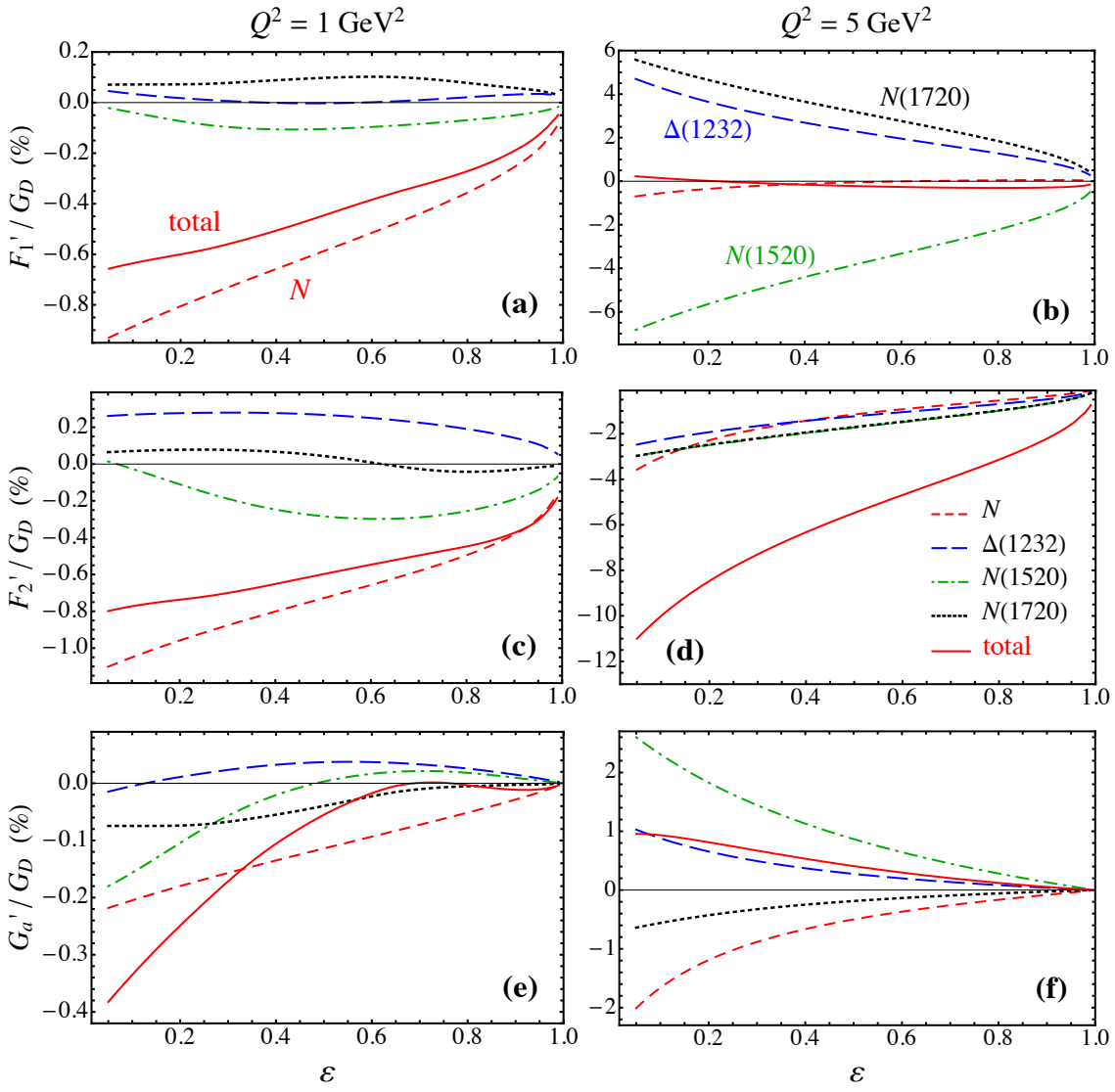

FIGURE 6.2: Generalized TPE form factors F_1' (a,b), F_2' (c,d), and G_a' (e,f), scaled by the dipole form factor G_D, versus ε at fixed $Q^2 = 1$ GeV^2 (left column) and 5 GeV^2 (right column) for the nucleon elastic (red dashed lines), $\Delta(1232)3/2^+$ (blue long-dashed lines), $N(1520)3/2^-$ (green dot-dashed lines), $N(1720)3/2^+$ (black dotted lines), and total TPE (red solid lines) contributions.

In fact, as observed by Borisyuk and Kobushkin [48], it is quite natural to combine the small G_a' contribution with the $F_1' + F_2'$ form factor combination into an effective "magnetic" TPE form factor $\mathcal{G}_M$ as in Eq. (3.23b). Observing that the TPE FFs in Fig. 6.2 do not in general show strong variation with ε, in Fig. 6.3 I display the Q^2 dependence of both the "electric" and "magnetic" TPE form factor $\mathcal{G}_E$ and $\mathcal{G}_M$, scaled by the dipole form factors, at a fixed value of $\varepsilon = 0.2$, where the TPE effects are not suppressed.

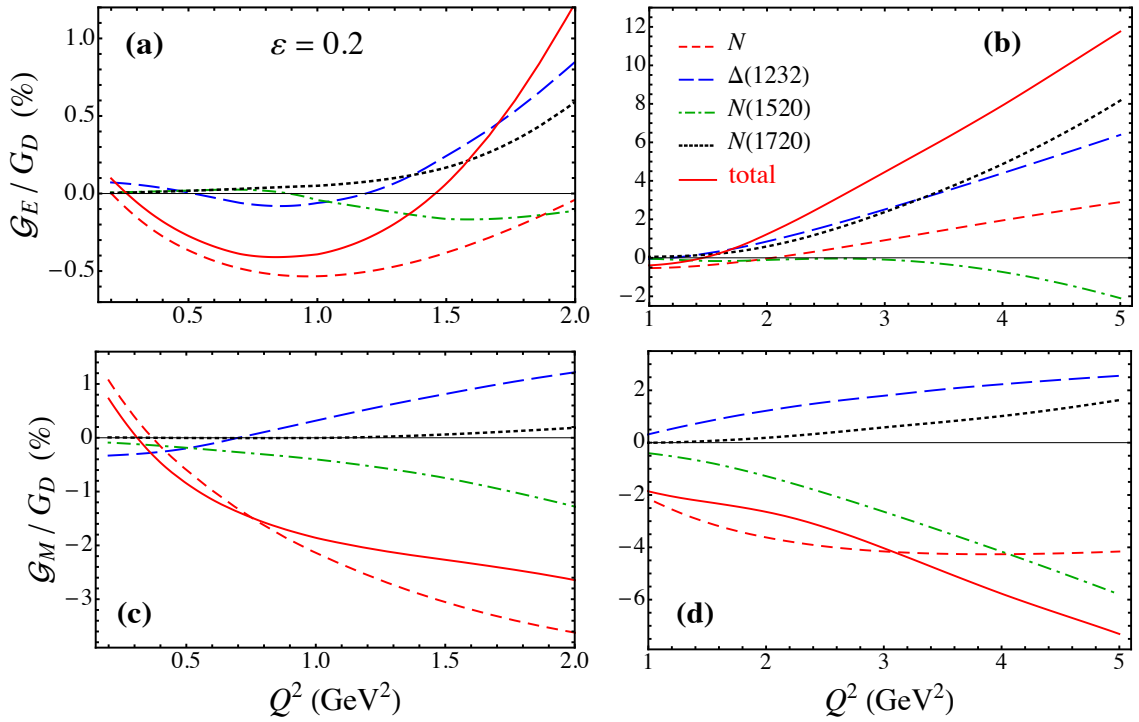

FIGURE 6.3: Generalized TPE form factors $\mathcal{G}_E$ (a,b) and $\mathcal{G}_M$ (c,d), scaled by the dipole form factor G_D, at fixed $\varepsilon = 0.2$ for low Q^2 ($Q^2 \leq 2$ GeV^2, left column) and high Q^2 ($1 \leq Q^2 \leq 5$ GeV^2, right column), for the nucleon elastic (red dashed lines), $\Delta(1232)3/2^+$ (blue long-dashed lines), $N(1520)3/2^-$ (green dot-dashed lines), $N(1720)3/2^+$ (black dotted lines), and total TPE (red solid lines) contributions.

For $Q^2 \gtrsim 2$ GeV^2 one observes that the magnitude of both the generalized electric $\mathcal{G}_E$ and magnetic $\mathcal{G}_M$ TPE form factors rises linearly with Q^2. The positive sign of $\mathcal{G}_E$ and the negative sign of $\mathcal{G}_M$ result in corrections to the effective Born level form factors that render the G_E/G_M ratio smaller than that naively extracted from cross section data without TPE corrections. This would make it more compatible with the G_E/G_M ratio extracted from the polarization transfer data, which suggest a strong fall-off of the ratio with Q^2 above $Q^2 \sim 1$ GeV^2, resolving the discrepancy with the Rosenbluth cross section results.

At low Q^2, $Q^2 \lesssim 1$ GeV^2, the TPE form factors are dominated by the nucleon elastic contribution, as already indicated in the Q^2 dependence of the total TPE correction δ in Fig. 6.7. For higher Q^2 values, $Q^2 \gtrsim 2$ GeV^2, the magnitudes of the various excited state contributions grow, with the $\Delta(1232)$ and $N(1720)$ contributions to both $\mathcal{G}_E$ and $\mathcal{G}_M$ remaining positive and the $N(1520)$ states negative.

More specifically, while the $N(1520)$ resonance state gives rather small corrections to $\mathcal{G}_E$ at most values of Q^2, its contribution to $\mathcal{G}_M$ becomes even more important than the nucleon elastic for the largest Q^2, $Q^2 \gtrsim 4$ GeV^2. Because of the τ factor in Eq. (3.24), the magnetic contribution to the total cross section dominates at high Q^2, so that the $N(1520)$ state plays the most significant role in the TPE cross section at high Q^2. At high Q^2 the negative sign of the $\mathcal{G}_M$ TPE form factor is driven by the nucleon elastic and $N(1520)$ states, while the positive sign of the $\mathcal{G}_E$ TPE form factor is due mostly to the $\Delta(1232)$ and $N(1720)$.

6.2 TPE correction to the e^--p elastic scattering cross section

The generated real parts of the form factors F_1', F_2', and G_a' for individual resonance intermediate states are plugged into Eq. (3.22) to get the corresponding cross section corrections δ. An analysis of the obtained δ (published in Ref. [73]) is presented in the following sections.

6.2.1 Resonance intermediate state contribution to TPE

Before analyzing the TPE cross section correction from all the individual resonance intermediate states let's discuss the correction from the most prominent excited state $\Delta(1232)3/2^+$. Figure 6.4 represents the TPE correction to the cross section, δ from this particular intermediate state as a function of ε at three fixed Q^2 values of (a) 1 GeV^2, (b) 3 GeV^2, and (c) 5 GeV^2.

It is evident from Fig. 6.4 that the difference between the cross section corrections from the two parametrizations of Aznauryan *et al.* [46, 53] and CLAS [54, 125] increases for lower values of Q^2. This could be anticipated from Fig. 5.4 where the difference between the two parametrizations themselves is noticeable for lower values of Q^2. However, for

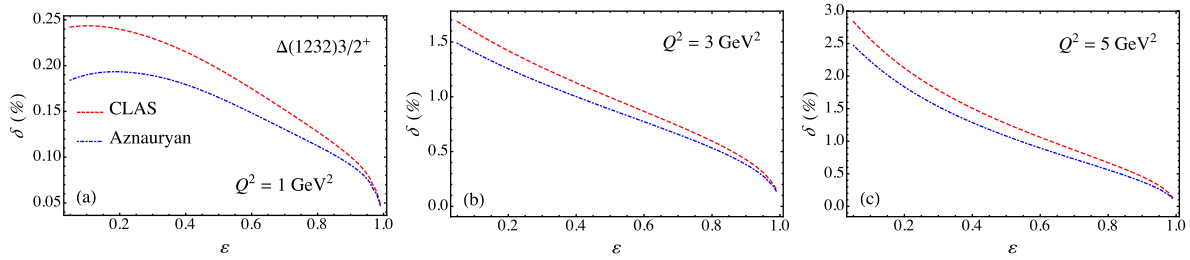

FIGURE 6.4: TPE cross section correction δ from $\Delta(1232)3/2^+$ resonance intermediate state as a function of ε at fixed values of Q^2: (a) 1 GeV^2, (b) 3 GeV^2, and (c) 5 GeV^2. The blue dot-dashed curve represents the result using Aznauryan [53] parametrization of G_M^*, G_E^*, and G_C^*, while the red dashed curve shows that using CLAS parametrization [54, 125].

$\Delta(1232)3/2^+$, the TPE cross section using Aznauryan parametrization [53] of G_M^*, G_E^*, and G_C^* is considered as the default one in rest of the thesis since this is obtained using the well established constrain of $G_M^*(0) = 3.0$.

The contributions to the TPE correction δ from the individual intermediate state resonances are shown in Fig. 6.5 versus ε, for fixed values of $Q^2 = 0.5$, 1, 2, 3 and 5 GeV^2. As mentioned earlier, we account for all 4 and 3-star spin-1/2 and spin-3/2 resonances with mass below 1.8 GeV from the Particle Data Group [129], which include the six isospin-1/2 states $N(1440)\,1/2^+$, $N(1520)\,3/2^-$, $N(1535)\,1/2^-$, $N(1650)\,1/2^-$, $N(1710)\,1/2^+$, and $N(1720)\,3/2^+$, and the three isospin-3/2 states $\Delta(1232)\,3/2^+$, $\Delta(1620)\,1/2^-$, and $\Delta(1700)\,3/2^-$. In our numerical calculations, for the resonance electrocouplings at the hadronic vertices we use the most recent helicity amplitudes extracted from the analysis of CLAS electroproduction data [54, 55], except for the $\Delta(1232)\,3/2^+$ resonance for which the alternative parametrization is discussed above. Apart from the elastic intermediate state contribution, the proton electric and magnetic form factors $G_E(Q^2)$ and $G_M(Q^2)$ are still required to be used in evaluation of δ for each resonance according to Eq. (3.22). In this case, one has the freedom to choose either of the parametrizations [72, 126, 127] since the pole issue only comes in the complex plane. However, for consistency, I use Kelly parametrization [126] of $G_{E,M}$ in Eq. (3.22) to evaluate the resonance contributions in δ.

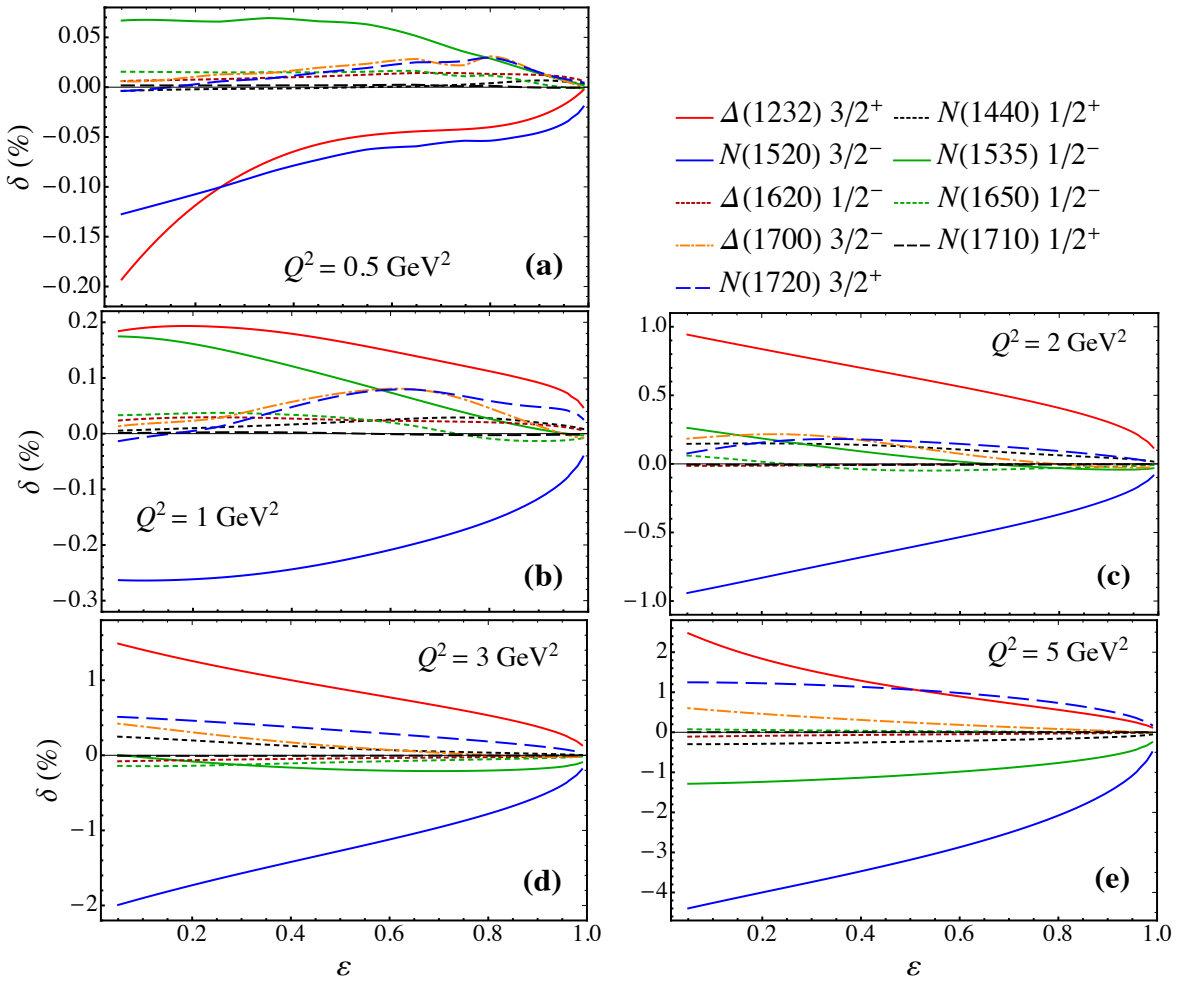

FIGURE 6.5: Relative contributions δ (in percent) to the TPE cross section for the nine spin-1/2 and spin-3/2 nucleon and Δ intermediate state resonances, as indicated in the legend, versus the virtual photon polarization ε for fixed Q^2 values: (a) 0.5 GeV^2, (b) 1 GeV^2, (c) 2 GeV^2, (d) 3 GeV^2, and (e) 5 GeV^2. Note the vertical scale is different in each panel.

In the low-Q^2 region, for Q^2 up to ~ 1 GeV^2, the $N(1520)3/2^-$ and $N(1535)1/2^-$ resonances give the most significant contributions, aside from the $\Delta(1232)3/2^+$ resonance, although the largest correction from the $\Delta(1232)3/2^+$ ranges within only 0.2% of the Born level cross section. We find an almost complete cancellation of the $N(1520)3/2^-$ state contribution by that from the sum of other higher-mass resonances, leaving a net correction that is well approximated by that from the $\Delta(1232)3/2^+$ alone. In this Q^2 range the $\Delta(1232)3/2^+$ contribution flips in sign and suppresses the elastic nucleon

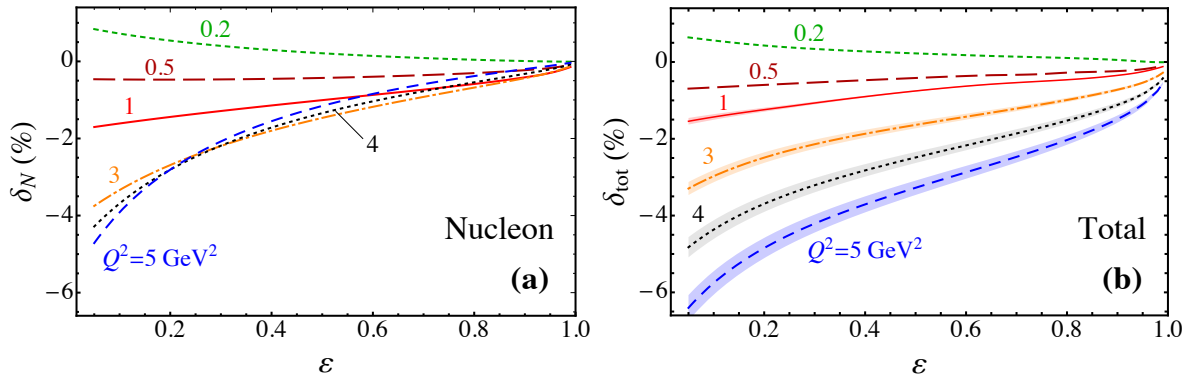

FIGURE 6.6: Contributions to the TPE correction δ (in %) versus the virtual photon polarization ε for (a) nucleon only, and (b) all spin-parity $1/2^{\pm}$ and $3/2^{\pm}$ states including the nucleon, at $Q^2 = 0.2$ GeV^2 (green dashed line), 0.5 GeV^2 (dark red long-dashed), 1 GeV^2 (red solid), 3 GeV^2 (orange dot-dashed),4 GeV^2 (black dotted), and 5 GeV^2 (blue dashed). The shaded bands in (b) correspond to the uncertainty propagated from the input electrocouplings.

intermediate state correction. At higher Q^2 values, $Q^2 \gtrsim 2$ GeV^2, the $N(1520)3/2^-$ overtakes the $\Delta(1232)3/2^+$ contribution to δ, but with opposite sign. Moreover, in the high-Q^2 region the $N(1535)1/2^-$ contribution flips sign from positive to negative, however, this effect is somewhat negated by the growth of the $N(1720)3/2^+$ and $\Delta(1700)3/2^-$ corrections. The overall effect is that the suppression of the TPE cross section (relative to the nucleon elastic contribution) by the $\Delta(1232)3/2^+$ is largely nullified by the $N(1520)3/2^-$, leaving a small increase in the total TPE correction over that from the nucleon intermediate state alone.

The combined effect on the TPE correction δ from all the spin-parity $1/2^{\pm}$ and $3/2^{\pm}$ resonances is illustrated in Fig. 6.6 as a function of virtual photon polarization, ε, for a range of fixed Q^2 values between 0.2 and 5 GeV^2. For contrast, the contribution from the nucleon elastic intermediate state alone is also shown at the same kinematics. At low Q^2 the excited state resonance contributions are found to be negligible, and the total correction is dominated by the nucleon elastic intermediate state. Note that the elastic contribution is positive at the lowest Q^2, $Q^2 = 0.2$ GeV^2, but rapidly changes sign and becomes increasingly more negative at higher Q^2. At $Q^2 = 5$ GeV^2 the nucleon contribution becomes as large as $4\% - 5\%$ at low values of $\varepsilon \approx 0.1 - 0.2$. There is also a trend toward increasing nonlinearity at higher Q^2 values, $Q^2 \gtrsim 3$ GeV^2, especially at

low ε.

The net effect of the higher mass resonances is to increase the magnitude of the TPE correction at $Q^2 \gtrsim 3$ GeV^2, due primarily to the growth of the (negative) odd-parity $N(1520)3/2^-$ and $N(1535)1/2^-$ resonances which overcompensates the (positive) contributions from the $\Delta(1232)3/2^+$. At the highest $Q^2 = 5$ GeV^2 value shown in Fig. 6.6, the total TPE correction $\delta_{\rm tot}$ reaches $\approx 6\% - 7\%$ at low ε. Note that the results shown in Fig. 6.6 follows Maximon and Tjon prescription [76] to control the IR divergence at the soft photon limit. For completeness, the TPE correction δ using the two different treatments of Maximon-Tjon [76] and Mo-Tsai [75] is contrasted in Appendix C.

An estimate of the theoretical uncertainties on the TPE contributions can be made by propagating the uncertainties on the fitted values of the transition electrocouplings [54], which are dominated by the $\Delta(1232)3/2^+$ and $N(1520)3/2^-$ intermediate states. At low Q^2, $Q^2 \lesssim 0.5$ GeV^2, the uncertainties are insignificant, but become more visible at higher Q^2 values, as illustrated by the shaded bands in Fig. 6.6(b) for $Q^2 = 1$ to 5 GeV^2. Uncertainties in the proton form factors G_E and G_M have a negligible effect on the largest contribution, δ_N, for two reasons: first, at large Q^2 the well-known magnetic coupling dominates; and second, the correlated uncertainties tend to cancel in the ratio of two-photon to one-photon exchange. For the $\Delta(1232)3/2^+$, the well-known magnetic transition amplitude also dominates.

To provide a more graphic illustration of the Q^2 dependence of the intermediate state resonance contributions to the cross section, I show in Fig. 6.7 the TPE corrections from the major individual contributors for Q^2 up to 5 GeV^2. A nominal value for the virtual photon polarization of $\varepsilon = 0.2$ is chosen in order to emphasize the largest effect on δ at backward angles. One of the prominent effects is the cancellation of part of the nucleon elastic contribution by the $\Delta(1232)3/2^+$ resonance across the entire Q^2 range. On the other hand, the sum of the higher-mass resonances has a mixed impact on δ. In the low-Q^2 region, $Q^2 \lesssim 1.8$ GeV^2, the higher resonance state corrections largely cancel, leaving an approximately zero net contribution. As Q^2 increases, the role of the $\Delta(1232)3/2^+$ is partially nullified by contributions from the higher mass resonances, and eventually

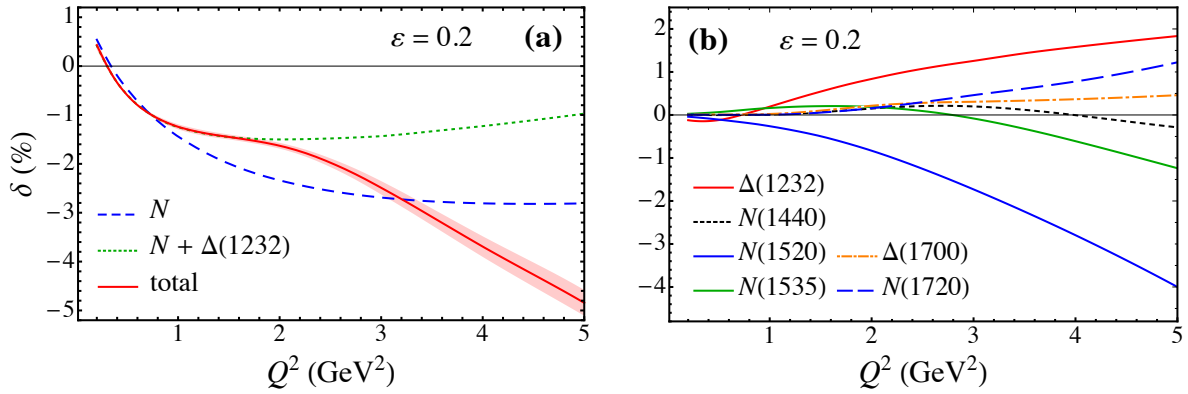

FIGURE 6.7: Contributions to the TPE correction δ (in %) versus Q^2 at backward scattering angles, $\varepsilon = 0.2$, for (a) nucleon only (blue dashed line), $N + \Delta(1232)$ (green dotted) and the sum of all resonances (red solid line, with uncertainty band), and (b) the major individual contributors at the same kinematics, including the $\Delta(1232)$ (red solid), $N(1440)$ (black dashed), $N(1520)$ (blue solid), $N(1535)$ (green solid), $\Delta(1700)$ (orange dot-dashed), and $N(1720)$ (blue dashed).

is outweighed by the heavier states. An overall increase in the total TPE cross section over that from the nucleon alone is thus observed for $Q^2 \gtrsim 3$ GeV^2.

In the low-Q^2 range, the odd parity $N(1520)3/2^-$ resonance state gives a comparable cross section to that from the $\Delta(1232)3/2^+$ state, but with opposite sign. The TPE correction from the $N(1520)3/2^-$ state keeps rising with Q^2 and becomes the largest contributor at $Q^2 \gtrsim 4$ GeV^2, outweighing even the elastic nucleon component. The other resonances largely cancel each other, leaving behind a negligible net contribution.

An earlier calculation of resonance TPE contributions by Kondratyuk and Blunden [41] correctly identified the $\Delta(1232)3/2^+$ and $N(1520)3/2^-$ resonances as the most important contributors, after the nucleon. At $Q^2 = 4$ GeV^2, for small values of ε, that analysis found $\delta_N \approx -4.7\%$, $\delta_{\Delta(1232)} \approx +1.9\%$, and $\delta_{N(1520)} \approx -0.7\%$. The nucleon and $\Delta(1232)$ corrections are in excellent agreement with the results in Fig. 6.7. Our $N(1520)$ correction of is larger in magnitude due to an improved parametrization of the electrocoupling from the recent CLAS data [54], whereas Ref. [41] used a cruder estimate based on a dressed K-matrix model.

As noted previously, for the default numerical calculations presented here the resonance width has been taken to be the constant total decay width, Γ_R, for each resonance R.

To explore the sensitivity of the TPE corrections to the assumptions about the width, in the next section I show other cases, including the zero-width approximation and an energy-dependent dynamical-width.

6.2.2 Nonzero resonance widths

As discussed in Sec. 5.4, the discontinuity in the imaginary part of the TPE amplitude for the case of zero-width resonances gives rise to cusps in the real part of the amplitude from physical threshold effects at specific kinematics. In this section I represent the threshold effect on the TPE correction for the three representative resonance states $\Delta(1232)3/2^+$, $N(1520)3/2^-$ and $N(1720)3/2^+$ discussed in Table 5.2.

The interplay between the resonance mass and the Q^2 and ε values at which the threshold effect appears is illustrated in Fig. 6.8, where the TPE correction δ is shown as a function of ε at several fixed values of Q^2. One observes that the higher the resonance mass, the higher the Q^2 value at which the cusp comes in. For the lowest-mass $\Delta(1232)$ excitation, the cusp at the lowest $Q^2 = 0.2$ GeV^2 value occurs at $\varepsilon \approx 0.06$, as indicated by the wiggle in Fig. 6.8(a). The effect of the constant, nonzero width, with a Breit-Wigner distribution centred at the resonance mass, is to smooth out the wiggles in the calculated δ, although the effect overall is not dramatic here. At higher Q^2, above the kinematic threshold, both curves are smooth, and the finite width has little impact on the TPE correction [Fig. 6.8(b) and (c)].

For the intermediate-mass $N(1520)3/2^-$ resonance, the effect of the kinematical threshold is more dramatic, with a prominent cusp visible for the zero-width result at $\varepsilon \approx 0.8$ for $Q^2 = 0.2$ GeV^2 [Fig. 6.8(d)], and a smaller cusp at $\varepsilon \approx 0.5$ for $Q^2 = 0.5$ GeV^2 [Fig. 6.8(e)]. In both cases the finite width of the resonance washes out the cusps, leaving a smooth function across the threshold. Above the threshold the contribution to δ is smooth [Fig. 6.8(f)], and the finite width has little impact. The most dramatic effect is seen for the heaviest $N(1720)3/2^+$ resonance, where the kinematic threshold produces strong cusps at $\varepsilon \approx 0.9$ for $Q^2 = 0.2$ GeV^2 [Fig. 6.8(g)] and $\varepsilon \approx 0.4$ for $Q^2 = 1$ GeV^2

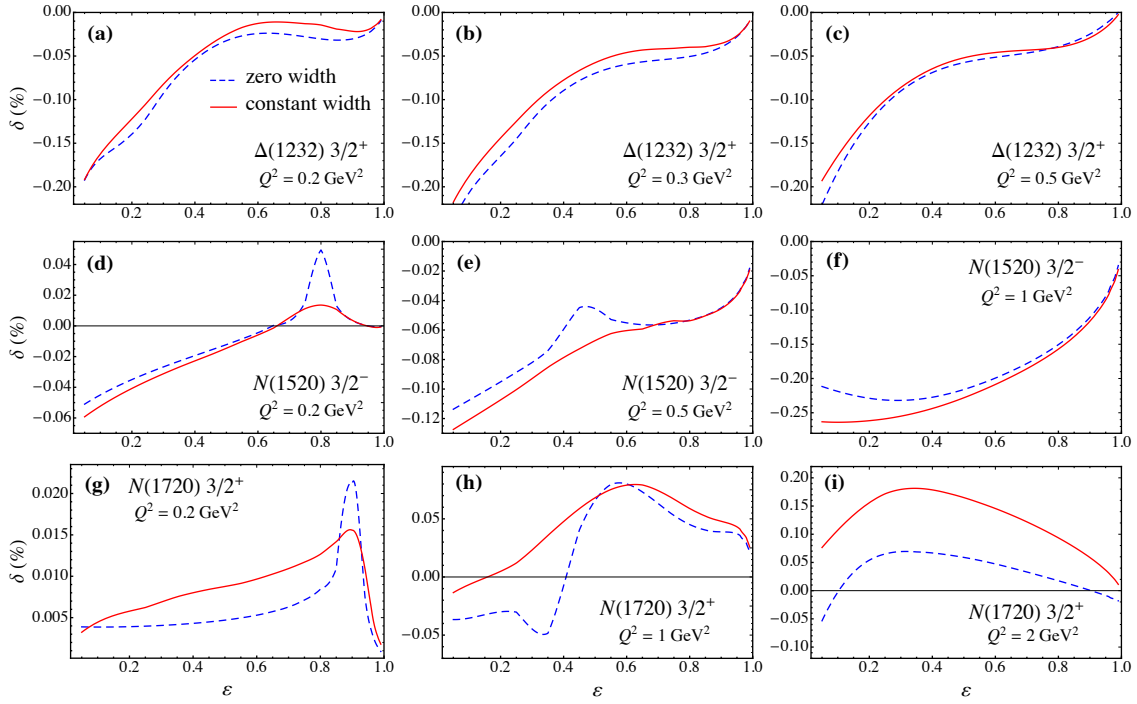

FIGURE 6.8: Effect of a finite resonance width on the TPE correction δ (in %) from three significant resonance intermediate states, $\Delta(1232)3/2^+$ (a–c), $N(1520)3/2^-$ (d–f), and $N(1720)3/2^+$ (g–i), as a function of ε at fixed Q^2 values. The kinematical kinks in the zero-width results (blue dashed lines) are smoothed out by the effect of the nonzero, constant width (red solid lines).

[Fig. 6.8(h)]. Once again the finite, constant width modulates the cusps and leads to considerably smoother results. At $Q^2 = 2$ GeV^2, above the kinematic threshold for this state, both the zero-width and finite-width results produce smooth curves, but the effect of the latter is still numerically significant [Fig. 6.8(i)].

To test the model dependence of the TPE correction on the resonance width prescription, we also consider the effect of including an energy-dependent dynamic decay width, $\Gamma(W)$, of Eq. (5.42) for each resonant intermediate state. We consider the energy-dependant $\Gamma(W)$ to have contributions from three different decay channels for each resonances, namely, πN, $\pi\pi N$, and ηN,

$$\Gamma(W) = \Gamma_{\pi N}(W) + \Gamma_{\pi\pi N}(W) + \Gamma_{\eta N}(W). \tag{6.2}$$

Following Ref. [54], the partial decay widths $\Gamma_{\pi(\eta)N}(W)$ and $\Gamma_{\pi\pi N}(W)$ are parametrized as

$$\Gamma_{\pi(\eta)N}(W) = \Gamma_R \beta_{\pi(\eta)N} \left(\frac{p_{\pi(\eta)}(W)}{p_{\pi(\eta)}(W_R)} \right)^{2L_R+1} \left(\frac{X^2 + p^2_{\pi(\eta)}(W_R)}{X^2 + p^2_{\pi(\eta)}(W)} \right)^{L_R}, \quad (6.3a)$$

$$\Gamma_{\pi\pi N}(W) = \Gamma_R \beta_{\pi\pi N} \left(\frac{p_{\pi\pi}(W)}{p_{\pi\pi}(W_R)} \right)^{2L_R+4} \left(\frac{X^2 + p^2_{\pi\pi}(W_R)}{X^2 + p^2_{\pi\pi}(W)} \right)^{L_R+2}, \quad (6.3b)$$

where the constant total decay width Γ_R of each resonance state is taken from Ref. [54], and we have assumed the centrifugal barrier penetration factors to be the major contributors to the off-shell behaviour of the resonances. Here the energy and momentum factors for the two-body channels are given by

$$p_{\pi(\eta)}(W) = \sqrt{E^2_{\pi(\eta)}(W) - m^2_{\pi(\eta)}}, \quad (6.4a)$$

$$E_{\pi(\eta)}(W) = \frac{W^2 + m^2_{\pi(\eta)} - M^2}{2W}, \quad (6.4b)$$

and for the three-body channel is given by

$$p_{\pi\pi}(W) = \sqrt{E^2_{\pi\pi}(W) - 4m^2_{\pi}}, \quad (6.5a)$$

$$E_{\pi\pi}(W) = \frac{W^2 + 4m^2_{\pi} - M^2}{2W}, \quad (6.5b)$$

where $m_{\pi(\eta)}$ is the mass of pion (η meson). The branching fractions for the resonance decays into the πN, $\pi\pi N$ and ηN channels are given by $\beta_{\pi N}$, $\beta_{\pi\pi N}$, and $\beta_{\eta N}$, respectively, and satisfy the relation $\beta_{\pi N} + \beta_{\pi\pi N} + \beta_{\eta N} = 1$. The values of the other parameters in Eqs. (6.3) — X, L_R, $\beta_{\pi N}$, $\beta_{\pi\pi N}$, and $\beta_{\eta N}$ — are taken from Ref. [54].

To illustrate the effect of the dynamical width, we select the two major resonance contributors to the total cross section, namely, the $\Delta(1232)3/2^+$ and $N(1520)3/2^-$ states. In Fig. 6.9(a-d) I compare the TPE correction δ using the dynamic, energy-dependent width with the results of the zero-width and constant-width calculations at fixed $Q^2 = 1$ and 3 GeV^2. At the higher $Q^2 = 3$ GeV^2 value, well above the kinematic thresholds, the dependence on the prescription for the width is negligibly small, with the dynamic-

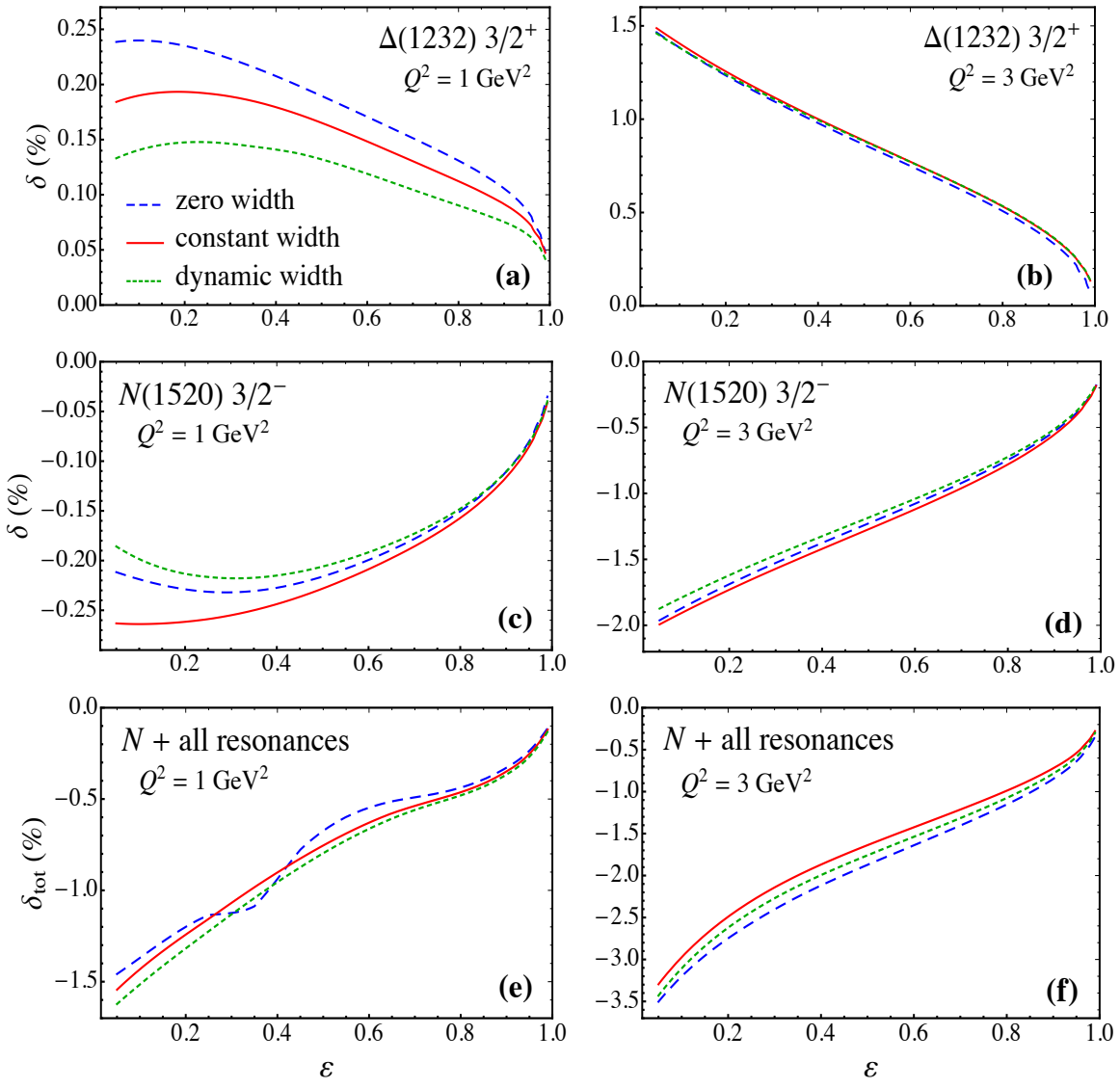

FIGURE 6.9: Comparison of the TPE correction δ (in %) computed for resonances with zero width (blue dashed lines), constant width (red solid lines) and a dynamical width (green dotted lines) for $Q^2 = 1$ GeV^2 (left panels) and 3 GeV^2 (right panels). Contributions from the $\Delta(1232)3/2^+$ (a–b) and $N(1520)3/2^-$ (c–d) states are shown separately, along with the sum of all resonance contributions (e–f).

and constant-width results very similar to those for the zero-width case. On the other hand, at $Q^2 = 1$ GeV^2 the details of the treatment of the widths are more important. In particular, for the $\Delta(1232)3/2^+$ the dynamical width leads to an $\approx 30\%$ reduction of the (positive) correction relative to the zero-width case across all ε, and a smaller but non-negligible increase in the (negative) $N(1520)3/2^-$ contribution at backward angles.

For the higher-mass resonances, the contributions again enter with oscillating signs,

producing a net effect of the width in the total TPE cross section ratio $\delta_{\rm tot}$, including nucleon elastic and all excited resonance states, that is very small across all ε values for both $Q^2 = 1$ and 3 GeV^2 [Fig. 6.9(e-f)] for all three width prescriptions. The kink in the zero-width result at $\varepsilon \approx 0.4$ for $Q^2 = 1$ GeV^2 arises from threshold effects in the third resonance region (see Table 5.2 and Fig. 6.8(h)). As for the $\Delta(1232)$ and $N(1520)$, the kink is eliminated by the tail effects of the resonances for either the constant-width or dynamical-width approximation, producing a smooth, monotonic result. At the higher $Q^2 = 3$ GeV^2 value the effects of the finite widths are negligible. Since the differences between the constant- and dynamical-width results are generally not large, for computational simplicity we employ the constant decay width approximation as the default throughout this work.

6.2.3 Spin, isospin and parity dependence

To further investigate the systematics of the TPE corrections from various intermediate states resonances, I compare the relative contributions from resonances with similar spin J, isospin I, and parity P. In Fig. 6.10 I show the combined effects of the different groupings versus Q^2 for two representative values of ε, where the TPE effects are relatively large (backward angles, $\varepsilon = 0.2$) and where they are relatively small (forward angles, $\varepsilon = 0.9$). To contrast the impact of the excited states, I show the resonance contributions separately from the nucleon elastic channel and the total (both of which are the same in the left and right columns).

For the resonance contributions with different spin, Fig. 6.10(a,b) shows qualitatively similar effects from excited states with spin $J = 1/2$ and those with spin $J = 3/2$. The sum of the resonances in both channels is significantly smaller than the nucleon elastic at low values of Q^2, and only starts to become non-negligible for larger Q^2, $Q^2 \gtrsim (3-4)$ GeV^2, with the relative impact somewhat greater at high ε than at low ε. The total TPE correction δ is therefore well approximated by the elastic term alone for $Q^2 \lesssim 3$ GeV^2 at $\varepsilon = 0.2$, and $Q^2 \lesssim 2$ GeV^2 at $\varepsilon = 0.9$.

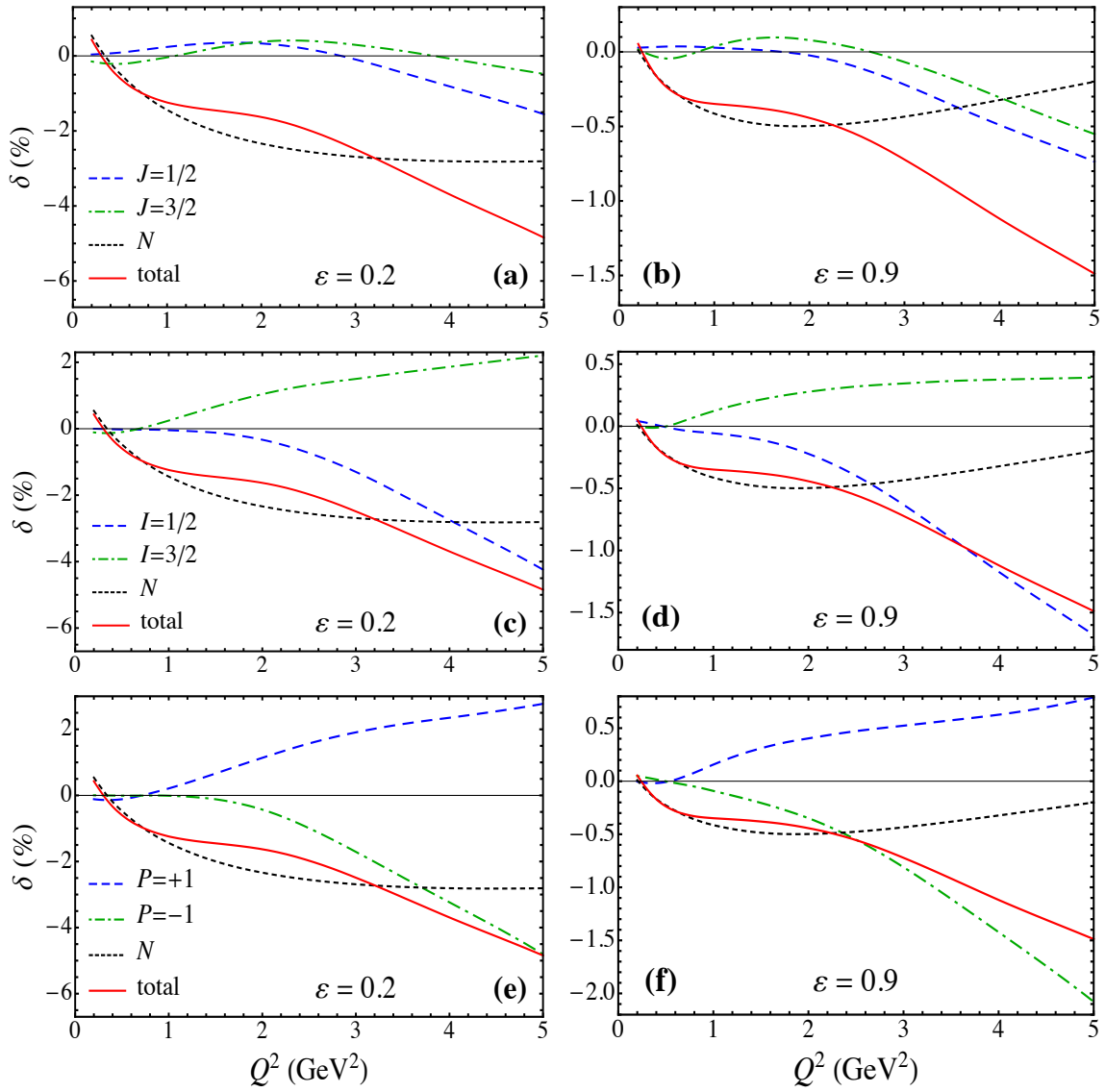

FIGURE 6.10: Comparison between the contributions to the TPE correction δ (in %) from intermediate state resonances with spin $J = 1/2$ and $J = 3/2$ (a–b), isospin $I = 1/2$ and $I = 3/2$ (c–d), and even parity $P = +1$ and odd parity $P = -1$ (e–f), for $\varepsilon = 0.2$ (left columns) and $\varepsilon = 0.9$ (right columns). The nucleon-only contribution (black dotted lines), which is not included in the other curves, and the total (red solid lines) are shown for comparison in each panel.

The decomposition into contributions from different isospins in Fig. 6.10(c,d) is rather more dramatic. Large cancellations occur between the (negative) isospin $I = 1/2$ intermediate states and the (positive) $I = 3/2$ states. At lower Q^2, $Q^2 \lesssim 2$ GeV^2, the $I = 3/2$ transitions are dominant, while at larger Q^2 the $I = 1/2$ intermediate states become more important, rendering the TPE effect more negative compared with the nucleon elastic term alone and contributing to the rapid increase in magnitude of the

(negative) total TPE correction with Q^2. This qualitative behaviour is similar at low and high ε.

Interestingly, a similar cancellation is found between the parity-even ($P = +1$) and parity-odd ($P = -1$) intermediate states in Fig. 6.10(e,f). In this case the $P = +1$ contributions to δ are positive, while the $P = -1$ contributions are negative, with the latter becoming more important with increasing Q^2. The qualitative behaviour of the curves for each of the spin, isospin and parity decompositions can be understood from the results illustrated in Fig. 6.5, where numerically the largest positive contribution is seen to be from the $\Delta(1232)3/2^+$, and the negative of that from $N(1520)3/2^-$ states. The former dominates the isospin 3/2 and even-parity channels, while the latter dominates the isospin 1/2 and odd-parity channels, but since both have spin 3/2 and enter with opposite signs, their combined contributions largely cancel, leaving the spin-1/2 channel as the relatively more important one phenomenologically.

6.3 TPE-sensitive observables

Having described the features of the TPE corrections from excited intermediate states to elastic ep scattering cross sections in the previous sections, in the remainder of this chapter I will discuss the impact of these corrections on observables sensitive to the TPE effects.

In particular, I analyze the numerical effects of the calculated TPE corrections on the elastic e^+p to e^-p cross section ratio measured recently by the CLAS [116], VEPP-3 [115] and OLYMPUS [117] experiments, as well as with polarization transfer data from the GEp2γ experiment [119] in Hall C at Jefferson Lab. In addition, I investigate the effect of the resonance contributions to the TPE on the proton G_E/G_M form factor ratio discrepancy between the LT and PT data [10, 11, 37, 42].

6.3.1 e^+p to e^-p elastic scattering ratio

Perhaps the most direct consequence of TPE in lepton scattering is the deviation from unity of the ratio of e^+p to e^-p elastic scattering cross sections. As explained in Sec. 3.4, the interference of the Born amplitude and the TPE amplitude depends on the sign of the lepton charge, so that the ratio

$$R_{2\gamma} \;=\; \frac{\sigma(e^+p)}{\sigma(e^-p)} \;\approx\; 1 - 2\,\delta_{\gamma\gamma}, \tag{6.6}$$

where $\sigma(e^\pm p) \equiv d\sigma(e^\pm p \to e^\pm p)/d\Omega$, is a direct measure of the TPE correction $\delta_{\gamma\gamma}$. Early measurements of $R_{2\gamma}$ in the 1960s at SLAC [108, 109], Cornell [110], DESY [111] and Orsay [112] obtained some hints of nonzero TPE effects, however, since the data were predominantly at low Q^2 and forward angles, the deviations of $R_{2\gamma}$ from unity were small and within the experimental uncertainties. The more recent experiments at Jefferson Lab [116], Novosibirsk [115] and DESY [117] have attempted more precise determinations of $R_{2\gamma}$ over a larger range of Q^2 and ε values than previously available.

The $R_{2\gamma}$ ratio from the CLAS experiment [116] is shown in Fig. 6.11 versus Q^2 at fixed averaged ε values, $\langle\varepsilon\rangle = 0.45$ and 0.88 (Fig. 6.11(a,b)), and versus ε for fixed averaged Q^2, $\langle Q^2\rangle = 0.85$ and 1.45 GeV^2 (Fig. 6.11(c,d)). The deviations from unity of the measured ratios are relatively small, with most of the data points consistent with no TPE effects within the relatively large experimental uncertainties. (Note that in Fig. 6.11 and in subsequent data comparisons, the statistical and systematic uncertainties are shown separately as inner and outer error bars, respectively.) The data are also consistent, however, with the calculated TPE corrections, which are $\lesssim 2\%$ in the measured region, but increase at lower ε and higher Q^2. A significant contribution to the cross section ratio is observed from the nucleon elastic intermediate state, with the $\Delta(1232)3/2^+$ resonance cancelling some of the deviation from unity. The higher mass resonances have little impact in the experimentally measured regions of ε and Q^2, but their contributions become more significant at higher Q^2 in particular, $Q^2 \gtrsim 3$ GeV^2.

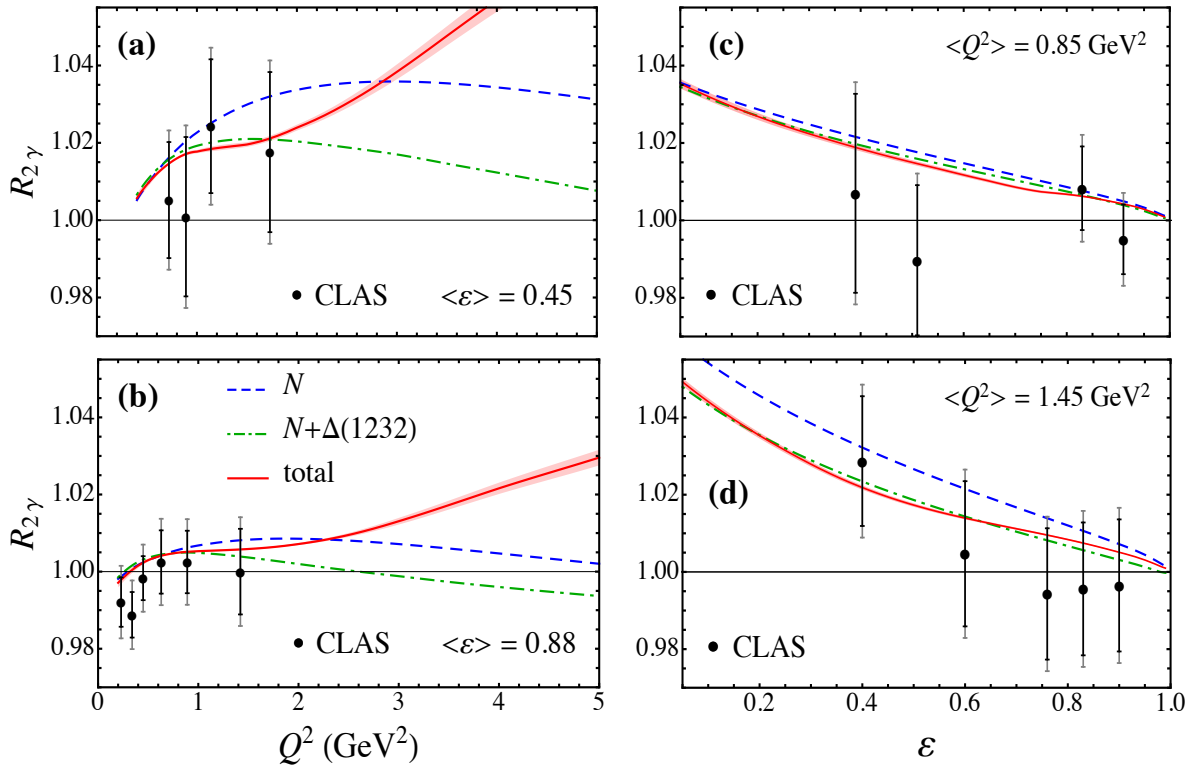

FIGURE 6.11: Ratio $R_{2\gamma}$ of e^+p to e^-p elastic cross sections from CLAS [116] (a) versus Q^2 for fixed averaged $\langle\varepsilon\rangle = 0.45$, and (b) $\langle\varepsilon\rangle = 0.88$, (c) versus ε for fixed averaged $\langle Q^2\rangle = 0.85$ GeV^2, and (d) $\langle Q^2\rangle = 1.45$ GeV^2, compared with the nucleon only (blue dashed lines), sum of nucleon and $\Delta(1232)$ (green dot-dashed lines), and sum of all intermediate state contributions (red solid lines). The experimental statistical and systematic uncertainties are indicated by the (black) inner and (grey) outer error bars, respectively.

A similar comparison of the calculated $R_{2\gamma}$ ratio with data from the VEPP-3 experiment at Novosibirsk [115] is shown in Fig. 6.12. The experiment scattered electrons at fixed beam energy $E = 0.998$ GeV (Fig. 6.12(a)), and $E = 1.594$ GeV (Fig. 6.12(b)), for ε down to ≈ 0.3. This corresponds to a Q^2 range between ≈ 0.3 GeV^2 and 1.5 GeV^2. At these Q^2 values the nucleon elastic intermediate state gives the largest contribution, with again the $\Delta(1232)$ cancelling some of the effect, and bringing the calculation with the TPE corrections in better agreement with the data. The contributions of the higher mass resonances at the kinematics of this experiment are negligible.

The most recent OLYMPUS experiment at DESY [117] measured the ratio $R_{2\gamma}$ over a range of ε from ≈ 0.46 to 0.9 at an electron energy $E \approx 2$ GeV, with Q^2 ranging up to ≈ 2 GeV^2. The results, illustrated in Fig. 6.13, indicate an enhancement of the ratio at

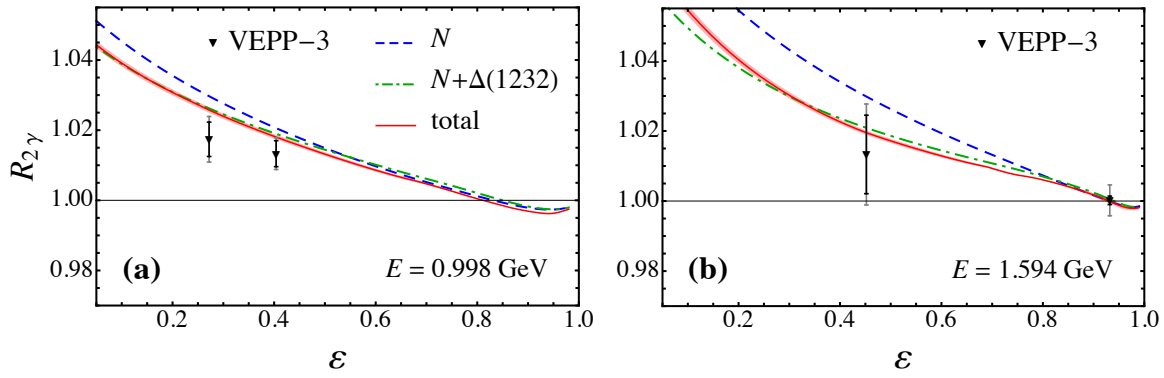

FIGURE 6.12: Ratio $R_{2\gamma}$ of e^+p to e^-p elastic cross sections versus ε from the VEPP-3 experiment [115] for beam energy (a) $E = 0.998$ GeV, and (b) $E = 1.594$ GeV, compared with the nucleon only (blue dashed lines), sum of nucleon and $\Delta(1232)$ (green dot-dashed lines), and sum of all intermediate state contributions (red solid lines). The experimental statistical and systematic uncertainties are indicated by the (black) inner and (grey) outer error bars, respectively.

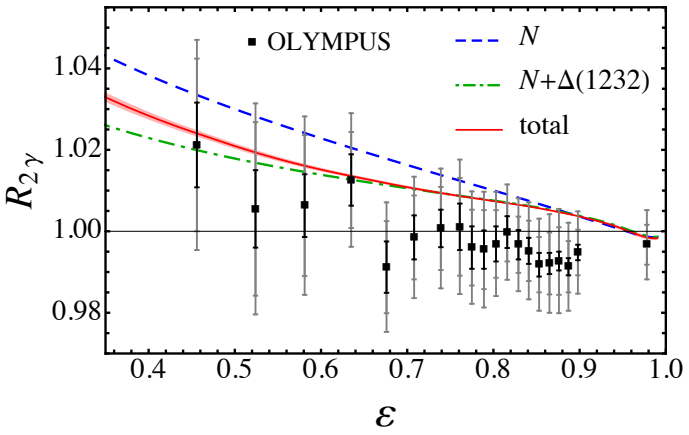

FIGURE 6.13: Ratio $R_{2\gamma}$ of e^+p to e^-p elastic cross sections versus ε from the OLYMPUS experiment [117] with beam energy $E = 2.01$ GeV, compared with the nucleon only (blue dashed lines), sum of nucleon and $\Delta(1232)$ (green dot-dashed lines), and sum of all intermediate state contributions (red solid lines). The experimental statistical and systematic uncertainties are indicated by the (black) inner and (grey) outer error bars, respectively.

$\varepsilon \lesssim 0.6$ and a dip below unity at $\varepsilon \gtrsim 0.7$, although still compatible with no deviation from 1 within the combined statistical and systematic uncertainties. The suppression of the ratio at large ε is in slight tension from other measurements, but again the effect is consistent within the errors [46]. Inclusion of the $\Delta(1232)$ intermediate state reduces the effect of the nucleon elastic contribution away from the forward scattering region, but the effect of the higher mass resonances is very small for all ε shown. The

overall agreement between the TPE calculation and the OLYMPUS data is reasonable within the experimental uncertainties, although there is no indication in our model for a decrease of the ratio below unity at large ε.

6.3.2 Polarization observables

In addition to the unpolarized e^+p to e^-p cross section ratio, other observables that are directly sensitive to the presence of effects beyond the Born approximation involve elastic scattering of longitudinally polarized electrons from unpolarized protons, with polarization transferred to the final state proton, $\vec{e}p \to e\vec{p}$. The relevant observables are the transverse and longitudinal polarizations, P_T and P_L, relative to the proton momentum in the scattering plane defined in Sec. 3.5 including the TPE effect. The ratio of the transverse to longitudinal polarizations, R_{TL} given by

$$R_{TL} = -\mu_p \sqrt{\frac{\tau(1+\varepsilon)}{2\varepsilon}} \frac{P_T}{P_L}, \tag{6.7}$$

reduces to the ratio of electric to magnetic form factors, $\mu_p G_E/G_M$, and becomes independent of ε. Since, any observed ε dependence of these polarization observables would be an indication of TPE effects an investigation of R_{TL} along with the ratio $P_L/P_L^{(0)}$ as a function of ε is represented in Fig. 6.14 at an average value of $Q^2 = 2.49$ GeV^2.

Data on the transverse and longitudinal polarizations were obtained from the GEp$_{2\gamma}$ experiment at Jefferson Lab [119], and are also shown in Fig. 6.14 for the ratio $P_L/P_L^{(0)}$ and R_{TL}. The calculated TPE effect in this model is almost negligible for the longitudinal polarization, giving very little additional ε dependence in the ratio $P_L/P_L^{(0)}$ in Fig. 6.14(a), and consistent within 1σ with the data. A larger TPE effect is found for the transverse polarization, where the nucleon alone gives a small slope in ε, with the effects of the $\Delta(1232)$ and higher mass intermediate states enhancing the TPE correction to $\approx 3\%$ effect at $\varepsilon \approx 0.2$. For the nucleon, and the sum of nucleon and $\Delta(1232)3/2^+$ intermediate states this was already concluded in the earlier analysis in Refs. [37, 46]. The data do not show any clear evidence for an ε dependence within the experimental

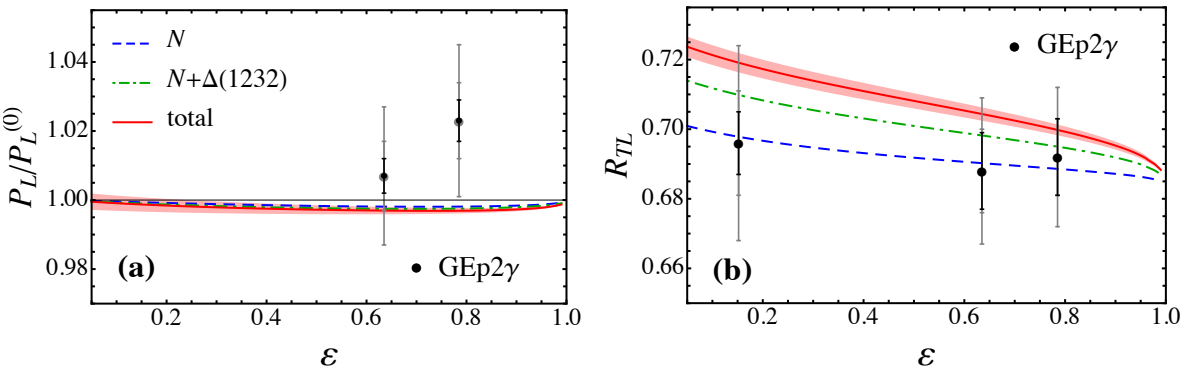

FIGURE 6.14: Effect of TPE corrections on polarization observables from the GEp2γ experiment at Jefferson Lab [119] for (a) longitudinal polarization P_L relative to the Born level result $P_L^{(0)}$, and (b) polarization transfer ratio R_{TL} at $Q^2 = 2.49$ GeV^2, compared with calculations including nucleon only (blue dashed lines), sum of nucleon and $\Delta(1232)$ (green dot-dashed lines), and sum of all intermediate state contributions (red solid lines). The experimental statistical and systematic uncertainties are indicated by the (black) inner and (grey) outer error bars, respectively.

uncertainties, although the calculated effect is also compatible with the data within 1σ errors.

6.3.3 Electric to magnetic form factor ratio $\mu_p G_E/G_M$

Perhaps the most well-known consequence of TPE that has been identified in the last two decades is the ratio of the electric to magnetic form factors extracted from elastic scattering cross sections using the LT separation method [10]. It is explained in Sec. 1.3.1 that the Longitudinal-transverse separation requires measurements of cross sections as a function of ε (or scattering angle) at fixed values of Q^2. In the Born approximation, the reduced cross section σ_R^{Born} in Eq. (1.13) is a linear function of ε, which allows the form factors G_M^2 and G_E^2 to be extracted from a linear fit to the reduced cross section data.

As observed in the preceding sections, the TPE correction induces an additional shift in the ε dependence, which alters the effective slope of the reduced cross section versus ε. Furthermore, since the ε dependence of the TPE effect is not restricted to be linear,

any nonlinearity introduced through radiative corrections could potentially complicate the form factor extraction via the LT analysis, especially at higher values of Q^2.

In Secs. 6.3.1 and 6.3.2 I compared the available data to calculations incorporating TPE effects. However, to extract G_E and G_M it is more appropriate to correct the data for TPE contributions at the same level as other radiative corrections in order to obtain the genuine Born contribution, $\sigma_{\rm R}^{\rm Born}$. The measured and Born cross sections can be related by

$$\sigma_{\rm R}^{\rm meas} \;=\; C_{\rm RC}^{\rm old}\,\left(\sigma_{\rm R}^{\rm Born}\right)^{\rm old} \;=\; C_{\rm RC}^{\rm new}\,\left(\sigma_{\rm R}^{\rm Born}\right)^{\rm new}\,, \tag{6.8}$$

where $C_{\rm RC}^{\rm old}$ is the radiative correction (RC) factor applied in the original analyses [2, 3], and $C_{\rm RC}^{new}$ incorporates any improvements, including the new TPE effects. For the RC factor $C_{\rm RC}$ we adopt the definition used by Gramolin and Nikolenko [39],

$$C_{\rm RC} \;\;=\;\; C_L \exp\left(\delta_{\rm RC} + \delta\right), \tag{6.9a}$$

where $\delta_{\rm RC}$ is given in Eq. (2.18), C_L (introduced in Sec. 2.3) is the correction factor for ionization losses in the target, and δ is the hard TPE correction ($\delta = \delta_{\gamma\gamma} - \delta_{\gamma\gamma}^{\rm IR}({\rm MTj})$) of Eq. (3.15). Although exponentiation is strictly only justified for the soft photon emission correction, it is conventionally applied to all RCs.

Gramolin and Nikolenko [39] reanalyzed the SLAC data [2, 3], which used the standard RCs of Mo and Tsai [75], to include improvements to $\delta_{\rm brems}$ as well as the use of the standard RCs of Maximon and Tjon [76]. Their Born cross section can be written in terms of that given in Refs. [2, 3] as

$$\left(\sigma_{\rm R}^{\rm Born}\right)^{\rm new} \;=\; \frac{C_{\rm RC}^{\rm old}}{C_{\rm RC}^{\rm new}}\left(\sigma_{\rm R}^{\rm Born}\right)^{\rm old}. \tag{6.10}$$

The ratio $C_{\rm RC}^{\rm old}/C_{\rm RC}^{\rm new}$ is tabulated for the SLAC data in Ref. [39], to which we add our calculated TPE contribution δ of this work. For the Super-Rosenbluth data [4] details

of the RCs that were applied are not available, so the improvements made to $\delta_{\rm RC}$ are restricted to using $\delta^{\rm IR}_{\gamma\gamma}$(MTj) instead of $\delta^{\rm IR}_{\gamma\gamma}$(MoT).

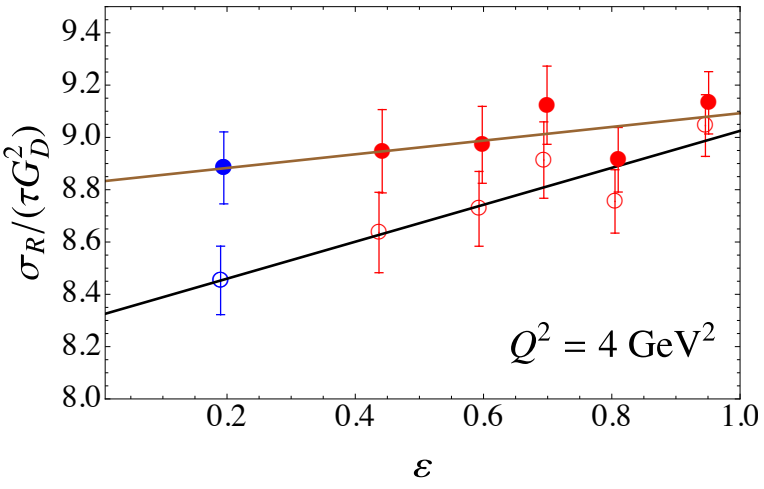

FIGURE 6.15: Reduced cross section $\sigma_{\rm R}^{\rm Born}$ at $Q^2 = 4$ GeV^2, scaled by τ times the dipole form factor squared G_D^2. Open circles are the original data points from Ref. [3]. Filled circles (slightly offset for clarity) include improved standard RCs from Ref. [39], together with the TPE corrections from the present work. The weighted least squares fits (solid lines) determine G_E^2 and G_M^2. Data points from the 8 GeV spectrometer are shown in red, while the data point from the 1.6 GeV spectrometer (which is separately normalized [3]) is shown in blue.

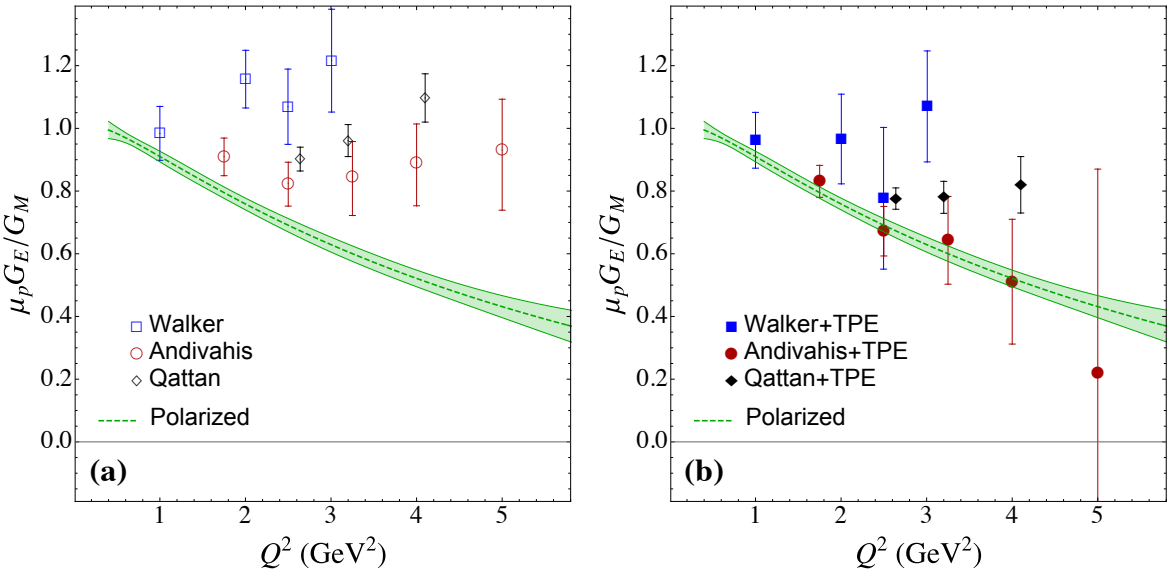

FIGURE 6.16: (a) Ratio of the proton electric to magnetic form factors, $\mu_p G_E/G_M$, versus Q^2, extracted using LT separation data [2–4]. A nonlinear fit to the combined PT results [5–9] at the 99% confidence limit is shown by the green band. (b) The ratio $\mu_p G_E/G_M$ extracted from a reanalysis of the LT data using improved standard RCs from Ref. [39], together with the TPE effects from the present work.

A comparison of the original reduced cross sections and the results with the improved RCs of Ref. [39] plus the TPE of this work is shown in Fig. 6.15 for the $Q^2 = 4$ GeV^2 data from Ref. [3]. We note that the original and the TPE-corrected data are equally well described by a linear dependence on ε, and no nonlinearity effects are apparent.

In Fig. 6.16 I show the G_E/G_M ratio extracted from this analysis for the SLAC [2, 3] and Jefferson Lab Super-Rosenbluth [4] experiments up to $Q^2 = 5$ GeV^2. To avoid clutter, the PT data from Refs. [5–9] are shown as a band, which is introduced also in Sec. 1.3.2. The original analysis, shown in Fig. 6.16(a), is consistent with $\mu_p G_E/G_M \approx 1$, while a progressively larger effect of TPE with increasing Q^2 for all LT data sets is seen in Fig. 6.16(b), with a commensurate increase in the uncertainty of G_E. In particular the LT data of Andivahis *et al.* [3] are striking in their consistency with the PT band, with a near linear falloff of G_E/G_M with Q^2. These results provide compelling evidence that there is no inconsistency between the LT and PT data once improvements in the RCs and TPE effects are made.

Chapter 7

Imaginary Part of TPE Amplitude

Having discussed the dispersive (real) part of the TPE correction in unpolarized *e-p* elastic scattering, I now switch to the absorptive (imaginary) part of this particular correction. But, this time the scattering requires either the beam or target being polarized. Polarizing the beam or target normal to the electron scattering plane gives direct access to the imaginary part of the TPE amplitude from the measured asymmetry in cross sections due to change of orientation of the polarization vector. Investigation of such asymmetry, known as single spin asymmetry (SSA), is the subject matter of this chapter. Before going into the technical details to calculate this observable quantity in Sec. 7.3, I explain the defining equation in the next section followed by a review of the estimated and measured values of this quantity in Sec. 7.2.

7.1 Single Spin Asymmetry (SSA)

The experimentally measured observable, transverse (normal) single spin asymmetry defined by

$$\mathrm{SSA} = \frac{\sigma^{\uparrow} - \sigma^{\downarrow}}{\sigma^{\uparrow} + \sigma^{\downarrow}}, \tag{7.1}$$

where $\sigma^{\uparrow}$ ($\sigma^{\downarrow}$) are the cross section of *e-p* elastic scattering with either beam or target spin polarized parallel (anti-parallel) to the normal, $\boldsymbol{S}_{\mathrm{n}}$, to the scattering plane formed

by the three-momenta of the incident and scattered particles $\boldsymbol{k}$ and $\boldsymbol{k}'$, respectively, as

$$\boldsymbol{S}_{\rm n} = \frac{\boldsymbol{k}\times\boldsymbol{k}'}{|\boldsymbol{k}\times\boldsymbol{k}'|}, \tag{7.2}$$

gets its leading term from the imaginary part of the TPE amplitude. It has been first shown by De Rujula *et al.* [131] that the time reversal invariance leaves zero contribution to SSA from the single photon exchange transition amplitude T_γ, and the leading term of beam/target normal SSA comes from the absorptive part of the TPE transition amplitude $T_{\gamma\gamma}$, in short Abs$[T_{\gamma\gamma}]$, according to the relation

$$\text{SSA} = \frac{\text{Im}\left(\sum\limits_{\text{spins}} T_\gamma^* \cdot \text{Abs}[T_{\gamma\gamma}]\right)}{\sum\limits_{\text{spins}} |T_\gamma|^2}. \tag{7.3}$$

Note there is a lot of inconsistency in the notation of this observable quantity in literature but the convention of $A_{\rm n}$ for target normal SSA and $B_{\rm n}$ for beam normal single spin asymmetry will be used in this thesis, particularly in the plots. However, the details of the calculation of $A_{\rm n}$ and $B_{\rm n}$ will be discussed in Sec. 7.3. Before discussing the technical details of the calculation, a brief review of the available data and model estimation is presented in the next section.

7.2 Review of SSA

Since the SSA (both $A_{\rm n}$ and $B_{\rm n}$) originates from the radiative correction TPE in its leading order it is expected to be of order α, the fine structure constant of QED, following Eq. (7.3). In addition to the factor α, $B_{\rm n}$ is also suppressed by the small factor $m_{\rm e}/E$, where $m_{\rm e}$ is the electron mass and E is the beam energy. As a consequence $B_{\rm n}$ is expected to be of order $10^{-6} - 10^{-5}$ for beam energies in GeV range. On the other hand, there is no additional suppression in $A_{\rm n}$, and hence it is anticipated to be of order $10^{-3} - 10^{-2}$ for the same beam energy. Alongside the importance in exploring the details of the TPE effect, $B_{\rm n}$ is particularly important in parity violating experiments

TABLE 7.1: Beam normal single spin asymmetry B_n from various experiments, along with the corresponding kinematics.

Exp. Name	E_{Lab} (GeV)	θ_{Lab} (°)	θ_{cm} (°)	Q^2 (GeV^2)	B_n (ppm)	Uncer.(ppm) Stat.	Sys.
Q_{weak} (2020) [132]	1.149	7.9	14.6	0.0248	−5.195	0.067	0.082
HAPPEX (2012) [60]	3.026	6.0	16.3	0.099	−6.800	1.540	
G0 (2011) [58]	0.362	108.0	122.7	0.220	−176.500	9.400	
	0.687		130.3	0.630	−21.000	24.000	
G0 (2007) [59]	3.031	7.5	20.2	0.150	−4.060	0.990	0.630
		9.6	25.9	0.250	−4.280	1.870	0.980
A4 (2020) [64]	0.315	34.1	43.1	0.032	−2.220	0.400	0.430
	0.420		46.1	0.057	−6.880	0.530	0.420
	0.510		47.8	0.082	−9.320	0.630	0.620
	0.855		54.6	0.218	−7.460	1.220	1.550
	1.508		64.4	0.613	−0.060	2.890	1.900
A4 (2017) [63]	0.315	145.0	152.6	0.220	−94.830	6.020	4.070
	0.420		154.2	0.350	−99.550	6.730	4.630
A4 (2005) [62]	0.855	35	56.2	0.230	−8.520	2.310	0.870
	0.569		50.4	0.106	−8.590	0.890	0.750
SAMPLE (2001)[133]	0.200	146.1	158.0	0.100	−15.400	5.400	

that use longitudinally polarized lepton beams to measure the asymmetry due to the spin flip. Usually that asymmetry is of order $\sim 10^{-6}$, while the beam normal SSA is also of the same order. In parity violating experiments, B_n is usually considered as a false asymmetry due to slow drift in rapid flip of beam polarization. As a requirement to control the possible systematic error all parity violating experiments determine the SSA as a by-product, which made B_n available at a large range of kinematics. Starting from the work of SAMPLE collaboration [133] at beam energy $E = 0.2$ GeV and averaged backward scattering angle in the laboratory frame $\theta_{Lab} = 146°$, there has been several measurements [58–64, 132] of B_n to date in a wide range of scattering angle. A summary of the findings of those experiments along with the corresponding kinematics is shown in Tab. 7.1. In a crude observation of the experimental results it is visible that B_n gets suppressed with increasing energy, even though no definite trend and interplay between energy and scattering angle can be concluded from the results displayed in the table. The backward scattering, at relatively low energies, of Refs. [58, 63] finds B_n of order

$\sim 10^{-5}$ (maximum value reaches -176.5 ppm in Ref. [58]). Whereas the recent work of A4 collaboration [64] in the near forward scattering ($\theta_{\rm Lab} \simeq 34.1^{\circ}$) obtained $B_{\rm n}$ of order 10^{-6} (-9.32 ppm at most) at the similar range of beam energies. Note that the SAMPLE [133] result at $E_{\rm Lab} = 0.2$ GeV and $\theta_{\rm Lab} = 146.1^{\circ}$ is little incompatible with the two other lower energy and backward angle measurements of Refs. [58, 63]. One possible reason, that would be clear in the subsequent chapters, might be the absence of contributions from the higher mass resonance states in the SAMPLE kinematics. The relatively higher energy ($1.15 \leq E_{\rm Lab} \leq 3.031$ GeV) experiments [59, 60, 64, 132] are in the small scattering angles (except the single data of Ref. [64]), and are consistently in the range of -6.80 to -4.06 ppm.

After the work of De Rujula *et al.* [131], the theoretical model estimations of $B_{\rm n}$ include the work in Refs. [66–69]. The hadronic approximation with a doubly virtual Compton scattering analogy of the imaginary part of the TPE correction is used in the calculation of Pasquini and Vanderhaeghen in Ref. [66, 67]. In this calculation πN intermediate state has been considered, along with the elastic nucleon, and the input were taken from the MAID electroproduction amplitudes [134]. However, the model is believed to be appropriate for the forward angle regions. The GPD approach, with a real Compton scattering analogy (RCS) suitable for forward angles as well, by Gorchtein in Ref. [68] found completely different outcomes even with an opposite sign to that obtained by Pasquini and Vanderhaeghen [66, 67]. This is not surprising since the GPD approach is found more useful in the high Q^2 region. Later on, Gorchtein also used a Quasi Real Compton Scattering (QRCS) formalism (more appropriate for backward angles) in estimation of the observable $B_{\rm n}$ (also $A_{\rm n}$). The results are still not coherent with that of Refs. [66, 67].

On the other hand, unfortunately, the target normal single spin asymmetry, $A_{\rm n}$, has no available data yet for the proton case. However, the first non-zero value of $A_{\rm n}$ has recently been measured for the neutron target, where the data was obtained from an $e-^3$He quasielastic scattering [135]. In that extraction the input of $A_{\rm n}$ for proton was

required which had been taken from the theoretical estimation of Ref. [136] that was calculated assuming only the nucleon intermediate state in the TPE box diagram.

7.3 Calculation of SSA

The one photon exchange transition amplitude T_γ can be substituted by the Born level amplitude $\mathcal{M}_\gamma$ of Eq. (1.1) and $T_{\gamma\gamma}$ by the TPE amplitude $\mathcal{M}_{\gamma\gamma}$ without loss of any factor including the total-momentum conserving delta function since SSA is a ratio of cross sections. Therefore, an equivalent form of SSA is

$$\mathrm{SSA} = \frac{\mathrm{Im}\left(\sum\limits_{\mathrm{spins}} \mathcal{M}_\gamma^* \cdot \mathrm{Abs}[\mathcal{M}_{\gamma\gamma}]\right)}{\sum\limits_{\mathrm{spins}} |\mathcal{M}_\gamma|^2}. \tag{7.4}$$

For convenience, reiterating the explicit form of the OPE amplitude $\mathcal{M}_\gamma$ here,

$$\mathcal{M}_\gamma = e^2\, \bar{u}_e(k')\, \gamma_\rho\, u_e(k)\, \frac{1}{Q^2}\, \bar{u}_N(p')\, \Gamma^\rho(q)\, u_N(p). \tag{7.5}$$

Each of the terms of Eq. (7.5) are introduced in Sec. 1.1. The complex conjugation of $\mathcal{M}_\gamma$ simply reverses the momentum of the virtual photon from $q \to -q$ in the hadronic transition current operator. Thus $\mathcal{M}_\gamma^*$ takes the form

$$\mathcal{M}_\gamma^* = e^2\, \bar{u}_e(k)\, \gamma_\rho\, u_e(k')\, \frac{1}{Q^2}\, \bar{u}_N(p)\, \Gamma^\rho(-q)\, u_N(p'). \tag{7.6}$$

The denominator of Eq. (7.4) is identical with the Born cross section for unpolarized e-p elastic scattering since the spin components (beam/target) has no impact at the Born level. The denominator of Eq. (7.4) can be written in terms of the invariant Mandelstam variable s as

$$\sum_{\mathrm{spins}} |\mathcal{M}_\gamma|^2 = \sum_{\mathrm{spins}} \mathcal{M}_\gamma^\dagger \mathcal{M}_\gamma = \frac{Q^4}{(4\pi\,\alpha)^2}\, D(s, Q^2), \tag{7.7}$$

where

$$D(s,Q^2) = 2(2M^4+Q^4-4M^2s-2Q^2s+2s^2)F_1^2(Q^2)+4Q^4F_1(Q^2)F_2(Q^2) + Q^2\left[M^4+2M^2(Q^2-s)+s(-Q^2+s)F_2^2(Q^2)\right]/M^2. \quad (7.8)$$

Note that the terms of the order of electron mass squared m_e^2 are ignored in the expression. To get the absorptive part of the TPE amplitude one can again exploit the Cutkosky cutting rules to put the intermediate lepton and hadron on-shell by the substitutions shown in Eq. (4.1b), while describing the dispersive method (Sec. 4.1). This substitution provides the discontinuity, $\mathrm{Disc}(i\mathcal{M}_{\gamma\gamma})$ (or $-2\,\mathrm{Im}\,\mathcal{M}_{\gamma\gamma}$), of the TPE box diagram of Fig. 3.1, and hence the absorptive part of TPE amplitude $-\mathrm{Abs}[\mathcal{M}_{\gamma\gamma}]$. It is important to note here that for the calculation of SSA one does not need to consider the crossed-box diagram, which is purely a real quantity. However, the absorptive part of the TPE amplitude in Eq. (7.4) can be expressed in the form

$$\mathrm{Abs}[\mathcal{M}_{\gamma\gamma}] = e^4\int\frac{d^3\boldsymbol{k}_1}{(2\pi)^3 2E_{k_1}}\frac{\bar{u}_e(k')\gamma_\mu(\not{k}_1+m_e)\gamma_\nu u_e(k)\mathcal{W}^{\mu\nu}}{(Q_1^2+\lambda^2)(Q_2^2+\lambda^2)}, \quad (7.9)$$

once the Cutkosky cutting rules are applied. Here the loop integration has been carried over the intermediate lepton four-momentum $k_1 = (E_{k_1}, \boldsymbol{k}_1)$, where E_{k_1} and $\boldsymbol{k}_1$ are the intermediate lepton energy and three-momentum, respectively. The hadronic tensor $\mathcal{W}^{\mu\nu}$ contains the information about the transition from proton to every possible intermediate states including the inelastic resonances and the elastic proton itself by the absorption of a virtual photon at the first vertex of TPE Feynman diagram of Fig. 3.1. As addressed before, SSA is calculated for each of the 4 and 3-star resonance intermediate states of PDG 2018 [129] below 1.8 GeV of invariant mass W. Then I sum up all the resonance contributions with the nucleons to get the total B_n and A_n. For elastic nucleon and inelastic spin-1/2 resonances, $\mathcal{W}^{\mu\nu}$ takes the simplified form

$$\mathcal{W}^{\mu\nu} = 2\pi\delta(W^2-W_i^2)\bar{u}_N(p')\,\Gamma^\mu_{R\to\gamma N}(p_R,-q_2)\,(\not{p}_R+W)\,\Gamma^\nu_{\gamma N\to R}(p_R,q_1)\,u_N(p), \quad (7.10)$$

where p_R is the intermediate hadron four-momentum, *i.e.* $p_R = p + q_1$. The Dirac δ function here sets the invariant mass W to a particular value W_i for individual resonance states. For elastic intermediate state, W_i^2 is substituted by M^2, the proton mass squared. On the other hand, in hadronic tensor for spin-3/2 resonances I use the Rarita-Schwinger spinors for each intermediate states. Thus the tensor becomes

$$\mathcal{W}^{\mu\nu} = -2\pi\delta(W^2 - W_i^2)\bar{u}_N(p')\,\Gamma^{\mu\alpha}_{R\to\gamma N}(p_R, -q_2)\,\mathcal{P}^{3/2}_{\alpha\beta}(p_R)\,(\not{p}_R + W)\,\Gamma^{\beta\nu}_{\gamma N\to R}(p_R, q_1)\,u_N(p), \tag{7.11}$$

where $\mathcal{P}^{3/2}_{\alpha\beta}$ is the spin-3/2 projection operator, associated with the Rarita-Schwinger spinor, defined in Eq. (3.8).

Using Eqs. (7.6), (7.7), and (7.9), one can write SSA as

$$\begin{aligned}\text{SSA} \;=\; & \frac{4\,\alpha Q^2}{8\pi^2 D(s,Q^2)} \sum_{\text{spins}} \int \frac{d^3\boldsymbol{k}_1}{2E_{k_1}} \frac{1}{(Q_1^2+\lambda^2)(Q_2^2+\lambda^2)} \\ & \times \bar{u}_e(k)\,\gamma_\rho\,u_e(k')\bar{u}_e(k')\gamma_\mu(\not{k}_1 + m_e)\gamma_\nu u_e(k)\bar{u}_N(p)\,\Gamma^\rho(-q)\,u_N(p')\mathcal{W}^{\mu\nu}.\end{aligned} \tag{7.12}$$

For the two different cases of beam and target normal SSA ($B_{\rm n}$ and $A_{\rm n}$) the spin sum will lead to two different expressions for SSA. Taking the spin sum one can express Eq. (7.13) in a concise form in terms of the leptonic and hadronic tensors $L_{\rho\mu\nu}$ and $H^{\rho\mu\nu}$, respectively, as

$$\text{SSA} = \frac{4\,\alpha Q^2}{8\pi D(s,Q^2)} \int \frac{d^3\boldsymbol{k}_1}{E_{k_1}} \frac{\text{Im}\, L_{\rho\mu\nu} H^{\rho\mu\nu}}{(Q_1^2+\lambda^2)(Q_2^2+\lambda^2)}. \tag{7.13}$$

For $B_{\rm n}$, the leptonic tensor $L_{\rho\mu\nu}$ contains the lepton polarization vector $S_n^\mu \equiv (0, \boldsymbol{S}_n)$, and takes the form

$$L_{\rho\mu\nu} = \frac{1}{2}\,\text{Tr}\left[(1+\gamma_5 \not{S}_n)(\not{k}+m_e)\gamma_\rho(\not{k}'+m_e)\gamma_\mu(\not{k}_1+m_e)\gamma_\nu\right]. \tag{7.14}$$

It is important to note that the imaginary part in Eq. (7.4) for $B_{\rm n}$ comes entirely from this spin polarization S_n^μ-dependent term. However, $H^{\rho\mu\nu}$ remains independent of the polarization of the target particle, *i.e.* remains equivalent to the case of the unpolarized e-p scattering. But it has two different expressions for spin-1/2 and -3/2 intermediate

hadrons as the Rarita-Schwinger spinors are used for the spin-3/2 states, while the usual Dirac spinors are used for spin-1/2 states. For spin-1/2 resonances, $H^{\rho\mu\nu}$ becomes

$$\begin{aligned} H^{\rho\mu\nu} &= \frac{1}{2}\,\mathrm{Tr}\left[(\not{p}+M)\Gamma_\rho(-q)(\not{p}'+M)\Gamma^\mu_{R\to\gamma N}(p_R,-q_2)(\not{p}_R+W)\right. \\ &\quad \left.\times\Gamma^\nu_{\gamma N\to R}(p_R,q_1)\right]\delta(W^2-W_i^2). \end{aligned} \tag{7.15}$$

For spin-3/2 resonances it is given by

$$\begin{aligned} H^{\rho\mu\nu} &= -\frac{1}{2}\,\mathrm{Tr}\left[(\not{p}+M)\Gamma_\rho(-q)(\not{p}'+M)\Gamma^{\mu\alpha}_{R\to\gamma N}(p_R,-q_2)\mathcal{P}^{3/2}_{\alpha\beta}(p_R)(\not{p}_R+W)\right. \\ &\quad \left.\times\,\Gamma^{\beta\nu}_{\gamma N\to R}(p_R,q_1)\right]\delta(W^2-W_i^2). \end{aligned} \tag{7.16}$$

On the other hand, for A_n, the spin sum leaves the leptonic tensor $L_{\rho\mu\nu}$ identical to that of the unpolarized e-p scattering, as the beam is unpolarized in this case. Thus, for A_n, $L_{\rho\mu\nu}$ can be written as

$$L_{\rho\mu\nu} = \frac{1}{2}\,\mathrm{Tr}\left[(\not{k}+m_e)\gamma_\rho(\not{k}'+m_e)\gamma_\mu(\not{k}_1+m_e)\gamma_\nu\right]. \tag{7.17}$$

Unlike B_n, the hadronic tensor $H^{\rho\mu\nu}$ contains the polarization vector S^μ_n in it's expression after the spin sum. For spin-1/2 resonances, $H^{\rho\mu\nu}$ becomes

$$\begin{aligned} H^{\rho\mu\nu} &= \frac{1}{2}\,\mathrm{Tr}\left[(1+\gamma_5\not{S}_n)(\not{p}+M)\Gamma_\rho(-q)(\not{p}'+M)\Gamma^\mu_{R\to\gamma N}(p_R,-q_2)(\not{p}_R+W)\right. \\ &\quad \left.\times\,\Gamma^\nu_{\gamma N\to R}(p_R,q_1)\right]\delta(W^2-W_i^2), \end{aligned} \tag{7.18}$$

whereas for spin 3/2 resonances, it is of the form

$$\begin{aligned} H^{\rho\mu\nu} &= -\frac{1}{2}\,\mathrm{Tr}\left[(1+\gamma_5\not{S}_n)(\not{p}+M)\Gamma_\rho(-q)(\not{p}'+M)\Gamma^{\mu\alpha}_{R\to\gamma N}(p_R,-q_2)\mathcal{P}^{3/2}_{\alpha\beta}(p_R)\right. \\ &\quad \left.\times\,(\not{p}_R+W)\Gamma^{\beta\nu}_{\gamma N\to R}(p_R,q_1)\right]\delta(W^2-W_i^2). \end{aligned} \tag{7.19}$$

It is convenient to transform the phase space integral, over the intermediate electron momentum $\boldsymbol{k}_1$, of Eq. (7.13) in terms of the Lorentz invariant Mandelstam variable s. Defining the kinematics in the centre-of-mass (CM) frame (see Appendix A), the

integration over $d^3\boldsymbol{k}_1 = |\boldsymbol{k}_1|^2\, d|\boldsymbol{k}_1|\, d\cos\theta_{k_1} d\phi_{k_1}$ can be written as

$$\int d^3\boldsymbol{k}_1 = -\frac{E_{k_1}^2}{2\sqrt{s}}\, 2\int_{M^2}^{s} dW^2 \int_{-1}^{1} d\cos\theta_{k_1} \int_0^{\pi} d\phi_{k_1}, \tag{7.20}$$

where the symmetry of the integral over the variable ϕ_{k_1} and the CM frame relation for the intermediate electron three-momentum $|\boldsymbol{k}_1| \simeq E_{k_1}$, with

$$E_{k_1} = \frac{s - W^2 + m_e^2}{2\sqrt{s}}, \tag{7.21}$$

from Eq. (A.3b) is utilized to get Eq. (7.20). Note that the negligibly small quantity of electron mass squared m_e^2 is not ignored in the expression of E_{k_1} on purpose that will be clarified, while discussing the Q_1^2 and Q_2^2 below. Use of Eq. (7.20) into Eq. (7.13) gives

$$\text{SSA} = -\frac{\alpha\, Q^2\, E_{k_1}}{\pi\, D(s,Q^2)\, 2\sqrt{s}} \int_{M^2}^{s} dW^2 \int_{-1}^{1} d\cos\theta_{k_1} \int_0^{\pi} d\phi_{k_1} \frac{\text{Im}\, L_{\rho\mu\nu} H^{\rho\mu\nu}}{(Q_1^2+\lambda^2)(Q_2^2+\lambda^2)}. \tag{7.22}$$

In the CM frame, Q_1^2 and Q_2^2 can be expressed as

$$Q_1^2 = 2\Big[E\, E_{k_1} - |\boldsymbol{k}| \cdot |\boldsymbol{k}_1| \cos\theta_{k_1} - m_e^2\Big], \tag{7.23a}$$

$$Q_2^2 = 2\Big[E\, E_{k_1} - |\boldsymbol{k}| \cdot |\boldsymbol{k}_1| \Big(\cos\theta \cos\theta_{k_1} + \sin\theta \sin\theta_{k_1} \cos\phi_{k_1} \Big) - m_e^2\Big], \tag{7.23b}$$

where θ is the CM frame scattering angle and the beam energy E can be expressed in CM frame in terms of the Mandelstam variable s as

$$E = \frac{s - M^2 + m_e^2}{2\sqrt{s}}, \tag{7.24}$$

the magnitudes of the incident and intermediate electron momenta are, respectively,

$$|\boldsymbol{k}| = \sqrt{E^2 - m_e^2}, \tag{7.25a}$$

$$|\boldsymbol{k}_1| = \sqrt{E_{k_1^2} - m_e^2}. \tag{7.25b}$$

It is important to note that unlike the numerical evaluation of the real part of the TPE in unpolarized e-p scattering, the small parameter of electron mass squared m_e^2 in the

expressions of Q_1^2 and Q_2^2, especially in the denominator of Eq. (7.22), is not neglected in this case. The consideration of massive lepton in the expressions of Q_1^2 and Q_2^2 is useful to avoid IR divergence of the integral of Eq. (7.22) by keeping the virtual photons away from the on-shell point, particularly for the calculation of SSA with resonance intermediate states.

Similar to the calculation of the real part of TPE, a non-zero finite resonance width with a Breit-Wigner distribution $f(W^2)$ given in Eq. (5.42) is also considered in the calculation of the imaginary part. To evaluate the W^2 integral of Eq. (7.22), the W^2 continuum is assumed as an infinite set of Dirac δ functions $\delta(W^2 - W_i^2)$ for each of the resonances. In practice, the total integral is evaluated at around 15-25 W_i points depending on the maximum range of the integration. The obtained values for the set of W_i points are interpolated using spline fit to get a functional form as $F(W^2)$. The function $F(W^2)$, weighted by the Breit-Wigner distribution $f(W^2)$, is again integrated over W^2 to get SSA for a particular resonance, with a constant total decay width, at the specific value of beam energy E and four-momentum transfer squared Q^2.

Chapter 8

SSA Results and Discussions

In this chapter I will discuss the calculated results of single spin asymmetry for both beam 8.1 and target 8.2 spin normal to the scattering plane at the kinematics of the experiments discussed in Table 7.1.

8.1 Beam normal single spin asymmetry

Using the CLAS electrocouplings (A_h) input in the hadronic transition currents for the excited resonance intermediate states with a finite constant total decay width and a Breit-Wigner distribution, the beam normal single spin asymmetry $B_{\rm n}$ is calculated numerically mostly for the beam energies corresponding to the kinematics of the performed experiments to date. To analyze the effect of each of the considered resonances in total $B_{\rm n}$, Fig. 8.1 illustrates the calculated $B_{\rm n}$ coming from the individual resonances at three different representative beam energies in the lab frame, $E_{\rm Lab} = 0.5$ (Fig. 8.1(a)), 1 (Fig. 8.1(b)), and 3 GeV (Fig. 8.1(c)), as function of the CM frame scattering angles $\theta_{\rm cm}$, ranging from $\sim 5^\circ$ to 170°. Among the resonances, the four spin-3/2 resonances $\Delta(1232)3/2^+$, $N(1520)3/2^-$, $\Delta(1700)3/2^-$, and $N(1720)3/2^+$ have sizeable effects with some partial cancellation between the contributions. Both the lower mass, spin-3/2 resonances $\Delta(1232)3/2^+$ and $N(1520)3/2^-$ have negative values of $B_{\rm n}$, while

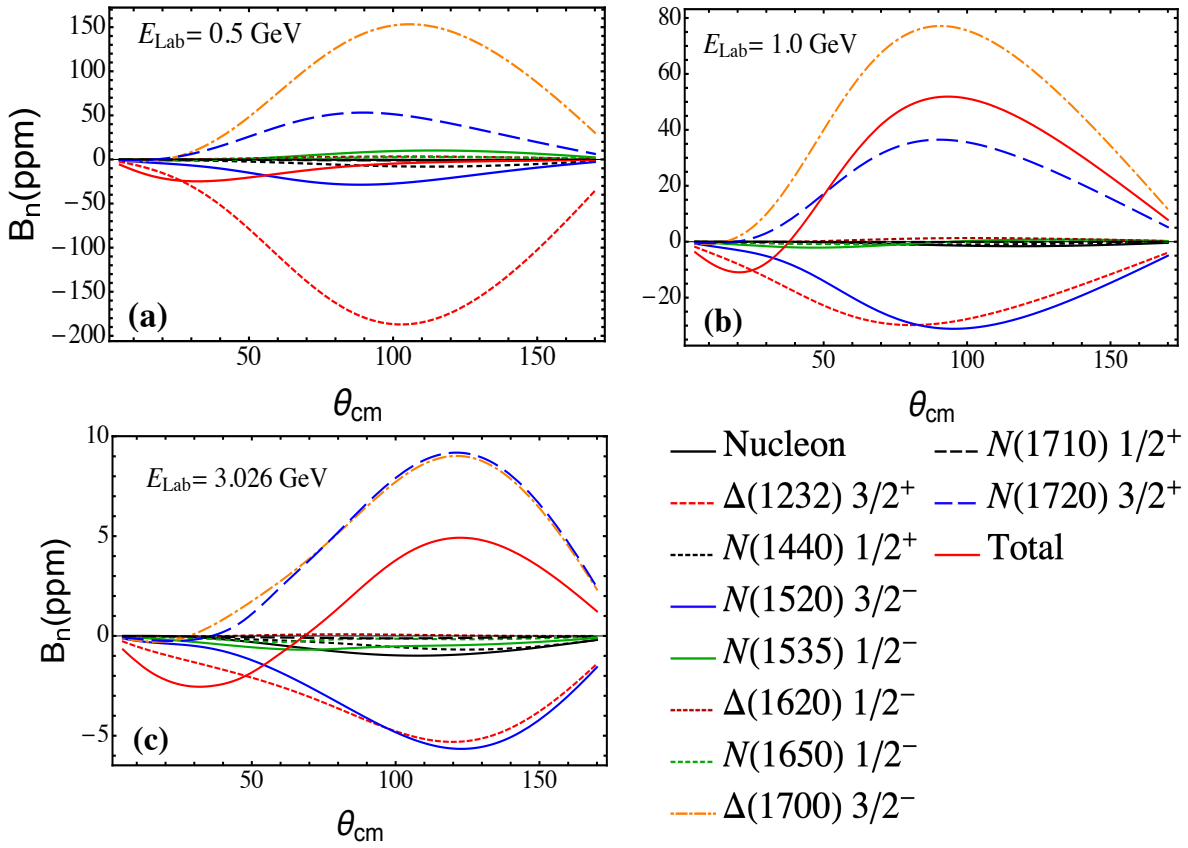

FIGURE 8.1: Elastic nucleon and resonance intermediate states contributions to the beam normal single spin asymmetry $B_{\rm n}$, along with the total, as a function of the centre-of-mass scattering angle $\theta_{\rm cm}$ at three representative beam energies E: (a) 0.5 GeV, (b) 1.0 GeV, and (c) 3.026 GeV, in the target rest (Lab) frame.

they are of different isospin and opposite parity. On the other hand, the two other higher mass, spin-3/2 states $\Delta(1700)3/2^-$ and $N(1720)3/2^+$, with opposite parity and different isospin, have positive contributions to the total $B_{\rm n}$. Therefore, no definite correlation between the isospin and parity is observed in the imaginary part of the TPE amplitude for the case of normally polarized electron and unpolarized proton elastic scattering. In the forward angles it is basically $\Delta(1232)3/2^+$ and $N(1520)3/2^-$ that are noticeable, while $\Delta(1700)3/2^-$ and $N(1720)3/2^+$ are the dominant contributors in the far-forward to backward scattering angles, except for the lower energies where $\Delta(1232)3/2^+$ has the highest magnitudes of $B_{\rm n}$ throughout the entire range of angles (Fig. 8.1(a)). It is interesting to note that the elastic nucleon intermediate state gives negligibly small effect in $B_{\rm n}$, unlike the real part of the TPE amplitude in case of unpolarized e-p elastic scattering. Overall, the net effect of all the resonances gives an oscillating $B_{\rm n}$ in the full

range of $\theta_{\rm cm}$. Note that for lower beam energies only the tail effects, due to non-zero finite width, of the higher mass resonances are accounted as the individual resonances require a minimum energy to be excited from the nucleon intermediate state. For example, at the beam energy $E_{\rm Lab} = 0.5$ GeV, the maximum W values covered in the numerical integration of Eq. (7.22) is $\sqrt{s} = M^2 + 2ME_{\rm Lab} \simeq 1.35$ GeV. Therefore, only the $\Delta(1232)3/2^+$ resonance contributes in the total $B_{\rm n}$ if the zero width approximation is considered. But in case of a more realistic assumption of constant finite non-zero resonance width all higher resonances will have the tail effect, and the total $B_{\rm n}$ is anticipated to be modified from that with zero width approximation. The effect of non-zero

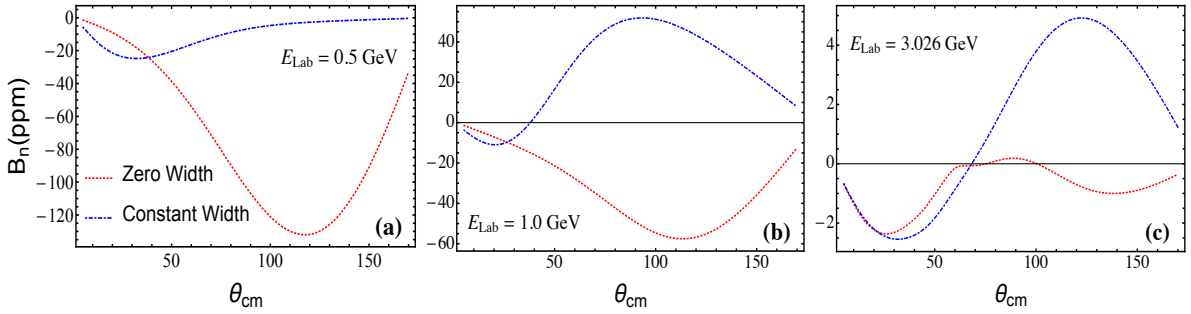

FIGURE 8.2: Non-zero finite resonance width effect on the calculated total beam normal single spin asymmetry $B_{\rm n}$ at three representative beam energies $E_{\rm Lab}$: (a) 0.5 GeV, (b) 1.0 GeV, and (c) 3.026 GeV. The dashed red line corresponds to zero width approximation and the solid blue line represents the results considering constant total decay width of each resonance.

resonance width in the total $B_{\rm n}$ is explained in Fig. 8.2 by comparing the results using zero width and constant total decay width approximations at the three same energy values of $E_{\rm Lab} = 0.5$ (a), 1.0 (b), and 3.026 (c) GeV. The consideration of constant total decay width, taken from Refs. [54, 137], with a Breit-Wigner distribution significantly alters $B_{\rm n}$ for all three energies except the forward directions. In case of sharp resonances, *i.e.* the zero width case, only the nucleon and $\Delta(1232)3/2^+$ intermediate states are accounted for $E_{\rm Lab} = 0.5$ GeV, and for $E_{\rm Lab} = 1.0$ GeV resonance states up to $N(1650)1/2^-$ are taken into account as the maximum allowed W is ~ 1.66 GeV for this case. The total exclusion of the two higher mass, spin-3/2 resonances $\Delta(1700)3/2^-$ and $N(1720)3/2^+$, mostly originating from the $\pi\pi N$ channel, significantly deviates $B_{\rm n}$ from the real value especially in the far-forward to backward scattering angles. The large positive contributions from $\Delta(1700)3/2^-$ and $N(1720)3/2^+$ (Fig. 8.1(a,b)) forces the total

B_n to oscillate and be positive in the backward direction as shown in Fig. 8.2(a,b) by the solid blue lines, whereas the zero width result remains significantly negative through out the entire range of θ_{cm}. At $E_{Lab} = 3.026$ GeV, all the resonance contributions are accounted in zero-width approximation as well but the two scenario are still surprisingly different at larger θ_{cm} (Fig. 8.2(c)). Contrary to the TPE correction to the unpolarized cross section, B_n is significantly modified by the width effect, since it involves the real excitation of resonances. Another possible reason for the dramatic influence of non-zero finite width in B_n would be the insignificant contribution from the most stable nucleon intermediate state, while it is the major contributor to the TPE cross section correction δ.

8.1.0.1 Experimental values

Beginning from the measurement of B_n by SAMPLE collaboration [133] in 2001 there have been several experiments performed both in the forward and backward scattering angles to date. One such measurement was performed by Q_{weak} experiment [138] in JLab Hall-C as part of the determination of the weak charge of proton in parity violating experiment with longitudinally polarized beam of electrons. The experiment was initiated with the electron beam of energy $E = 1.149$ GeV and a small four-momentum transfer squared $\langle Q^2 \rangle = 0.0248$ GeV^2 corresponding to a centre-of-mass scattering angle $\theta_{CM} = 14.62^o$ ($\theta_{Lab} = 7.9^o$). Figure 8.3 represents the calculated B_n at the beam energy of Q_{weak} experiment as function of θ_{CM} ranging up to the backward angle of 170^0 (Fig.8.3(a)). The right panel is a magnified version in θ_{cm} contrasting the Q_{weak} data with the prediction well. The red solid line considers only the elastic nucleon intermediate state which has a very tiny effect. The total value of B_n coming from the inelastic spin-1/2 and -3/2 resonance states along with nucleon itself is shown by the blue solid line. The Q_{weak} value of B_n is coherent in sign with the calculated value presented here. Even though the magnitudes are of the same order but the difference is still non-negligible. In the forward angles, B_n flips sign and reaches a peak value of about $\sim$ 80ppm at around $\theta_{CM} \simeq 90°$. Note that the resonance states considered in

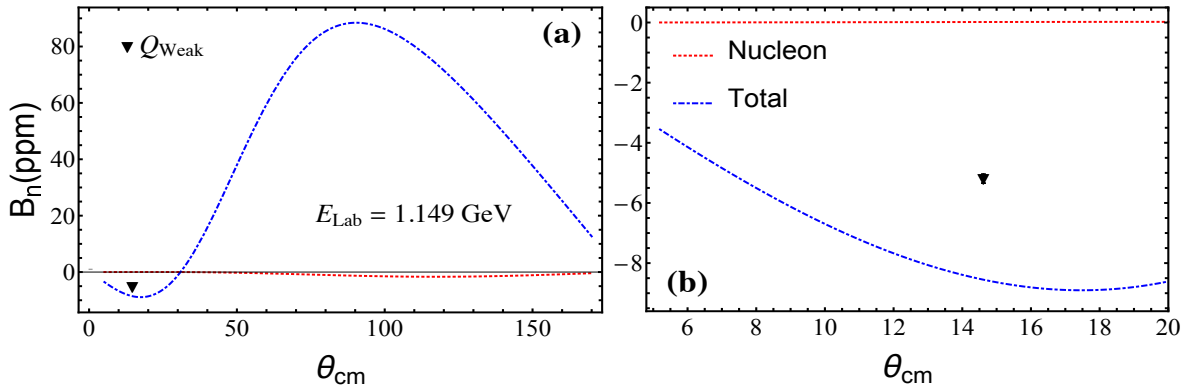

FIGURE 8.3: Beam normal single spin asymmetry B_n as a function of the centre-of-mass scattering angle θ_{cm} at the kinematics of the Q_{weak} [138] experiment. The red line represents the B_n from nucleon intermediate state alone, while the blue line accounts all the 4 and 3-star, spin-1/2, and -3/2 resonances along with the elastic nucleon. The data point is the measured B_n by Q_{weak} collaboration. A magnified version is presented in the right panel.

calculation of the imaginary part of the TPE amplitude covers the $\pi N, \pi\pi N$, and ηN decay channels as was considered in the real part of the TPE calculation. Thus the results presented here has the impact of resonances with the decay channels beyond πN.

Earlier in 2007, the HAPPEX collaboration [61] at Hall-A, JLab has published the measured value of $B_n = -6.58 \pm 1.47$ (stat) ± 0.24 (syst) ppm at higher beam energy $E_{Lab} \simeq 3$ GeV and forward angle $\theta_{cm} \simeq 16^\circ$. At the similar kinematics G0 collaboration [59] also performed the parity violating e-p scattering experiment and measured B_n in 2007. Later in 2011, they measured B_n at smaller values of beam energies $E_{Lab} = 0.362$ and 0.687 GeV but in the backward angles. Figure 8.4 compares the calculated result with the measured values from these two experimental groups. At the forward angles and $E_{Lab} \simeq 3.0$ GeV, the measured B_n from G0 experiment is in agreement within the uncertainty range whereas the HAPPEX data is well below the estimated value of my work. The G0 data at $E_{Lab} \simeq 0.362$ GeV and $\theta_{cm} \simeq 123^\circ$ are of the same order and sign even though the magnitudes are not within the error bar of the measured value [8.4(c)]. Surprisingly, the backward angle G0 data at the beam energy $E_{Lab} = 0.687$ GeV is of negative sign and relatively small magnitude whereas our calculation predicts it to be of positive sign with significantly higher magnitude

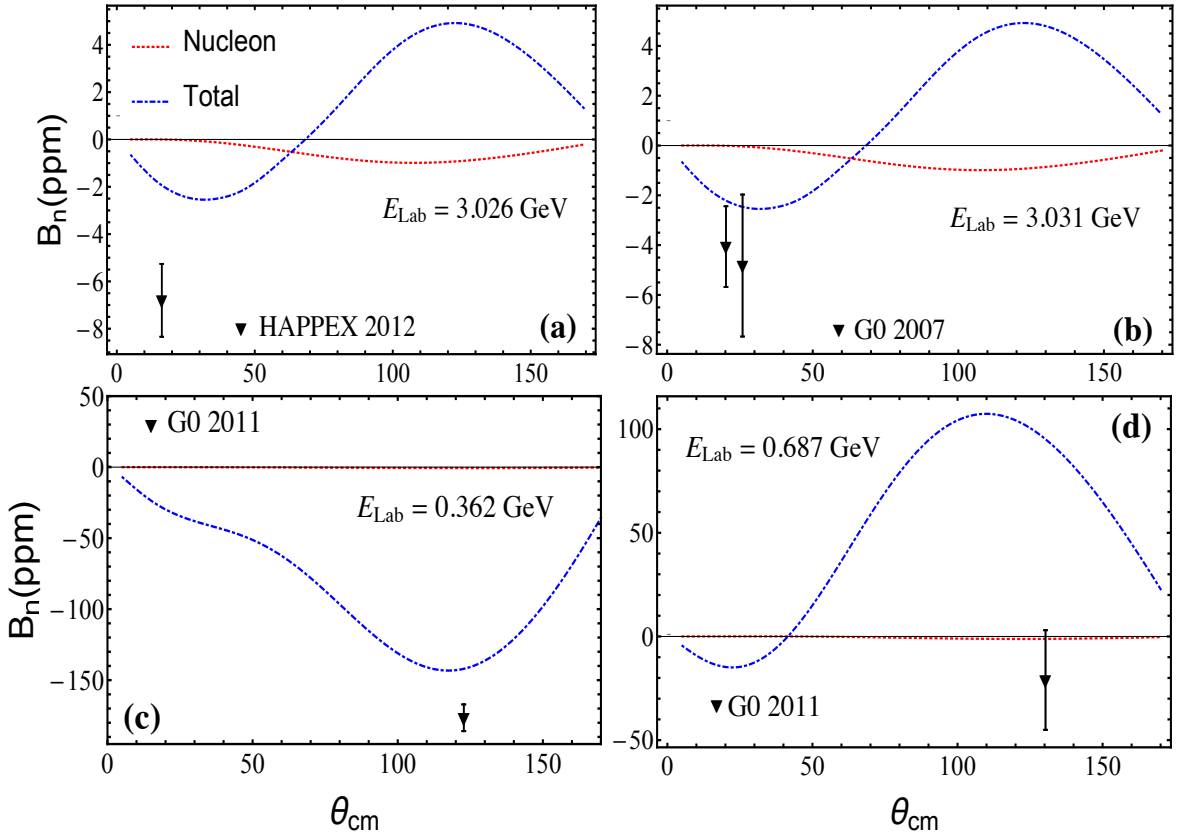

FIGURE 8.4: Beam normal single spin asymmetry $B_{\rm n}$ as a function of the centre-of-mass scattering angle $\theta_{\rm cm}$ at the kinematics of (a) HAPPEX Collaboration [60], (b-d) G0 Collaboration [58, 59]. The red line represents the nucleon intermediate state contribution, while the blue line accounts all the 4 and 3-star, spin-1/2, and -3/2 resonances along with elastic nucleon.

[8.4(d)]. It is important to note that the sign flip of $B_{\rm n}$ at $\theta_{\rm cm} \gtrsim 40^\circ$ is due to the tale effect of the two spin-3/2 resonances $\Delta(1700)3/2^-$ and $N(1720)3/2^+$, corresponding to the $\pi\pi N$ decay channel, which has very large contribution in the backward angles.

Starting from the 2005 measurement the A4 collaboration has initiated series of experiments [62–64], including the most recent one in 2020 [64], both in the forward and backward angles but mostly at smaller beam energies. The measurements in 2005 [62] and 2020[64] are in the near-forward angle around $\theta_{\rm cm} \simeq 50^\circ$, while the 2017 measurement considered the backward angle $\theta_{\rm cm} \simeq 150^\circ$. Considering the magnitude, the most recent measurement from A4 at $\theta_{\rm cm} \simeq 50^\circ$ underestimates $B_{\rm n}$ according to this numerical evaluation as shown in Figs. 8.5(a-c,e). The backward angle data from A4 [63] is comparatively closer to the calculated value for $E_{\rm Lab} = 0.315$ GeV (Fig. 8.5(a)), while for

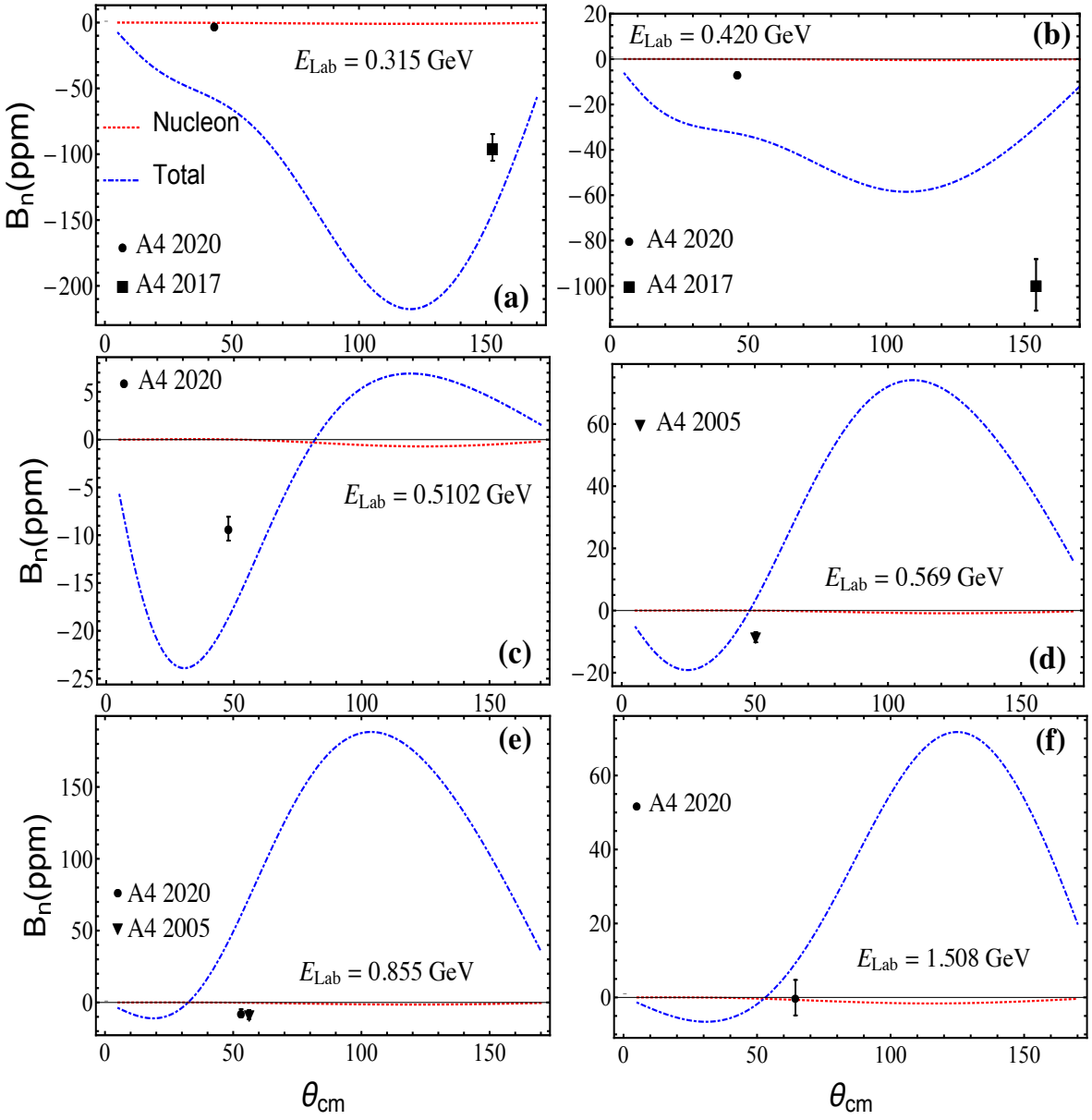

FIGURE 8.5: $B_{\rm n}$ vs. $\theta_{\rm cm}$ plots at the kinematics of the PVA4 Collaboration [62–64]. The filled circles are the most updated data in the forward angles from Ref. [64], filled squares in the backward angles are from Ref. [63], and the filled triangles are from Ref. [62].

$E_{\rm Lab} = 0.420$ GeV the scenario is even more frustrating (Fig. 8.5(b)). The calculated $B_{\rm n}$ of Fig. 8.5(c-f) flips the sign, due to the interplay between the effect of higher and lower mass resonances, near to the scattering angle $\theta_{\rm cm} \simeq 50^{\circ}$ where A4 collaboration [62, 64] has performed their measurement. Overall, in a naked eye, the calculated curves seem to be shifted, perhaps due to any missing effect, from the measured points along the horizontal axis. It is important to note here that the effect of the spin-5/2 resonances

is left as an outstanding task which might play a significant role in evaluation of B_n.

8.2 Target normal single spin asymmetry (A_n)

I begin this section with an illustration of the numerically calculated results of target normal single spin asymmetry A_n at the beam energies corresponding to the first non-zero experimental determination of the quantity [135], but for neutron target, in addition to the lower energies $E_{Lab} = 0.5$ and 1.0 GeV. Figure 8.6 shows the contribution of elastic nucleon and nine spin-1/2 and -3/2 excited resonance intermediate states to the total A_n along with the net result. As anticipated, A_n is in the range of sub-percent to percent level, and keeps increasing with beam energy in the backward direction contrary to B_n. To further compare with B_n, the nucleon intermediate state alone has significant impact on the total A_n for any value of E. While there is an overall oscillation of A_n between the negative and positive values in the entire range of scattering angles, a closer look at the plots of Fig. 8.6 shows that the magnitude of the negative peak remains roughly constant but the negative half cycle shrinks in width with increasing beam energy.

It is interesting to note that in the forward angles, $\theta_{cm} \lesssim 20^\circ$, the only sizeable contribution comes from $\Delta(1232)3/2^+$. The other resonance and elastic nucleon effect becomes comparable with $\Delta(1232)3/2^+$ at relatively larger scattering angles. However, considering the total range of θ_{cm}, $\Delta(1232)3/2^+$ is still the highest contributor among all the resonances. At $E = 0.5$ GeV, it even exceeds the nucleon contribution in magnitude but with negative sign in the entire range of θ_{cm}. As energy increases, A_n from $\Delta(1232)3/2^+$ starts oscillating (Fig. 8.6(b,c)) as function of the scattering angle θ_{cm} with a reduced magnitude. Figure 8.6(d,e) shows, it again exceeds the elastic nucleon contribution at $\theta_{cm} \gtrsim 80^\circ$ and 60° for $E_{Lab} \simeq 2.4$ and 3.6 GeV, respectively.

Surprisingly, unlike B_n and the real part of TPE correction, A_n from the spin-3/2 state $N(1520)3/2^-$ is relatively insignificant for any value of energy E in the entire range of θ_{cm}. The two other spin-3/2 resonances $\Delta(1700)3/2^-$ and $N(1720)3/2^+$ have noticeable

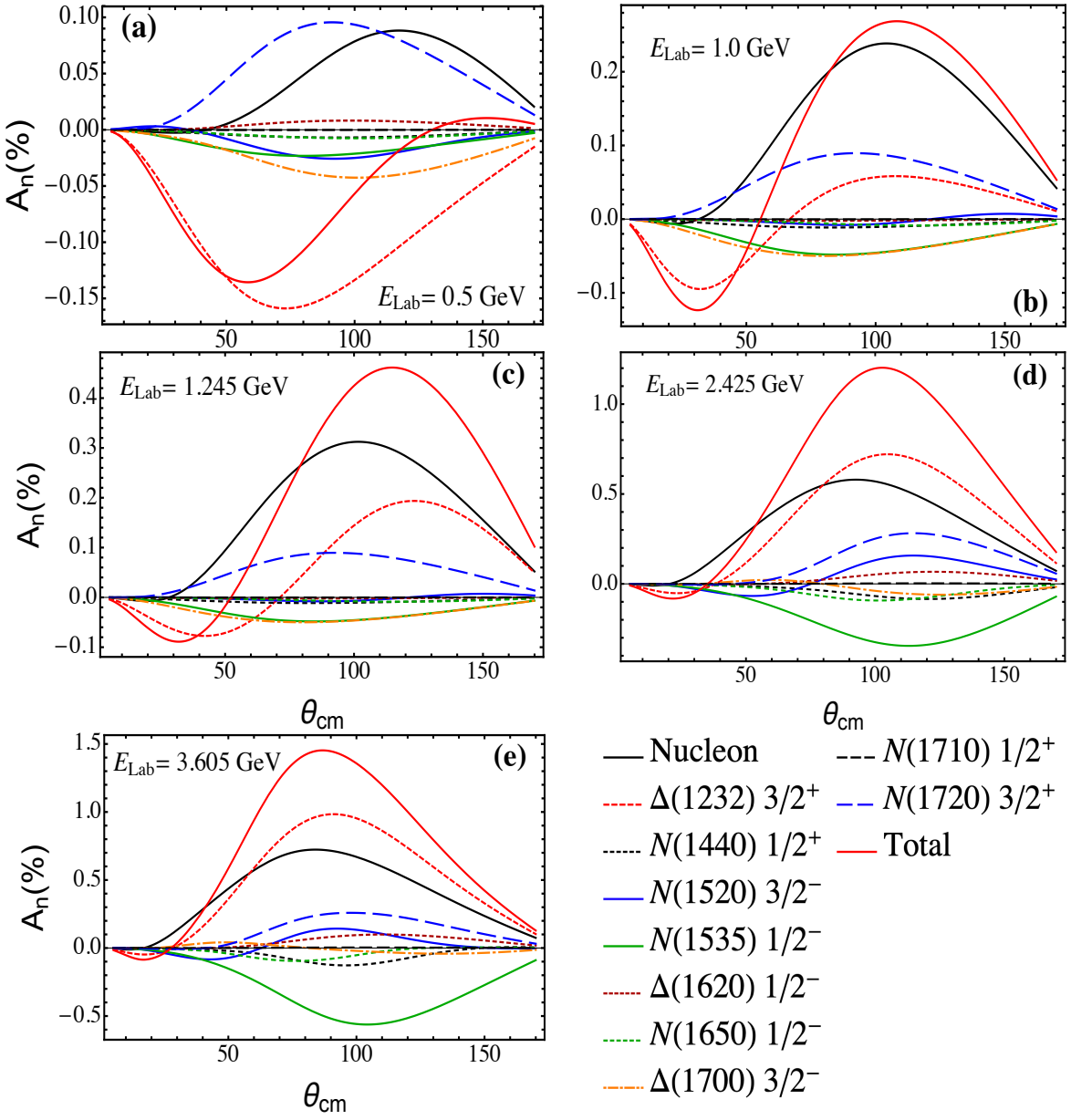

FIGURE 8.6: Elastic nucleon and individual resonance intermediate state contributions to the target normal single spin asymmetry A_n, along with the total, as a function of θ_{cm} at five representative beam energies E: (a) 0.5 GeV, (b) 1.0 GeV, (c) 1.245 GeV, (d) 2.425 GeV, and (e) 3.605 GeV, in the Lab frame.

contributions, especially for smaller E, but they are of opposite sign. The only non-negligible spin-1/2 state $N(1535)1/2^-$ significantly negates the net positive values of A_n, for $E \gtrsim 1$ GeV, from rest of the states in the far-forward to backward angles. Overall, the higher resonances beyond $\Delta(1232)3/2^+$ almost cancel out their net effect. As a consequence, the sum of elastic nucleon and $\Delta(1232)3/2^+$ contributions seems to be a

good approximation in evaluation of A_n.

Note that the width effect of the resonances in A_n is found minimal above the threshold energies of all the resonance excitation. Therefore, the discussion is left for Appendix. D.

8.2.0.1 Comparison with other sources

The only available measurement of A_n, that shows non-vanishing TPE effect in the scattering of electron off a polarized ^{3}He target in the quasi-elastic region, for neutron was performed in Jefferson Lab Hall A [135]. The term "quasi-elastic scattering" implies that the scattering is from one of the nucleons within the nucleus. However, the experiment scattered unpolarized electron beams of energies $E_{\rm Lab} = 1.245$, 2.425, and 3.605 GeV by the ^{3}He target polarized normal to the scattering plane. The scattered electrons were detected at the scattering angle $\theta_{\rm Lab} = 17^\circ$ corresponding to three different CM angles $\theta_{\rm cm} \simeq 32^\circ$, 41°, and 48° for the three respective beam energies. Note that the experiment finally determined the asymmetry A_n for the target neutron case, using a calculated input of $A_n = (0.01 \pm 0.22)\%$, $(0.24 \pm 2.96)\%$, and $(0.62 \pm 1.09)\%$, for the target proton, from Ref. [136] at the above mentioned beam energies. It is important to address here that the theoretical estimation [136] of A_n, that has been used as input in experimental determination of A_n, considered only the elastic intermediate state contribution.

Table 8.1 contrasts the numerical results obtained in this work at the kinematics of the JLab Hall A experiment [135] and the input A_n used in Ref. [135] from the source [136]. It is interesting to note that the estimation of A_n (proton target) from Ref. [136], assuming only the elastic nucleon intermediate state contributes, agrees very well with our calculated values considering nucleon intermediate state alone at $E_{\rm Lab} = 1.245$ and 2.425 GeV. But the inclusion of the resonance intermediate states alters A_n significantly. Hence, the calculated value in Ref. [136] seem to be an overestimation even though the calculated result of this work is still within the estimated large uncertainty range of

TABLE 8.1: A comparison of the target normal single spin asymmetry A_n (for proton target) from elastic nucleon (N), and sum of nucleon (N) and all the resonance intermediate states at the kinematics of Ref. [135]. The last two columns show the values used as input in Ref. [135] from the source [136] and third columns are the corresponding results calculated in this work.

E_{Lab}	A_n(This Work)		A_n([135, 136])	
(GeV)	Intermediate State			
	N	N + Resonances	N	N + Resonances
1.245	0.008	-0.089	0.01 ± 0.22	-
2.425	0.173	0.076	0.24 ± 2.96	-
3.605	0.400	0.501	0.62 ± 1.09	-

JLab Hall A experiment [135]. Coincidentally for $E_{Lab} = 3.605$ GeV, the used value of proton A_n in Ref. [135] is close to our total A_n including all the resonances.

Chapter 9

Conclusions

In this study we have applied the recently developed dispersive formalism of Ref. [46] to compute the TPE corrections to elastic electron-proton cross sections, including for the first time contributions from all $J^P = 1/2^{\pm}$ and $3/2^{\pm}$ excited intermediate state resonances with mass below 1.8 GeV. For the resonance electrocouplings at the hadronic vertices we employed newly extracted helicity amplitudes from the analysis of CLAS meson electroproduction data at $Q^2 \lesssim 5$ GeV^2 [54–56].

To assess the model dependence of the resonance calculations, we investigated the effects of finite Breit-Wigner resonance widths, comparing the TPE results for the point-like, constant width and variable width approximations. We found that for the point-like case kinematical thresholds produce artificial cusps at specific values of Q^2 and ε, however, these are effectively smoothed out across all kinematics when a nonzero width is introduced. The effect of using a constant or dynamical width was less dramatic, with the latter reducing somewhat the magnitude of some of the low-lying resonances, such as the $\Delta(1232)$, at low $Q^2 \sim 1$ GeV^2 and at backward angles.

We also examined the spin, isospin and parity dependence of the resonance contributions to the TPE amplitudes, finding large cancellations between the (negative) isospin $I = 1/2$ and the (positive) $I = 3/2$ intermediate states, as well as between the parity-even and parity-odd contributions. This behaviour is mostly driven by the dominance

of the (positive) $\Delta(1232)3/2^+$ and (negative) $N(1520)3/2^-$ contributions to the TPE amplitudes, especially at larger Q^2 values.

More specifically for the individual hadronic intermediate states, at low Q^2, $Q^2 \lesssim 1$ GeV^2, the nucleon elastic state dominates, with contributions from excited states there mostly negligible. For $Q^2 \approx (1--2)$ GeV^2, the $\Delta(1232)$ resonance starts to play a more important role, and here the sum of $N+\Delta(1232)$ provides a good approximation to the total TPE amplitude. At still larger Q^2, the $N(1520)$ gives the largest contribution among the higher-mass resonances, exceeding even the nucleon component for $Q^2 \gtrsim 4$ GeV^2. The higher-mass resonances each grow with increasing Q^2, but enter with different signs and largely cancel each other's contributions. Compared to the nucleon elastic component alone, the resonance excitations give rise to an overall enhancement of the TPE cross section correction for $Q^2 \gtrsim 3$ GeV^2.

The excited state resonance contributions generally provide some improvement of the phenomenological description of observables that are sensitive to TPE corrections, such as the ratios of e^+p to e^-p elastic cross sections measured recently in dedicated experiments at Jefferson Lab [116], Novosibirsk [115] and DESY [117]. Unfortunately most of these data are in kinematic regions where resonance contributions are not large, and in some cases the results are consistent with no TPE effect within the experimental uncertainty.

Among the inelastic processes involving the imaginary part of TPE amplitudes, the beam normal single spin asymmetry B_n has minimal contribution from the elastic nucleon intermediate state of TPE box diagram. At the lower beam energies (e.g. $E_{\rm Lab} = 0.5$ GeV) $\Delta(1232)3/2^+$ is the major contributor which is partially negated by the other isospin-3/2 and spin-3/2 state $\Delta(1700)3/2^-$. The next two more significant contributors (spin-3/2) $N(1520)3/2^-$ and $N(1720)3/2^+$ are again nullifying their net effect. With increasing beam energies, $\Delta(1700)3/2^-$ and $N(1720)3/2^+$ become dominant having the same sign (positive), while the combined negative effect of $\Delta(1232)3/2^+$ and $N(1520)3/2^-$ partially cancels out the effect of the two earlier states. However, for B_n, no definite correlation is observed between different spin, isospin and parity states.

Overall, the calculated total $B_{\rm n}$ falls down from the order of $\sim 10^{-4}$ to 10^{-6} in the range of $E_{\rm Lab} \simeq 0.5$ to 3.0 GeV respectively.

In case of $A_{\rm n}$, the higher resonances beyond $\Delta(1232)3/2^+$ almost have zero net effect. But, interestingly, unlike $B_{\rm n}$ (like δ), the elastic nucleon has significant contribution in the entire range of energy, $E_{\rm Lab} \simeq 0.5.$ to 3.6 GeV, considered in this work. The sum of nucleon and $\Delta(1232)3/2^+$ contribution is found nearly the net $A_{\rm n}$. Again, contrary to $B_{\rm n}$, the peak value of $A_{\rm n}$ against $\theta_{\rm cm}$ increases with energy by ~ 10 times in magnitude in the range from $E_{\rm Lab} = 0.5$ to 3.6 GeV.

Improvements on the theoretical front should involve exploration of the effects from spin-5/2 intermediate resonant states, as well as incorporation of nonresonant contributions [52] at larger Q^2 values. For the real part of TPE effect, future precision measurements at higher Q^2 values and backward angles (small ε), where the TPE effects are expected to be most significant, would be helpful for better constraining the TPE calculations. This would provide a more complete understanding of the relevance of TPE in the resolution of the proton G_E/G_M form factor ratio puzzle, and better elucidate the role of multi-photon effects in electron scattering in general.

Appendix A

Scattering Kinematics in CM frame

In CM frame, e-p elastic scattering kinematics are defined below:

$$k = (E,\, 0,\, 0,\, |\mathbf{k}|), \tag{A.1a}$$

$$p = (E_p,\, 0,\, 0,\, -|\mathbf{k}|), \tag{A.1b}$$

$$k' = (E,\, |\mathbf{k_1}| \sin\theta,\, \mathbf{0},\, |\mathbf{k_1}| \cos\theta), \tag{A.1c}$$

$$k_1 = (E_{k_1}, |\mathbf{k_1}| \sin\theta_{\mathbf{k_1}} \cos\phi_{\mathbf{k_1}}, |\mathbf{k_1}| \sin\theta_{\mathbf{k_1}} \sin\phi_{\mathbf{k_1}}, |\mathbf{k_1}| \cos\theta_{\mathbf{k_1}}). \tag{A.1d}$$

Here

$$|\mathbf{k}| = \sqrt{E^2 - m_e^2}, \tag{A.2a}$$

$$E_p = \sqrt{\boldsymbol{k}^2 + M^2}, \tag{A.2b}$$

$$|\mathbf{k_1}| = \sqrt{E_{k_1}^2 - m_e^2}. \tag{A.2c}$$

The incoming and intermediate electron energies E and E_{k_1} can be written in terms of the invariant Mandelstam variable s as

$$E = \frac{s - M^2 + m_e^2}{2\sqrt{s}}, \tag{A.3a}$$

$$E_{k_1} = \frac{s - W^2 + m_e^2}{2\sqrt{s}}. \tag{A.3b}$$

In the massless electron limit they get the simplified forms

$$E = \frac{s - M^2}{2\sqrt{s}}, \tag{A.4a}$$

$$E_{k_1} = \frac{s - W^2}{2\sqrt{s}}. \tag{A.4b}$$

The squared four-momentum transfers Q^2, Q_1^2, and Q_2^2 can also be given the form using s as

$$\begin{aligned} Q^2 &= -q^2, \\ &= -(k - k')^2, \\ &= 2(E^2 - m_e^2)(1 - \cos\theta), \\ &= \left[\frac{(s - M^2 + m_e^2)^2}{2s} - 2m_e^2\right](1 - \cos\theta). \end{aligned} \tag{A.5}$$

In the massless electron limit Q^2 becomes

$$Q^2 = \frac{(s - M^2)^2}{2s}. \tag{A.6}$$

The two other virtual photon four-momentum transfers squared can be derived as

$$\begin{aligned} Q_1^2 &= -q_2^2, \\ &= -(k - k_1)^2, \\ &= 2k.k_1 - 2m_e^2, \\ &= 2\Big[E\,E_{k_1} - |\boldsymbol{k}| \cdot |\boldsymbol{k}_1| \cos\theta_{k_1} - m_e^2\Big], \end{aligned} \tag{A.7a}$$

$$\begin{aligned} Q_2^2 &= -q_2^2, \\ &= (k_1 - k')^2, \\ &= 2k'.k_1 - 2m_e^2, \\ &= 2\Big[E\,E_{k_1} - |\boldsymbol{k}| \cdot |\boldsymbol{k}_1|\Big(\cos\theta\cos\theta_{k_1} + \sin\theta\sin\theta_{k_1}\cos\phi_{k_1}\Big) - m_e^2\Big]. \end{aligned} \tag{A.7b}$$

Since for the on-shell intermediate massless electron, $E_{k_1} = |\mathbf{k}_1|$ one can write Q_1^2 and Q_2^2 in a simplified form as

$$Q_1^2 = 2EE_{k_1}(1 - \cos\theta_{k_1}), \tag{A.8a}$$

$$Q_2^2 = 2EE_{k_1}(1 - \cos\theta\cos\theta_{k_1} - \sin\theta\sin\theta_{k_1}\sin\phi_{k_1}). \tag{A.8b}$$

Appendix B

Generalized form factors

B.1 Imaginary part of form factors for $\Delta(1232)3/2^+$

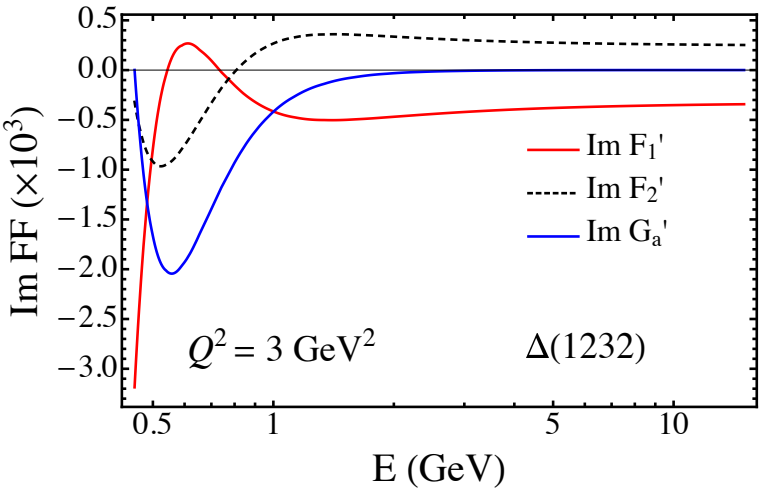

FIGURE B.1: Imaginary part of the form factors F_1', F_2', and G_a' as a function of energy E for $\Delta(1232)3/2^+$ intermediate state at $Q^2 = 3$ GeV^2. Note that the energy is in logarithmic scale.

B.2 Imaginary part of form factors for all resonances

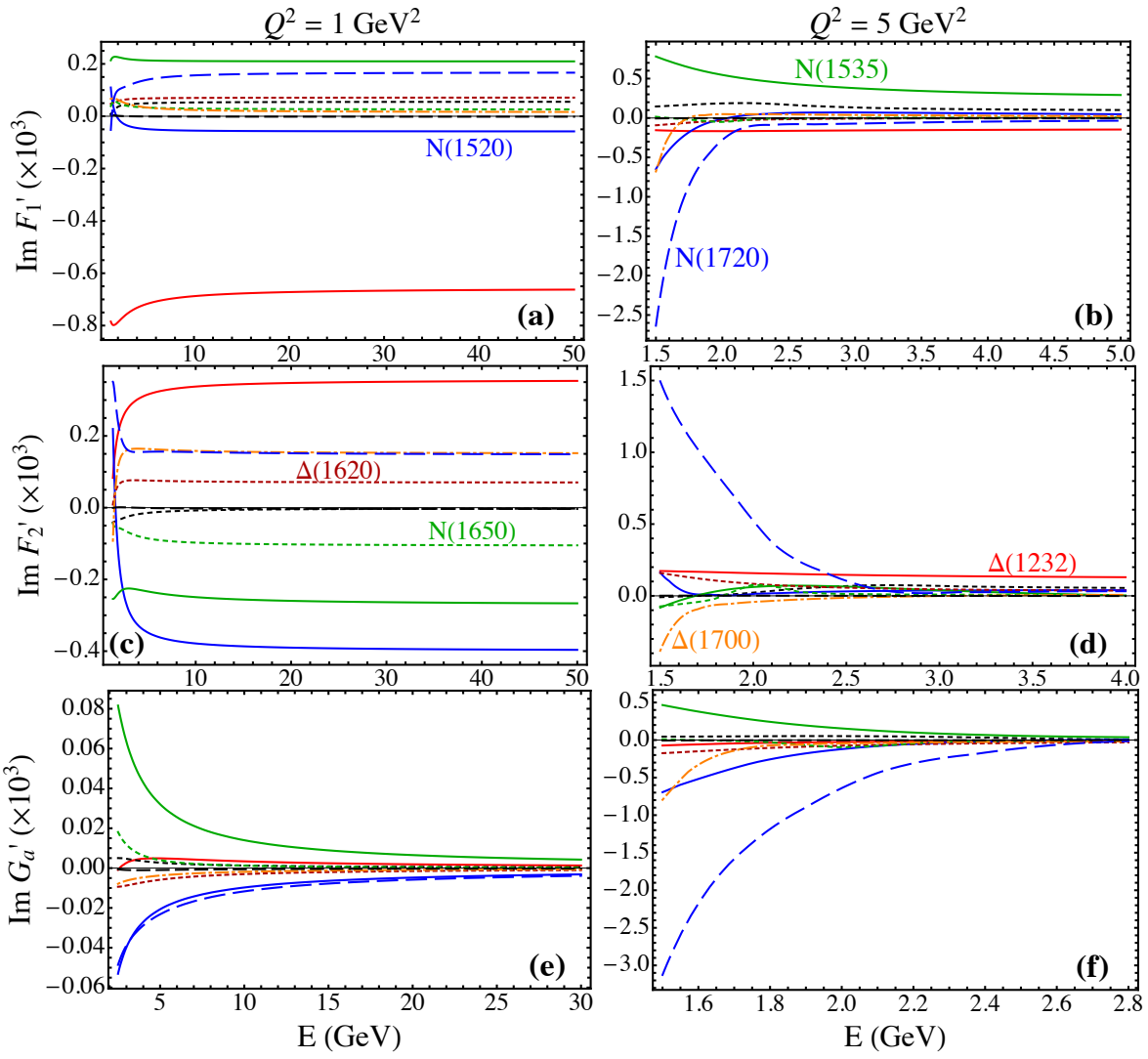

FIGURE B.2: Imaginary part of the form factors F_1' (top row), F_2' (middle row), and G_a' (bottom row) for all the resonance intermediate states as a function of energy E at fixed $Q^2 = 1$ GeV^2 (left panel) and $Q^2 = 5$ GeV^2 (right panel).

B.3 Real part of the form factors

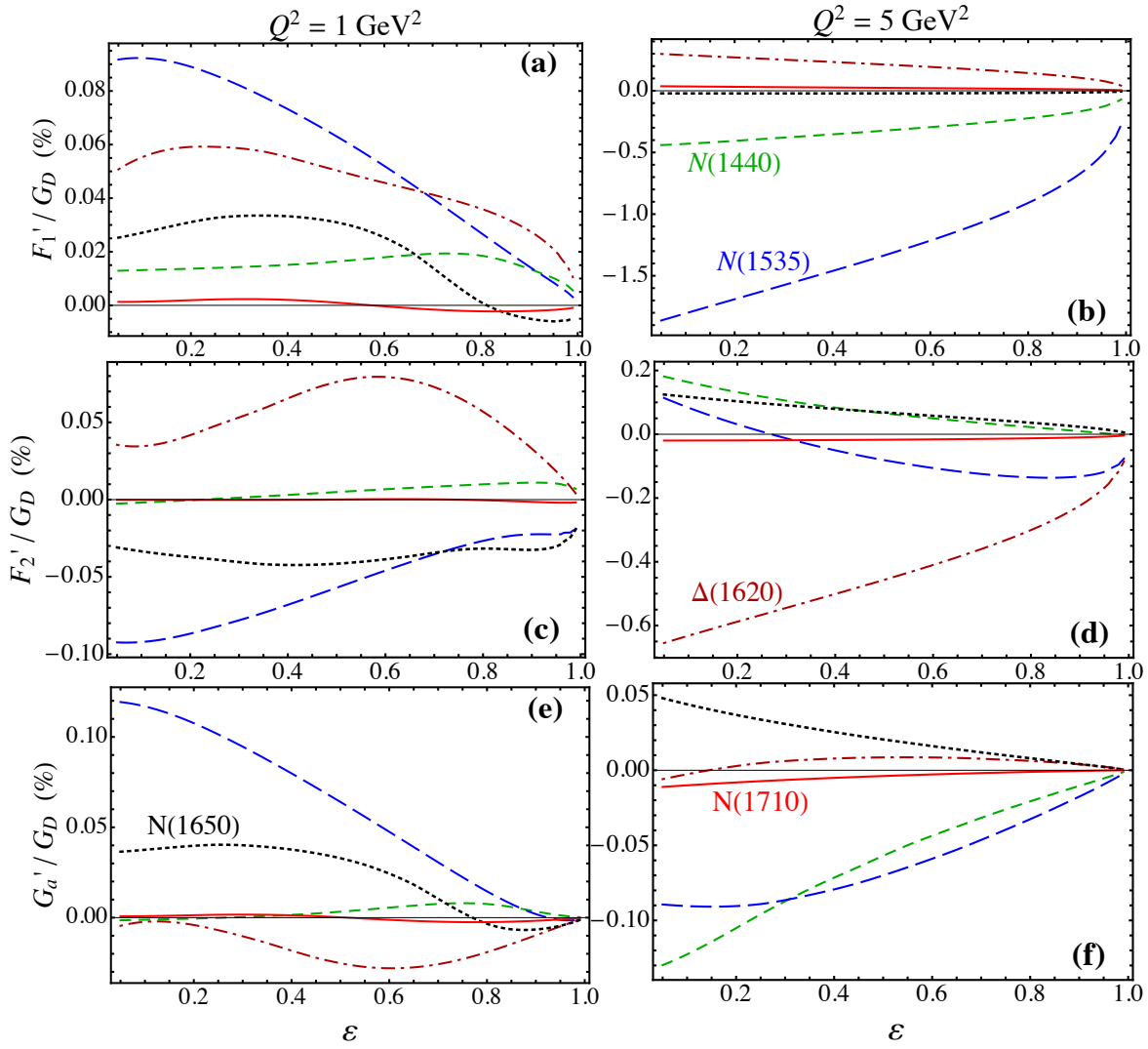

FIGURE B.3: Real part of the form factors F_1' (top row), F_2' (middle row), and G_a' (bottom row) for $N(1440)1/2^+$, $N(1535)1/2^-$, $\Delta(1620)1/2^-$, $N(1650)1/2^-$, and $N(1720)1/2^+$ resonance intermediate states as a function of energy E at fixed $Q^2 = 1$ GeV^2 (left panel) and $Q^2 = 5$ GeV^2 (right panel).

Appendix C

Maximon-Tjon vs. Mo-Tsai prescriptions

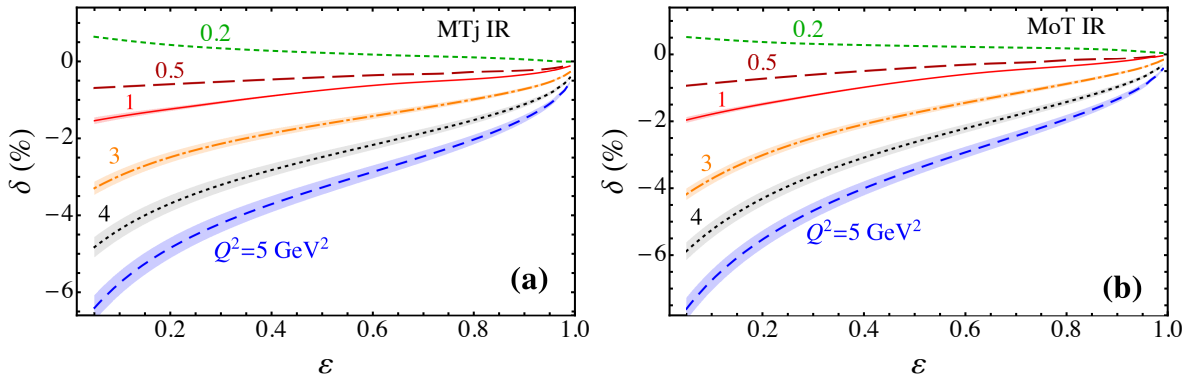

FIGURE C.1: Comparison of the IR finite TPE correction δ (in %) using the treatments of (a) Maximon and Tjon [76], and (b) Mo and Tsai [75], to separate the IR divergent part from the hard TPE. The chosen kinematics are the same as Fig. 6.6, *i.e.* at $Q^2 = 0.2$ GeV^2 (green dashed line), 0.5 GeV^2 (dark red long-dashed), 1 GeV^2 (red solid), 3 GeV^2 (orange dot-dashed), 4 GeV^2 (black dotted), and 5 GeV^2 (blue dashed).

Figure C.1 contrasts the model dependence of the soft photon treatment in total TPE correction δ, including the effect of elastic nucleon and all the discussed resonance intermediate states. The left panel shows the correction using the Maximon-Tjon [76] method of treating the soft photon limit, while the right panel represents the same from the Mo-Tsai [75] prescription. The later treatment enhances the magnitude by $\sim 1.0 - 1.2\%$ in the backward angles ($\varepsilon \lesssim 0.1$) for the highest value of $Q^2 = 5$ GeV^2.

The nonlinearity in δ vs. ε curve is also increased with the second method of IR divergence control. Therefore, it is obvious that one needs to be cautious during any reanalysis of e-p scattering data regarding the soft photon treatment.

Appendix D

Width effect in A_n

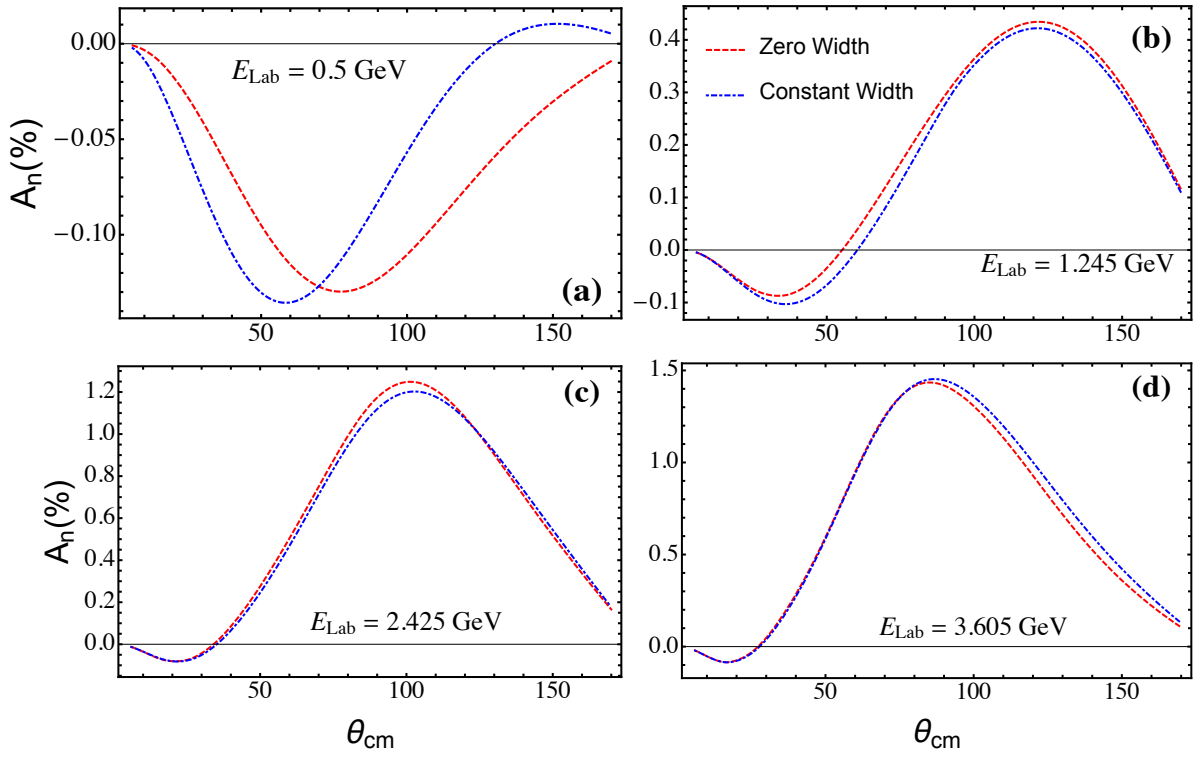

FIGURE D.1: Effect of constant total decay width and zero-width approximation of resonance intermediate states of TPE box diagram in A_n. The red dashed lines represent the results assuming zero-width approximation and the blue dot-dashed lines correspond to that assuming a constant total decay width in Breit-Wigner distribution.

The width effect of the resonances in A_n is shown in Fig. D.1. Clearly the effect is negligible above the threshold energies of all the resonance excitation (Fig. D.1(b-d)).

However, for lower beam energies (e.g. $E_{\rm Lab} = 0.5$ GeV), the difference between the zero-width and a constant total decay width with a Breit-Wigner distribution cases is non-negligible as the effect of most of the higher resonances are absent in the zero-width approximation. The tale effect of the higher resonances (beyond $\Delta(1232)3/2^+$) alters A_n from the sharp resonance consideration, as shown in Fig. D.1(a).

Bibliography

[1] E. Rutherford, The London, Edinburgh, and Dublin Philosophical Magazine and Journal of Science **21**, 669 (1911).

[2] R. Walker *et al.*, Phys. Rev. D **49**, 5671 (1994).

[3] L. Andivahis *et al.*, Phys. Rev. D **50**, 5491 (1994).

[4] I. Qattan *et al.*, Phys. Rev. Lett. **94**, 142301 (2005).

[5] M. K. Jones *et al.*, Phys. Rev. Lett. **84**, 1398 (2000).

[6] O. Gayou *et al.*, Phys. Rev. Lett. **88**, 092301 (2002).

[7] A. Puckett *et al.*, Phys. Rev. Lett. **104**, 242301 (2010).

[8] A. Puckett *et al.*, Phys. Rev. C **85**, 045203 (2012).

[9] V. Punjabi *et al.*, Phys. Rev. C **71**, 055202 (2005).

[10] P. Blunden, W. Melnitchouk, and J. Tjon, Phys. Rev. Lett. **91**, 142304 (2003).

[11] P. A. Guichon and M. Vanderhaeghen, Phys. Rev. Lett. **91**, 142303 (2003).

[12] J. Arrington, P. Blunden, and W. Melnitchouk, Prog. Part. Nucl. Phys. **66**, 782 (2011).

[13] M. D. Schwartz, *Quantum field theory and the standard model* (Cambridge University Press, 2014).

[14] F. Halzen and A. D. Martin, *Quarks & Leptons: An Introductory Course In Modern Particle Physics* (John Wiley & Sons, 2008).

[15] A. W. Thomas and W. Weise, *The structure of the nucleon* (John Wiley & Sons, 2001).

[16] D. Yennie, M. Levy, and D. Ravenhall, Rev. Mod. Phys. **29**, 144 (1957).

[17] F. Ernst, R. Sachs, and K. Wali, Phys. Rev. **119**, 1105 (1960).

[18] M. N. Rosenbluth, Phys. Rev. **79**, 615 (1950).

[19] R. Walker *et al.*, Phys. Lett. B **224**, 353 (1989).

[20] M. Christy *et al.*, Phys. Rev. C **70**, 015206 (2004).

[21] J. Bernauer *et al.*, Phys. Rev. C **90**, 015206 (2014).

[22] I. A. Qattan, nucl-ex/0610006 (2006).

[23] T. Janssens, R. Hofstadter, E. Hughes, and M. Yearian, Phys. Rev. **142**, 922 (1966).

[24] J. Litt *et al.*, Phys. Lett. B **31**, 40 (1970).

[25] W. Bartel *et al.*, Nucl. Phys. B **58**, 429 (1973).

[26] A. Sill *et al.*, Phys. Rev. D **48**, 29 (1993).

[27] P. Bosted *et al.*, Phys. Rev. Lett. **68**, 3841 (1992).

[28] C. Berger, V. Burkert, G. Knop, B. Langenbeck, and K. Rith, Phys. Lett. B **35**, 87 (1971).

[29] A. Afanasev, P. Blunden, D. Hasell, and B. Raue, Prog. Part. Nucl. Phys. **95**, 245 (2017).

[30] O. Gayou *et al.*, Phys. Rev. C **64**, 038202 (2001).

[31] G. Ron *et al.*, Phys. Rev. Lett. **99**, 202002 (2007).

[32] G. Ron *et al.*, Phys. Rev. C **84**, 055204 (2011).

[33] G. MacLachlan, A. Aghalaryan, and A. Ahmidouch, (2006).

[34] X. Zhan *et al.*, Phys. Lett. B **705**, 59 (2011).

[35] J. Arrington, Phys. Rev. C **68**, 034325 (2003).

[36] J. Arrington, Phys. Rev. C **69**, 022201 (2004).

[37] P. Blunden, W. Melnitchouk, and J. Tjon, Phys. Rev. C **72**, 034612 (2005).

[38] H.-Q. Zhou and S. N. Yang, Eur. Phys. J. A **51**, 105 (2015).

[39] A. Gramolin and D. Nikolenko, Phys. Rev. C **93**, 055201 (2016).

[40] S. Kondratyuk, P. Blunden, W. Melnitchouk, and J. Tjon, Phys. Rev. Lett. **95**, 172503 (2005).

[41] S. Kondratyuk and P. Blunden, Phys. Rev. C **75**, 038201 (2007).

[42] Y.-C. Chen, A. Afanasev, S. Brodsky, C. Carlson, and M. Vanderhaeghen, Phys. Rev. Lett. **93**, 122301 (2004).

[43] A. V. Afanasev, S. J. Brodsky, C. E. Carlson, Y.-C. Chen, and M. Vanderhaeghen, Phys. Rev. D **72**, 013008 (2005).

[44] N. Kivel and M. Vanderhaeghen, Phys. Rev. Lett. **103**, 092004 (2009).

[45] D. Borisyuk and A. Kobushkin, Phys. Rev. D **79**, 034001 (2009).

[46] P. Blunden and W. Melnitchouk, Phys. Rev. C **95**, 065209 (2017).

[47] M. Gorchtein, Phys. Lett. B **644**, 322 (2007).

[48] D. Borisyuk and A. Kobushkin, Phys. Rev. C **78**, 025208 (2008).

[49] D. Borisyuk and A. Kobushkin, Phys. Rev. C **89**, 025204 (2014).

[50] D. Borisyuk and A. Kobushkin, Phys. Rev. C **92**, 035204 (2015).

[51] O. Tomalak and M. Vanderhaeghen, Eur. Phys. J. A **51**, 24 (2015).

[52] O. Tomalak, B. Pasquini, and M. Vanderhaeghen, Phys. Rev. D **96**, 096001 (2017).

[53] I. G. Aznauryan and V. D. Burkert, Prog. Part. Nucl. Phys. **67**, 1 (2012).

[54] A. N. Hiller Blin *et al.*, Phys. Rev. C **100**, 035201 (2019).

[55] V. I. Mokeev *et al.*, Phys. Rev. C **86**, 035203 (2012).

[56] V. I. Mokeev *et al.*, Phys. Rev. C **80**, 045212 (2009).

[57] R. D. Carlini *et al.*, arXiv:1202.1255 (2012).

[58] D. Androić *et al.*, Phys. Rev. Lett. **107**, 022501 (2011).

[59] D. Armstrong *et al.*, Phys. Rev. Lett. **99**, 092301 (2007).

[60] S. Abrahamyan *et al.*, Phys. Rev. Lett. **109**, 192501 (2012).

[61] L. Kaufmana, Transverse beam asymmetries measured from ^{4}he and hydrogen targets, in *Proceedings of The 3rd Workshop From Parity Violation to Hadronic Structure and more...*, pp. 135–137, Springer, 2007.

[62] F. Maas *et al.*, Phys. Rev. Lett. **94**, 082001 (2005).

[63] D. B. Ríos *et al.*, Phys. Rev. Lett. **119**, 012501 (2017).

[64] B. Gou *et al.*, Phys. Rev. Lett. **124**, 122003 (2020).

[65] M. Gorchtein and C. J. Horowitz, Phys. Rev. C **77**, 044606 (2008).

[66] B. Pasquini and M. Vanderhaeghen, Phys. Rev. C **70**, 045206 (2004).

[67] B. Pasquini and M. Vanderhaeghen, Eur. Phys. J. A **24**, 29 (2005).

[68] M. Gorchtein, P. Guichon, and M. Vanderhaeghen, Nucl. Phys. A **741**, 234 (2004).

[69] M. Gorchtein, Phys. Rev. C **73**, 055201 (2006).

[70] M. Gorchtein, Phys. Lett. B **644**, 322 (2007).

[71] A. V. Afanasev and N. Merenkov, Phys. Lett. B **599**, 48 (2004).

[72] J. Arrington, W. Melnitchouk, and J. Tjon, Phys. Rev. C **76**, 035205 (2007).

[73] J. Ahmed, P. Blunden, and W. Melnitchouk, Phys. Rev. C **102**, 045205 (2020).

[74] Y.-S. Tsai, Phys. Rev. **122**, 1898 (1961).

[75] L. W. Mo and Y.-S. Tsai, Rev. Mod. Phys. **41**, 205 (1969).

[76] L. Maximon and J. Tjon, Phys. Rev. C **62**, 054320 (2000).

[77] Y. Tsai, slac-pub-0848 (1971), 1971.

[78] R. Gerasimov and V. Fadin, Physics of Atomic Nuclei **78**, 69 (2015).

[79] R. P. Feynman, Phys. Rev. **76**, 769 (1949).

[80] Y. S. Tsai, Phys. Rev. **120**, 269 (1960).

[81] A. Gramolin *et al.*, J. Phys. G **41**, 115001 (2014).

[82] H. Jones and M. Scadron, Ann. Phys. (NY) **81**, 1 (1973).

[83] R. Devenish, T. Eisenschitz, and J. Körner, Phys. Rev. D **14**, 3063 (1976).

[84] M. L. Goldberger, Y. Nambu, and R. Oehme, Ann. Phys. **2**, 226 (1957).

[85] Y. C. Chen, A. Afanasev, S. Brodsky, C. Carlson, and M. Vanderhaeghen, Phys. Rev. Lett. **93**, 122301 (2004).

[86] W. Beenakker and A. Denner, Nucl. Phys. B **338**, 349 (1990).

[87] D. Borisyuk and A. Kobushkin, Phys. Rev. C **75**, 038202 (2007).

[88] D. Borisyuk and A. Kobushkin, Phys. Rev. C **86**, 055204 (2012).

[89] O. Tomalak, B. Pasquini, and M. Vanderhaeghen, Phys. Rev. D **95**, 096001 (2017).

[90] A. Radyushkin, Phys. Rev. D **58**, 114008 (1998).

[91] P. Mergell, U.-G. Meißner, and D. Drechsel, Nucl. Phys. A **596**, 367 (1996).

[92] E. J. Brash, A. Kozlov, S. Li, and G. M. Huber, Phys. Rev. C **65**, 051001 (2002).

[93] G. Passarino and M. Veltman, Nucl. Phys. B **160**, 151 (1979).

[94] G. Van Oldenborgh and J. A. Vermaseren, Zeitschrift für Physik C Particles and Fields **46**, 425 (1990).

[95] W. A. McKinley Jr and H. Feshbach, Phys. Rev. **74**, 1759 (1948).

[96] S. Kondratyuk and O. Scholten, Phys. Rev. C **64**, 024005 (2001).

[97] J. Tjon, P. Blunden, and W. Melnitchouk, Phys. Rev. C **79**, 055201 (2009).

[98] K. Nagata, H. Q. Zhou, C. W. Kao, and S. N. Yang, Phys. Rev. C **79**, 062501 (2009).

[99] H. Q. Zhou, C. W. Kao, S. N. Yang, and K. Nagata, Phys. Rev. C **81**, 035208 (2010).

[100] K. M. Graczyk, Phys. Rev. C **88**, 065205 (2013).

[101] I. Lorenz, U.-G. Meißner, H.-W. Hammer, and Y.-B. Dong, Phys. Rev. D **91**, 014023 (2015).

[102] M. E. Peskin and D. V. Schroeder, *An Introduction to Quantum Field Theory* (Westview Press, 1995).

[103] R. E. Cutkosky, J. Math. Phys. **1**, 429 (1960).

[104] D. Drechsel, S. Kamalov, and L. Tiator, Eur. Phys. J. A **34**, 69 (2007).

[105] I. Qattan, D. Homouz, and M. Riahi, Phys. Rev. C **97**, 045201 (2018).

[106] I. Qattan, A. Alsaad, and J. Arrington, Phys. Rev. C **84**, 054317 (2011).

[107] I. Qattan, Phys. Rev. C **95**, 055205 (2017).

[108] A. Browman, F. Liu, and C. Schaerf, Phys. Rev. **139**, B1079 (1965).

[109] J. Mar *et al.*, Phys. Rev. Lett. **21**, 482 (1968).

[110] R. Anderson *et al.*, Phys. Rev. Lett. **17**, 407 (1966).

[111] W. Bartel *et al.*, Phys. Lett. B **25**, 242 (1967).

[112] B. Bouquet *et al.*, Phys. Lett. B **26**, 178 (1968).

[113] S. Hartwig *et al.*, Lett. Nuo. Cim. **12**, 30 (1975).

[114] D. Yount and J. Pine, Phys. Rev. **128**, 1842 (1962).

[115] I. Rachek *et al.*, Phys. Rev. Lett. **114**, 062005 (2015).

[116] D. Rimal *et al.*, Phys. Rev. C **95**, 065201 (2017).

[117] B. Henderson *et al.*, Phys. Rev. Lett. **118**, 092501 (2017).

[118] E. Tomasi-Gustafsson, M. Osipenko, E. Kuraev, and Y. M. Bystritskiy, Physics of Atomic Nuclei **76**, 937 (2013).

[119] M. Meziane *et al.*, Phys. Rev. Lett. **106**, 132501 (2011).

[120] C. E. Carlson and M. Vanderhaeghen, Ann. Rev. Nucl. Part. Sci. **57**, 171 (2007).

[121] M. Veltman and G. Hooft, Nuclear Physics: B **153**, 365 (1979).

[122] R. Mertig, M. Böhm, and A. Denner, Computer Physics Communications **64**, 345 (1991).

[123] V. Shtabovenko, R. Mertig, and F. Orellana, Computer Physics Communications **207**, 432 (2016).

[124] T. Hahn and M. Perez-Victoria, Computer Physics Communications **118**, 153 (1999).

[125] CLAS Collaboration, Clas resonance electrocouplings, `https://userweb.jlab.org/~isupov/couplings/`.

[126] J. Kelly, Phys. Rev. C **70**, 068202 (2004).

[127] S. Venkat, J. Arrington, G. A. Miller, and X. Zhan, Phys. Rev. C **83**, 015203 (2011).

[128] M. Ripani *et al.*, Nucl. Phys. **A672**, 220 (2000).

[129] M. Tanabashi *et al.*, Phys. Rev. D **98**, 030001 (2018).

[130] M. Dugger *et al.*, Physical Review C **79**, 065206 (2009).

[131] A. De Rújula, J. Kaplan, and E. De Rafael, Nucl. Phys. B **35**, 365 (1971).

[132] D. Androic *et al.*, arXiv:2006.12435 (2020).

[133] S. Wells *et al.*, Physical Review C **63**, 064001 (2001).

[134] D. Drechsel, O. Hanstein, S. Kamalov, and L. Tiator, Nucl. Phys. A **645**, 145 (1999).

[135] Y.-W. Zhang *et al.*, Phys. Rev. Lett. **115**, 172502 (2015).

[136] A. Afanasev, I. Akushevich, and N. Merenkov, Nucleon compton scattering with two space–like photons, in *Exclusive Processes At High Momentum Transfer*, pp. 142–150, World Scientific, 2002.

[137] Particle Data Group, online review (2017), `http://pdg.lbl.gov/2017/listings/contents_listings.html`.

[138] B. P. Waidyawansa *et al.*, arXiv:1604.04602 (2016).